

NORTHWESTERN UNIVERSITY

Surface Functionalization and DNA-Mediated Colloidal Crystal Engineering of
Metal-Organic Framework Nanoparticles

A DISSERTATION

SUBMITTED TO THE GRADUATE SCHOOL

IN PARTIAL FULFILLMENT OF THE REQUIREMENTS

for the degree

DOCTOR OF PHILOSOPHY

Field of Chemistry

By

Shunzhi Wang

EVANSTON, ILLINOIS

December 2018

ABSTRACT

Surface Functionalization and DNA-Mediated Colloidal Crystal Engineering of

Metal-Organic Framework Nanoparticles

Shunzhi Wang

Metal-organic frameworks (MOFs) are a class of highly modular materials with well-defined three-dimensional architectures, permanent porosity, and diverse chemical functionalities, which show promise for a wide range of applications, including gas storage and separation, drug delivery, chemical sensing, and catalysis. Nanoparticle forms of MOFs have similar properties but are dispersible in solution, and therefore could serve as useful components in biological probes, membrane separation materials, and building blocks for colloidal crystal engineering. In this dissertation, we present a series of fundamental studies centered on the synthesis and surface functionalization of MOF nanoparticles (MOF NPs), with an emphasis on the realization of uniform NP size and phase, surface functionalization of MOF NPs with DNA, and the incorporation of MOF NPs as a new class of building blocks for colloidal crystal engineering strategies.

The first chapter provides a history and introduction to the study of MOF NPs, with an emphasis on how such structures form and grow, and ways to address their external surface architectures with organic ligands. Chapter two describes two chemical approaches that we developed to control the size, shape, and phase uniformity of MOF NPs. The critical role of a series of chemical modulators in the crystallization process of MOF NPs is evaluated. These

modulators significantly influence the resulting MOF NP polydispersity and colloidal stability. Next, we introduce a straightforward electrostatic based purification strategy to separate mixed-phase MOF NPs, which allows one to access pure phase MOF NPs for further investigations. In chapter three, we discuss a post-synthetic surface functionalization strategy that selectively modifies the external surface of MOF NPs with phosphate-terminated lipids. Strong coordination between coordinatively unsaturated metal sites and phosphate surface ligands promotes efficient surface modification under mild conditions with retained internal porosity. The fourth chapter describes the first general and direct method to interface MOF NPs with DNA employing terminal phosphate modified oligonucleotides appended to nine archetypical MOFs at high surface coverage. Design rules emerge from this study that predict the surface DNA coverage as a function of MOF surface metal node density, metal cluster connectivity, and metal-phosphate bond strength. Further, we show that nucleic acid-MOF NP conjugates are promising for the intracellular delivery of functional proteins. Taking advantage of the unique programmability of DNA surface ligands, we describe in chapter five the realization of hierarchical colloidal crystal engineering incorporating DNA functionalized MOF NPs as a novel class of building blocks. Finally, chapter six summarizes these data and their impact, and puts them in context regarding future opportunities. Descriptions of the materials and methods used to synthesize these materials are included at the end of each chapter.

ACKNOWLEDGEMENTS

During my time in graduate school at Northwestern, I have always felt lucky to work with many people who have made my graduate experience enjoyable and memorable. Their guidance, support, critical insights, and discussions helped me to become a better scientist. I am sincerely grateful for their invaluable contributions to me and this thesis.

First and foremost, I would like to thank my advisor, Professor Chad Mirkin, for giving me the opportunity to work in such a fantastic research environment, the freedom I was given in pursuing my own research ideas, and for always challenging me to do better as a scientist. Chad has taught me a number of important skills, including the ability to think critically about my science and that of others, the ability to effectively and confidently communicate my research, and the desire to always pushing a field forward rather than following in the footsteps of others. Many thanks to my thesis committee, Professor David Harris, Professor Vinayak Dravid, and Professor Fraser Stoddart, for their helpful discussions throughout the last five years. In addition to my thesis committee, I would like to thank Professor Omar Farha for his mentorship, support and encouragement. Dr. Byeongdu Lee was an outstanding collaborator and was particularly helpful to my learning and understanding X-ray characterization techniques. Thanks to Prof. Teri Odom for invaluable scientific discussions. Special thanks to my undergraduate supervisors, Professor Wenbin Lin and Prof. Maurice Brookhart at UNC Chapel Hill, for first introducing me to scientific research and for their continuing support throughout my career.

Next, I would like to thank my mentors: Dr. William Morris and Dr. Youngeun Kim, who got me started at the Mirkin Lab and introduced me to the DNA mediated colloidal crystal engineering. Throughout graduate school, I am very lucky to have the opportunity to work with a group of talented collaborators and write paper together. I would like to thank: Dr. C. Michael McGuirk, Dr. Haixin Lin, Dr. Sarah Park, Dr. Hang Xing, Dr. Michael Ross, Dr. Jarad Mason, Shuya Wang, Yijun Liao, Andrea d'Aquino, Jinghan Zhu, Pengcheng Chen, Yuan Liu, Dr. Peng Li, Jingshan Du, Lin Sun, Dr. Anindita Das, Dr. Martin Girard.

In addition to my collaborators, I recall lessons, advice, and great memories from a number of friends and group mates who made me both a better scientist and a better person. These people include (though not exhaustively): Xiaoxiao Huang, Kacper Skakuj, Janet McMillan, Oliver Hayes, Dr. Qingyuan Lin, Dr. Jessie Ku, Dr. Mary Wang, Dr. Eileen Seo, Dr. Monica Guan, Dr. Liangliang Hao, Dr. Jose Mendez, Dr. Shu He, Wenjie Zhou, Ziyin Huang, Dr. Chuan Zhang, Taegon Oh, Dr. Ryan Thaner, Dr. Stacey Barnaby, Dr. Chuyang Cheng, Dr. Jessica Rouge, Dr. Mari Rosen, Dr. Jeffrey Brodin, Dr. Katherine Bujold, Dr. Xiaohan Zeng.

This dissertation would not have been possible without the support of my family. I would like to thank my parents, Dr. Tingjie Wang and Qun Guan. Nine years ago, they first sent me to the US for college, and throughout the years, they have always been there for me – whether it is to share my pleasure or to cheer me up at my lows. I couldn't feel luckier to have parents like them who are so understanding, supportive, and loving. I am extremely grateful for their continued support throughout all my endeavors. Lastly, a special thank you to Kexin Liu, who has been my closest friend and confidant since the start of this graduate school journey.

TABLE OF CONTENTS

ABSTRACT	2
ACKNOWLEDGEMENTS	4
TABLE OF CONTENTS	6
LIST OF FIGURES.....	9
CHAPTER ONE: Metal-Organic Framework Nanoparticles as a Novel Class of Modular Nanomaterials	14
1.1 Metal-Organic Frameworks at the Nanoscale	15
1.2 Approaches for the Synthesis of Uniform MOF Nanoparticles	17
1.3 Surface Functionalization Strategies	30
1.4 Beyond MOF Nanoparticles	40
CHAPTER TWO: Synthetic and Post-Synthetic Purification Strategies to Control Size, Surface Charge, and Phase Uniformity of Metal-Organic Framework Nanoparticles	43
2.1 Abstract	44
2.2 Introduction and Background	45
2.3 Results and Discussion	50
2.31 Modulated Solvothermal Synthesis of UiO-66 MOF Nanoparticles.....	50
2.32 Role of Modulators in Controlling MOF Nanoparticle Polydispersity	51
2.33 Surface Defects Dictate Particle Surface Charge and Colloidal Stability	53
2.34 Electrostatic Purification of Mixed-Phase MOF Nanoparticles	57
2.35 Modification of MOF Particle Surface Charge via Ligand Coordination	58

2.4 Conclusions	7
2.5 Experimental Methods and Supplementary Materials	61
CHAPTER THREE: Surface Functionalization of Metal-Organic Framework Nanoparticles via Coordination Unsaturated Metal Sites	77
3.1 Abstract	78
3.2 Introduction and Background	78
3.3 Results and Discussion	80
3.31 Surface Functionalization of MOF Nanoparticles with Phospholipid	80
3.32 Quantification of Surface Ligand Coverage	85
3.33 Controlling Surface Properties via Ligand Functionalization	87
3.4 Conclusions	87
3.5 Experimental Methods and Supplementary Materials	88
CHAPTER FOUR: Interfacing Metal-Organic Framework Nanoparticles with Oligonucleotides for Biological Probes and Intracellular Protein Delivery Vehicles	101
4.1 Abstract	102
4.2 Introduction and Background	103
4.3 Results and Discussion	107
4.31 Surface Functionalization of MOF Nanoparticles with Terminal Phosphate Modified Oligonucleotides	107
4.32 Design Rules for Modifying MOF Nanoparticles with Oligonucleotide	110
4.33 Synthesis of DNA Interconnected MOF-Gold Nanoparticle Assemblies.....	112
4.34 Encapsulation of Proteins in DNA-Modified MOF Nanoparticles	118
4.35 Cellular Uptake of DNA Functionalized MOF Nanoparticles	122

4.4 Conclusions	8
4.5 Experimental Methods and Supplementary Materials	124
CHAPTER FIVE: Hierarchical Colloidal Crystal Engineering with Metal-Organic Framework	
Nanoparticles	144
5.1 Abstract	145
5.2 Introduction and Background.....	145
5.3 Results and Discussion.....	147
5.31 Synthesis of MOF Programmable Atom Equivalents (MOF PAEs).....	147
5.32 Colloidal Crystal Engineering with MOF PAEs.....	150
5.33 Binary Superlattices Prepared by MOF and Gold PAEs.....	152
5.34 MOF NP Shape as a Superlattice Structure Influencing factor.....	154
5.4 Conclusions	156
5.5 Experimental Methods and Supplementary Materials	157
CHAPTER SIX: Conclusions and Future Outlook	180
6.1 Outlook	180
6.2 Synthesis of Uniform MOF NPs by Isolating Nucleation and Growth	180
6.3 Intracellular Delivery of Therapeutics using DNA Functionalized MOF NPs.....	181
6.4 Hybrid MOF-Polymer Composites and Stimuli-Responsive MOF Superlattices	183
6.5 Conclusions and Future Remarks	185
REFERENCES	186
CURRICULUM VITAE	220

LIST OF FIGURES

CHAPTER ONE

Figure 1.1. Schematic representation of the modular synthesis of MOF NPs, with control over size, morphology, and surface functionality.

Figure 1.2. Schematic representation of MOF NP nucleation and growth according to the LaMer model.

Figure 1.3. Schematic representation of CP NPs synthesized by the fast precipitation method.

Figure 1.4. Schematic representation of a reverse-phase microemulsion serving as a nanoreactor for MOF NP syntheses.

Figure 1.5. Schematic illustration of coordination modulation strategy impacting NP shape by selectively binding to specific crystal facets, and crystallite size by controlling the number of nucleation sites produced.

Figure 1.6. Schematic illustration of post-synthetic modification of MOF NP external surfaces through covalent bonds and coordinative bonds at the SBUs.

Figure 1.7. Schematic representation of post-synthetic external surface functionalization via different kinds of covalent bond formation.

Figure 1.8. Schematic representation of post-synthetic external surface functionalization via different coordinative interactions.

CHAPTER TWO

Figure 2.1. The carboxylic-acid modulated synthesis of UiO-66.

Figure 2.2. Powder X-ray diffraction data for UiO-66 synthesized with different modulators over a series of acid concentrations: acetic acid, formic acid, dichloroacetic acid, and trifluoroacetic acid.

Figure 2.3. STEM images of UiO-66 synthesized with different acid modulators and concentrations.

Figure 2.4. The size of UiO-66 as a function of acid modulator concentration, and the coefficient of variation as a function of size.

Figure 2.5. The impact of modulator concentration and acid utilized on porosity. BET adsorption isotherm for UiO-66 colloids synthesized with different modulators.

Figure 2.6. A summary of MOF nanoparticle size measurements determined by STEM and DLS, as a function of modulator relative acidity and molar concentration.

Figure 2.7. Schematic illustration of the synthesis of mixed-phase MOF NPs and their magnetic beads-assisted separation.

Figure 2.8. SEM images of MOF NP mixtures separated by MBs.

Figure 2.9. Schematic illustration of MIL-88B, MIL-101 and UiO-66 surface charge modulation with HBPA, and Zeta potential measurements of MOF particles before and after HBPA modification.

CHAPTER THREE

Figure 3.1. Synthesis and DOPA functionalization of a series of zirconium MOF NPs (UiO-66, UiO-67, and BUT-30) with the same underlying topology.

Figure 3.2. Powder X-ray diffraction (PXRD) patterns and scanning electron microscopy (SEM) images of the as-synthesized MOF NPs.

Figure 3.3. IR and XPS analysis of DOPA-MOF NPs.

Figure 3.4. The impact of DOPA functionalization on porosity and colloidal stability. BET adsorption isotherm before and after DOPA functionalization for UiO-66 nanoparticles.

Figure 3.5. DOPA surface density for different size UiO-66, UiO-67 and BUT-30 MOF nanoparticles.

CHAPTER FOUR

Figure 4.1. Schematic representation of solvothermal synthesis of UiO-66 MOF nanoparticles, DNA modification of MOFs, and assembly of MOF-NP core-satellite hybrid architectures.

Figure 4.2. Schematic illustration of insulin encapsulation in the mesoporous channels of MOF NPs followed by DNA surface functionalization.

Figure 4.3. Characterization of DNA functionalized MOF nanoparticles with STEM and ^{31}P SSNMR spectra of phosphate functionalized oligonucleotide.

Figure 4.4. A library of nine MOFs were synthesized and further functionalized with DNA. DNA surface coverage was plotted against surface SBU density, SBU coordination number, and M-O bond dissociation energy.

Figure 4.5. TEM images of DNA modified MOF NP core assembled with complementary DNA-modified AuNPs of various shapes: spheres, cubes, octahedrons, and prisms.

Figure 4.6. TEM images of 225 nm DNA modified MOF NP core assembled with complementary DNA-modified AuNPs of various shapes

Figure 4.7. Exploration of the assembly of DNA-modified metal NPs (silver nanoparticles, gold nanostars, and iron oxide nanoparticles) as characterized by energy dispersive spectroscopy and UV-vis spectroscopy.

Figure 4.8. DNA mediated guest release experiments of encapsulated caffeine inside UiO-66-AuNP nanoclusters.

Figure 4.9. MOF-NP nanoclusters show enhanced cellular uptake capability as compared to that of single strand DNA.

Figure 4.10. Negligible cytotoxicity or anti-proliferative effects was induced by MOF-NP nanoclusters as verified by MTT assays.

Figure 4.11. Scanning electron microscopy, transmission electron microscopy, and DLS characterization of the as-synthesized MOF NPs.

Figure 4.12. Confocal fluorescence characterization and serum stability test of protein encapsulated DNA-MOF NPs.

Figure 4.13. Cellular uptake and cytotoxicity assay of insulin delivered by DNA-PCN-222 and DNA-NU-1000 NPs.

CHAPTER FIVE

Figure 5.1. Schematic illustration of the synthesis of MOF NP-based PAEs and their DNA-programmed assembly.

Figure 5.2. Characterization of fcc and bcc colloidal superlattices assembled from UiO-66 MOF PAEs by radially averaged 1D SAXS patterns.

Figure 5.3. SAXS data STEM characterization of rhombic dodecahedra single crystal superlattice of binary superlattices assembled from combination of MOF and Au PAEs.

Figure 5.4. Schematic representation, SAXS, and TEM images of anisotropic MOF NP superlattices.

CHAPTER SIX

Figure 6.1. Separation of nucleation and crystal growth leads to monodisperse particle size distribution and core-shell structures.

Figure 6.2. Schematic illustration of protein therapeutics and cell penetrating peptide co-delivered by DNA functionalized MOF NPs.

Figure 6.3. Creation of dynamically responsive, structurally sophisticated, and highly functional nanoparticle superlattice crystals.

CHAPTER ONE: Metal-Organic Framework Nanoparticles as a Novel Class of Modular Nanomaterials

Materials in this chapter is based upon published work:

Wang, S.; McGuirk, C. M.; d'Aquino, A.; Mason, J. A.; Mirkin, C. A. *Adv. Mater.*

2018, DOI: [10.1002/adma.201800202](https://doi.org/10.1002/adma.201800202).

1.1 Metal–Organic Frameworks at the Nanoscale

Metal–organic frameworks (MOFs), also known as porous coordination polymers (PCPs), are three-dimensional ordered porous materials composed of inorganic clusters bridged by organic ligands, which, in certain cases, exhibit record-setting internal surface areas.²⁻⁴ Through judicious choice of organic and inorganic components, the crystalline structure and chemical functionalities of MOFs can be deliberately modulated, which has led to their use in a wide range of applications, including gas storage and separations,⁵ chemical sensing,⁶ membranes,⁷ catalysis,⁸ and drug delivery.⁹ Since their discovery, the vast majority of MOF studies have focused on bulk phases composed of polydisperse mixtures of crystallites that span multiple orders of magnitude in size, however, more recently, significant effort has been dedicated towards the realization of uniform MOF nanoparticles (NPs), leading to the discovery of a variety of properties not observed or relevant in bulk systems, such as accelerated adsorption/desorption kinetics and improved bioavailability (**Figure 1.1**).¹⁰⁻¹¹ Indeed, ways of preparing uniform MOF NPs are critical to expanding our understanding of MOF structure-function relationships and applications based upon the unusual properties of such structures.

In contrast with conventional inorganic and organic NPs, for which syntheses and post-synthetic functionalization procedures are well established, the development of generalizable and mechanistically understood methodologies for MOF NP synthesis is still in its infancy. The ability to rapidly and reproducibly synthesize MOF NPs of uniform size and well-defined surface chemistry is highly desirable, as precise control over these factors is not only critical to the understanding of structure–function relationships, but also has significant impact on porosity,¹² catalytic activity,¹³ and cellular uptake.¹⁴ Indeed, it was not until inorganic and organic NPs could

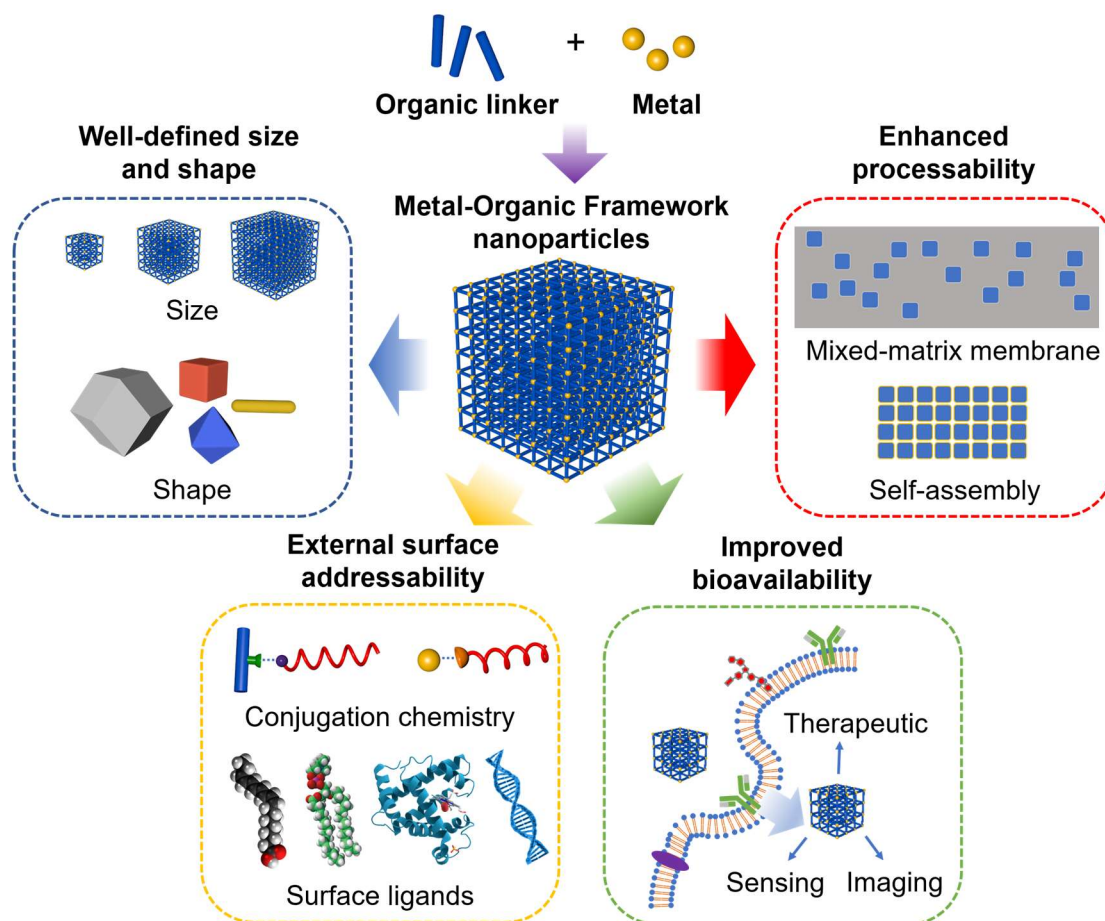


Figure 1.1. Schematic of the modular synthesis of MOF NPs, with control over size, morphology, and surface functionality. Such physical and chemical addressability render them advantageous over bulk MOFs.

be reliably synthesized in monodisperse form and with controlled surface chemistry that their potential as applied materials and nanoscale building blocks could be realized.¹⁵ At present, a large variety of inorganic NPs can be routinely synthesized with a coefficient of variation (CV) of less than 5%, whereas MOF NPs have only been achieved with a limited number of canonical frameworks, and often suffer from undesirable large size distributions (CV = 10–30%).^{11, 16} In order to realize the full potential of MOF NPs, a firm understanding of the mechanisms underlying NP syntheses and methodologies for post-synthetic surface functionalization must be

established.¹⁷⁻¹⁸ In order to address this challenge, recent effort has been devoted toward elevating the study of MOF NPs to similar standards of rigorous characterization,¹⁹ mechanistic understanding,²⁰⁻²³ and chemical control that are characteristic of their purely inorganic and organic nanomaterial counterparts.¹⁶⁻¹⁸

1.2 Approaches for the Synthesis of Uniform MOF Nanoparticles

Although syntheses of nanoscale MOF crystallites have been reported, the reliable preparation of uniform NPs remains a significant challenge.¹⁶ For one, the thermodynamics of MOF formation can vary significantly for different metal–ligand combinations and framework topologies, thus synthetic methodologies must often be tailored for each individual framework. Kinetically, the formation of the relatively weak coordination bonds that drives MOF NP growth is typically slow (timescale of seconds) relative to the precursor diffusion rate in solution,²⁴ leading to extended periods of homogeneous nucleation and a broad particle size distribution.^{22, 25} These variable contributions result in complex NP nucleation and growth processes that can be difficult to separate and independently control, including a number of mechanistic considerations not encountered in metallic NP analogs, such as linker deprotonation, solvent decomposition, and the formation of secondary building units (SBUs).²⁶

These challenges have prompted extensive analytical studies of the mechanisms of MOF NP nucleation and growth. In particular, extended X-ray absorption fine structure (EXAFS),²⁶ time-resolved static light scattering (SLS),²⁰ small- and wide-angle X-ray scattering (SAXS and WAXS),²¹ liquid cell transmission electron microscopy (LCTEM),²² and high resolution TEM have aided in this effort.²³ As a consequence of these studies, the LaMer model of NP growth has been invoked as a primary tool for understanding MOF NP formation.²⁷⁻²⁸ According to the LaMer

model, the process of nucleation and growth occurs in four successive steps: (1) a rapid increase in the concentration of reactive monomers in solution (Figure 1.2, stage I), (2) a homogeneous nucleation “burst” as

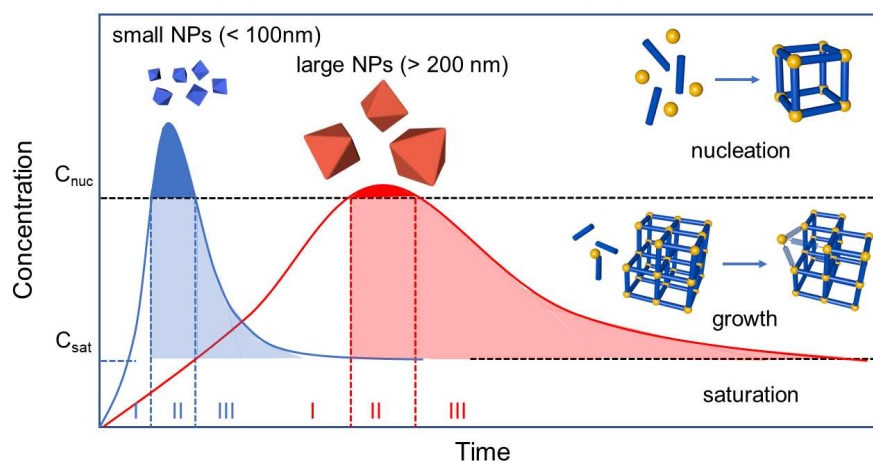


Figure 1.2. Schematic representation of MOF NP nucleation and growth according to the LaMer model. Blue trace: the synthesis of uniform small MOF NPs typically involves fast formation of abundant nuclei. Red trace: a small number of nuclei and slow growth rate results in uniform large NPs.

the concentration of reactive monomers exceeds the critical nucleation concentration (C_{nuc}), (3) a rapid reduction in the concentration of monomers in solution, halting further nucleation events (Figure 1.2, stage II), and (4) extended crystal growth upon reaching the saturation concentration (C_{sat} , *i.e.*, the concentration at which the NP growth rate equilibrates with the solvation rate) (Figure 1.2, stage III). The short nucleation period of the LaMer mechanism, which temporally separates crystal nucleation from crystal growth, is critical for the synthesis of uniform NPs. To obtain small, uniform (10–100 nm) MOF NPs (Figure 1.2, blue trace), it is essential to generate a large number of nuclei via burst nucleation, and then to rapidly terminate particle growth through depletion of all precursors. However, to obtain large (200 nm – 1 μ m) MOF NPs (Figure 1.2, red trace), slow particle nucleation and growth are needed to limit the number of nucleation sites, such that all precursors will react with fewer nuclei to form larger particles. To control these underlying factors and therefore NP size, most MOF NPs are synthesized via one of the following strategies,

or some combination thereof: (1) rapid nucleation, (2) nanoreactor confinement, and/or (3) coordination modulation.

1.21 Rapid Nucleation

Before the realization of crystalline MOF NPs, much of the early work on nanoscale inorganic–organic hybrid materials focused on amorphous coordination polymers (CPs). Although analogously composed of tailorable ligands and metal cations, these systems lack long-range structural order and permanent porosity. Nonetheless, nanoscale amorphous CPs served as an important predecessor in the development of crystalline MOF NPs.²⁹⁻³⁰ Taking advantage of solubility differences between molecular precursors and the resulting polymer particulates, CP NPs were typically synthesized through manipulation of precursor concentration, pH of the reaction mixture, or introduction of precipitating solvents. For example, in 2005 Wang and coworkers reported the synthesis of 300 nm spherical CP NPs derived from a mixture of H_2PtCl_6 and *p*-phenylenediamine in aqueous solution at room temperature.³¹ The NP size and polydispersity were controlled by the molar ratio and concentration of reactants. Separately, Mirkin and co-workers pioneered an “initiation-solvent” approach, whereby the controlled introduction of a secondary initiation anti-solvent into the homogeneous precursor solution led to the formation of amorphous M-BMSB NPs ($\text{M} = \text{Zn}^{2+}$, Cu^{2+} and Ni^{2+} ; BMSB = bis-metallo-tridentate Schiff base) (**Figure 1.3b**). Particle sizes were reduced from 2 μm to 190 nm ($\text{CV} = 20 \sim 30\%$) via fast addition of initiation solvent, however, the resulting particles were relatively polydisperse. In some cases, the simple mixing or addition of initiation solvent alone is not sufficient to induce fast nucleation, and base can be added to deprotonate acidic pro-ligands and accelerate initial coordination events. Indeed, Lin and coworkers improved upon the initiation-solvent method by deprotonating precursor ligands to accelerate nucleation rates, leading to the formation of 58 ± 8 nm ($\text{CV} \sim 15\%$)

$\text{Tb}_2(\text{DSCP})_3(\text{H}_2\text{O})_{12}$ (DSCP = disuccinatocisplatin) NPs (**Figure 1.3c**). Interestingly, these CP NPs composed of Tb^{3+} and a Pt(IV) pro-drug were shown to be an effective anti-cancer therapeutic agent. To date, a variety of amorphous CP NPs have been synthesized via the rapid precipitation strategy; however, few examples of uniform crystalline frameworks synthesized in this fashion exist, as rapid NP formation at room temperature precludes the necessary high degree of reversible bond formation achieved under solvothermal conditions for the realization of crystalline order.¹⁶
¹⁸ Therefore, alternative synthetic approaches that promote reversible metal–ligand coordination bond formation are critical for the synthesis of uniform crystalline MOF NPs.

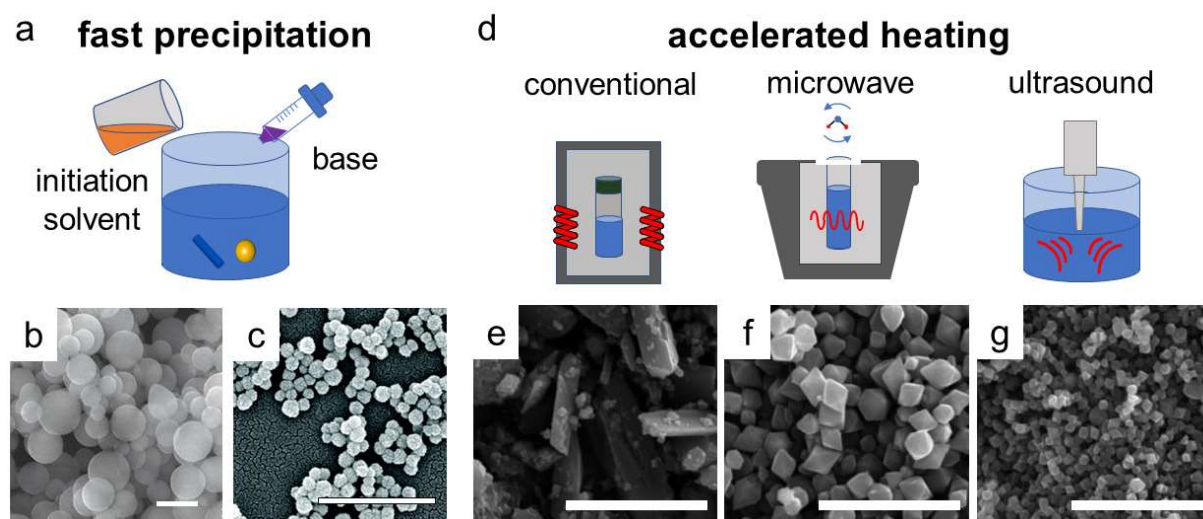


Figure 1.3. (a) Schematic representation of CP NPs synthesized by the fast precipitation method. (b) SEM image of spherical Zn-BMSB CP NPs synthesized via initiation-solvent approach. Scale bar = 200 nm. Reproduced with permission. Copyright 2005, Nature Publishing Group. (c) SEM image of spherical $\text{Tb}_2(\text{DSCP})_3(\text{H}_2\text{O})_{12}$ CP NPs synthesized via the deprotonation method. Scale bar = 500 nm. Reproduced with permission. Copyright 2008, American Chemical Society. (d) Schematic representation of MIL-53 MOF NPs synthesized by three different heating methods and their corresponding SEM images: (e) conventional electric heating, (f) microwave, and (g) ultrasound. Scale bar = 10 μm . Reproduced with permission. Copyright 2010, Wiley-VCH.

In this vein, accelerated heating is an important strategy for achieving rapid nucleation of crystalline NPs. Due to its fast heating, uniform energy generation throughout the bulk of the material, and ability to exceed the boiling point of a solvent through the use of pressurized vessels, microwave heating has been broadly applied as a tool for the realization of concentrated and small nuclei, which rapidly consume precursors and produce NPs with relatively narrow size distributions.³² In 2006, Masel and coworkers performed the first microwave-assisted solvothermal synthesis of MOF NPs. Cubic $Zn_4O(BDC)_3$ (IRMOF-1/MOF-5, BDC = 1,4-benzenedicarboxylate) NPs, ranging from 4 μm to 200 nm in edge length (CV \sim 30%), were synthesized by reducing reactant concentrations. Notably, NPs were synthesized in less than a minute, whereas conventional heating takes tens of hours. Building on this initial work, much attention has focused on extending this technique to a variety of canonical frameworks. For example, Serre and coworkers optimized the synthesis of sub-100 nm uniform $\text{Fe}_3\text{O}(\text{H}_2\text{O})_3(\text{fum})_3$ NPs (Fe-MIL-88A, fum = trans-butenedioic acid) (CV < 10 %).³³ In this study, the authors systematically investigated synthetic parameters that control MOF NP size, including precursor concentration, reaction time, and temperature. Furthermore, Feldhoff and coworkers reported the microwave-assisted synthesis of $\text{Zn}(\text{PhIm})_2$ (zeolitic imidazolate framework-7 (ZIF-7), PhIm = benzimidazolate) NPs, in which diethylamine was added to further accelerate the nucleation rate, promoting a series of NPs ranging from 40 nm to 140 nm (CV = 10 \sim 20%).³⁴

In addition to microwave-based heating, ultrasound has been demonstrated as a useful tool for accelerating precursor dissolution and nucleation. Ultrasound effects originate from acoustic cavitation which generates local hot spots (ring of \sim 200 nm) with transient high temperature (\sim 5000 K), high pressure (> 1000 bar), and rapid heating and cooling rates.³⁵ The nucleation and growth of particles preferably occurs in these transient hot spots (within milliseconds), effectively

limiting particle size to the nanoscale.³⁶ In a comprehensive kinetic study of Fe(OH)BDC (MIL-53-Fe) NP crystallization, Jung and coworkers studied how microwave, ultrasound, and conventional electric heating methods can drastically affect MOF nucleation and growth kinetics (**Figure 1.3d-g**). In this study, the temperature was kept constant across heating methods, and the reaction time was varied to investigate the crystallization process. The authors found that crystal growth rates were comparable across all three methods, however MOF NP size inversely correlated with nucleation rate (conventional heating \ll microwave $<$ ultrasound), and that uniform, geometrically defined NPs were only obtained from microwave and ultrasound syntheses. This study provided direct evidence that the methods used to promote rapid nucleation, namely heating rates and temperature profiles within reaction containers, have a significant impact on particle size and uniformity. It should be noted that although ultrasound irradiation provides the fastest heating acceleration, it often suffers from relatively low yield, poor temperature control, and the formation of mixed-phase frameworks.³⁷ Because of these challenges, microwave-assisted synthesis has been more widely adopted.^{9, 33, 38-42}

1.22 Nanoreactor Confinement

Different from burst nucleation via rapid precipitation or accelerated heating, nanoreactor confinement strategies regulate MOF NP size via the isolation of nucleation sites in a physically confined space. In this approach, immiscible solvents, such as water and “oil” (a complex mixture of different hydrocarbons and olefins), are mixed to produce emulsions of monodisperse nanoscale droplets, and both the emulsion size and reagent solubility can be tuned by varying the concentration of amphiphilic surfactants (**Figure 1.4a**).⁴³ In the presence of MOF precursors, these droplets serve as size-limiting reaction containers, in which particle nucleation kinetics are controlled by emulsion size, rate of mixing, and reaction temperature.¹⁶ It is important to recognize

that these microemulsion systems are dynamic, with micelles frequently colliding and coalescing, allowing reagents solubilized in separate micellar solutions to mix and react. Subsequently at the latter stage of particle growth, steric stabilization provided by the surfactant layer prevents NPs from aggregating.

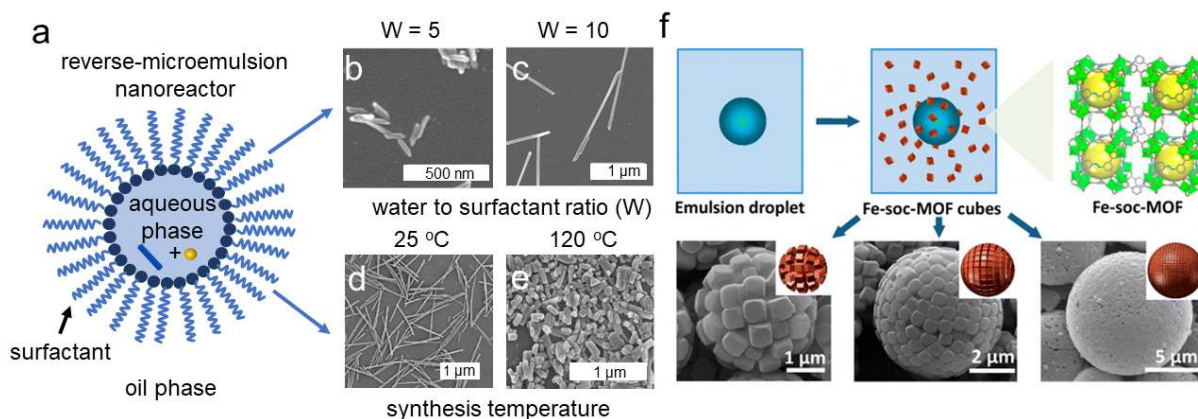


Figure 1.4. (a) Schematic representation of a reverse-phase microemulsion serving as a nanoreactor for MOF NP syntheses. (b-c) SEM images of $\text{Ln}_2(\text{BDC})_3(\text{H}_2\text{O})_4$ particles synthesized at different water to surfactant ratios which effect the resulting aspect ratio. Reproduced with permission. Copyright 2006, American Chemical Society. (d-e) SEM images of $\text{Mn}(\text{BTC})_2(\text{H}_2\text{O})_6$ particles synthesized at different temperatures where lower aspect ratios and smaller size result from higher temperature. Reproduced with permission. Copyright 2008, American Chemical Society. (f) Schematic representation of synthesis and integration of Fe-soc-MOF cubes into hollow colloidosomes and corresponding SEM images. Reproduced with permission. Copyright 2013, American Chemical Society.

Lin and coworkers first synthesized crystalline nanorods of $\text{Ln}_2(\text{BDC})_3(\text{H}_2\text{O})_4$ ($\text{Ln} = \text{Eu}^{3+}$, Gd^{3+} , or Tb^{3+}) by reacting LnCl_3 and bis(methylammonium)-BDC in an emulsion system composed of isooctane/1-hexanol/water and varying the amount of the surfactant cetyltrimethylammonium bromide (CTAB). By varying the ratio of water to surfactant from 10:1 to 5:1, the size of the nanorods could be tuned from $2 \mu\text{m} \times 100 \text{ nm}$ to $125 \text{ nm} \times 40 \text{ nm}$ (**Figure 1.4b-c**), where emulsions with higher water:surfactant ratios yielded MOF NPs with higher aspect ratios. Additionally, the average particle size decreased as reactant concentrations increased,

presumably because more micelles contained reactants and thus more nucleation sites were generated, leading to a reduction in particle size. Such a reverse-phase microemulsion (water-in-oil) was extended to synthesize a series of Mn-based MOF NPs. Nanorods of $\text{Mn}(\text{BTC})_2(\text{H}_2\text{O})_6$ (with diameters of 50–100 nm and lengths of 750 nm to several μm) were synthesized in a CTAB/1-hexanol/n-heptane/water microemulsion containing equal molar MnCl_2 and bis(methylammonium)-BDC. Notably, as the reaction temperature increased from room temperature to 120 °C, the aspect ratio of the NPs decreased dramatically (**Figure 1.4d-e**). Recently, Zheng and coworkers synthesized $\text{Zn}(\text{mIM})_2$ (ZIF-8, mIM = 2-methylimidazolate) NPs with narrow size distribution using reverse-phase micelles ($\text{CV} < 10\%$).⁴⁴ By tuning the precursor concentration, reaction temperature and surfactant species, NP sizes were modulated between 30–300 nm, which in turn demonstrated distinct size-dependent catalytic activity for a Knoevenagel condensation reaction. Further, Eddaoudi and Zeng reported an emulsion-templating approach to prepare cubic $[\text{Fe}_3\text{O}(\text{ABTC})_{1.5}(\text{H}_2\text{O})_3](\text{H}_2\text{O})_3(\text{NO}_3)$ MOF NPs (**Fe-soc-MOF**, H_4ABTC = 3,3',5,5'-azobenzenetetracarboxylic acid).⁴⁵⁻⁴⁶ Notably, due to the high uniformity of **Fe-soc-MOF** NPs and the presence of emulsion droplet induced by polyoxyethylene (20) sorbitan trioleate (tween-85) surfactant, these cubic MOF NPs self-assembled into hollow colloidosomes during the one pot synthesis (**Figure 1.4f**). The relative size of the hollow colloidosomes are dependent upon the size of emulsion droplets, which inversely correlates to with the concentration of tween-85. Inspired by conventional emulsion methods, Maspoeh and coworkers developed a novel and general spray-drying technique to synthesize MOF NPs.⁴⁷ This approach conceptually mimics the emulsion strategy that confines the synthesis of materials, but does not require secondary immiscible solvents or surfactants as templates. In a typical synthesis, droplets containing MOF precursors are vaporized via spraying and then heated, leading to sub-5- μm

hollow spherical superstructures with localized crystallization of MOF NPs at the droplet-air interface.⁴⁸ The disassembly of the superstructures by sonication yields discrete but nonuniform MOF NPs. In general, the microemulsion approach provides an effective way to regulate MOF NP size and to reduce size distribution; however, drawbacks exist, including: 1) relatively low yields, 2) poor reproducibility associated with complicated micelle formation and droplet coalescence processes, and 3) harsh conditions or multiple washing steps to completely remove all surfactants and organic solvents. These challenges potentially limit the practical use of MOF NPs in biomedical applications.

1.23 Coordination Modulation

Coordination modulation is a general approach to regulate MOF NP synthesis via chemically controlling ligand–metal interactions, which can be applied in conjunction with rapid nucleation and nanoreactor confinement strategies. Coordination modulators are primarily monotopic (*i.e.*, non-bridging) ligands that are added to the reaction mixture to either affect linker deprotonation equilibria or reversibly compete with bridging linkers for available metal ion/cluster coordination sites.⁴⁹ Chemical modulators are able to impact NP size and shape by controlling the number of nucleation sites produced and preferentially binding to certain crystal facets (**Figure 1.5a**). Indeed, the pK_a , steric profile, and concentration of such modulators are variable properties that play crucial roles in regulating particle size, shape and uniformity.⁵⁰

In an early exploration of the effect of modulators on amorphous CP NP growth, Kitagawa and coworkers demonstrated the size modulating effect of poly(vinylpyrrolidone) (PVP), a weakly coordinating polytopic polymer, on Prussian blue NP formation.⁵¹⁻⁵² The authors reported that the use of this competitive ligand produced a significant reduction in particle size, from 300 nm to 16 nm, along with improved size uniformity. Huber and Fischer further demonstrated size control for

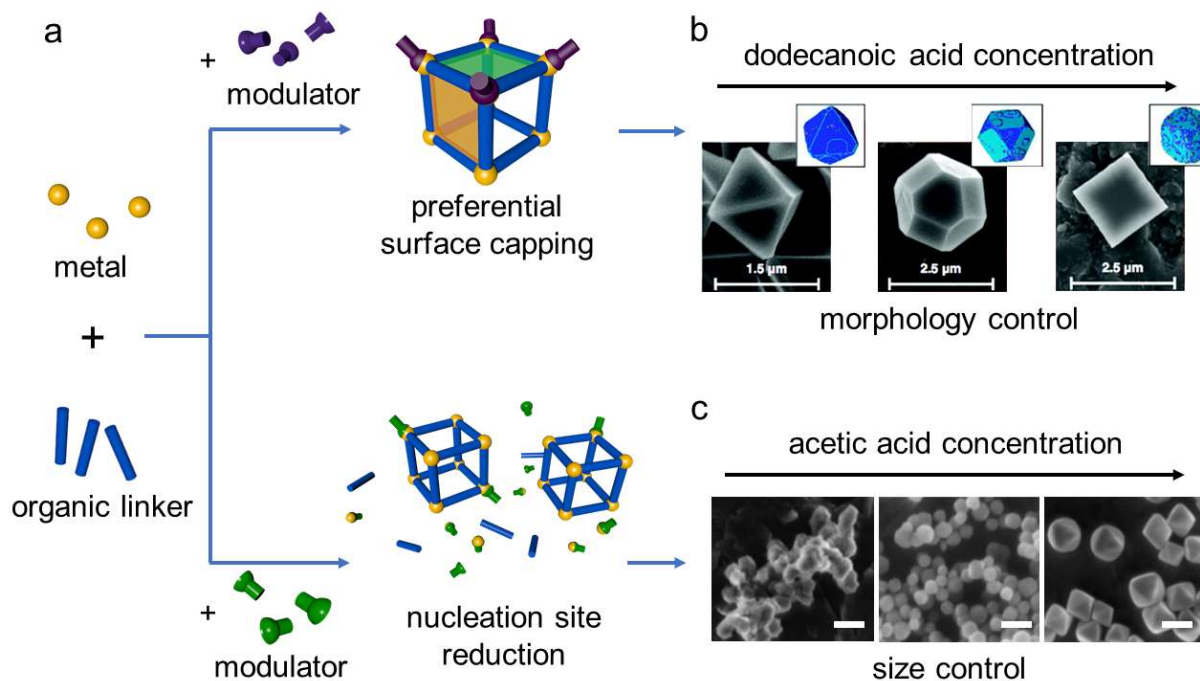


Figure 1.5. (a) Schematic illustration of coordination modulation strategy impacting NP shape by selectively binding to specific crystal facets, and crystallite size by controlling the number of nucleation sites produced. (b) SEM images showing morphology of HKUST-1 NPs transitioning from octahedra to cuboctahedra to cube as the dodecanoic acid modulator concentration increases. Reproduced with permission. Copyright 2011, American Chemical Society. (c) SEM images of UiO-66 NPs showing that particle size positively correlates with increasing acetic acid modulator concentration. Scale bar = 200 nm. Reproduced with permission. Copyright 2011, Wiley-VCH.

crystalline MOF-5 NPs by influencing the particle nucleation rate via the addition of *p*-perfluoroethylbenzoic acid modulator.²⁰ In addition to size control, shape control has also been achieved via coordination modulation by employing surfactant/blocking/capping agents that interact with specific crystal facets, deterring particle growth in that direction. For example, Oh and coworkers discovered that the aspect ratio of In(OH)(BDC) hexagonal nanorods can be controlled by increasing the amount of pyridine from 0.11 to 0.91.⁵³ The authors postulated that in the presence of excess pyridine, particle growth in the direction of the hexagonal facets is effectively blocked, resulting in hexagonal disks. In a more straightforward system, Kitagawa and coworkers studied

the modulated growth of pillar-layered MOF $\text{Cu}_2(\text{ndc})_2(\text{dabco})$ (ndc = 1,4-naphthalene dicarboxylate; dabco = 1,4-diazabicyclo[2.2.2]octane) NPs, which feature two separate coordination modes: Cu–ndc (carboxylate) to form 2-D sheets and Cu–dabco (amine) to bridge the 2-D sheets.⁵⁴ By adding an acetic acid modulator, square-rod anisotropic NPs were selectively formed due to Cu-acetic acid coordination on the (100) surface, which induces selective crystal growth along the [001] direction. Following up on this work, control over the crystal morphology of $\text{Cu}_3(\text{BTC})_2$ (HKUST-1, BTC = benzene-1,3,5-tricarboxylic acid) particles was achieved by simultaneously tuning the concentration of the two modulators, acetic and dodecanoic acid.⁵⁵⁻⁵⁶ In particular, by varying the dodecanoic acid concentration from 0.234 M–1.188 M, HKUST-1 particles were synthesized with a crystal morphology transitioning from nanoscale octahedra to micron-sized cuboctahedra to micron-sized cubes (**Figure 1.5b**). By employing coarse-grained modeling, the authors suggested that the preferential capping of the modulator at certain nucleation sites was dictated by differences in the relative crystal facet surface energy, leading to different morphologies. In addition to modulating crystal morphology during solvothermal synthesis, post-synthetic etching strategies also have been realized.⁵⁷⁻⁵⁸ For example, Maspoch and coworkers demonstrated the surface-selective anisotropic etching of ZIF-8 and ZIF-67 ($\text{Co}(\text{mIM})_2$) NPs via ligand protonation and subsequent metal ion sequestration.⁵⁹ Specifically, the addition of xylenol orange, a weak acid and metal sequestering agent, protonates the 2-mIM linkers, breaking the Zn/Co-2-mIM bonds and preferentially etching the external crystal surfaces with the highest density of Zn/Co 2-mIM bonds. By adjusting the pH of the xylenol orange solution, the morphology of ZIF NPs can be converted from rhombic dodecahedra to hollow boxes. The ability to control crystal morphology represents a significant advancement, as the predictable exposure of certain crystal facets allows control over surface reactivity and diffusion kinetics.⁶⁰

More recently, significant attention has been given to the synthesis of zirconium-based MOFs, such as the UiO (University of Oslo) and PCN (Porous Coordination Network) families, due to their exceptional stability in aqueous solutions—a desirable property for many biological applications. In prototypical bulk syntheses of $\text{Zr}_6\text{O}_4(\text{OH})_4(\text{BDC})_6$ (UiO-66), the fast kinetics and low reversibility of bond formation between highly oxophilic Zr^{4+} salts and the terephthalic acid linker precludes control over particulate size and morphology. Therefore, the development of chemical modulators that effectively slow down the reaction and increase reversibility are highly desirable for the synthesis of homogeneous crystalline Zr MOF NPs. In this vein, Behrens and co-workers first reported that benzoic and acetic acids could be used as modulators in the size controlled synthesis of Zr-based UiO-66 and UiO-67 NPs (**Figure 1.5c**).⁶¹ The addition of these monotopic acids led to the initial formation of Zr–modulator coordination complexes, where the modulators were slowly replaced by ditopic linker molecules to form the frameworks. Such exchange equilibrium provided control over crystallization rates (especially nucleation rates) and changed the product morphology from aggregates of inter-grown crystallites to individual NPs. With this understanding, Zhou and coworkers systematically controlled the size of $\text{Zr}_6\text{O}_4(\text{OH})_4(\text{TCPP-H}_2)_3$ (PCN-224/MOF-525, TCPP = tetrakis(4-carboxyphenyl)porphyrin) NPs with benzoic acid. They reported a series of uniform MOF NPs, ranging from 33 ± 4 nm to 189 ± 11 nm, which allowed for the evaluation of size-dependence on cellular uptake and subsequent use in photodynamic therapy efficacy. In addition to size and morphology, the $\text{p}K_a$ of the acidic modulator can be leveraged to control UiO-66 NP porosity,⁶² surface charge, colloidal stability, and size dispersity.⁶³

The use of chemical modulators has led to some of the most uniform MOF NPs (CV~5%) reported to date, which has enabled the exploration of incorporating these materials into higher

ordered structures. In such cases, chemical modulators often not only control NP growth, but also serve as surfactants that manipulate NP surface properties and facilitate self-assembly processes. For example, the Langmuir-Blodgett technique has been employed to prepare 2-D monolayer films of $\text{Al}_{12}\text{O}(\text{OH})_{18}(\text{H}_2\text{O})_3(\text{Al}_2(\text{OH})_4)(\text{BTC})_6$ (Al-BTC), $[\text{M}_3\text{O}-(\text{C}_{16}\text{N}_2\text{O}_8\text{H}_6)_{1.5}(\text{H}_2\text{O})_3](\text{H}_2\text{O})_3(\text{NO}_3)$ (M-**sof**-MOF, M = In and Ga) and UiO-66 NPs.⁶⁴⁻⁶⁶ Further, Granick and coworkers synthesized homogeneous PVP coated ZIF-8 NPs (CV~4.5%) and showed that these rhombic dodecahedron particles assemble into interesting structures driven either by capillary forces or an applied external electric field.⁶⁷⁻⁶⁸ Recently, MasPOCH and López elegantly demonstrated CTAB mediated self-assembly of uniform polyhedral ZIF-8 and UiO-66 NPs (~200 nm with CV~5%) into millimeter-sized three-dimensional photonic materials.⁶⁹ These superstructures feature a photonic bandgap that can be tuned by controlling the size of the NPs and are responsive to the adsorption of guest molecules in the MOF pores, providing a glimpse into potential sensing applications.

Overall, coordination modulation has emerged as the most versatile and effective strategy for synthesizing highly uniform MOF NPs with narrow size distribution. However, it should also be noted that, at present, the choice of modulator greatly relies on empirical knowledge and size and morphology controlled are achieved by changing the conventional solvothermal reaction conditions in a trial-and-error fashion. Therefore, it is highly desirable to improve upon this approach with the development of high-throughput synthetic screening and characterization methodologies to effectively identify and evaluate the optimal modulator species, reagent concentration, as well as reaction temperature and time for synthesizing diverse, high quality MOF NPs.⁷⁰⁻⁷¹

1.3 Surface Functionalization Strategies

In addition to nanoscale architectural features, surface ligands play a critical role in dictating the chemical and physical properties of nanomaterials.¹⁵ Indeed, properties such as solubility, cellular uptake, molecular recognition and catalytic reactivity can be post-synthetically modulated by surface ligands. This tailorability has proven to be important for the realization of many promising

applications, including drug-delivery, light-induced catalysis, and self-assembly.⁷²⁻⁷⁴

Similar to inorganic and organic NPs, as-synthesized MOF

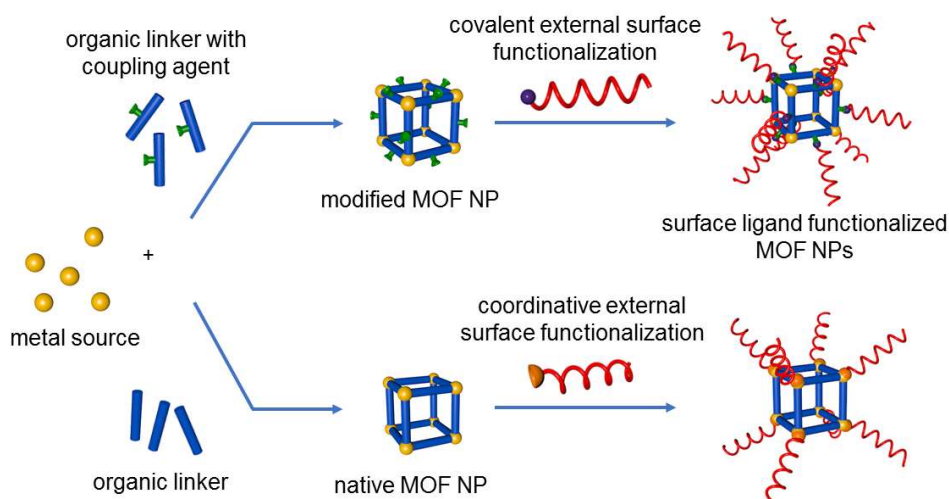


Figure 1.6. Schematic illustration of post-synthetic modification of MOF NP external surfaces through covalent bonds (top) and coordinative bonds (bottom) at the SBUs.

NPs often exhibit unfavorable surface properties, such as limited colloidal stability and poor bioavailability/pharmacokinetics.⁷⁵ Therefore, post-synthetic modification (PSM) of the external surface of MOF NPs has been proposed as a generalizable tool for mitigating these concerns and imbuing MOF NPs with desired functionality, such as enhanced colloidal stability, stimuli-responsive guest release, improved cellular-uptake, and biomarker targeting.⁷⁶⁻⁷⁷ Specifically, polymers and biomacromolecules, including lipids, peptides and nucleic acids, are particularly attractive choices as surface ligands, owing to their exceptional chemical tailorability and steric

inability to diffuse into the pores of most MOFs, limiting functionalization to the external surface. Although various approaches have been reported for PSM of MOF NPs, we have chosen to focus on those that occur through direct bonding interactions between ligands and the NP's external surface. Below, we highlight two important external surface PSM strategies, which vary in the bonding mode at the ligand-NP interface, namely: 1) covalent surface functionalization, and 2) coordinative surface functionalization (**Figure 1.6**). We discuss the relative advantages and disadvantages of the two approaches and their potential applications. It should be noted that much effort has been devoted to developing nonspecific interactions and encapsulation-based PSM strategies, however these approaches are challenging to quantify and tend to reduce MOF porosity.

1.31 Covalent External Surface Functionalization

Covalent PSM of substituted organic linkers is a robust and versatile strategy for imparting functionality to MOF NPs without interfering with the particle crystallization processes. This approach relies on the pre-synthetic installation of reactive functional groups onto the organic linkers of MOF NPs, which are reacted post-framework synthesis with exogenous ligands containing compatible organic units. Foresight into potential deleterious cross talk between linker and SBU is critical in this approach, as the installation of such reactive functional units can necessitate long and/or complex organic syntheses. As will be discussed below, these organic functional groups are typically amines, carboxylic acids, and azides, which are able to subsequently react with carbonyl, amine, and alkyne groups, respectively, installed on the exogenous ligand.⁷⁸ Below, we discuss a series of reports in which the external surface of MOF NPs are modified through the formation of organic covalent bonds between the linkers of the framework and secondary surface ligands.

Owing to the near ubiquity of carboxylic acid-based ligands, post-synthetic reactions at surface exposed, non-metal bound linker carboxylates were a logical starting point for PSM via organic covalent bonds. As an important note, early efforts required no additional functionalization of the native linker. Generally, carboxylate units on MOF NP surfaces were targeted for conjugation with primary amine bearing ligands or modified biomacromolecular ligands such as peptides and proteins. For example, Park and Huh first demonstrated the use of carbodiimide coupling agents to promote the conjugation of free carboxylate units on the bulk MOF surface with proteinaceous amines. Importantly, this approach retained the endogenous catalytic activity and enantioselectivity of the protein.⁷⁹ In 2012, Huang and Lin covalently bound the protease trypsin onto free hanging carboxylate moieties of $\text{Cr}_3\text{O}(\text{H}_2\text{O})_3(\text{BDC-NH}_2)_3$ [MIL-88B-NH₂ (Cr)] via an endogenous terminal amino-group using a similar carbodiimide-mediated coupling reaction, to afford a reusable bovine serum albumin (BSA) digestion system.⁸⁰ In a demonstration of increased generality, Lei and coworkers employed 1-ethyl-3-(3-dimethylaminopropyl)-carbodiimide/N-hydroxysuccinimide (EDC/NHS) to graft the protein streptavidin to HKUST-1 and $\text{Fe}_3\text{O}(\text{TCPP})_3$ (FeTCPP, $\text{TCPP}^{4-} = 4,4',4'',4'''$ -(porphine-5,10,15,20-tetrayl)tetrakisbenzoate) MOF NPs for electrochemical DNA sensing.⁸¹ In addition to peptides and proteins, poly(ethylene glycol) (PEG) is an important class of macromolecule that is routinely employed to functionalize NP surfaces. PEGylation effectively prevents non-specific protein adsorption onto NP surfaces, promoting desirable biomedical applications, such as prolonged blood-circulation time and reduced immune response.⁸² Lächelt and Wuttke recently reported the functionalization of the surface of 150 nm $\text{Fe}_3\text{F}(\text{H}_2\text{O})_2\text{O}(\text{BTC})_2$ (MIL-100(Fe)) NPs with amino-PEG 5000 and Stp10-C, an oligoaminoamide hetero-bifunctional linker) (**Figure 1.7a**). Their study revealed that significantly enhanced colloidal stability and efficient dye-labelling can be achieved, which are extremely

important for exploring the biomedical applications of MOF NPs. Although these reports demonstrate the versatility of addressing unbound ligand units on MOF NP surfaces, limitations exist, such as relatively low density of surface functionalization.⁷⁵ Additionally, reaction with the linker unit of the framework can cause orthogonality issues, as the labile surface metal–linker coordination bond may undergo dissociation or dynamic ligand exchange.⁸³

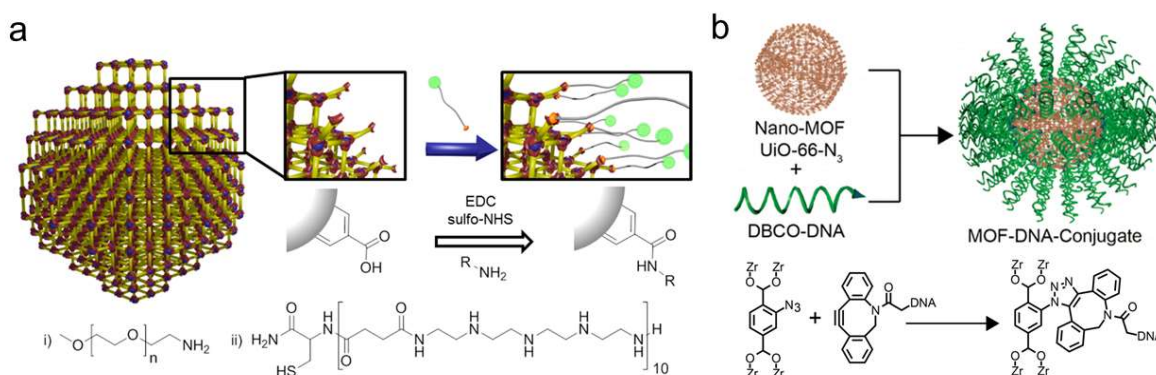


Figure 1.7. Schematic representation of post-synthetic external surface functionalization via different kinds of covalent bond formation: (a) carbodiimide catalyzed polymer and peptide surface functionalization of MIL-100-Fe MOF NPs with (i) amino-PEG 5000 and (ii) Stp10-C respectively, and (b) oligonucleotide functionalization of UiO-66-N₃ MOF NPs with DBCO modified DNA via click chemistry. (a) is reproduced with permission. Copyright 2016, American Chemical Society and (b) is reproduced with permission. Copyright 2014, American Chemical Society.

In contrast to the previous approach, linker modification should yield a high density of reactive surface sites whose location and density can be predicted from the structure of the framework. Using this approach, Qiao and Webley showed that surface functionalization with hydrophilic PEG prevents NP aggregation and greatly improves colloidal stability in water.⁸⁴ Specifically, amino-functionalized $\text{Zr}_6\text{O}_4(\text{OH})_4(\text{BDC-NH}_2)_6$ (UiO-66-NH₂) was first anchored with a polymerization initiator by reacting with bromoisobutryl bromide (BiBB), followed by the atom-transfer radical polymerization (ATRP) of the macromonomer poly(ethylene glycol) methyl ether methacrylate (PEGMA) initiated from the MOF surface. The PEG-grafted MOFs obtained

from this procedure showed excellent dispersity in aqueous solution. Using a chemically identical framework, Sada and Kokado reported the covalent attachment of the NHS-modified thermosensitive polymer poly(N-isopropylacrylamide) (PNIPAM-NHS).⁸⁵ The pores of PNIPAM-functionalized NPs were loaded with guest molecules and the hybrid material was shown to exhibit temperature controlled guest release, arising from the coil–globule transition of the thermo-responsive polymer. Surface functionalization employing amino-modified linkers has become a generalizable approach to tune MOF NP surface chemistry; however, the installation of these linker modifications can be tedious and often requires additional coupling reagents. Therefore, specific and robust conjugation chemistries that operate under mild conditions have been sought extensively.

Owing to the near ubiquitous nature of the highly specific and chemically orthogonal Huisgen “click” reaction, azide- or alkyne-functionalized organic linkers have been extensively used for covalent PSM with a diverse array of organic units.⁸⁶ Recently, Mirkin and coworkers reported the preferential functionalization of oligonucleotides onto the surface of both infinite coordination polymer (ICP) NPs and MOF NPs via a copper-free, strain-promoted azide-alkyne cycloaddition.⁸⁷⁻⁸⁸ Azide-functionalized 15 nm and 500 nm $Zr_6O_4(OH)_4(BDC-N_3)_6$ (UiO-66- N_3) NPs were prepared and subsequently reacted with dibenzylcyclooctyne (DBCO)-terminated DNA (**Figure 1.7b**). Through this approach, the authors were able to achieve a sufficiently high surface coverage of DNA so as to imbue the MOF NPs with key properties previously observed for DNA-modified gold NPs. Namely: 1) improved colloidal stability, 2) participation in materials assembly via cooperative DNA hybridization, and 3) cellular uptake through endogenous endocytosis.⁸⁹ Through a slight modification of this approach, Garcia and Willner demonstrated how PSM of the reactive linker moiety can be leveraged to overcome synthetic hurdles.⁹⁰⁻⁹¹ Specifically, amino-

functionalized $Zr_6O_4(OH)_4(TPDC-NH_2)_6$ (UiO-68, TPDC-NH₂ = 2'-amino-1,1':4,1''-terphenyl-4,4''-dicarboxylic acid) NPs were reacted with t-butyl nitrite and trimethylsilyl azide to convert the linker amino- unit into an azide functionality, which could then be “clicked” with DBCO-modified nucleic acids. This post-synthetic organic transformation was conducted due to synthetic incompatibilities associated with the installation of the desired azide unit before the framework was assembled. These nucleic acid-functionalized NPs were then used to realize two different stimuli-responsive materials in which specific stimuli induced the reconfiguration of the surface DNA gates, thus triggering the release of a molecular load stored in the framework pores. In addition to incorporating coupling agents via organic linker substitution, Forgan and coworkers reported an alternative approach based on decorating the framework with azide-functionalized modulators.⁹² In this study, 200 nm UiO-66 MOF NPs were synthesized in the presence of acidic modulators containing azido or propargyl units (para-azidomethylbenzoic acid and para-propargyloxybenzoic acid) that attach to Zr₆ sites on UiO-66 NPs surface, and thus allow for subsequent PEGylation via click chemistry. It was demonstrated that surface PEGylation endowed the NPs with enhanced stability toward phosphates and prevented undesirable “burst release” in drug-delivery. Additionally, the cell-uptake behavior of these NPs could be altered, where increased caveolae-mediated endocytosis occurred for UiO-66 NPs functionalized with long chain PEGs (PEG2000) as compared to short chain PEGs (PEG550). Overall, these reports illustrate how surface functionalization, especially with nucleic acids and biocompatible polymers, can lead to the development of novel platforms with a multitude of applications in the biological sciences and medicine.⁹³

Indeed, PSM via the formation of covalent organic bonds is a powerful tool for functionalizing the surface of MOF NPs with a diverse range of ligands, thus enhancing their

desirable physical properties or endowing them with new chemical and biochemical properties. Nevertheless, this approach does have its drawbacks, namely: 1) ligand modification with reactive organic moieties is often synthetically challenging, 2) pre-synthetic linker modification permanently alters the inner pore environment of the resulting framework, leading to a reduction in porosity, and 3) many desirable covalent surface functionalization reactions require catalysts that may not be compatible with the framework or biomacromolecule. With these potential complications in mind, we discuss an alternative approach that precludes the modification of organic linkers and potentially permits PSM of a broader scope of frameworks.

1.32 Coordinative Surface Functionalization

The development of a generalizable methodology that obviates organic modification of the native framework is highly desirable, as this would maintain the innate bulk properties of the framework and preclude tedious linker syntheses. Intriguingly, MOF crystallites often contain a high density of surface metals sites that are weakly bound to non-bridging linkers or solvent molecules. It was therefore proposed that these accessible coordination sites could be harnessed as a place to post-synthetically anchor ligands that were functionalized with more strongly coordinating moieties. As these weakly coordinated surface sites are widely present in unmodified MOF NPs, external surface PSM via coordination bonds represents a generalizable approach to surface functionalization.⁹⁴ Compared to the covalent bond functionalization strategy, this metal–ligand coordination approach offers two powerful advantages: 1) straightforward synthesis without the use of coupling reagents or substituted linkers, and 2) applicability to all frameworks that are stable in the presence of coordinative surface ligands.⁸³ Therefore, a growing number of macromolecules, such as polymers and peptides, have been functionalized with terminal coordinating groups for PSM of unmodified MOF NPs.

Kitagawa and coworkers first demonstrated this approach using carboxylate-terminated ligands for the functionalization of micrometer-scale Zn-based particles.⁹⁵ The authors were successful in functionalizing the particles with a monolayer of carboxylate-terminated BODIPY dye, however, elevated temperatures (120 °C) and long incubation times (48 h) were necessary due to the similar coordination strength of the two ligands being exchanged. More recently, Cha and coworkers demonstrated an elegant approach to functionalizing PCN-224 NPs, composed of Zr₆-based SBUs, with DNA.⁹⁶ PCN-224 NPs were first reacted with N α ,N α -bis(carboxymethyl)-L-lysine hydrate, which contains three carboxylic acid functional groups that can coordinate cooperatively and strongly with the surface Zr sites, promoting facile surface ligand exchange and exposing a targetable alkyl amine group on the surface of the MOF. The amine-modified NPs were then functionalized with a NHS-DBCO linker via NHS-amine chemistry, which was followed by DNA conjugation with azido-terminated oligonucleotides. With the surface oligonucleotides installed, the MOF NPs were predictably assembled via hybridization with complementary DNA-modified upconversion NPs leading to enhanced singlet oxygen production at the porphyrin ligand upon irradiation. While this work required multiple steps to achieve the desired surface modification, it is a compelling demonstration of the power of direct coordination to labile surface metal sites, and highly orthogonal organic click chemistry to install complex, programmable ligands.

Importantly, this general approach is not limited to carboxylate-terminated ligands. For example, nitrogen-bearing ligands have been demonstrated as useful coordinating moieties for ligand installation.⁹⁷ Granick and coworkers showed that an imidazolate-modified BODIPY dye could be functionalized onto the surface of ZIF-8 (Zn₂(methylimidazolate) via surface ligand exchange under relatively mild conditions.⁶⁷⁻⁶⁸ Confocal microscopy was employed to verify that

the scope of functionalization was limited to the particle surface, as predicted by the relative size of the BODIPY dye and the narrow pores of the ZIF-8 MOF. The amine-based coordinative ligand was further improved by Wuttke and Lächelt, who developed a versatile oligohistidine tag-based coordination strategy to immobilize a series of peptides and proteins onto three archetypical carboxylate-based MOF NPs: MIL-88A-Fe, HKUST-1 and *Zr-fum* (**Figure 1.8a**). In this report, surface exchange of the nitrogen-based ligands was ensured by designing the ligand in such a way that two histidine groups would cooperatively chelate individual surface metal atoms. This chelation strategy proved highly successful, yielding dense surface coverage and allowing for explorations of cellular uptake coinciding with peptide and protein delivery.

While the aforementioned systems employ ligand modifications that closely mimic the coordinating moieties of the framework linkers, phosphate units have shown great promise in PSM surface functionalization. In a series of studies, Lin and coworkers elegantly showed that a monolayer of phosphate-terminated lipids could be attached to MOF and nanoscale coordination polymer (NCP) external surfaces.⁹⁸⁻¹⁰¹ Intriguingly, a second layer of lipid molecules could be subsequently coated onto the lipid-terminated particles to form asymmetric lipid bilayers, a process driven by hydrophobic-hydrophobic interactions. With this approach, Lin and coworkers developed the first self-assembled NCP for highly delivery of the anti-cancer prodrug cisplatin (**Figure 1.8b**). The authors employed a micro-emulsion technique to synthesize Zn NCPs in the presence of 1,2-dioleoyl-sn-glycero-3-phosphate sodium salt (DOPA), a phosphate-terminated lipid that coordinates strongly to the surface zinc atoms of the NCPs. The DOPA-coated NCPs were then coated with 1,2-dioleoyl-sn-glycero-3-phosphocholine (DOPC), cholesterol, and 1,2-

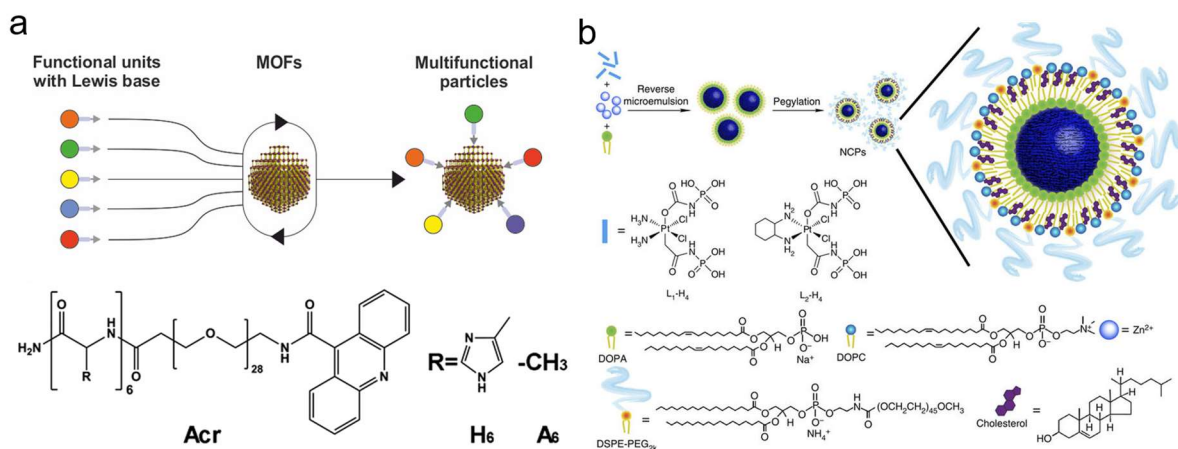


Figure 1.8. Schematic representation of post-synthetic external surface functionalization via different coordinative interactions. (a) MOF NPs functionalized with diverse surface ligands via chelation of SBUs with datively bound histidine (imidazole) units (panel a bottom). Reproduced with permission. Copyright 2017, American Chemical Society. (b) Zinc bisphosphonate NCPs functionalized with DOPA, and assembled into asymmetric lipid bilayers via hydrophobic-hydrophobic interactions between DOPA and DOPC/cholesterol/DSPE-PEG_{2k} (bottom right). Reproduced with permission. Copyright 2014, Nature Publishing Group.

distearoyl-*sn*-glycero-3-phosphoethanolamine-*N*-[methoxy(polyethyleneglycol)-2000] (DSPE-PEG_{2k}) in a 4:4:2 molar ratio via hydrophobic interactions, leading to self-assembled asymmetric lipid bilayers. In addition to coordination chemistry approaches, external surface functionalization with lipids has also been achieved through electrostatic interactions and solvent-exchange deposition strategies.^{98, 102} For example, with the goal of developing new nanoscale drug delivery vehicles for cancer treatment, Wuttke and coworkers reported the encapsulation of Fe-MIL-88A NPs within exosomes, which are endogenous cell-derived vesicles composed of phospholipid bilayers.¹⁰³ The encapsulation of drug-loaded MOF NPs was realized using the fusion method, as developed by Liu and coworkers,¹⁰⁴ leading to a versatile drug delivery vehicle with efficient cell uptake and no premature leakage. Surface functionalization with lipid bilayers offers several advantages: 1) stabilizing the NPs and facilitating their internalization into cells,¹⁰² 2) decreasing

cargo release rate,⁹⁸ and 3) improving the chemical tailorability of MOF NP due to the diverse range of lipid bilayer compositions available.¹⁰⁵

Collectively, these advances in the realm of PSM through covalent and coordinative bonds paved the way towards addressing some of the major challenges in surface functionalization of MOF NPs. These studies demonstrated enhanced control over surface ligand density, MOF NP colloidal stability, and modular design of functional MOF NP architectures that show promise for a variety of biomedical applications.

1.4 Beyond MOF Nanoparticles

Herein, we summarize recent advances in synthetic strategies to obtain modular MOF NPs with control over particle size, shape, and surface chemistry. Although remarkable progress has been made, there remains significant room for improvement in the understanding of key features of MOF NP synthesis and functionalization.

In particular, explanations of the initial mechanisms of particle nucleation and how factors such as modulators, temperature, and solvent affect these primary events remain mainly postulation. As such, improved characterization and mechanistic understanding of nucleation and subsequent crystal growth will drastically improve our ability to convert MOF NP synthesis from empirically driven guesswork to a highly predictable science. Chapter two presents a comprehensive study of the role of chemical modulators in the crystallization process of MOF NPs, which highlights their impacts on the resulting MOF NP polydispersity and colloidal stability. Additionally, although macroscopic MOF single crystals have been routinely synthesized, undesired impurity phases are sometimes obtained in MOF NP syntheses as kinetic byproducts, where purification remains challenging. To resolve this issue, we introduce a straightforward

electrostatic based purification strategy to separate mixed-phase MOF NPs, leading to facile access to pure phase MOF NPs for further investigations.

Further, it is desirable to expand the synthetic toolbox to control MOF NPs surface architectures, which can be predictably tailored for a wide range of attractive applications. Specifically, programmable surface ligands, such phospholipids and oligonucleotides, shall be targeted. In Chapter three, we discuss a post-synthetic surface functionalization strategy that selectively modifies the external surface of MOF NPs with phosphate-terminated lipids. Strong coordination between coordinatively unsaturated metal sites and phosphate surface ligands promotes efficient surface modification under mild conditions with retained internal porosity. In Chapter four, we show the generality of such coordination-based strategy by interfacing MOF NPs with terminal phosphate modified DNA. Design rules are emerging from this study that allow us to predict DNA surface coverage as a function of surface metal SBU density, metal SBU connectivity, and metal-phosphate bond strength. As a proof-of-concept, a novel intracellular protein delivery strategy is developed based upon these DNA functionalized MOF NPs.

Finally, hierarchical materials composed of precisely-assembled MOF NP building blocks are very attractive, as they exhibit properties unique from those demonstrated with conventional inorganic NPs owing to their porosity, tailorable host-guest interactions, and chemical and physical modularity. Thus far, few examples of ordered structures have been prepared from MOF NP building blocks, all of which are entropically driven to form closed packed assemblies. Taking advantage of the programmability of DNA surface ligands, Chapter five describes a colloidal crystal engineering strategy incorporating DNA functionalized MOF NPs as a novel class of building blocks. We have shown that such building blocks provide access to a diverse set of

colloidal crystals spanning numerous crystal symmetries with tunable lattice parameters. Importantly, the complex crystal shapes afforded by MOF NPs allows one to control DNA bond directionality and facet-facet interactions. When combined with all that is known about MOF NP shape control, these experiments suggest that in addition MOF NPs being a new compositionally diverse set of building blocks with which colloidal crystal properties can be tuned, particle shape-induced bonding interactions with MOF PAEs will be extremely useful for engineering crystal outcomes.

Through these advances, and additional improvements in synthesis and characterization methodologies, which are discussed in Chapter six, we believe MOF NPs will emerge as a promising new class of functional nanomaterials with the potential to significantly impact the fields of catalysis,⁸ separations,¹⁰⁶ and nanomedicine.¹⁰⁷

CHAPTER TWO: Synthetic and Post-Synthetic Purification Strategies to Control Size, Surface Charge, and Phase Uniformity of Metal-Organic Framework Nanoparticles

Materials in this chapter is based upon published work:

Morris, W.; Wang, S.; Cho, D.; Auyeung, E.; Li, P.; Farha, O. K.; Mirkin, C. A. *ACS Appl. Mater. Interfaces* **2017**, *9*, 33413-33418.

Wang, S.; Liao, Y.; Farha, O.; Xing, H.; Mirkin, C. A. *Chem. Mater.* **2018**, DOI: [10.1021/acs.chemmater.8b01164](https://doi.org/10.1021/acs.chemmater.8b01164).

2.1 Abstract

Chemical modulators play critical roles in regulating the crystallization of MOF NPs. Herein, we chose UiO-66 (UiO = University of Oslo, $Zr_6(OH)_4O_4(C_8O_4H_4)_6$) as a model MOF to systematically evaluate the impact of a series of carboxylic acid modulators, R-COOH (where R = H, CH₃, CF₃, and CHCl₂), on the resulting MOF NP crystallite size, shape, uniformity, surface charge, and porosity. The phase purity and size of each MOF NP was confirmed by powder X-ray diffraction (PXRD), BET surface area analysis, and scanning transmission electron microscopy (STEM). Size control of UiO-66 crystals from 20 nm to over 1 micron was achieved and confirmed by STEM. The colloidal stability of each MOF NP was evaluated by dynamic light scattering and was found to be highly dependent on the modulator conditions utilized in the synthesis, with both lower pK_a and higher acid concentration resulting in more stable structures. Furthermore, STEM was carried out on both colloidally stable samples and those that exhibited a large degree of aggregation, which allowed for visualization of the different degrees of dispersion of the samples. The use of modulators at higher concentrations and with lower pK_a s leads to the formation of more defects, as a consequence of terephthalic acid ligands being replaced by modulator molecules, thereby enhancing the colloidal stability of the UiO-66 nanoparticles. These findings could have a significant impact on nanoscale MOF material syntheses and applications, especially in the areas of catalysis, and drug delivery.

In addition to controlling the size uniformity of MOF NPs by chemical modulators, it is equally important to ensure their phase purity. Although macroscopic MOF single crystals have been routinely synthesized, undesired impurity phases are sometimes obtained in MOF NP syntheses, where purification remains challenging. Herein, we report an electrostatic adsorption

strategy to separate mixed phases of MOF NPs based on their metal cluster dependent surface charge differences. As proof-of-concept, two groups of mixed-phase MOF NPs were synthesized and subsequently separated based on their different Coulombic attraction to negatively charged magnetic beads (MBs). Different frameworks form based upon the conditions used. In the first group, a combination of three possible iron-terephthalate frameworks were evaluated: MIL-53, MIL-88B, and MIL-101 (MIL = Material Institute Lavoisier). In the second group, two Zr-terephthalate frameworks were separated: MIL-140A and UiO-66. MIL-53 and MIL-140A are not positively charged and do not adsorb to the MBs. The extraction of adsorbed MIL-88B, MIL-101, and UiO-66 MOF NPs from the MBs was achieved by adding 4-hydroxybenzophosphonate, a surface capping ligand that neutralizes the charge of the MOF NPs and, therefore, results in their desorption from the MBs. The phase purities of the isolated NPs were verified by PXRD, as well as scanning electron microscopy (SEM). This straightforward purification strategy provides quick access to phase-pure MOF NPs, which is important for their use as biological probes, catalysts, and building blocks for colloidal crystal engineering strategies.

2.2 Introduction and Background

Nanoscale porous structures, namely, Infinite Coordination Polymers (ICPs) and MOFs, constructed from metal containing moieties connected in three dimensions by rigid organic ligands, are becoming topics of significant interest in nanoscience.^{16, 30,108} Solvothermal control techniques, microwave methods, and chemical modulator guided routes have been developed for synthesizing them.^{20, 109} Additionally, studies have been performed to better understand how particle size affects the gas adsorption, ion exchange, and catalytic properties of MOFs.^{13, 110}

In 2011, Behrens and coworkers first reported that chemical modulators could be used in the size-controlled synthesis of UiO-66.⁶¹ Such modulators, which are typically acids have been proposed to compete for metal binding sites, thereby controlling the number of nucleation sites available for crystal growth, which in turn impacts crystallite size.⁵⁵ Since that initial work, modulators have been employed extensively in the size-controlled synthesis of UiO-66 and its analogues, which led to the first single crystal X-ray diffraction structure determination of UiO-66.¹¹¹ Structural characterization carried out by Wu *et. al.* and Cliffe *et. al.* further revealed that both “missing linker” and “missing metal cluster” defects (with respect to the ideal UiO-66 MOF structure) exist as a result of terephthalic acid ligands being replaced by modulator molecules.¹¹²⁻¹¹³ Indeed, the number of defects found in crystals of UiO-66 and its analogues depends on the solvothermal conditions utilized for synthesis, with modulator concentration playing a key role.¹¹⁴ Importantly, increasing the number of defects in a MOF crystal leads to both enhanced catalytic and gas adsorption properties.¹¹⁴{Shearer, 2016 #223, ¹¹⁵ From these synthetic studies, it is clear that both the size of the MOF crystallite and the number of defects within the bulk crystals can be systematically controlled by adjusting the pK_a and concentration of modulators during synthesis. With changes in modulators dictating the chemistry of bulk MOF structure, one might expect surface properties at the nanoscale to be affected. Therefore, we have set out to systematically investigate the role that modulators play in altering the colloidal stability of UiO-66.

Colloidally stable nanoparticles are important for applications in biology, materials assembly, and catalysis. With MOF nanoparticles, colloidal stability typically has been realized by surface functionalization with polymers, silica, DNA, and lipids.^{75, 88, 93, 116-117} These multistep methods can be complicated and often block access to the pores. Therefore, simpler methods for controlling colloidal stability while maintaining porosity are required. Herein, we evaluate a

strategy to stabilize MOF colloids using acidic synthetic modulators that typically are used to control crystallite size, catalytic activity, and shape uniformity.^{55,118} Specifically, we evaluate how the type, pK_a , and concentration of the modulation can be used to control the surface charge on the MOF nanoparticle, which directly corresponds to colloid stability.

Herein, we present the first systematic study of the role of modulators, type and concentration, in controlling the size dispersity and colloidal stability of nanoscale UiO-66. Samples of UiO-66, $Zr_6(OH)_4O_4(C_8O_4H_4)_6$, were synthesized

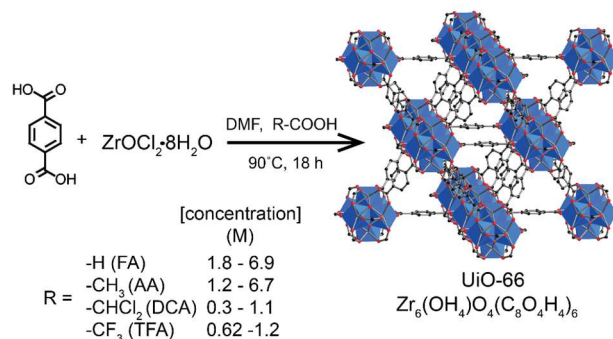


Figure 2.1. The carboxylic-acid modulated synthesis of UiO-66.

using four different modulating acids (acetic acid (AA), formic acid (FA), dichloroacetic acid (DCA), and trifluoroacetic acid (TFA)) across a range of concentrations (**Figure 2.1**). Powder X-ray Diffraction (PXRD) was then used to evaluate the phase purity of each sample, STEM was utilized to determine the size dispersity of each MOF structure, and BET analysis of nitrogen adsorption-desorption isotherms was used to determine the underlying porosity of the samples. Dynamic light scattering (DLS) studies performed on the as-synthesized MOFs revealed that the modulators utilized during synthesis dramatically impacted the colloidal stability of the particles. In particular, MOF particles of analogous size showed different degrees of aggregation in aqueous solution depending on the acid used in their synthesis. Importantly, this work reveals that modulator-MOF reaction conditions can dictate colloidal stability, a parameter that significantly impacts the scope of utility of these emerging nanoscale materials for a variety of intended uses.

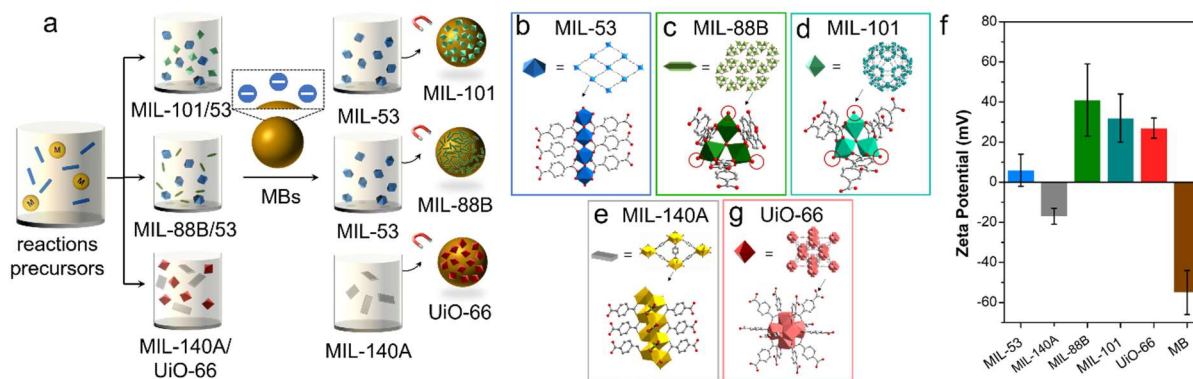


Figure 2.2. (a) Schematic illustration of the synthesis of mixed-phase MOF NPs and their magnetic beads-assisted separation. (b-g) Crystal structures and SBUs of MOF MIL-53, MIL-88B, MIL-101, MIL-140A and UiO-66 with CUS highlighted by red circles. (f) Surface charge measurements of macroscopic MOFs and MBs.

Methods for isolating, separating, and purifying chemical compounds are some of the most important and energy-consuming processes in the chemical industry.¹¹⁹ Although techniques, such as extraction, chromatography, and crystallization have been developed to purify small molecules and certain biological products,¹²⁰ effective ways of separating and isolating colloidal nanomaterials are often limited to materials that differ significantly in composition, size, or density.¹²¹⁻¹²⁵ Recently, MOF NPs have emerged as a novel class of crystalline porous materials that are promising for many potential applications, including drug delivery, bioimaging, gas separations, and chemical sensing.^{9, 108, 126-129} However, despite the variety of approaches that have been developed to control the nucleation and growth of MOF NPs, mixed-phase frameworks are occasionally obtained from one-pot solvothermal syntheses.^{71, 130-135} These mixed-phase MOF NPs emerge from different metal-ligand connectivity or the formation of different metal cluster secondary building units (SBUs), leading to frameworks with unpredictable internal surface areas, ill-defined pore structures, and inconsistent gas adsorption isotherms, which significantly limit their utility.¹³⁶⁻¹³⁷ Although density-based separation techniques have been developed,¹³⁸⁻¹³⁹ they

are limited to mixtures of sufficiently large bulk MOF crystals (tens of μm to a few mm). Moreover, the relatively small density differences between different phases and the small size of MOF NPs make them difficult to separate based upon density driven techniques.¹⁴⁰⁻¹⁴¹ Indeed, at present, no effective approach exists to purify nanoscale MOFs consisting of mixed phases.

Herein, we describe a facile purification strategy for selectively separating colloidal solutions of mixed-phase MOF NPs based on their metal cluster-dependent surface charge (**Figure 2.2a**). Previously, we and others have observed that MOF particles with coordinatively unsaturated metal sites (CUS) have significantly more positive surface charge as compared to those without.^{75, 94, 142} Therefore, we hypothesized that such charge disparities would allow for particle separation based upon Coulombic attraction with the negatively charged surface of a MB. In this vein, MBs were used as a support to study the separation of mixtures of particles consisting of different phases of MOFs, in two proof-of-concept examples. In the first example, three phases of iron-terephthalate frameworks were studied: MIL-53 ($\text{FeOH}(\text{BDC})$),¹⁴³ MIL-88B ($\text{Fe}_3\text{O}(\text{DMF})_2\text{Cl}(\text{BDC})_3$),¹⁴⁴ and MIL-101 ($\text{Fe}_3\text{O}(\text{DMF})_2\text{Cl}(\text{BDC})_3$) ($\text{H}_2\text{-BDC}$ = terephthalic acid).¹⁴⁵ In the second example, two zirconium-terephthalate frameworks were similarly studied: MIL-140A ($\text{ZrO}(\text{BDC})$) and UiO-66 ($\text{Zr}_6\text{O}_4(\text{OH})_4(\text{BDC})_{12}$).^{115, 146} In principle, this strategy can be generalized for isolating and purifying many other MOF NPs containing coordinatively unsaturated metal sites, as long as they differ in surface charge.

The frameworks explored in this study are connected by identical metal and organic precursors, and mixed-phase NPs were often obtained in one-pot syntheses, especially between MIL-53 (a thermodynamic product) and MIL-101 (a kinetic by-product).¹⁴⁷ As such, to develop an effective structure-based purification strategy, the SBUs of these frameworks were first

carefully investigated. As shown in **Figure 2.2 b-g**, two distinct types of metal clusters exist in these closely related frameworks, namely: 1) infinite 1D chains of octahedral Fe(III) centers for MIL-53 and Zr(IV) oxide for MIL-140A, and 2) discrete SBUs of trinuclear oxo-centered Fe(III) cluster (exposing three solvent-binding sites as potential CUSs) for MIL-101 and MIL-88B, and a Zr₆(IV) oxo cluster (having a significant number of missing-linker defects as potential CUSs) for UiO-66.¹¹²

2.3 Results and Discussion

2.3.1 Modulated Solvothermal Synthesis of UiO-66 MOF Nanoparticles

Initially, reaction conditions were systematically screened to select for UiO-66 particles between the 20 nm and 1 μm size range. Over twenty different samples of UiO-66 were synthesized in this study by utilizing four modulators over a range of concentrations (Table S1). The four modulators and the concentration ranges utilized were formic acid (FA) (1.8 – 6.9 M), acetic acid (AA) (1.2 – 6.7 M), dichloroacetic acid (DCA) (0.3- 1.1 M), and trifluoroacetic acid (TFA) (0.62 – 1.2 M). Each sample of UiO-66 was synthesized in a solvothermal reaction at 90 °C for 18 h, employing the selected modulator at the given concentration. At concentrations above 1.1 and 1.2 M for TFA and DCA, respectively, no product was observed after 18 h at 90 °C. In reactions where product was formed, analysis by PXRD was carried out after solvent exchange and drying (**Figure 2.3**). PXRD data collected from each sample was successfully indexed to simulated patterns generated from the reported structure of UiO-66, which confirmed the expected **fcu**

topology (Scheme 1).¹⁴⁸ At low concentrations of modulator, peak broadening was observed, which is indicative of nanoscale crystallites.⁶¹

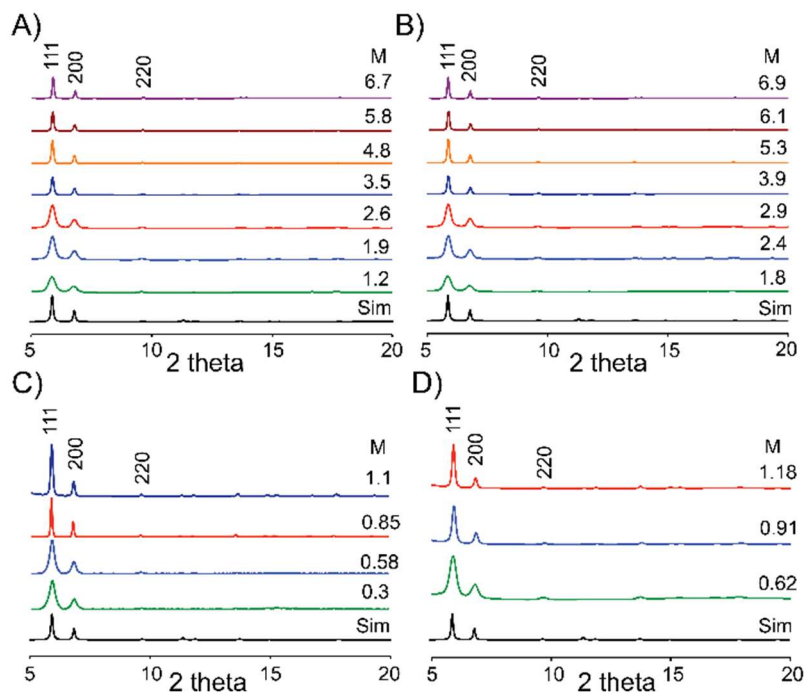


Figure 2.3. a-d Powder X-ray diffraction data for UiO-66 synthesized with different modulators over a series of acid concentrations (molarity is designated on far right): a) acetic acid, b) formic acid, c) dichloroacetic acid, and d) trifluoroacetic acid. Sim = simulated pattern of UiO-66.

2.32 Role of Modulators in Controlling MOF Nanoparticle Polydispersity

To evaluate the role of modulators on crystallite size and polydispersity, we utilized STEM to visualize the synthesized samples (**Figure 2.4**). For each acidic modulator, the size of the MOF crystallites increased as a function of acid concentration. The morphologies of the crystals change as a function of acid concentration, with low concentrations producing UiO-66 with a quasi-spherical morphology and higher concentrations leading to the formation of octahedral UiO-66 crystals. To evaluate the size and polydispersity of each sample, the dimensions (diameter for

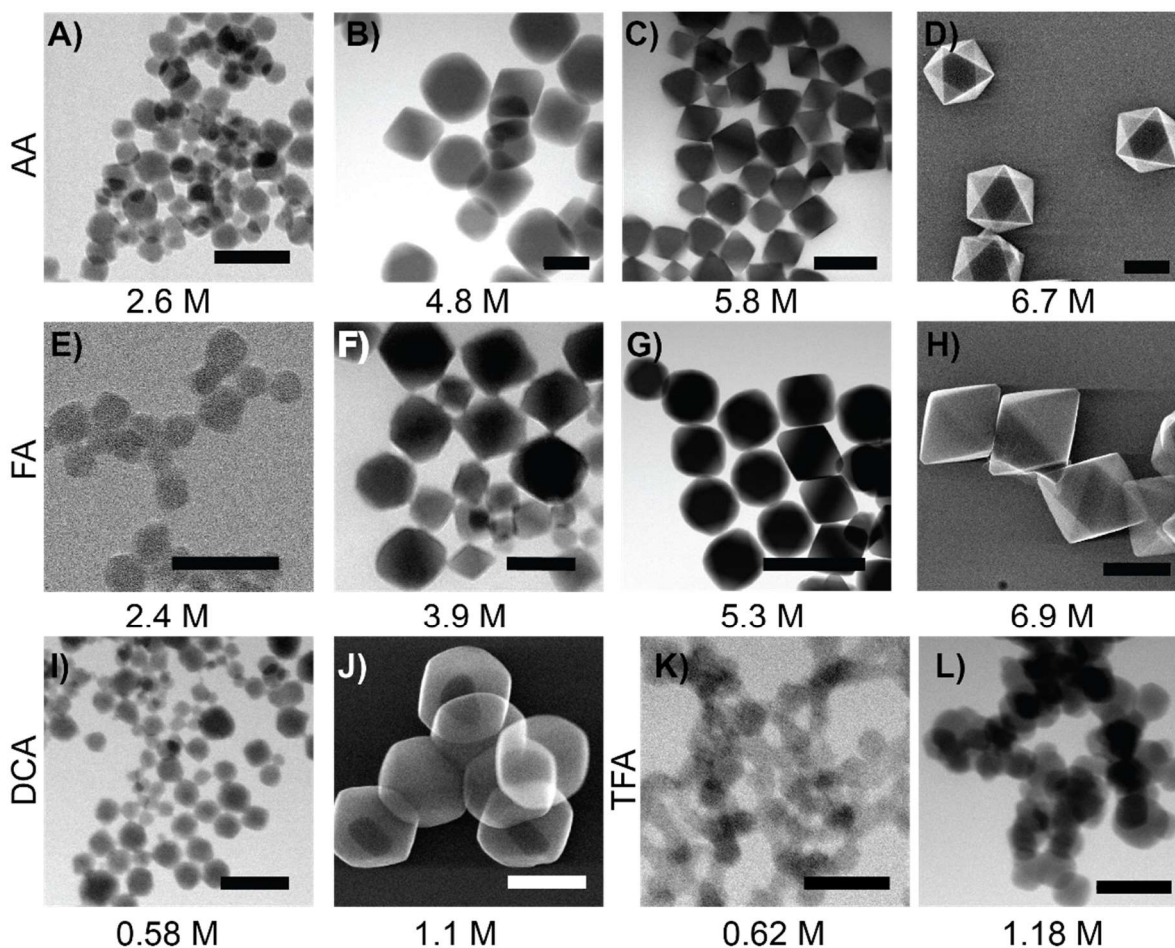


Figure 2.4. STEM images of UiO-66 synthesized with different acid modulators and concentrations. a-d) UiO-66 synthesized with acetic acid: a) 2.6 M, b) 4.8 M, c) = 5.8 M, and d) 6.7 M. E-H) UiO-66 synthesized with formic acid: e) 2.4 M, f) 3.9 M, g) = 5.3 M, and h) 6.9 M. i) and j) UiO-66 synthesized with dichloroacetic acid: i) 0.58 M and j) 1.1 M. K and l) UiO-66 synthesized with trifluoroacetic acid: k) 0.62 M, and l) 1.18 M. Scale bars a = 100 nm, b = 200 nm, c = 500 nm d = 500 nm, e = 100 nm, f = 100 nm, g = 1000 nm, h = 1000 nm, i = 100 nm, j = 500 nm, k = 100 nm, and l = 500 nm.

quasi-spherical particles, and edge length for octahedral shape particles) of fifty crystals from one synthesis were determined from the STEM images (**Figure 2.5**). Depending on acid concentration, the size of the crystals varied from 17(2)–721 (56) nm, 17(4)–1174 (258) nm, 19(5)–550 (51), and 38(7)–227 (46) for AA, FA, DCA, and TFA, respectively (Table S1). Therefore, we have

determined that by using analogous synthetic conditions and simply changing the modulator and its concentration, one can realize size control from 20 nm to over one micron (Table S1). To further evaluate the dispersity of the MOF crystals, a coefficient of variation (CV) was calculated for each sample (**Figure 2.5**) and determined to be between 20 and 30%. Significantly, acetic acid was shown to produce samples with the narrowest size distribution at both high and low concentrations of modulator (**Figure 2.5**).

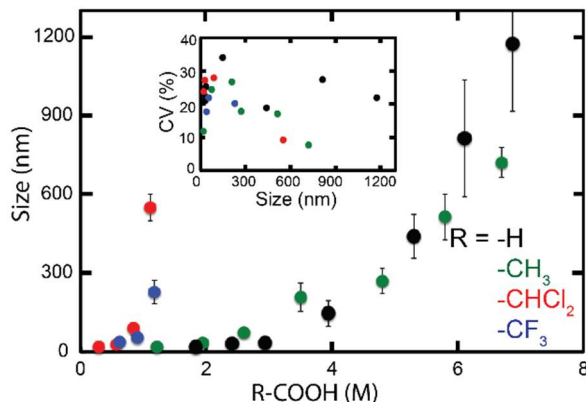


Figure 2.5. The size of UiO-66 as a function of acid modulator concentration, and the coefficient of variation (CV) as a function of size.

2.33 Surface Defects Dictate Particle Surface Charge and Colloidal Stability

To characterize the porosity of each MOF synthesized, we performed N_2 isotherms and evaluated their surface area by BET analysis (**Figure 2.6**). Prior to the surface area measurements, the samples were activated to remove solvent from the pores of the MOF (see the Supporting Information). In each case, the MOFs synthesized using higher modulator concentrations, exhibited higher surface areas compared to the ones prepared with lower modulator concentrations (**Figure 2.6a**). Similarly, UiO-66 nanocrystals of comparable size (~ 20 nm) synthesized with strong modulators, DCA and TFA, exhibited higher porosity as compared to those synthesized with the weaker modulator, acetic acid (**Figure 2.6b**). Compared to terephthalic acid linkers, deprotonated strong modulators have higher binding affinities for Zr clusters, resulting in a high concentration of missing cluster defects in the MOF structures. Since the pK_a values of formic acid

(3.77) and acetic acid (4.76) are similar to that of terephthalic acid (1st 3.51 and 2nd 4.82), they compete with terephthalic acid to form coordination bonds with available Zr (in solution and on the surface of the

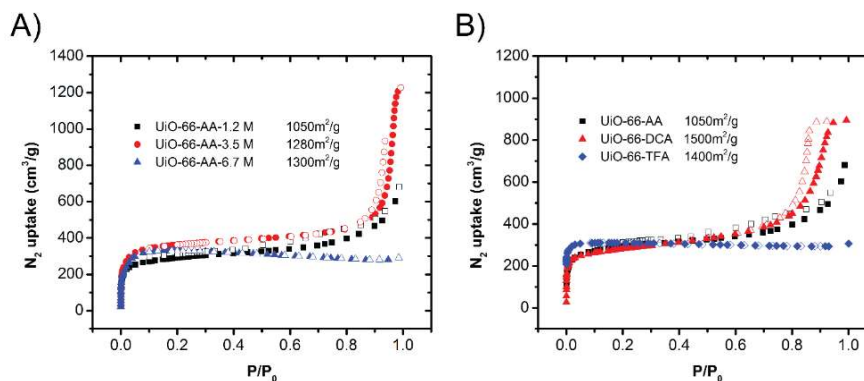


Figure 2.6. The impact of modulator concentration and acid utilized on porosity. BET adsorption isotherm for a) three concentrations of acetic acid modulated UiO-66 colloids, 1.2 M (black), 3.5 M (blue) and 6.7 M (red), respectively. b) Three different acid modulated UiO-66 colloids, AA (1.2 M, black), DCA (0.58 M, red), and TFA (0.62 M, blue), respectively.

growing MOF), which in turn slows down particle nucleation and promotes slow growth of the MOF, favoring larger crystals with fewer defects.⁶² This is important because BET area analysis of UiO-66 shows that the number of defects in the MOF correlate with the modulator used in the synthesis.^{62, 111, 149-150}

To investigate how modulator type and concentration affect the colloidal stability of the MOF nanoparticles, DLS measurements were carried out to evaluate the average hydrodynamic radius of each MOF nanoparticle sample in water as well as the absence of aggregates. As shown in **Figure 2.7 a-b**, the hydrodynamic radius of MOF nanoparticles increases as modulator concentration increases, and in general DLS measurements are in agreement with particle size measurements obtained from microscopy images. Samples synthesized with FA, DCA, and TFA were colloidally stable, as probed by DLS, with average particle sizes closely reflecting those measured by STEM (Table S1). When acetic acid was used as a modulator, similar behavior was observed, however, when UiO-66 was synthesized with acetic acid as the modulator at low

concentrations (1.2 M and 1.9 M), significant particle aggregation occurred (**Figure 2.7b**, purple). The MOF nanoparticle sizes were determined to be 17(2) and 34(22) nm from STEM measurements, respectively, but no meaningful determinations could be made by DLS measurements on these samples due to aggregation (**Figure 2.7c**). In contrast, the sample that was prepared with DCA did not show any visible aggregation (DCA = 0.58 M, **Figure 2.7d**), and when dispersed and dried on a TEM grid, STEM measurements revealed well-formed particles and no

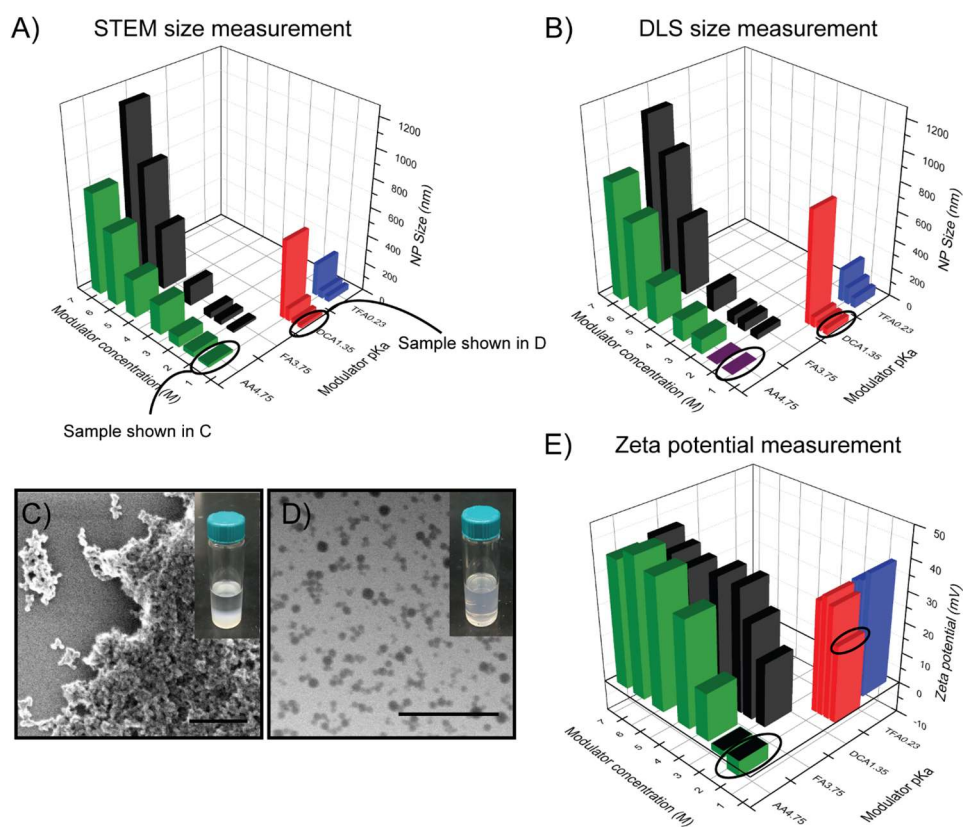


Figure 2.7. A summary of MOF nanoparticle size measurements determined by a) STEM and b) DLS, as a function of modulator relative acidity and molar concentration. The acids utilized are FA (black), AA (green), DCA (red), and TFA (blue). The purple region in b) corresponds to highly aggregated samples where particle size cannot be determined by DLS. STEM image and digital photographs of UiO-66 dispersed in H₂O synthesized with different modulators: C) UiO-66 synthesized with AA (1.2 M) and D) UiO-66 synthesized with DCA (0.58 M). E) Zeta potential measurements as a function of modulator relative acidity and molar concentration. Scale bars C = 200 nm and D = 500 nm.

evidence of aggregation (**Figure 2.7e**). Therefore, by simply choosing the appropriate modulator used during synthesis, one can deliberately generate colloids of stable UiO-66 particles across a wide size range.

To further understand the surface chemistry and colloidal stability of the MOF nanoparticles,^{75, 151} the zeta potential of each sample was evaluated (**Figure 2.7e**). The zeta potential of the MOF nanoparticles can be altered by varying the number of defects introduced in the samples, which can be accomplished by (i) changing the concentration of modulator or (ii) using modulators with different acid strengths. For all particles synthesized with acetic acid as the modulator, zeta potential measurements spanned the broadest range from -5 to 41 mV. Samples of UiO-66 synthesized with low concentrations of acetic acid were colloidally unstable with zeta potentials close to zero, while samples synthesized with high concentrations of acetic acid were colloidally stable with zeta potentials of approximately +40 mV. These results suggest that as the concentration of acetic acid modulator is increased, more surface defects are incorporated which increases the surface charge and hence the repulsion between neighboring nanoparticles. The zeta potential was also dramatically altered by using modulators with different acid strength which also controls the number of defects introduced into the nanoparticles. Moreover, the use of strong acid modulators allows for the synthesis of sub-50 nm nanocrystals that are highly defective and colloidally stable. Colloidal stability is in large part a consequence of the repulsion between MOF nanoparticles, which can be controlled by tuning the zeta potential of the particles. Indeed, the zeta potential is correlated with the number of defects in the particle samples.

2.34 Electrostatic Purification of Mixed-Phase MOF Nanoparticles

To evaluate the particle separation strategy, the surface charges of phase-pure micrometer-sized MOFs in ethanol were measured. Zeta potential measurements verify that MIL-88B, MIL-101 and UiO-66 exhibit positive surface charge ($+41 \pm 18$, $+32 \pm 12$ and $+27 \pm 5$ mV respectively), while MIL-53 is close to neutral ($+6 \pm 8$ mV) and MIL-140A is negatively charged (-17 ± 4 mV). This metal cluster-dependent surface charge difference provides a basis for selective electrostatic adsorption.

MIL-53 MOF particles with MIL-101 impurities were synthesized by reacting $\text{FeCl}_3 \cdot 6\text{H}_2\text{O}$ with terephthalic acid in DMF under sonication according to literature methodology.¹⁵² The particles were synthesized in the form of an orange colloid, collected via centrifugation, and redispersed in DMF, a process that was repeated two more times to remove all excess precursor. The particles were ultimately collected one final time by centrifugation and redispersed in ethanol. SEM images of the particle sample, after drying on a TEM grid, reveal that the MOF NPs consist of two particle populations, hexagonal bipyramids (MIL-53) and octahedra (MIL-101) (**Figure 2.8a**). Carboxylic acid-modified MBs dispersed in ethanol were added to the crude reaction

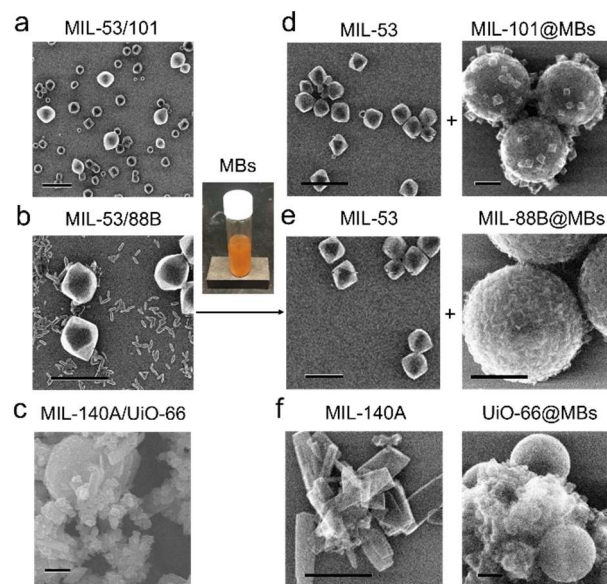


Figure 2.8. SEM images of MOF NP mixtures separated by MBs. (a-c) SEM images of as-synthesized NP mixtures: (a) MIL-53/101, (b) MIL-53/88B, and (c) MIL-140A/UiO-66 NPs; (d-f) SEM images of unbounded particles in the supernatant (left column) and particles adsorbed by MBs (right column). Scale bar = 1 μm .

mixtures, and aggregation was observed immediately, due to a precipitation reaction induced by the Coulombic attraction between the positively charged MOF NPs and negatively charged MBs. The mixture was incubated for 10 min with gentle shaking, and the color of the supernatant slowly faded due to the adsorption of MOF NPs on the MBs. Then, a magnet was used to separate the MIL-101 NPs adsorbed on the MBs from the unbound MIL-53 NPs in the colloid. In a typical experiment, MIL-101 NPs (0.3 mg) were adsorbed onto 1 g of MBs, and multiple extractions were performed to completely separate the two phases due to the relatively low adsorption capacity. To examine the efficiency of the purification, the supernatants and the aggregated MBs were collected and imaged by SEM (**Figure 2.8d**). Significantly, only hexagonal bipyramid MIL-53 NPs were observed in the supernatant while octahedron MIL-101 NPs were observed on the surface of the MBs. Similarly, a mixture of MIL-53 and MIL-88B NPs was also purified using this strategy.¹⁴³ SEM images verified that MIL-88B NPs of elongated hexagonal bipyramid morphology were electrostatically adsorbed onto MBs and separated from the MIL-53 NPs in the supernatant (**Figure 2.8b and 2.8e**). In a typical experiment, MIL-88B NPs (0.5 mg) were adsorbed onto 1 g of MBs. These experiments show that MIL-101 and MIL-88B NPs with CUS-rich SBUs can be selectively adsorbed onto MBs and separated from MIL-53 NPs, which have no CUS.

2.35 Modification of MOF Particle Surface Charge via Ligand Coordination

To further validate the separation strategy, a mixture of MIL-140A and UiO-66 NPs was purified using a process analogous to the one described above. MIL-140A particles (with sheet-like morphologies) with UiO-66 impurities (octahedra/amorphous) were synthesized by reacting $ZrCl_4$ with terephthalic acid in DMF under microwave-assisted solvothermal conditions, according to literature methodology (Supporting Information).¹⁵³ SEM images verified that UiO-66 NPs were electrostatically adsorbed onto MBs and separated from the MIL-140A plate particles in the

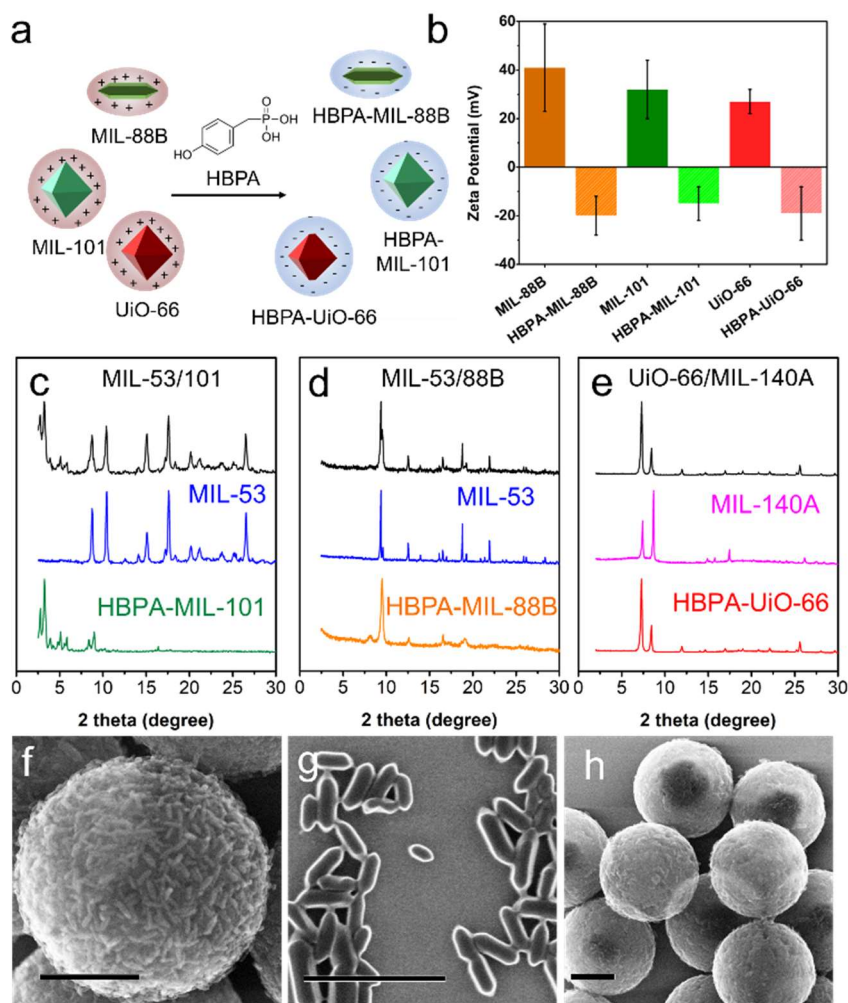


Figure 2.9. (a) Schematic illustration of MIL-88B, MIL-101 and UiO-66 surface charge modulation with HBPA. (b) Zeta potential measurements of MOF particles before and after HBPA modification. (c–e) PXRD patterns of (c) MIL-53 and MIL-101, (d) MIL-53 and MIL-88B, and (e) MIL-140A and UiO-66 NP mixtures and their respective phase-pure MOF NPs post purification. (f–h) SEM images of MIL-88B MOFs adsorbed on MBs prior to HBPA addition (f), eluted MIL-88B NPs (g), and recycled MBs after HBPA modification (h). Scale bars = 1 μm .

supernatant (Figure 2.8c and 2.8f). These experiments demonstrate that UiO-66 NPs with discrete SBUs can be selectively adsorbed onto MBs and effectively separated from MIL-140A particles that are composed of linear chain SBUs.

To release adsorbed MIL-88B, MIL-101 and UiO-66 NPs from MBs, 4-hydroxybenzophosphonic acid (HBPA) was used to neutralize the NP charge and release the MB bound particles (Figure 2.9a). As

a consequence of the strong coordination between phosphate and metal clusters on the MOF NP surface, HBPA efficiently binds to the surface CUSs (Fe^{3+} and Zr^{4+}), which significantly reduces the MOF NP surface positive charge, thereby releasing adsorbed MOF NPs from MBs.¹⁵⁴⁻¹⁵⁵ In a

typical experiment, HBPA was added to the MOF-bound MB ethanol dispersion (final concentration ~ 1 mM HBPA ethanol solution), incubated for 1 minute, and then sonicated for 30 seconds at room temperature to release the MOF NPs from the MBs in nearly quantitative yield. Subsequently, the supernatant, was collected to yield isolated MIL-101, MIL-88B NPs and UiO-66 NPs. The collected particles and MBs were then washed separately with ethanol three times until no excess HBPA could be detected in the supernatant by inductively coupled plasma atomic emission spectroscopy (**Figure S14**). Zeta potential measurements verified the reduction of surface charge of the MIL-88B ($+41 \pm 18$ mV to -20 ± 8 mV), MIL-101 NPs ($+32 \pm 12$ mV to -14 ± 7 mV), UiO-66 NPs ($+27 \pm 5$ mV to -17 ± 9 mV) post-HBPA treatment (**Figure 2.9b**). To confirm the successful separation of the two MOF NP populations, PXRD was used to determine the phase purities of the separated MOF NPs. The crude products were shown to contain mixed phases, while pure phase MOF NPs were present post-separation (**Figure 2.9 c-e, S4-S9**). Due to the intrinsic flexibility of the MIL-53 framework, its PXRD pattern is known to vary, depending on the type and extent of solvent trapped inside the pores.³¹ Here, the PXRD spectra of MIL-53 in **Figure 2.9 c-d** correspond to open and closed states respectively, which are in good agreement with literature reports.^{41, 109, 156} Importantly, no appreciable morphology change was observed for MIL-88B NPs post-HBPA functionalization (**Figure 2.9 f-h**). To determine if HBPA capping significantly alters the porosity of the MOF NPs, we performed N₂ adsorption-desorption isotherms for MIL-101 and UiO-66 NPs before and after HBPA functionalization (MIL-88B was not tested due to its breathing behavior), and no appreciable reduction of porosity was observed (**Figure S10-S13**). The regenerated MBs were recycled by repeating the above procedures at least 3 times with no significant adsorption activity loss observed (**Figure S15**).

2.4 Conclusions

In summary, the work described herein shows that modulators can be used to control UiO-66 nanoparticle surface charge, stability (in the context of a colloid), and size dispersity. Indeed, through systematic studies, we have identified conditions suitable for making colloidally stable UiO-66 particles that are sub-50 nm in size and relatively monodisperse. Furthermore, in principle, the methodology can be extended to related MOF and ICP architectures, thereby allowing them to be compared to more conventional classes of nanoparticles based upon noble metals, Fe₂O₃, and quantum dots.³¹⁻³⁶ Indeed, convenient methods for preparing colloidally stable MOF nanoparticles will set the stage for using such particles and surface modified forms of them in a variety of areas spanning the life sciences and energy conversion.

Further, a novel electrostatic adsorption strategy was developed to maximize selectivity between MOF NPs with different surface zeta potentials caused by different SBUs. The structure-property relationships between MOF NP surface charge and SBUs have been identified, and subsequently used for the purification of mixed phases of MOF NPs that are otherwise challenging to separate. The extension of this work to many more mixed phases MOFs, infinite coordination polymers, and more efficient, larger surface area adsorption media should allow for straightforward purification of a large variety of coordination polymer nanomaterials.¹⁵⁷ The ability to quickly access more pure forms of these particles, may facilitate their use as biological probes,¹⁰⁷ for energy conversion,³⁰ catalysts,⁸ and as building blocks for colloidal crystal engineering.^{11, 158-159}

2.5 Experimental Methods and Supplementary Materials

S2.1 Size analysis of UiO-66 NP synthesized with different modulators

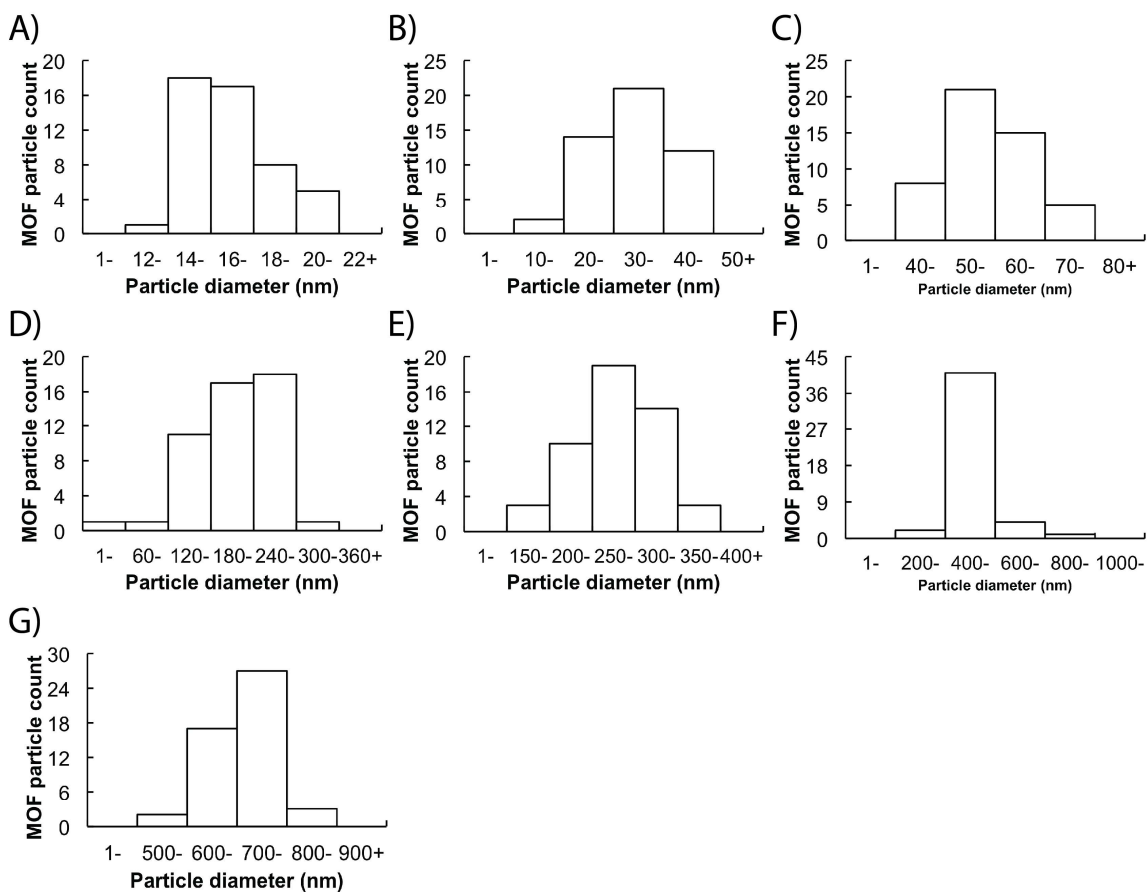


Figure S2.1. Size analysis of UiO-66 nanoparticle synthesized with acetic acid. A = 1.2 mmol/ml, B = 1.9 mmol/ml, C = 2.6 mmol/ml, D = 3.5 mmol/ml, E = 4.8 mmol/ml, F = 5.8 mmol/ml, and G = 6.7 mmol/ml.

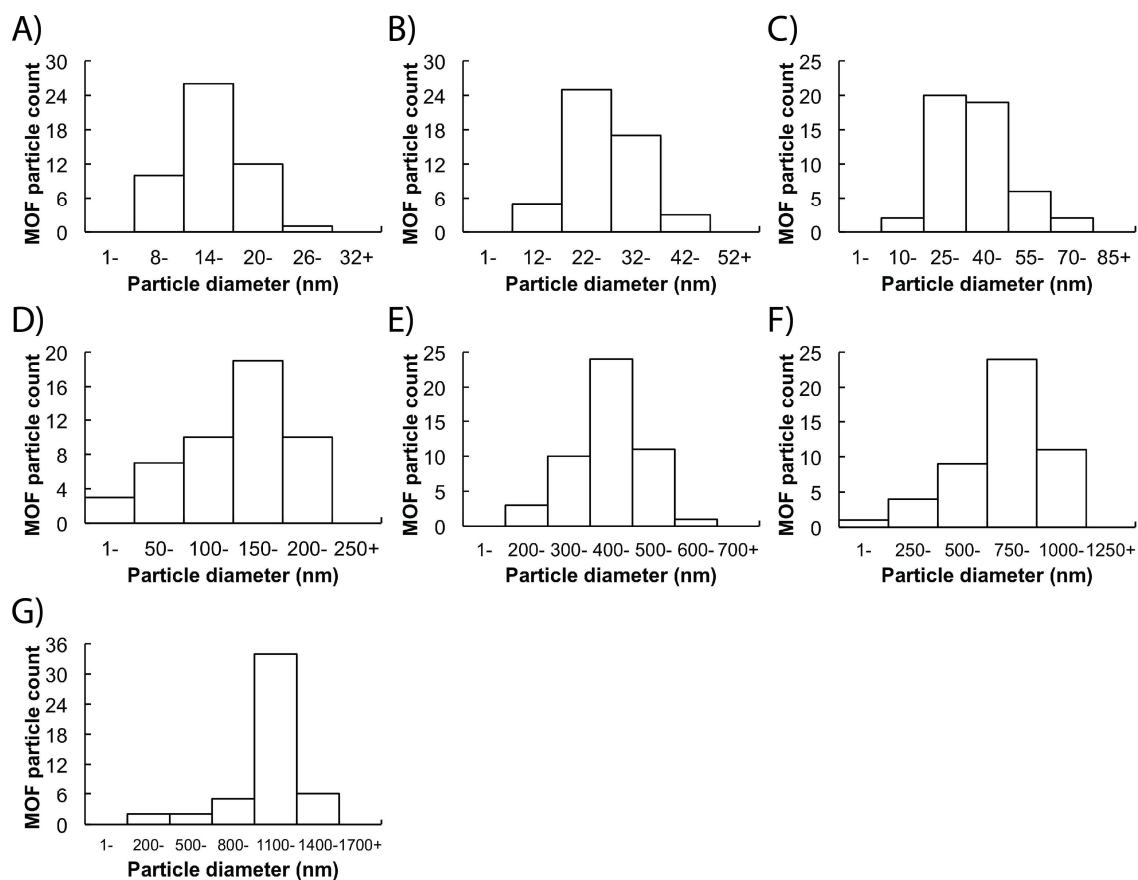


Figure S2.2. Size analysis of UiO-66 nanoparticle synthesized with benzoic acid. A = 1.8 mmol/ml, B = 2.4 mmol/ml, C = 2.9 mmol/ml, D = 3.9 mmol/ml, E = 5.3 mmol/ml, F = 6.1 mmol/ml, and G = 6.9 mmol/ml.

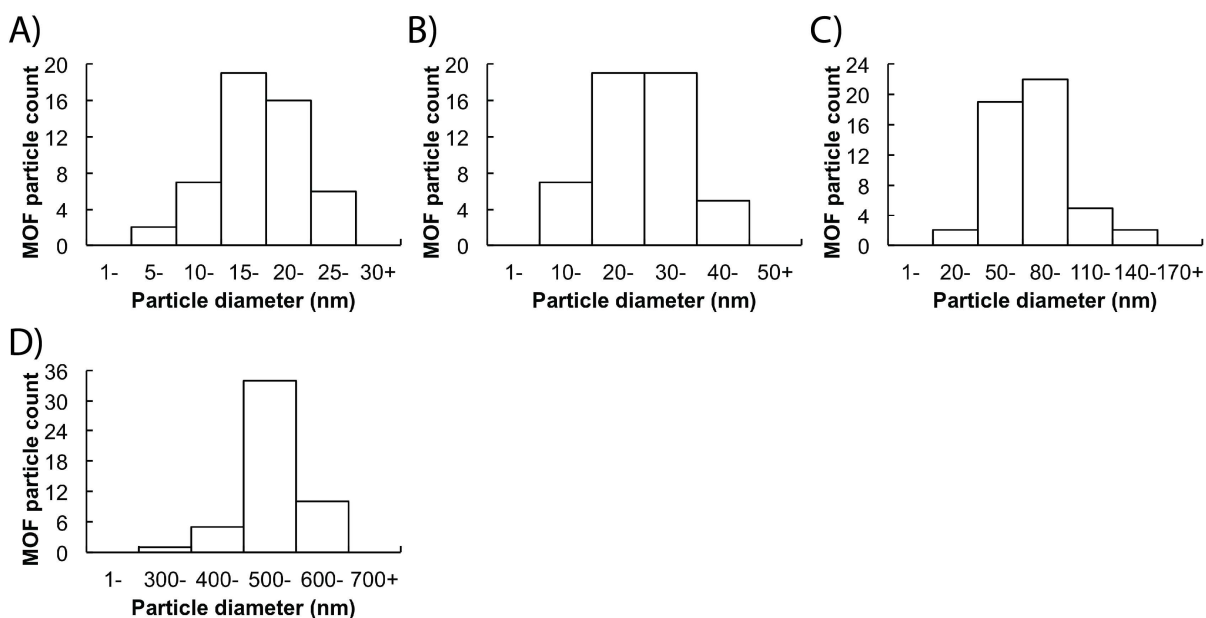


Figure S2.3. Size analysis of UiO-66 nanoparticle synthesized with dichloroacetic acid. A = 0.3 mmol/ml, B = 0.58 mmol/ml, C = 0.85 mmol/ml, and D = 1.1 mmol/ml.

Dynamic light scattering analysis

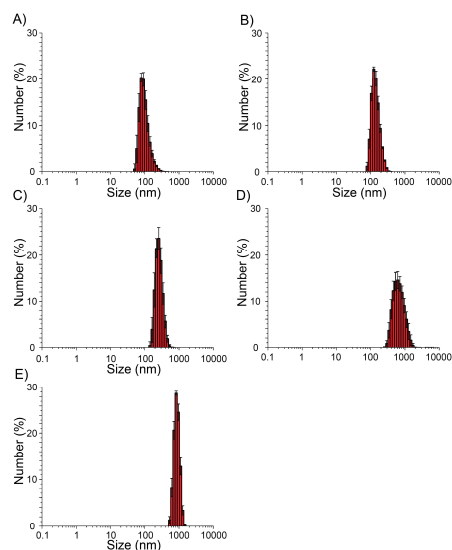


Figure S2.4. DLS number analysis of UiO-66 nanoparticle synthesized with acetic acid. A = 2.6 mmol/ml, B = 3.5 mmol/ml, C = 4.8 mmol/ml, D = 5.8 mmol/ml, and E = 6.7 mmol/ml.

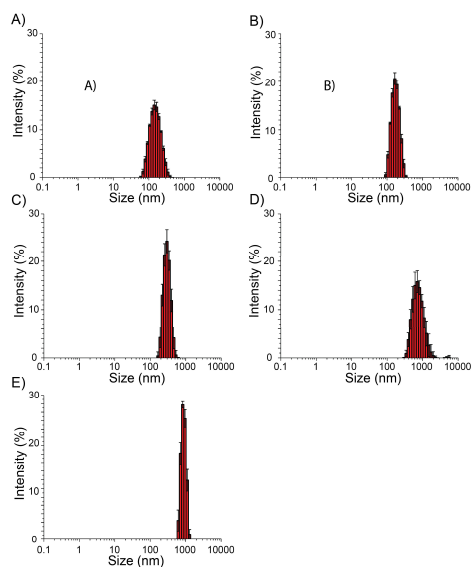


Figure S2.5. DLS intensity analysis of UiO-66 nanoparticle synthesized with benzoic acid. A = 2.6 mmol/ml, B = 3.5 mmol/ml, C = 4.8 mmol/ml, D = 5.8 mmol/ml, and E = 6.7 mmol/ml.

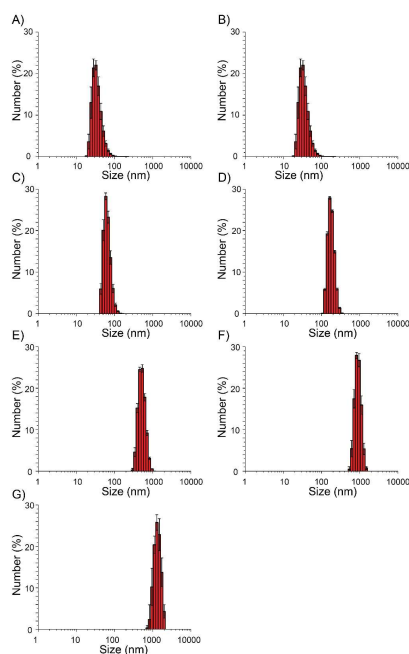


Figure S2.6. DLS number analysis of UiO-66 nanoparticle synthesized with formic acid A = 1.8 mmol/ml, B = 2.4 mmol/ml, C = 2.9 mmol/ml, D = 3.9 mmol/ml, E = 5.3 mmol/ml, F = 6.1 mmol/ml, and G = 6.9 mmol/ml.

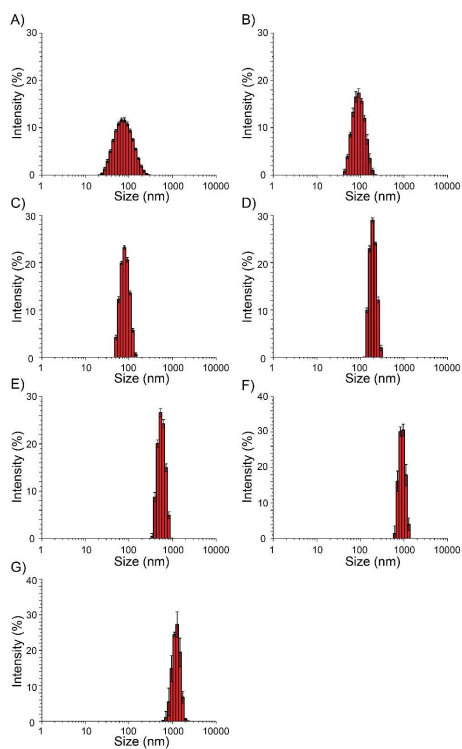


Figure S2.7. DLS intensity analysis of UiO-66 nanoparticle synthesized with formic acid A = 1.8 mmol/ml, B = 2.4 mmol/ml, C = 2.9 mmol/ml, D = 3.9 mmol/ml, E = 5.3 mmol/ml, F =

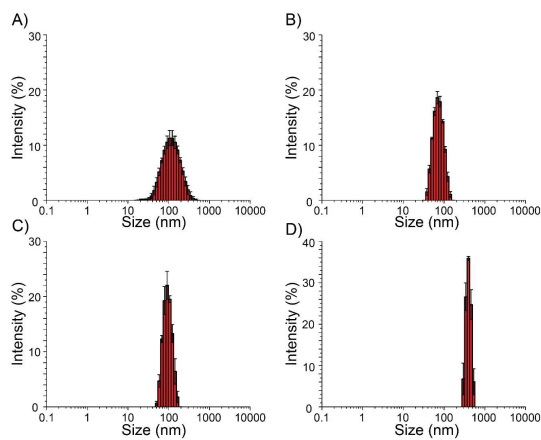


Figure S2.8. DLS intensity analysis of UiO-66 nanoparticle synthesized with dichloroacetic acid. A = 0.3 mmol/ml, B = 0.58 mmol/ml, C = 0.85 mmol/ml, and D = 1.1 mmol/ml.

S2.2 Synthesis of MOF NPs

UiO-66 nanoparticles

A stock solution of zirconyl chloride octahydrate was prepared by dissolving zirconyl chloride octahydrate (210 mg, 0.9 mmol) in 30 mL of *N,N*-Dimethylformamide (DMF). A second stock solution comprised of terephthalic acid (500 mg, 3.01 mmol) in 10 mL of DMF was prepared. Zirconyl chloride octahydrate stock solution (3 mL) was added to terephthalic acid stock solution (1 mL) in a 10 mL scintillation vial. A set concentration of modulating acid was added to each vial. The concentration ranges studied were 1.2 – 6.7 M for acetic acid, 1.8 – 6.4 M for formic acid, 0.3 – 1.1 M for dichloroacetic acid, and 0.62 – 1.18 M for trifluoroacetic acid. The solution was heated at 90 °C for 18 h to yield UiO-66 $Zr_6O_4(OH)_4(C_8H_3O_4)_6$.

Table S1. Summary of data collected for samples of UiO-66 synthesized with different modulators and different concentrations of modulator. STEM, DLS, and measurements of zeta potential. (Agg = Aggregated). The size of crystals by STEM was determined to be the edge length for octahedral particles or the diameter in the case of spherical particles.

Acid	[Conc]	STEM	DLS	DLS	Zeta potential
	(M)	size/ nm	intensity /nm	number /nm	/mV
AA	1.2	17(2)	Agg	Agg	-5(5)
	1.9	34(22)	Agg	Agg	-2(5)
	2.6	72(18)	158(19)	100 (36)	15(5)

	3.5	208(56)	173(40)	146 (38)	34(6)
	4.8	270(48)	319(67)	263 (62)	42(7)
	5.8	514(88)	677(204)	614 (207)	45(9)
	6.7	721(56)	826(135)	818 (159)	41(6)
FA	1.8	17(4)	83(38)	39(12)	20(7)
	2.4	31(5)	89(25)	62(16)	30(7)
	2.9	44(12)	94(19)	68(15)	39(9)
	3.9	147(50)	175(31)	159(33)	39(6)
	5.3	439(83)	559(110)	518(116)	37(11)
	6.1	813(223)	919(144)	910(170)	39(13)
	6.9	1174 (258)	1208 (275)	1128 (251)	42(9)
DCA	0.3	19(5)	132(72)	42(15)	24(5)
	0.58	29(8)	74(18)	55(13)	35(10)
	0.85	88(25)	95(24)	71(17)	37(7)
	1.1	550(51)	784(70)	786(107)	35(4)
TFA	0.62	38(7)	100(29)	69(18)	39(11)
	0.91	53(12)	140(30)	117(27)	36(11)
	1.18	227(46)	277(80)	224(67)	35(5)

Mixed-phase MIL-53 and MIL-101

Mixed-phase MIL-53 and MIL-101 nanoparticles were synthesized using a previously reported sonication-assisted method.¹⁶⁰ In brief, in a 50 mL glass beaker, 1.35 g of $\text{FeCl}_3 \cdot 6\text{H}_2\text{O}$ and 0.830 g of H_2BDC were mixed in 25 mL of DMF. The beaker was placed in a probe sonicator

(500 watt Vibra-Cell™ VC 505, Sonics & Materials, Inc., Newtown, CT, USA) and subjected to ultrasonic irradiation for 10 min at 70% of the maximum power; the temperature was not controlled. The as-synthesized product was isolated by centrifugation, followed by DMF washing, and then overnight drying.

Mixed-phase MIL-53 and MIL-88B

Mixed-phase MIL-53 and MIL-88B nanoparticles were synthesized using a previously reported solvothermal method with minor modification.¹⁶¹ In brief, a solution of 1.62 g FeCl₃ and 1.66 g terephthalic acid in 5 mL DMF was reacted in a 23 mL Teflon lined steel autoclave at a temperature 150°C for 75 min. Large aggregates from the as-synthesized product were first removed by low-speed centrifugation, followed by DMF washing, and then overnight drying.

Mixed-phase MIL-140A and UiO-66

Mixed-phase MIL-140A and UiO-66 nanoparticles were synthesized using a previously reported solvothermal method with minor modification.¹⁵³ In brief, a solution of 58 mg ZrCl₄, 83 mg terephthalic acid and 40 μL acetic acid in 2.5 mL DMF was reacted in a 30 mL glass microwave vial. The solution was heated to 185°C within 2 min and held at this temperature for 6 mins. The reaction was quenched by adding 20 mL ethanol. The as-synthesized product was isolated by centrifugation, followed by DMF washing, and then overnight drying.

Powder X-ray diffraction data

To determine the crystallinity of each MOF nanoparticle, powder X-ray diffraction data (PXRD) were collected at Argonne National Laboratory using the Dow-Northwestern-Dupont Collaborative Access team (DND-CAT) Beamline 5-ID-D at the Advanced Photon Source (APS). A wavelength of 1.239 Å with an exposure time of 1 sec was used for each measurement. Two-dimensional scattering data were converted to one-dimensional spectra by taking a radial average of the two-dimensional data. Prior to data collection, as-synthesized MOF nanoparticles were centrifuged at 15,000 rpm for one hour and washed sequentially with DMF three times and then water three times. Air-dried samples for PXRD were placed in quartz capillaries (Charles Supper Company) (1.5 mm) for measurement. The size and dispersity of UiO-66 were evaluated using a Hitachi HD-2300 scanning transmission electron microscope in SE or TE modes depending on the crystallite size with an accelerating voltage of 200 kV. Samples were dispersed onto TEM grids by drop-casting a dilute solution containing MOF crystals. The average crystal size for each synthesis was determined by measuring at least fifty crystals. Zeta potential and DLS size measurements of hydrodynamic radii were made on a Malvern Zetasizer Nano-ZS (Malvern Instruments). Results were averaged over ten measurements.

Transmission electron microscopy and scanning electron microscopy

MOF nanoparticles were analyzed using a Hitachi HD-2300 scanning transmission electron microscope in SE, ZC and TE modes with an acceleration voltage of 200 kV. Samples were dispersed onto TEM grids by drop-casting a dilute ethanol solution containing MOF NPs.

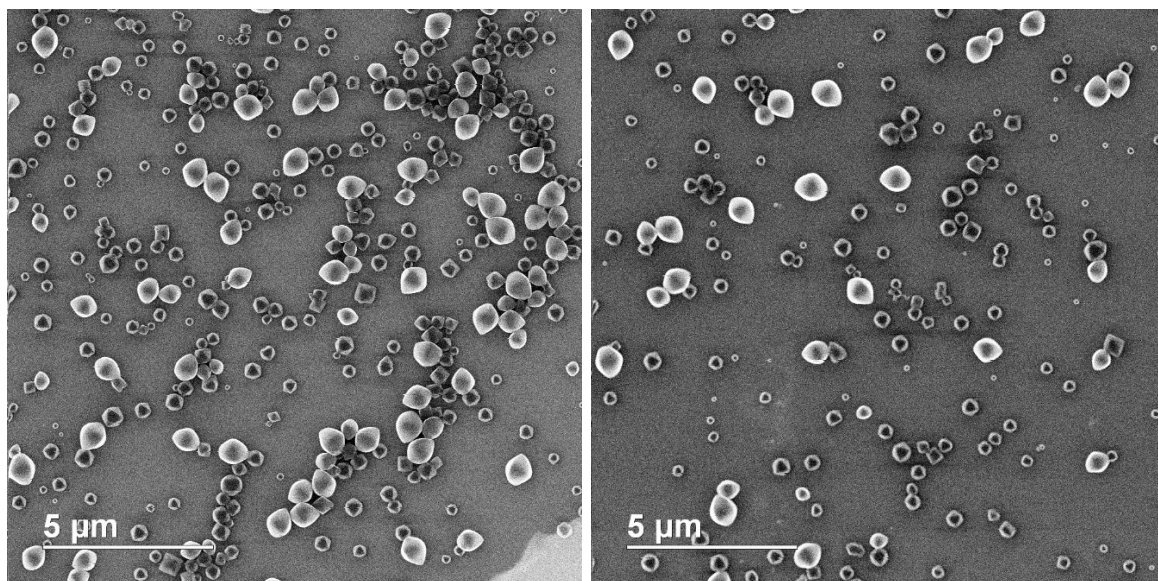


Figure S2.9. SEM images of as-synthesized MIL-53 and MIL-101 mixtures.

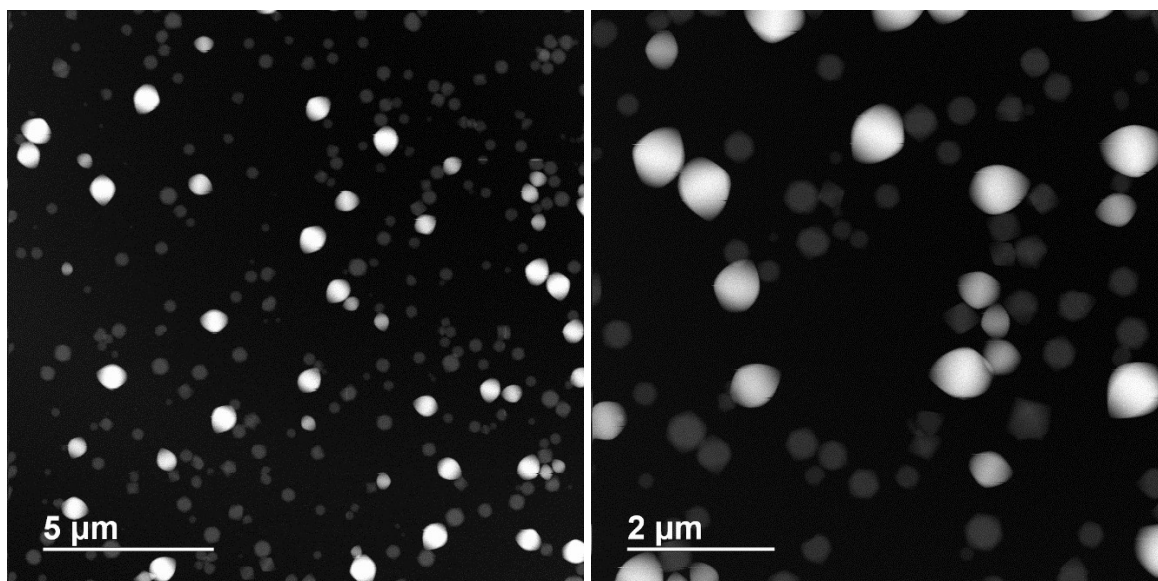


Figure S2.10. High-angle annular dark-field images (HAADF) of as-synthesized MIL-53 and MIL-101 mixtures at different magnification.

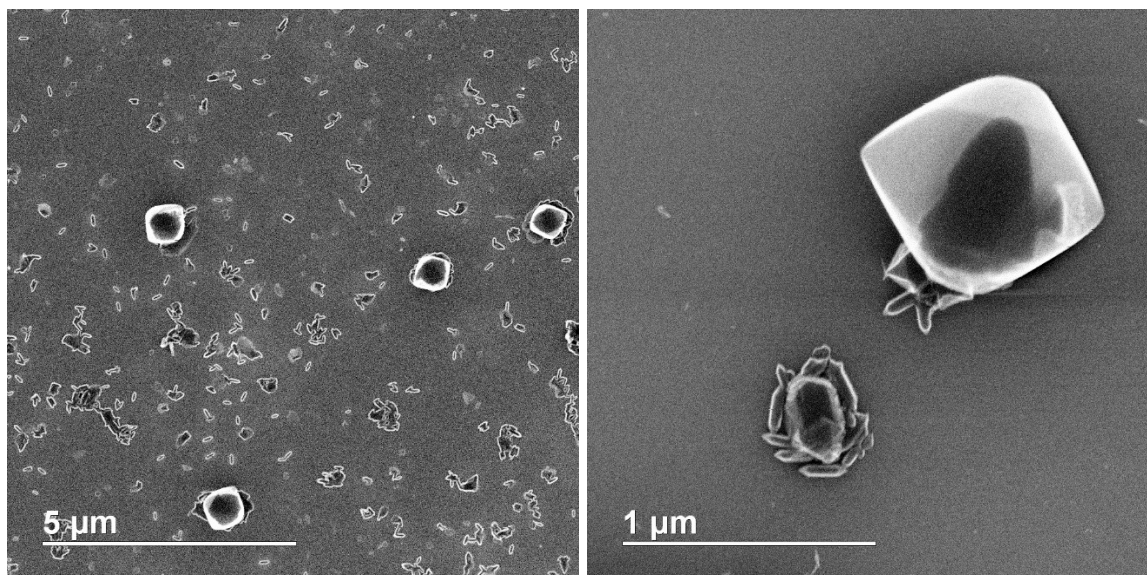


Figure S2.11. SEM images of MIL-53 and MIL-88B mixtures at different magnification.

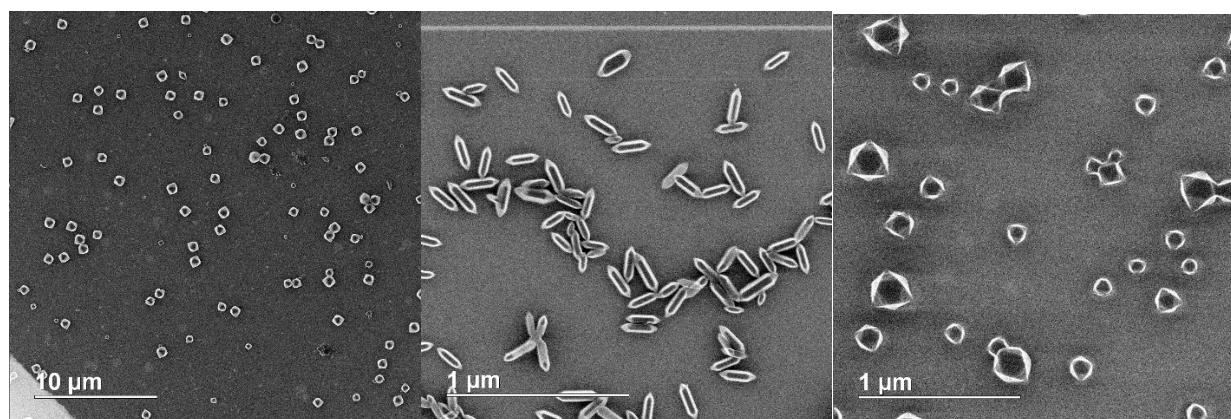


Figure S2.12. SEM images of purified MIL-53, MIL-88B, and MIL-101 nanoparticles.

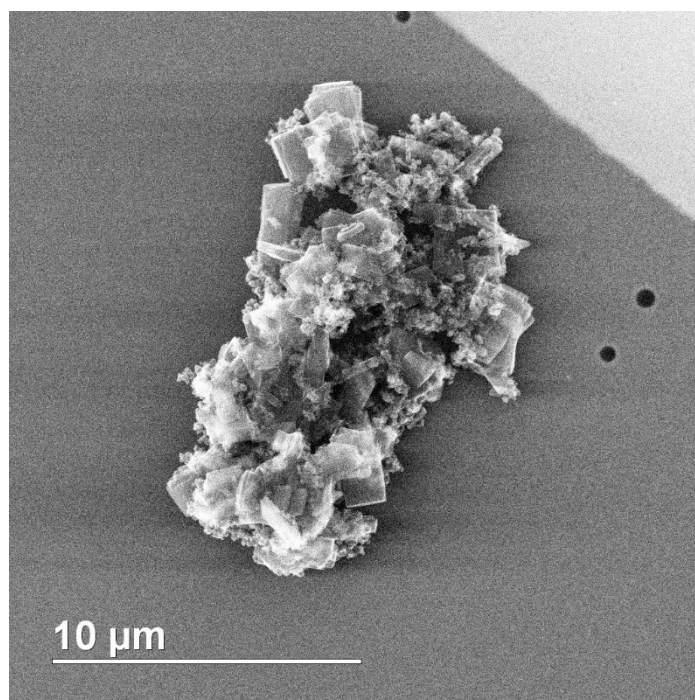


Figure S2.13. SEM images of SEM images of MIL-140A and UiO-66 mixtures.

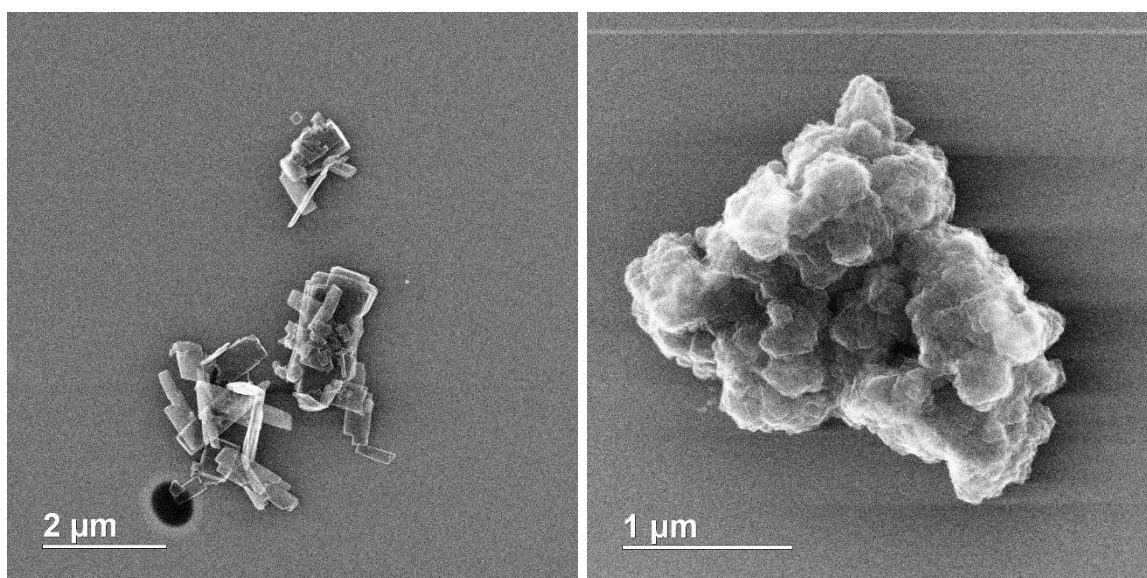


Figure S2.14. SEM images of purified MIL-140A particles.

S2.3 Nitrogen sorption isotherm measurements

N₂ sorption isotherm measurements were performed on a Micromeritics Tristar II 3020 (Micromeritics, Norcross, GA) at 77K. Surface areas were estimated by applying the Brunauer–Emmett–Teller (BET) equation. T-plot internal and external surface area were determined by Harkins and Jura equation in the second linear regions of N₂ isotherms (0.26 P/P_0 to 1.0 P/P_0).

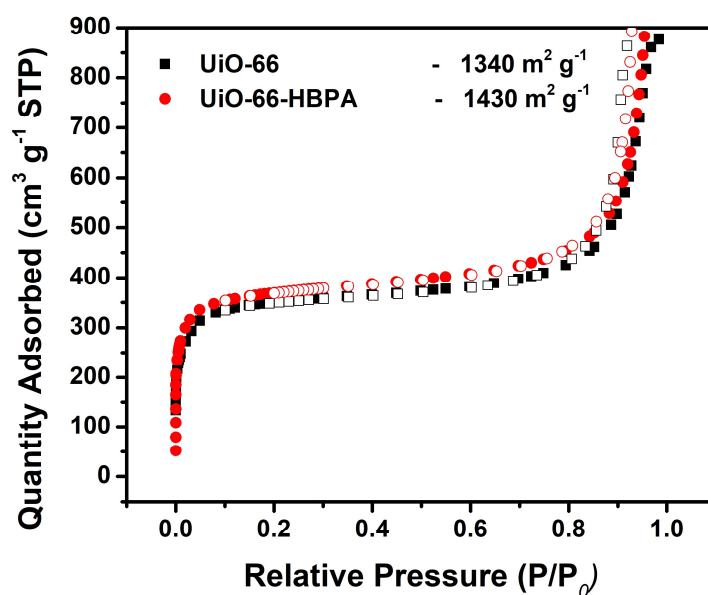


Figure S2.15. N₂ adsorption-desorption isotherms of UiO-66 reveal no significant surface area change post-HBPA functionalization.

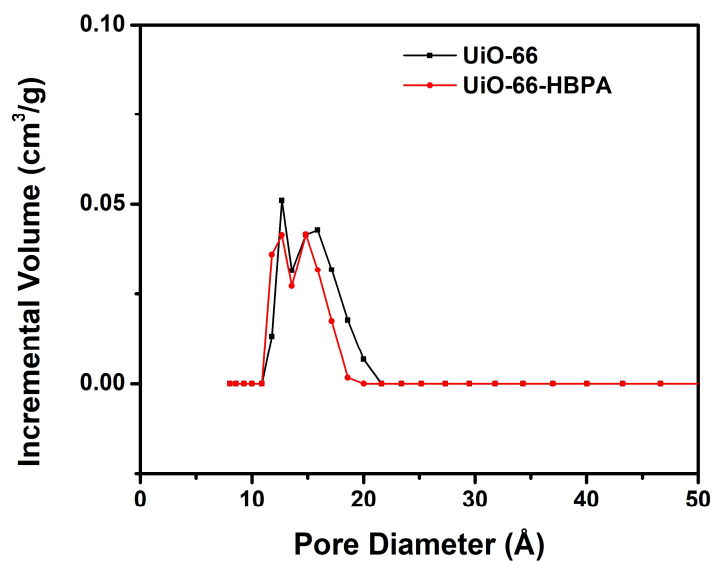


Figure S2.16. DFT pore size distribution analysis of UiO-66 reveal no appreciable change post-HBPA functionalization.

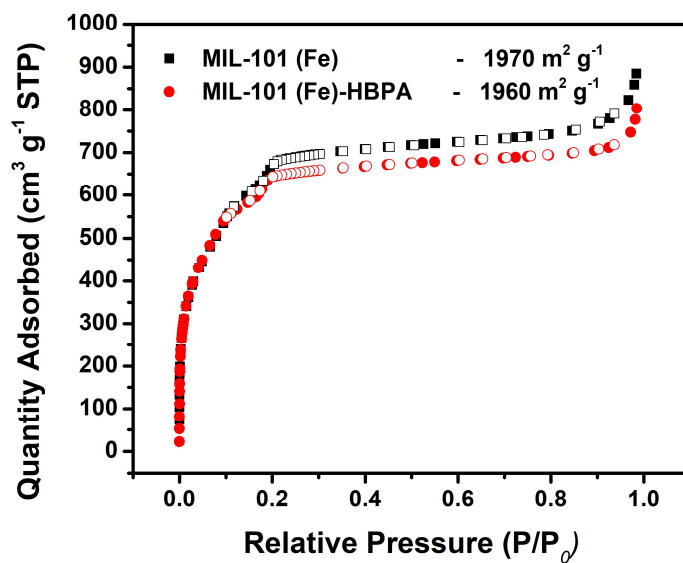


Figure S2.17. N₂ adsorption-desorption isotherms of MIL-101(Fe) reveal no significant surface area change post-HBPA functionalization.

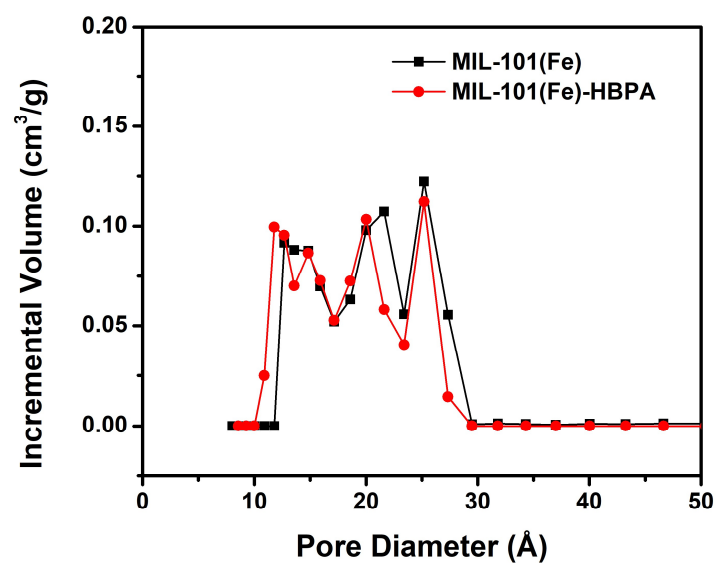


Figure S2.18. DFT pore size distribution analyses of MIL-101(Fe) reveal no appreciable change post-HBPA functionalization.

CHAPTER THREE: Surface Functionalization of Metal-Organic Framework Nanoparticles via Coordination Unsaturated Metal Sites

Materials in this chapter is based upon published work:

Wang, S.; Morris, W.; Liu, Y.; Zhou, Y.; Hupp, J.; Farha, O.; Mirkin, C. A. *Angew. Chem., Int. Ed.* **2015**, *54*, 14378-14742.

3.1 Abstract

In this chapter, we discuss a method for modifying the external surfaces of a series of MOF NPs with 1,2-dioleoyl-sn-glycero-3-phosphate (DOPA). A series of zirconium-based MOF NPs of the same topology, UiO-66, UiO-67, and BUT-30 were synthesized, isolated as aggregates, and then conjugated with DOPA to create stably dispersed colloids. BET surface area analysis revealed that these structures maintain their porosity post surface-functionalization, providing evidence that DOPA functionalization only occurs on the external surface. Additionally, dye-labelled ligand loading studies revealed that the density of DOPA on the surface of the nanoscale MOF correlates to the density of metal nodes on the surface of each MOF. Importantly, the surface modification strategy described herein will allow for the general and divergent synthesis and study of a wide variety of nanoscale MOFs as stable colloidal materials

3.2 Introduction and Background

Metal-organic frameworks (MOFs) and infinite coordination polymers (ICPs) are porous materials composed of organic ligands coordinated to metal containing units.^{4 16, 162} The pore sizes and functionalities of these materials can be deliberately modulated through the choice of organic ligands and metal containing units. This structural tailorability has led to the study of these materials for a variety of applications, including gas storage,¹⁰⁸ chemical sensing,¹⁶³ membrane separations,⁷ catalysis.⁸ A pivotal feature of designing MOFs for such applications, especially on the nanoscale, is a firm understanding of the underlying MOF structure, particularly that of the surface.

MOFs are crystalline structures, and therefore, their bulk structure is well understood as a result of single crystal studies and refinement of Powder X-ray Diffraction (PXRD) data. Recently, there has been significant effort aimed at realizing generalizable methodologies to post-synthetically functionalize the bulk MOF structure, such as coordination at activated metal-binding sites and linker modification.^{61, 164} However, the surface chemistry of MOFs likely deviates from the bulk structure, due to the presence of additional vacant coordination sites, surface defects, and the binding of synthetic modulators.^{11, 126} Despite this expected deviation in structure from bulk to surface, only a few studies have focused on the characterization and modulation of the external surface of MOFs.^{67, 97, 165-166} Importantly, it has been repeatedly shown that for nanoscale materials (e.g., metal nanoparticles) surface chemistry tends to dictate physical properties and chemical function.¹⁶⁷ Therefore, for the advancement and application of MOFs on the nanoscale, the development of general methodologies for surface functionalization must be developed. In this vein, we herein describe a method for the facile surface functionalization of a series of isoreticular, chemically stable MOF NPs with the phosphate-containing amphiphilic ligand DOPA via well-defined coordination chemistry. Additionally, we demonstrate the ability to control the density of surface ligands, as well as solvent compatibility of the MOF, all while preserving the structural integrity and porosity of the MOF architecture.

3.3 Results and Discussion

3.3.1 Surface Functionalization of MOF Nanoparticles with Phospholipid

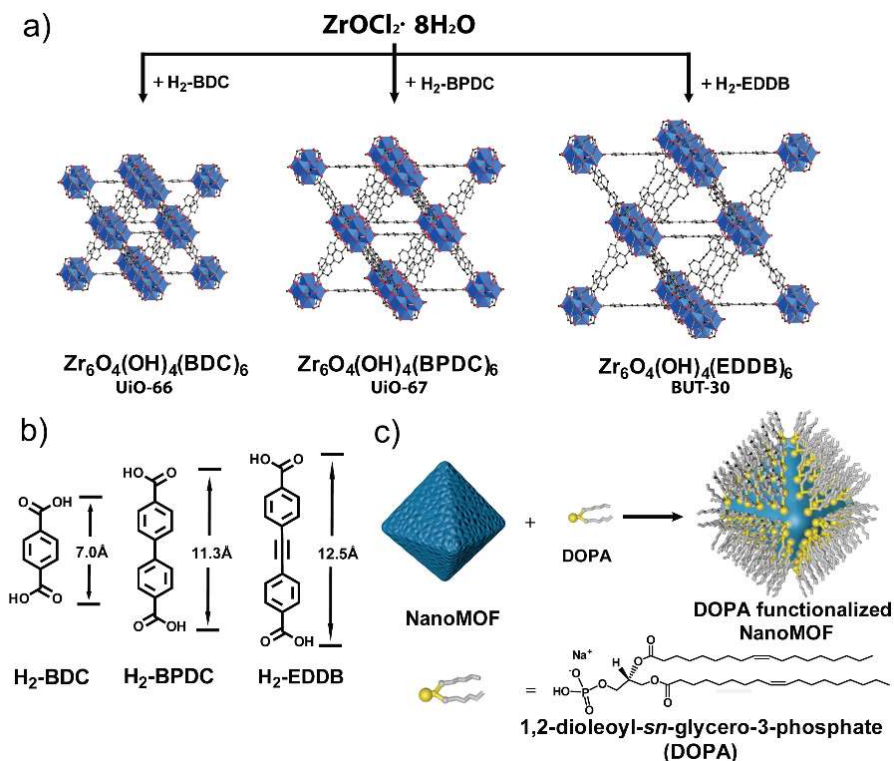


Figure 3.1. Synthesis and DOPA functionalization of a series of zirconium MOF NPs with the same underlying topology. a) Synthetic scheme for the preparation of UiO-66, UiO-67, and BUT-30 b) The series of ligands utilized in the synthesis of nanoscale MOFs and their lengths. $\text{H}_2\text{-bdc}$ = terephthalic acid ($\text{C}_6\text{H}_6\text{O}_4$), $\text{H}_2\text{-bpdc}$ = biphenyldicarboxylic acid ($\text{C}_{14}\text{H}_{10}\text{O}_4$), and $\text{H}_2\text{-eddb}$ = 4,4'-(ethyne-1,2-diyl)dibenzoic acid ($\text{C}_{16}\text{H}_{10}\text{O}_4$). c) Synthetic scheme for functionalization for MOF nanoparticles utilizing DOPA.

In order to carry out this study, we chose a family of isorecticular MOFs with different linker lengths, in which the bulk structure was well characterized, the framework was chemically stable under various conditions, and the modular nanoscale synthesis had been realized.¹⁴⁸ Therefore, we selected three zirconium-based frameworks with the same underlying topology, namely UiO-66 ($\text{Zr}_6\text{O}_4(\text{OH})_4(\text{BDC})_6$),¹¹⁵ UiO-67 ($\text{Zr}_6\text{O}_4(\text{OH})_4(\text{BPDC})_6$),¹¹⁵ and BUT-30

($Zr_6O_4(OH)_4(EDDB)_6$).¹⁶⁸ Importantly, within this family, the density of metal nodes decreases as a function of increasing organic ligand length (**Figure 3.1 a-b**). These three frameworks were functionalized with DOPA to give DOPA-UiO-66, DOPA-UiO-67 and DOPA-BUT-30 (Scheme 1c). DOPA was selected as a ligand because it was expected to coordinate strongly to the Zr(IV) metal containing units, but, importantly, not too strongly as to disturb the underlying coordination framework of the MOF.¹⁵⁴⁻¹⁵⁵ Upon functionalization with DOPA, the surface ligand density, as well as the bulk MOF porosity and structure, were evaluated. Additionally, the colloidal stability of the MOF NPs was determined to be dramatically altered upon DOPA surface functionalization. Namely, it was found that unfunctionalized UiO-66, UiO-67, and BUT-30 aggregate extensively in nonpolar solvents; however, after surface modification with DOPA, MOF NPs can easily be dispersed and suspended in solvents with low polarity. Via BET surface area measurements, we show that the porosity of the MOFs is maintained post-functionalization. Importantly, for the application of MOFs on the nanoscale, this general methodology for surface modification based on straightforward coordination chemistry allows for the modulation of the density of surface ligands. Thus, allowing one to finely tune the colloidal properties of these constructs as highlighted within.

The isorecticular zirconium MOF NPs were synthesized under solvothermal conditions utilizing acetic acid to modulate crystallite size. For example, 22 ± 8 nm UiO-66 particles were synthesized from the reaction of $ZrOC12 \cdot 8H_2O$ (21 mg, 65.1 μ mol) with terephthalic acid (50 mg, 0.3 mmol) modulated by 0.3 mL acetic acid in 4 mL DMF at 90 °C for 18 hours. For each structure, acetic acid concentration was modulated to access the desired nanoscale crystallite parameters. PXRD analysis was utilized to confirm the bulk structure of each synthesized MOF (**Figure 3.2a**). All three MOFs possess the expected fcu topology, with pore size and the density of zirconium

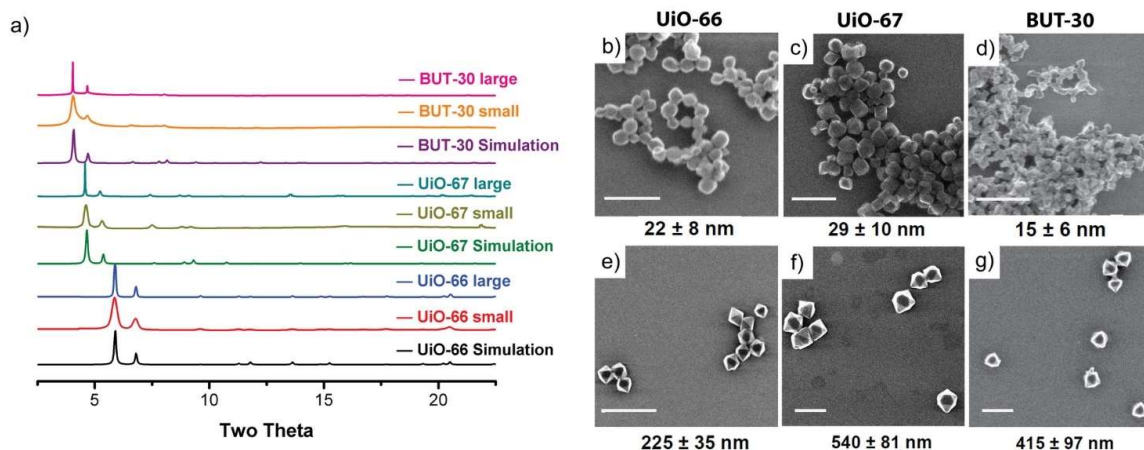


Figure 3.2. Powder X-ray diffraction (PXRD) patterns and scanning electron microscopy (SEM) images of the as-synthesized MOF NPs. (a) Simulated and experimental PXRD patterns of UiO-66, UiO-67, and BUT-30. SEM images of (b,e) UiO-66, (c,f) UiO-67, and (d,g) BUT-30. Scale bar: 100 nm for (b-d) and 1 μ m for (e-g).

units being determined by linker length (**Figure 3.1b**). For each MOF, small nanoparticles (<30 nm) and large nanoparticles (>200 nm) were synthesized, with the size being confirmed by scanning transmission electron microscopy (STEM) (**Figure 3.2b**). After the synthesis and characterization of the nanoscale zirconium-based MOF family, the particles were functionalized with DOPA. First, to remove the excess and encapsulated DMF remaining from the solvothermal synthesis, UiO-66, UiO-67, and BUT-30 MOF nanoparticles were solvent exchanged by several rounds of centrifugation and subsequently redispersed in chloroform. Due to their hydrophilicity, the MOF NPs were observed to aggregate extensively in the chloroform suspension. To disperse the nanoparticles, excess DOPA (sodium salt) was added to the MOF aggregates, which were subsequently sonicated for one hour at room temperature, then left on a shaker overnight. The resulting DOPA-MOF NP conjugate was then washed with chloroform three times until no excess DOPA could be detected in the resulting supernatant via ICP-AES (**Figure S3.9**). Additionally, by using a large excess of DOPA, we assume that the surface is coordinatively saturated by the ligand

(vide infra). Importantly, through PXRD studies and STEM, we were able to confirm that the framework crystallinity and crystallite size were maintained after functionalization.

To confirm the presence of DOPA on the MOFs, multiple spectroscopy techniques were used. First, infrared spectroscopy (IR) was carried out for each sample. IR spectroscopy of the DOPA- MOF NP conjugates revealed alkane (C-H) and carbonyl (C=O) vibrations at 2950 cm^{-1}

and 1597 cm^{-1} , respectively, which correlate well with the spectra of free DOPA, and are not present in the IR spectra of the unmodified MOFs (**Figure 3.3a**).

Additionally, X-Ray Photoelectron Spectroscopy (XPS) shows a peak at 134 eV confirming the presence of phosphate in the DOPA functionalized samples (**Figure 3.3 b-c**). Finally, $^{31}\text{P}\{^1\text{H}\}$ Magic Angle Spinning (MAS) NMR spectroscopy was performed to directly

examine coordination of the phosphate group of DOPA to the zirconium cluster.

For the DOPA-functionalized MOF NPs, a broad resonance at -3.2 ppm, along with

two symmetric satellite resonances (58.1 ppm and -65.3 ppm) was observed. In contrast, the free DOPA molecule exhibits a single sharp resonance at 2.1 ppm (**Figure S3.7**). Taken together, these

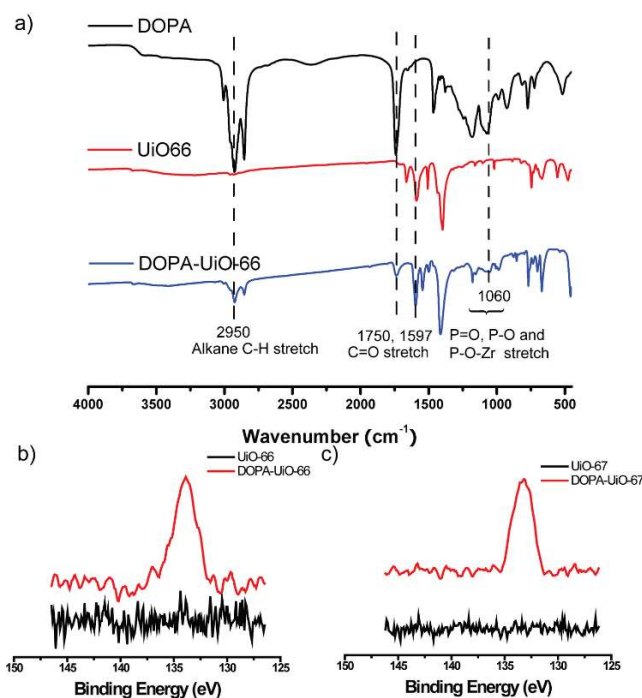


Figure 3.3. IR and XPS analysis of DOPA-MOF NPs. a) Comparison of unfunctionalized DOPA molecule (top, black), UiO-66 particles (middle, red), and DOPA-UiO-66 (bottom, blue). b) XPS spectra of UiO-66 and UiO-67 before (black) and after (red) DOPA functionalization.

results strongly suggest that the phosphate ligands coordinate to the zirconium-oxide nodes on the external surface of the MOF nanoparticle.

To characterize the porosity of the DOPA-functionalized MOF nanoparticles, we performed N₂ isotherms and evaluated their surface area via BET analysis (**Figure 3.4**). Prior to the surface area measurements, the samples were activated to remove solvent from the pores of the MOF (See Supporting Information). The N₂ adsorption isotherm for each MOF at 77 K exhibits type-I behavior. In each case, the larger MOF crystallites (>200 nm), which were realized by using higher modulator concentrations, exhibit higher surface area when compared to the smaller MOF nanocrystals of the same underlying structure. This finding correlates well with previous studies, which show that the surface area of UiO-66 is dependent on the defects induced by modulator used in the synthesis.¹⁶⁹ The gradual increase in N₂ uptake at high P/P₀ values (**Figure 3.4a**) is most likely due to N₂ condensation in interparticulate voids generated by nano-crystallite packing. After DOPA functionalization, the N₂ isotherms show that each MOF maintained its porosity, suggesting

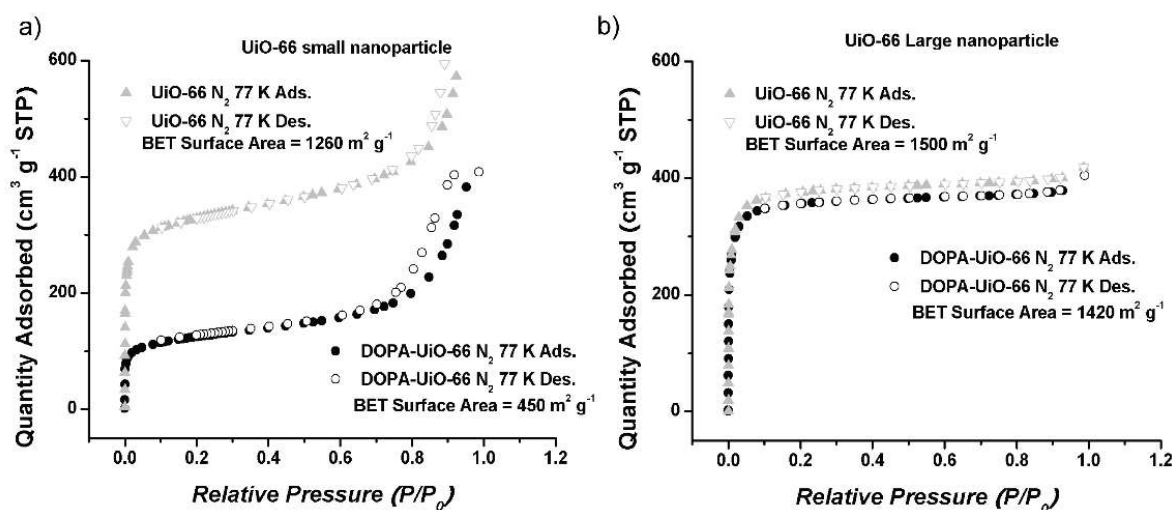


Figure 3.4. The impact of DOPA functionalization on porosity and colloidal stability. BET adsorption isotherm before and after DOPA functionalization for a) 25 nm UiO-66, b) 225 nm UiO-66.

that the pores of each MOF are still accessible. Interestingly, in the case of small nanocrystallites, a significant decrease in porosity was observed, whereas the larger nanocrystallites demonstrated porosities much closer to the unfunctionalized structures (**Figure 3.4**). For example, in UiO-66 a 64 % and 5 % drop in surface area was seen for the small (<30 nm) and large (>200 nm) nanocrystals, respectively. The apparent difference in porosity change between small and large MOF NP samples upon DOPA surface functionalization can be attributed to the disparity in external surface-to-volume ratio between the two particle sizes. In the case of small nanoparticles, approximately 50 % of the zirconium secondary building units are found within one unit cell of the external surface, which is in stark contrast to the large nanoparticles, in which less than 5 % of the zirconium units are this close to the surface. This significant difference leads to a higher weight percentage of DOPA in samples of small crystallites, thus reducing their gravimetric surface area. This trend is observed for all three MOF architectures. Additionally, these results support the hypothesis that DOPA functionalization is limited to the external surface of each MOF, as no surface area would be expected if the crystal was completely modified.

3.32 Quantification of Surface Ligand Coverage

Quantitative analysis of DOPA coverage for each MOF architecture was conducted via ICP-AES. By measuring the phosphorous and zirconium amount, we determined the DOPA loading of each MOF NP sample from the ratio of Zr and P (**Figure 3.5a**). These results showed that UiO-66 had the highest DOPA loading (212 (57) pmol/cm²), and BUT-30 had the lowest (83 (20) pmol/cm²). This significant difference in loading between UiO-66 and BUT-30 supports the hypothesis that DOPA binds to the Zr surface units, as decreasing the density of these Zr surface sites results in lower surface coverage of DOPA ligands (**Figure 3.5a**). In order to verify the results

of the above ICP-AES study, the MOF NPs were surface functionalized with a dye-labelled analogue of DOPA, 1-oleoyl-2-{12-[(7-nitro-2-1,3-benzoxadiazol-4-yl)amino]dodecanoyl}-*sn*-glycero-3-phosphate (NBD-DOPA), and their surface coverage was measured via UV-vis absorption studies at 460 nm (See Supporting Information for details). Importantly, this absorbance study strongly agrees with the loading densities determined by ICP-AES (**Figure 3.5a**). The synchronous results of the ICP-AES and absorption studies support the hypothesis that DOPA binding is limited to the surface, as the observed loading densities are in close alignment with an average of two DOPA molecules coordinated to each of the surface metal-containing units. Additionally, confocal fluorescence microscopy was performed which verified that the dye is primarily localized on the periphery of the MOF nanoparticles (**Figure S3.12**).

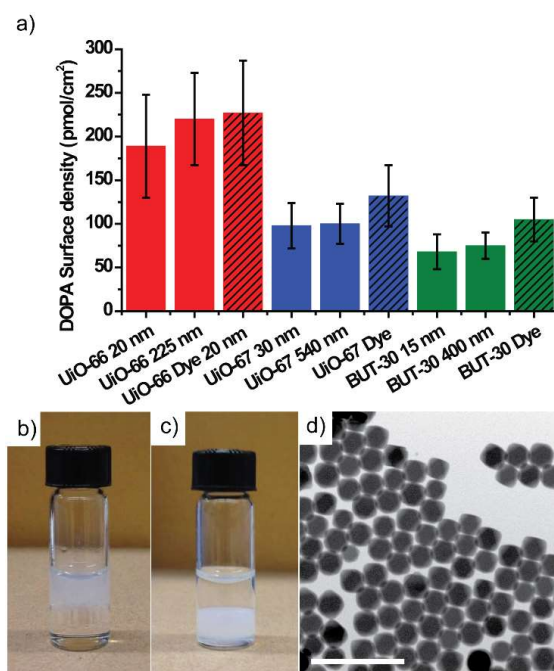


Figure 3.5. a) DOPA surface density for different size UiO-66, UiO-67 and BUT-30 MOF nanoparticles, b) digital photograph showing MOF NPs suspended in an aqueous phase after being transferred to c) a chloroform phase after DOPA functionalization, d) SEM image of drop-casted colloiddally stable DOPA-UiO-66 in CHCl₃. Scale bar: 1 μm.

3.33 Controlling Surface Properties via Ligand Functionalization

The main goal of this study was to evaluate a synthetic method for promoting the colloidal stability of a series of hydrophilic MOF nanoparticles in low polarity media via surface functionalization. Therefore, the colloidal stability of these nanoscale MOFs was evaluated before and after surface modification (**Figure 3.5b-d**). First, unfunctionalized MOF NPs were suspended in CHCl₃/water mixtures. From simple visualization, the MOF nanoparticles were clearly selectively suspended in the aqueous layer (**Figure 3.5b**). In contrast, upon DOPA functionalization, the MOF nanoparticles became preferentially suspended in the CHCl₃ layer (**Figure 3.5c**). This binary contrast in solvent selectivity directly demonstrates that nanoparticle properties can be deliberately tailored via surface functionalization with organic ligands. Additionally, this modulation of the colloidal stability of the MOF nanoparticles was supported by SEM imaging and Dynamic Light Scattering (DLS). SEM images of non-functionalized MOF nanoparticles that have been drop-cast from CHCl₃ show significant aggregation (See Supporting Information), whereas the DOPA-functionalized MOFs exist as discrete nanoparticles when similarly drop-cast from CHCl₃ (**Figure 3.5d**), thus, again demonstrating the colloidal stability of the surface-modified particles in solvents with low polarity.

3.4 Conclusions

In summary, we have developed a general methodology for the selective surface functionalization of MOF NPs, which yields the ability to disperse crystalline MOF NPs as colloids into a variety of solvents and chemical environments. The selective coordination of

organophosphates to metal binding sites on MOF nanoparticle surfaces allows control of ligand density and type, while retaining crystallinity and permanent porosity. This strategy is general and, in principle, can be used to generate a large pool of multi-functional porous materials with surface chemistries that can be deliberately and finely tuned through choice of coordination ligands. Looking forward, this work should also facilitate the integration of nanoscale MOFs into structurally tailorable particle assemblies,¹⁷⁰ opening the door for realizing functional materials with applications spanning optically responsive devices,¹⁷¹⁻¹⁷² adsorption-based chemical sensors,¹⁷³ and plasmonic-enhanced catalysis.¹⁷⁴

3.5 Experimental Methods and Supplementary Materials

S3.1 Synthesis and purification of MOF nanoparticles

UiO-66 ($\text{Zr}_6\text{O}_4(\text{OH})_4(\text{C}_8\text{H}_4\text{O}_4)_6$)

UiO-66 was synthesized via solvothermal reaction conditions similar to a previously published protocol.^[1] 1,4-benzenedicarboxylic acid (50 mg, 0.30 mmol) was dissolved in 1 mL of *N,N*-dimethylformamide (DMF). In a separate vial, zirconyl chloride octahydrate (21 mg, 0.066 mmol) was dissolved in 3 mL of DMF. The two solutions were mixed together in a 10 mL scintillation vial, and acetic acid was added to the reaction mixture. Two different concentrations were used to achieve two different particle sizes (1.54 M for 22 ± 8 nm UiO-66 nanoparticles and 3.43 M for 225 ± 35 nm UiO-66 nanoparticles). After brief sonication, the solution was heated at 90 °C for 18 h to yield UiO-66 ($\text{Zr}_6\text{O}_4(\text{OH})_4(\text{C}_8\text{H}_4\text{O}_4)_6$).

UiO-67 ($\text{Zr}_6\text{O}_4(\text{OH})_4(\text{C}_{14}\text{H}_8\text{O}_4)_6$)

UiO-67 was synthesized with a similar method. Biphenyl- 4,4'-dicarboxylic acid (20 mg, 0.08 mmol) was added to 1 mL of DMF, resulting a white suspension. In a separate vial, zirconyl chloride octahydrate (9 mg, 0.028 mmol) was dissolved in 3 mL of DMF. The two fractions were mixed together in a 10 mL scintillation vial, and acetic acid was added to the reaction mixture (0.42 M for 29 ± 10 nm UiO-67 nanoparticle and 1.90 M for 540 ± 81 UiO-67 nanoparticle). After brief sonication, the suspension was heated at 90°C for 18 h to yield UiO-67 ($\text{Zr}_6\text{O}_4(\text{OH})_4(\text{C}_{14}\text{H}_8\text{O}_4)_6$).

BUT-30 ($\text{Zr}_6\text{O}_4(\text{OH})_4(\text{C}_{16}\text{H}_8\text{O}_4)_6$)

BUT-30 was synthesized with a similar method. 4,4'-(ethyne-1,2-diyl)dibenzoic acid (20 mg, 0.075 mmol) was added to 1 mL of DMF, resulting a light yellow suspension. In a separate vial, zirconyl chloride octahydrate (5 mg, 0.016 mmol) was dissolved in 3 mL of DMF. The two fractions were mixed together in a 10 mL scintillation vial, and acetic acid was added to the reaction mixture (0.42 M for 15 ± 6 nm BUT-30 nanoparticle and 1.05 M for 415 ± 97 nm BUT-30 nanoparticle). The suspension was heated at 90°C for 18 h to yield BUT-30 ($\text{Zr}_6\text{O}_4(\text{OH})_4(\text{C}_{16}\text{H}_8\text{O}_4)_6$).

MOF nanoparticle purification

As-synthesized MOF nanoparticles were purified by centrifugation (15000 rpm, 60 min for small nanoparticles; 4000 rpm, 10 min for large nanoparticles) followed by solvent exchange ($3 \times$ DMF) over a 24 h period. MOF nanoparticles were suspended in DMF for characterization.

S3.2 Synthesis and purification of DOPA-MOF NP conjugates

DOPA functionalization

Purified UiO-66, UiO-67, and BUT-30 MOF nanoparticles suspended in DMF were solvent exchanged with chloroform by three rounds of centrifugation to remove remaining DMF. DOPA (0.2 g/mL, 0.28 M in chloroform) was added to the MOF nanoparticle suspension. For example, to 1 mL of small UiO-66 nanoparticles suspended in chloroform (22 nm, 2.3 μ M) 100 μ L of the DOPA solution (28 μ mol) was added; to 1 mL of large UiO-66 nanoparticles (225 nm, 1.3 nM) 50 μ L of the DOPA solution (14 μ mol) was added. The mixture was sonicated until no insoluble aggregates could be visually observed.

DOPA- MOF NP conjugate purification

Excess DOPA was removed by four rounds of centrifugation (15000 rpm, 60 min for small nanoparticles; 4000 rpm, 10 min for large nanoparticles) followed by redispersion in chloroform over a 24 h period. The DOPA-MOF NP conjugates were suspended in chloroform for future characterization. The average functionalized nanoparticle size was determined by measuring the edge length of greater than fifty crystals from multiple functionalizations.

Powder X-ray diffraction data (PXRD)

The crystallinity of the synthesized MOF NPs and DOPA-MOF NP conjugates was confirmed by powder X-ray Diffraction (PXRD). Powder X-ray diffraction data (PXRD) were collected at Argonne National Laboratory using the DOW-Northwestern-Dupont Collaborative Access team (DNDCAT) Beamline 5-ID-D at the Advanced Photon Light Source (APS). A wavelength of 1.239 Å was used for the data collection with an exposure time of 1 second. Two-dimensional scattering data were converted to 1D data by taking a radial average of the 2D data. Prior to data collection, as-synthesized MOF nanoparticles were dried by filtration and washed

with acetone. Samples for PXRD were placed in quartz capillaries (Charles Supper Company) (1.5 mm) for data collection.

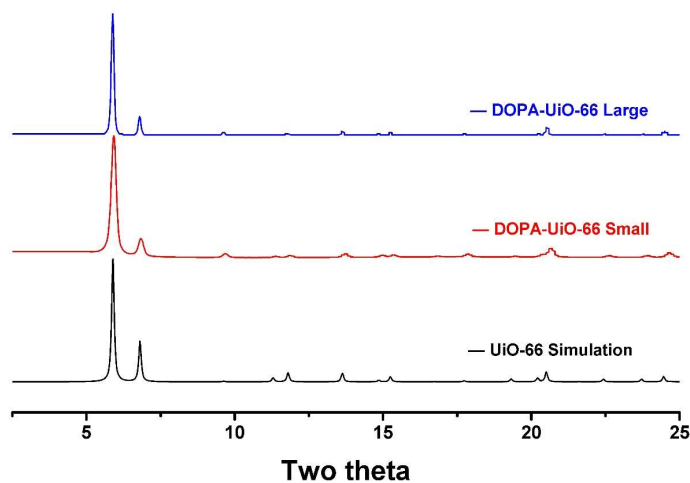


Figure S3.1. PXRD spectra verify that both small and large DOPA-UiO-66 nanoparticles maintain their crystallinity after DOPA functionalization.

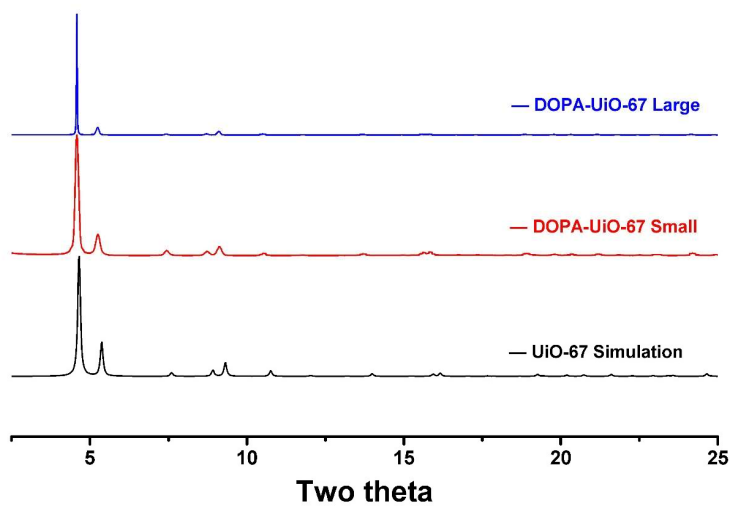


Figure S3.2. PXRD spectra verify that both small and large DOPA-UiO-67 nanoparticles maintain their crystallinity after DOPA functionalization.

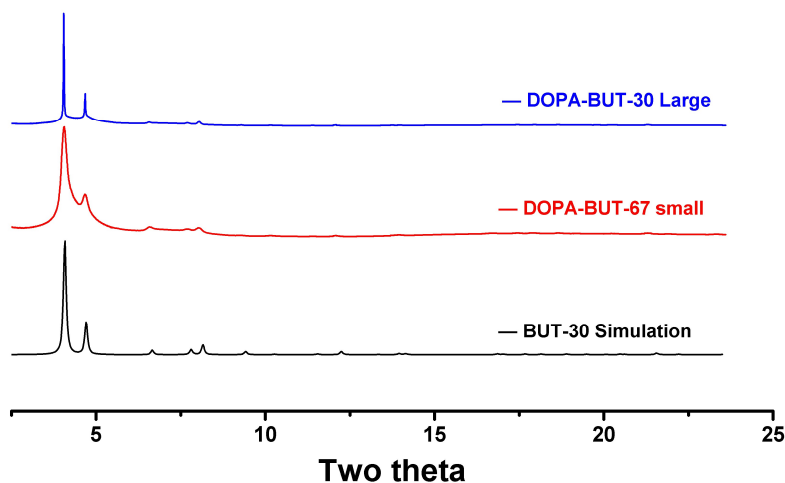


Figure S3.3. PXRD spectra verify that both small and large DOPA-BUT-30 nanoparticles maintain their crystallinity after DOPA functionalization.

Scanning Transmission Electron Microscopy (STEM)

MOF nanoparticles were analyzed using a Hitachi HD-2300 scanning transmission electron microscope in either SE or TE modes with an accelerating voltage of 200 kV. Samples were dispersed onto TEM grids by drop-casting a dilute ethanol solution containing MOF crystals or MOF conjugates directly onto TEM grids. The average crystal size for each synthesis was determined by measuring the edge length of greater than fifty crystals from multiple syntheses under analogous synthetic conditions.

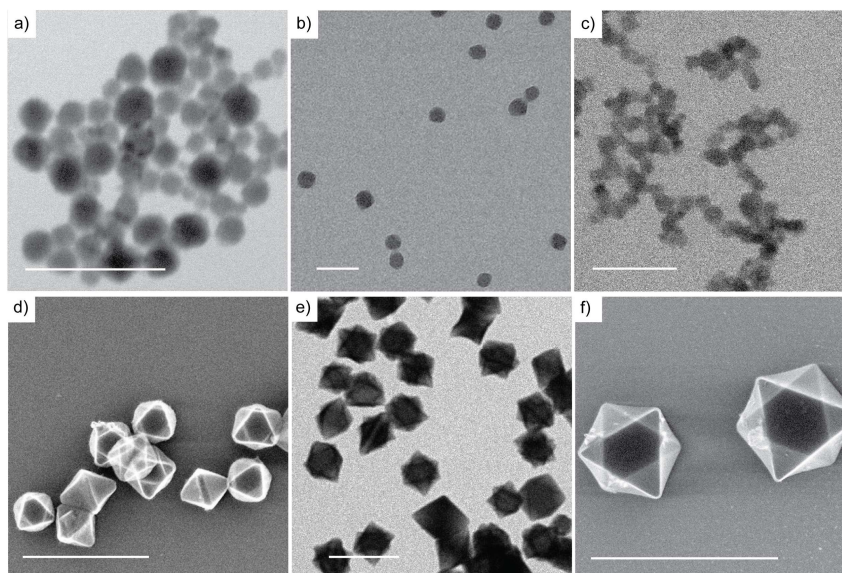


Figure S3.4. DOPA-functionalized MOF nanoparticles of different sizes and topologies. DOPA-UiO-66: a) 25 ± 7 nm, d) 220 ± 31 nm; DOPA-UiO-67: b) 30 ± 8 nm, e) 515 ± 78 nm; DOPA-BUT-30: c) 15 ± 4 nm, f) 430 ± 75 nm. Scale bar: 100 nm for a), b), and c); $1 \mu\text{m}$ for d), e) and f).

S3.3 Nitrogen adsorption measurement

N_2 adsorption and desorption isotherm measurements were performed on a Micromeritics Tristar II 3020 (Micromeritics, Norcross, GA) at 77 K. Before each isotherm, samples were activated either via supercritical CO_2 drying or by heating for 3 hours under high vacuum on an ASAP- 2020 (Micromeritics, Norcross, GA). Between 30 and 100 mg of material was used for each measurement. Data was analyzed using the ASAP 2020 software (Micromeritics, Norcross, GA). All gases used were Ultra High Purity Grade 5 as obtained from Airgas Specialty Gases (Chicago, IL).

Supercritical CO_2 drying was performed using a TousimisTM Samdri[®] PVT-30 critical point dryer (Tousimis, Rockville, MD, USA). Supercritically dried samples were prepared in the following manner. The solvent from freshly prepared samples was decanted and replaced with fresh DMF. The product was allowed to settle over the course of 2 hours. This process was repeated

2 x with DMF, followed by 3 x with ethanol. The ethanol-dispersed sample was transferred into a Tousimis Samdri-PVT-3D supercritical CO₂ dryer. The temperature was lowered to 0 °C-10°C, and the chamber was filled with liquid CO₂ (ultrahigh grade CO₂ with a siphon from Air-Gas Inc was used). The sample was soaked for 8 hours total, venting for five minutes every two hours. The chamber was then heated to 40 °C, and the supercritical CO₂ was bled off at a rate of 1 mL/min until the chamber reached ambient pressure (approximately 12 hours). The chamber was opened and the dried sample was transferred into a pre-weighed glass sample tube, which was sealed and quickly transferred to a system providing 10⁻⁴ torr dynamic vacuum. The sample was kept under vacuum at room temperature for 6 hours and was then used for N₂ adsorption measurements.

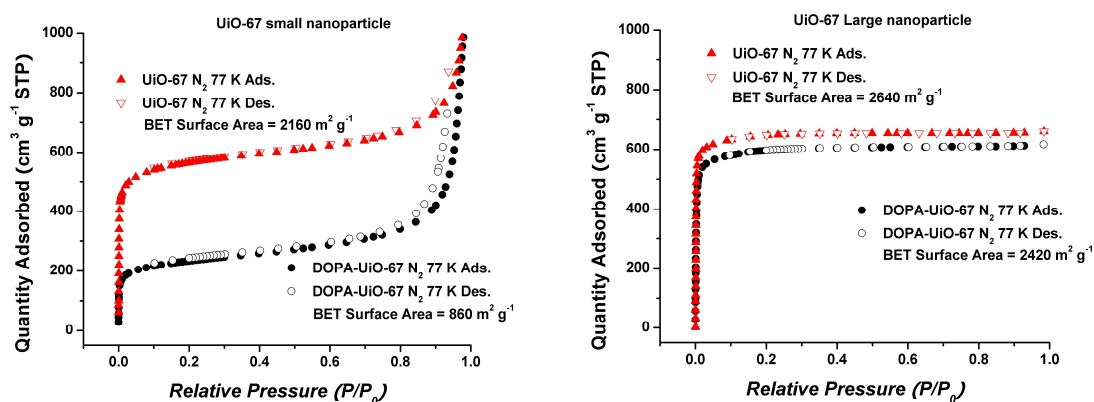


Figure S3.5. BET adsorption isotherm before and after DOPA functionalization for 30 nm (left) and 500 nm (right) UiO-67 nanoparticles.

S3.4 X-ray photoelectron spectroscopy (XPS)

XPS measurements were made using Thermo ESCA Lab 250Xi scanning XPS spectrometer, Al K α radiation and a pass energy of 150 eV (spot size 500 μ m). The XPS system analysis pressure was kept at 5×10^{-10} mbar. The binding energy (BE) and the kinetic energy (KE)

scales were adjusted by setting the C1s transition to 284.6 eV. BE and KE values were determined with the peak-fit software of the spectrometer.

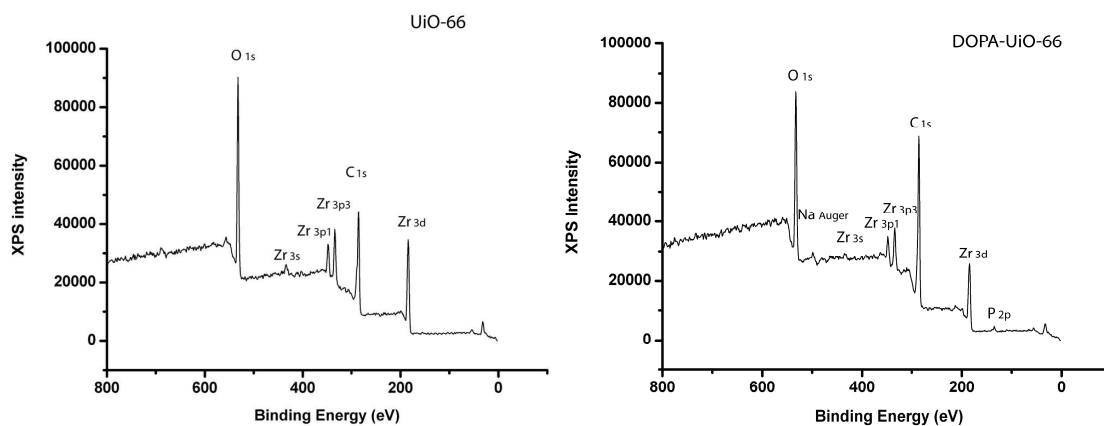


Figure S3.6. XPS survey spectra of UiO-66 and DOPA functionalized UiO-66 MOF NPs. (Similar spectra were observed for DOPA functionalized UiO-67 and BUT-30 MOF nanoparticle)

S3.5 $^{31}\text{P}\{^1\text{H}\}$ Magic Angle Spinning (MAS) Nuclear Magnetic Resonance Spectroscopy (MAS NMR)

$^{31}\text{P}\{^1\text{H}\}$ Magic Angle Spinning (MAS) NMR spectroscopy was performed on a Varian 400 MHz VNMRS system to investigate the direct bonding between the phosphate moiety of DOPA and the zirconium-oxo cluster. Free DOPA was first measured (**Figure S3.7**, bottom spectrum). On the basis of enhanced molecular mobility, the sharp peak at 2.06 ppm is attributed to the free organic phosphate ligand. We then measured the 50 nm DOPA-functionalized UiO-66 MOF nanoparticles (purified and isolated as a white powder) with identical conditions. A broad peak is observed at -3.24 ppm (**Figure S3.7**, top spectrum). The broad signal, as well as two symmetric spinning side bands (58.09 ppm and -65.31 ppm), was attributed to the phosphate phosphorus

bound to Zr. Additionally, a small shoulder peak appearing in the top spectrum is attributed to a trace amount of free DOPA molecule remaining in the sample.

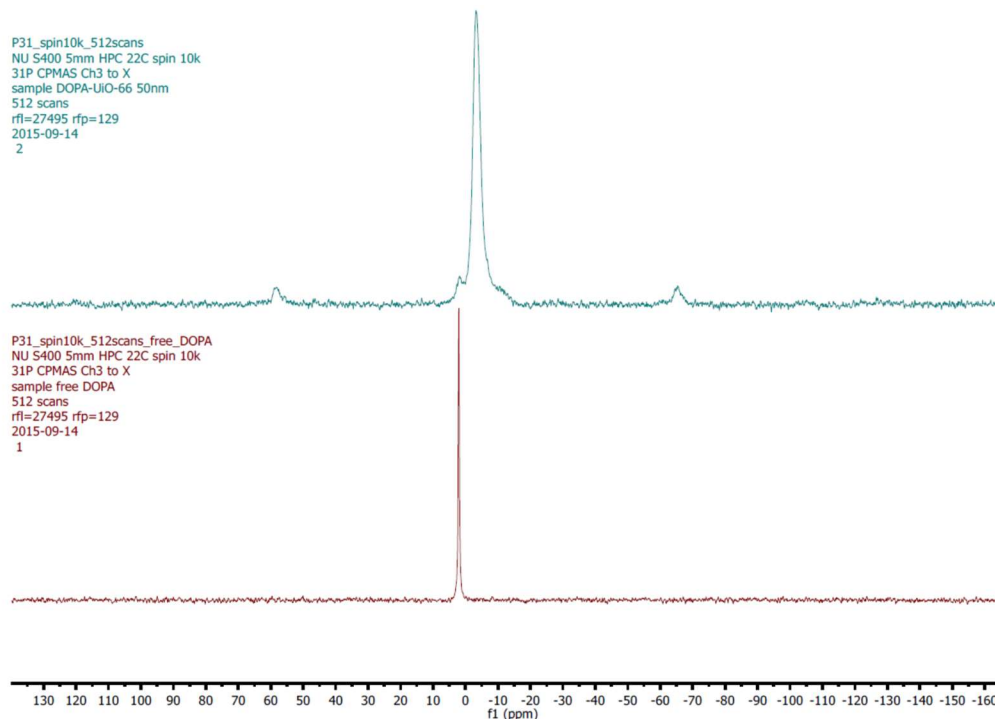


Figure S3.7. $^{31}\text{P}\{^1\text{H}\}$ NMR spectra (400 MHz, MAS) of free DOPA (bottom trace, red) and 50 nm DOPA-UiO-66 nanoparticles (top, blue). 512 scans were accumulated with a 5 s recycle time and a 10,000 Hz spin rate.

S3.6 Inductively Coupled Plasma-Atomic Emission Spectroscopy (ICP-AES)

The zirconium contents of the as-synthesized MOF samples after solvent exchange ($3 \times$ DMF) and MOF-DOPA constructs after solvent exchange ($3 \times \text{CHCl}_3$) were determined by ICP-AES. ICP-AES analysis was carried out on a Thermo iCap 7600 ICP-OES instrument with an automated sample changer. MOF samples were dispersed in DMF (1 mL), and 10 μl of the MOF sample was added to HNO_3 (990 μl). The samples were heated at 60 $^\circ\text{C}$ for 15 h to fully digest the MOF. Unknown samples were prepared with an internal multi-element standard and compared to a standard curve generated using a zirconium standard. In determining particle concentration, a

unit cell size of 20.84 Å and a unit cell composition of $C_{192}H_{96}Zr_{24}O_{128}$ were used for UiO-66; a unit cell size of 27.13 Å and a unit cell composition of $C_{216}H_{112}Zr_{24}O_{128}$ were used for UiO-67; and unit cell size of 30.20 Å and a unit cell composition of $C_{224}H_{112}Zr_{24}O_{128}$ were used for BUT-30.

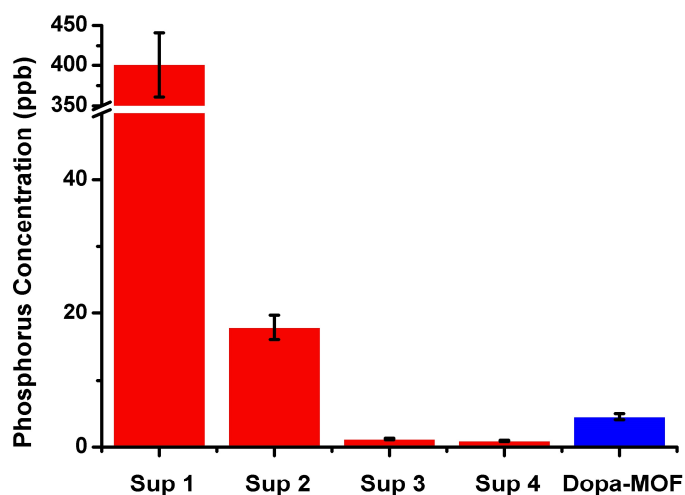


Figure S3.8. ICP-AES measurement of phosphorus concentration for chloroform supernatant collected after each washing step and the final functionalized MOF nanoparticle.

Shown in **Figure S3.8**, it was verified that the concentration of excess DOPA decreases dramatically after each successive centrifugation-solvent exchange cycle. In the final DOPA-MOF NP solution, free DOPA in solution is negligible compared to those immobilized on particle.

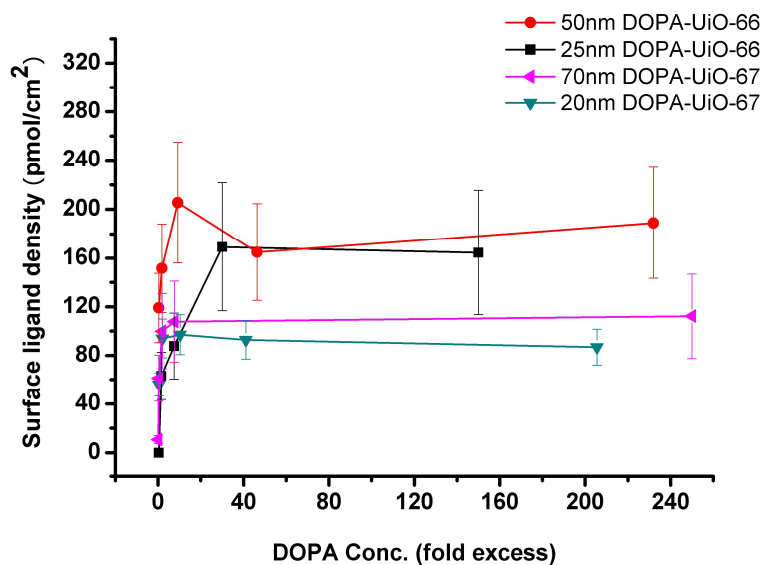


Figure S3.9. Surface ligand loading density modulated with addition of DOPA.

UV-Vis spectroscopy was performed on a Cary 5000 (Agilent) UV-Vis spectrometer fitted with a temperature stage. 1 cm quartz optical cells were utilized to make measurements.

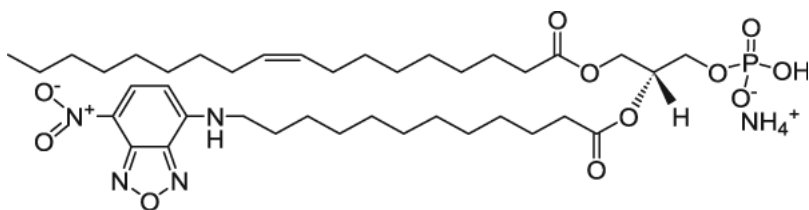


Figure S3.10. Fluorescent dye-labeled phosphate lipid (NBD-DOPA) was used for the ligand loading study.

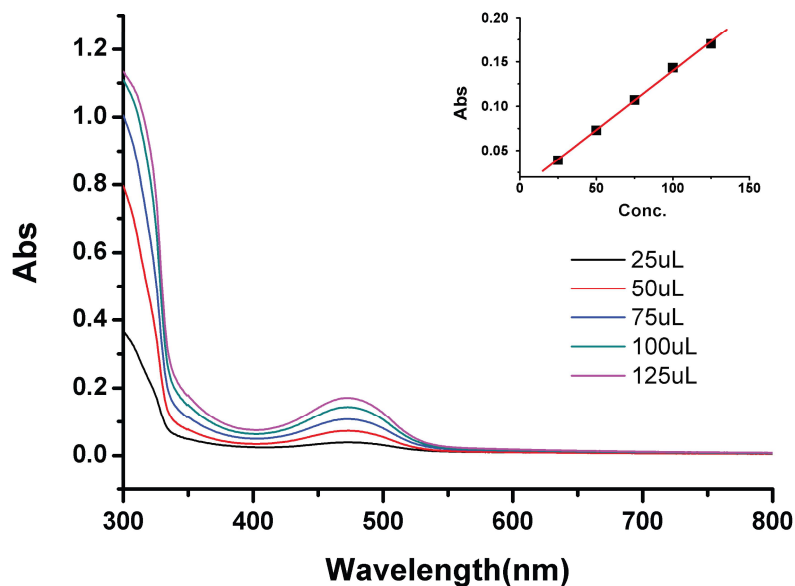


Figure S3.11. Working curve for NBD-DOPA functionalized UiO-66 MOF nanoparticles.

S3.7 Confocal Fluorescence Microscopy

Confocal fluorescence microscopy was performed on a Nikon A1R+ confocal laser microscope system to verify the selective localization of the dye-functionalized ligand to the periphery of the nanoparticles. UiO-67 nanoMOF particles of approximately 600 nm in edge length were selected. Due to the relatively small size of the nanoparticle sample, the photo bleaching effect significantly limited the laser excitation gain we could use. Consequently, the cross section images we obtained suffer from low brightness. However, the observable thin layer of fluorescent corona surrounding the dark nanoparticle cores show that the internal pores of MOF nanoparticle were not functionalized by the fluorescently labeled DOPA ligands.

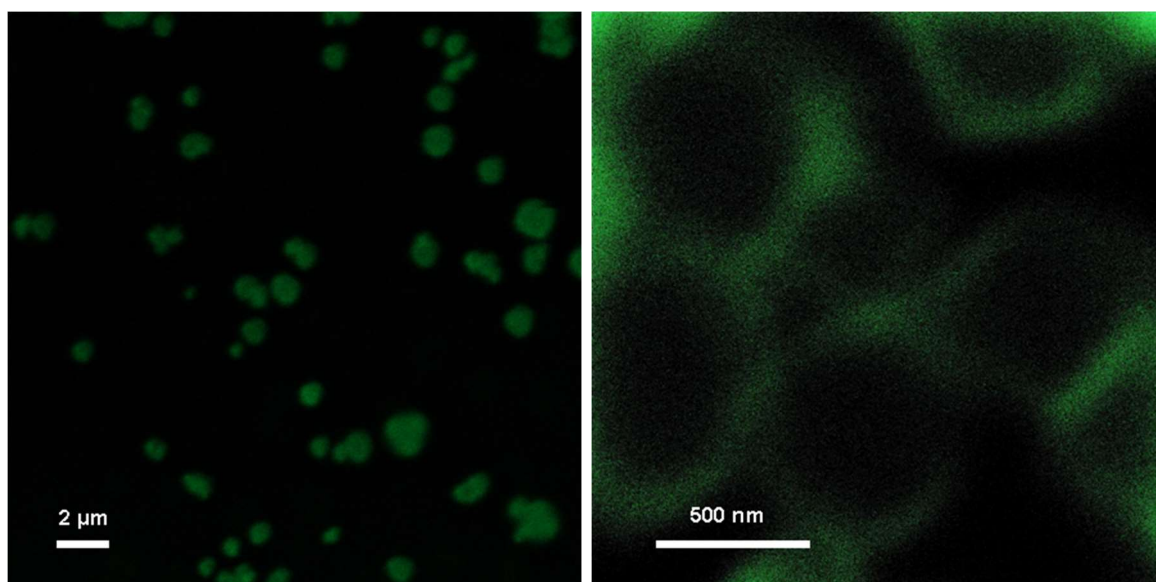


Figure S3.12. Zoomed out confocal fluorescence microscopy image of UiO-67 MOF nanoparticles with NBD-DOPA coordinated to the surface (left). Zoomed in view of cross section image of UiO-67 MOF nanoparticles with NBD-DOPA coordinated to the surface (right). The brightness of the image was with adjusted with ACDSee 9.0 for clarity.

CHAPTER FOUR: Interfacing Metal-Organic Framework Nanoparticles with Oligonucleotides for Biological Probes and Intracellular Protein Delivery Vehicles

Materials in this chapter is based upon published work:

Wang, S.; McGuirk, C. M.; Ross, M.; Wang, S.; Chen, P.; Xing, H.; Liu, Y.; Mirkin, C. A. *J. Am. Chem. Soc.* **2017**, *139*, 9827-9830.

Wang, S.; Chen, Y.; Wang, S.; Li, P.; Farha, O.; Mirkin, C. A. **2018**, to be Submitted.

4.1 Abstract

A generalizable approach to modify MOF nanoparticle surfaces would allow one to impart chemical functionality onto the particle surface that is independent of the bulk MOF structure. Moreover, the use of a chemically programmable ligand, such as DNA, would allow for the manipulation of inter-particle interactions. In this chapter, we discuss a coordination chemistry-based strategy for the surface functionalization of the external metal nodes of MOF nanoparticles with terminal phosphate-modified oligonucleotides. The external surfaces of nine distinct archetypical MOF particles containing four different metal species (Zr, Cr, Fe, and Al) were successfully functionalized with oligonucleotides, illustrating the generality of this new strategy. By taking advantage of the programmable and specific interactions of DNA, eleven distinct MOF particle-inorganic particle core-satellite clusters were synthesized. In these hybrid nanoclusters, the relative stoichiometry, size, shape, and composition of the building blocks can all be independently controlled. This work provides access to a new set of nucleic acid-nanoparticle conjugates, which may be useful as programmable material building blocks and as probes for measuring and manipulating intracellular processes.

We further exploited the use of nucleic acid modified MOF NPs for the storage and transport of a variety of chemical and biological cargoes, such as proteins. Due to their large size, charged surfaces, and environmental sensitivity, proteins do not naturally cross cell-membranes and therefore are difficult to deliver for both diagnostic and therapeutic purposes. Based upon the observation that clustered oligonucleotides can naturally engage scavenger receptors that facilitate cellular transfection, novel nucleic acid-metal organic framework nanoparticle (MOF NP) conjugates have been designed and synthesized from NU-1000 and PCN-222/MOF-545,

respectively, and phosphate-terminated oligonucleotides. They have been characterized structurally and with respect to their ability to enter mammalian cells. The MOFs act as protein hosts, and their densely functionalized oligonucleotide-rich surfaces make them colloidally stable and ensure facile cellular entry. Insulin was chosen as the model protein for this system. High protein loading (~ 40 wt%) and a 10-fold enhancement of cellular uptake (as compared to that of the native protein) were achieved using this strategy. Importantly, this approach could be generalized to facilitate the delivery of a variety of proteins as biological probes or potential therapeutics.

4.2 Introduction and Background

DNA is a versatile and powerful ligand for modifying nanomaterials, by virtue of its programmable and sequence-specific interactions.¹⁷⁵⁻¹⁷⁷ For example, by densely functionalizing DNA onto spherical nanoparticles (NPs), one can orient the oligonucleotides (3'-5' or 5'-3') and generate spherical nucleic acid-nanoparticle conjugates (SNAs),⁸⁹ which exhibit unusual biological properties that have enabled a wide variety of applications in research and medicine. Indeed, many biodiagnostic systems,¹⁷⁸⁻¹⁷⁹ therapeutic lead compounds for gene regulation,¹⁸⁰ and immunotherapeutic agents are now based upon SNAs.¹⁸¹ In addition, they have become the central building blocks for crystal engineering approaches based upon the concept of DNA-programmable assembly.^{158, 182-183} Thus far, several approaches have been developed for modifying noble metal,^{175-176, 184} oxide,¹⁸⁵ quantum dot nanoparticles with DNA.¹⁸⁶ However, there are no general ways for *directly* modifying MOF nanoparticles with oligonucleotides in a preferential end-on manner. Indeed, all previous approaches have utilized either nonspecific interactions such as electrostatic adsorption and van der Waals interactions,^{93, 187} or required a coupling agent that is

necessarily immobilized on the particle surface prior to functionalization with DNA,^{88,90} rendering less control and generality.

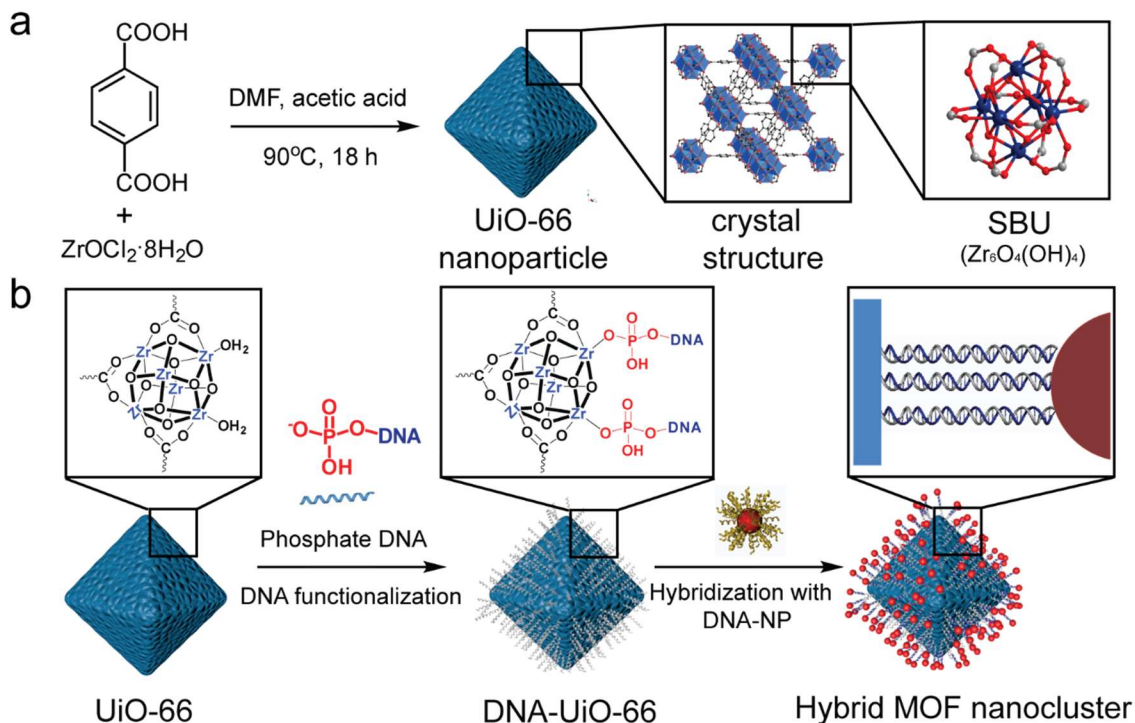


Figure 4.1. (a) Schematic representation of solvothermal synthesis of UiO-66 MOF nanoparticles. Inset: $Zr_6O_4(OH)_4$ secondary building units (SBU). (b) DNA modification of MOFs, utilizing terminal phosphate-modified DNA and subsequent sequence-specific assembly of MOF-NP core-satellite hybrid architectures.

Herein, we describe a general strategy for functionalizing MOF nanoparticles with oligonucleotides at high density. Using terminal phosphate-modified oligonucleotides, we can chemically address the dense coordinatively unsaturated metal sites (CUS) on a MOF nanoparticle surface.^{75,97,117,188-189} Solid-state nuclear magnetic resonance (SSNMR) spectroscopy and powder X-ray diffraction (PXRD) confirm both that the DNA-functionalization of MOFs occurs by metal-phosphate coordination and that the structural integrity and porosity of the MOF architecture are preserved post modification. As proof-of-concept of generality, this approach has

been extended to a series of nine different MOFs, featuring four metal nodes (Zr, Fe, Cr, Al) and four different organic linkers.

Equipped with these above design considerations, we continue to design these nucleic acid-metal organic framework nanoparticle conjugates as intracellular delivery vehicles for proteins. Proteins play key roles in living systems, and the ability to deliver active proteins to cells is attractive for both diagnostic and therapeutic purposes.¹⁹⁰ Potential uses involve the evaluation of metabolic pathways,¹⁹¹ regulation of cellular processes,¹⁹² and treatment of disease involving protein deficiencies.¹⁹³⁻¹⁹⁵ During the past decade, a series of techniques have been developed to facilitate protein internalization by live cells, including the use of complementary transfection agents, nanocarriers,¹⁹⁶⁻¹⁹⁸ and protein surface modifications.¹⁹⁹⁻²⁰² Although each strategy has its own merit, none are perfect solutions; they can cause cytotoxicity, reduce protein activity, and suffer from low delivery payloads.²⁰³ For example, we have made the observation that one can take almost any protein and functionalize its surface with DNA to create entities that will naturally engage the cell-surface receptors involved in spherical nucleic acid (SNA) uptake.^{175, 202, 204-205} While this method is extremely useful in certain situations, it requires direct modification of the protein and relatively large amounts of nucleic acid, on a per-protein basis, to effect transfection. Ideally, one would like to deliver intact, functional proteins without the need to chemically modify them, and to do so in a nucleic-acid efficient manner.

MOFs have emerged as a class of promising materials for the immobilization and storage of functional proteins.²⁰⁶ Their mesoporous structures allow for exceptionally high protein loadings, and their framework architectures can significantly improve the thermal and chemical stabilities of the encapsulated proteins.^{80, 189, 207-210} However, although MOF NPs have been recognized as potentially important intracellular delivery vehicles for proteins,²¹¹⁻²¹³ their poor colloidal stability

and positively charged surfaces,^{11, 63} inhibit their cellular uptake and have led to unfavorable bioavailabilities.^{107, 214-216} Therefore, the development of general approaches for reducing MOF NP aggregation, minimizing positive charge (which can cause cytotoxicity), and facilitating cellular uptake is desirable.^{88, 93}

Herein, we report a new method for the intracellular delivery of proteins that relies on nucleic acid-MOF NP conjugates (**Figure 4.2a**).^{88, 93, 159, 217} In this protocol, two water stable zirconium mesoporous MOFs, NU-1000 and PCN-222/MOF-545,²¹⁸⁻²²⁰ were synthesized in nanoparticle form and used to encapsulate insulin, a model protein for the studies described herein (**Figure 4.2B**).²²¹⁻²²² Next, via modification of literature procedures, these insulin@MOF NPs were surface

functionalized with terminal phosphate-modified DNA to yield insulin@DNA-MOF NPs (**Figure 4.2C**).¹⁵⁹ The 3D oligonucleotide shell creates a steric and electrostatic barrier to stabilize MOF NPs in high dielectric media and renders them functional with respect to cellular entry.⁸⁸ In principle, this strategy can be generalized to MOFs with different pore sizes and topologies, thereby creating an arsenal of nucleic acid-MOF-based delivery vehicles for transporting functional enzymes across cellular membranes with high payloads.

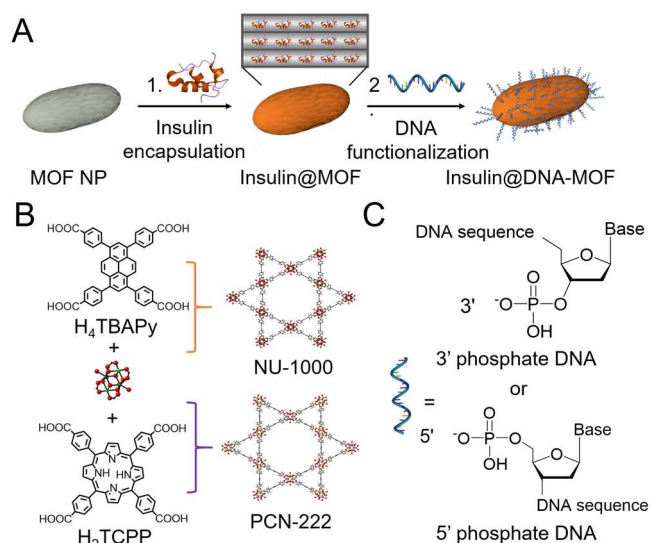


Figure 4.2. (A) Schematic illustration of insulin encapsulation in the mesoporous channels of MOF NPs followed by DNA surface functionalization. (B) Crystal structures of two mesoporous Zr MOFs: NU-1000 and PCN-222/MOF-545 and their respective organic linkers. (C) The terminal phosphate modified nucleic acid (3' or 5') used for DNA functionalization.

4.3 Results and Discussion

4.3.1 Surface Functionalization of MOF Nanoparticles with Terminal Phosphate Modified Oligonucleotides

For our initial study, UiO-66 was chosen due to its high stability and extensively characterized structure.¹¹⁵ UiO-66 was synthesized under solvothermal conditions, using acetic acid to modulate crystallite size, resulting in 225 ± 35 nm (edge length) octahedral nanoparticles. The crystallinity and crystallite size of UiO-66 were determined by PXRD and Scanning electron microscopy (SEM) analysis, respectively (**Figure 4.3a and 4.3d**). Next, phosphate-modified nucleic acids were synthesized on a DNA synthesizer employing chemically modified

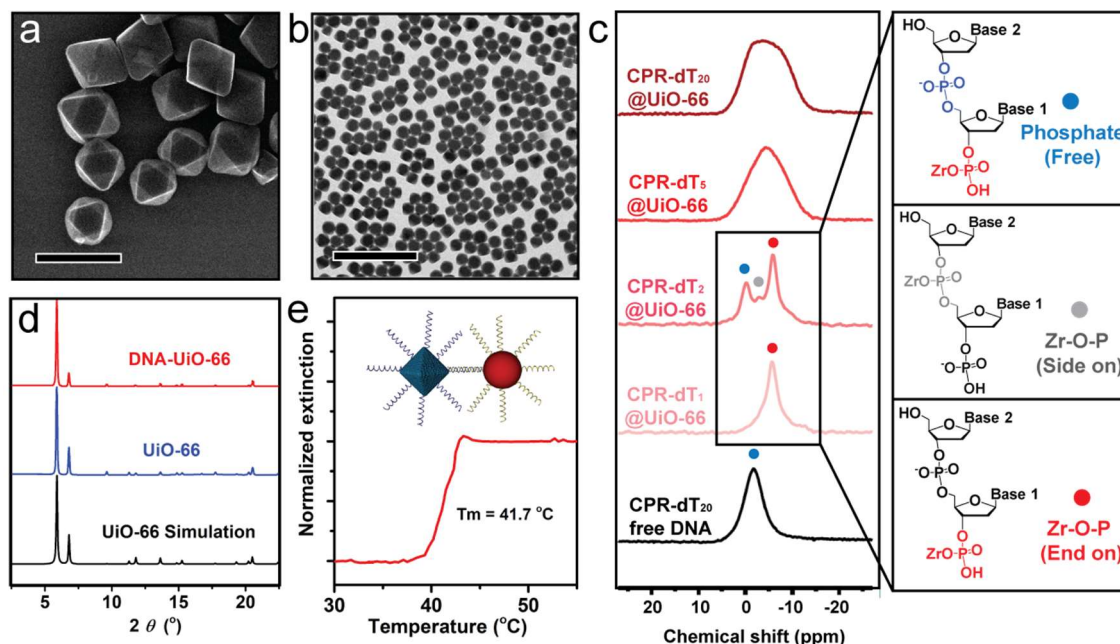


Figure 4.3. Characterization of DNA functionalized MOF nanoparticles: (a) SEM of UiO-66 and (b) TEM images of DNA functionalized UiO-66. (c) $^{31}\text{P}\{^1\text{H}\}$ SSNMR spectra of phosphate functionalized oligonucleotide. Inset: three phosphorous resonances corresponding to unbound phosphodiester (blue), side on Zr bound phosphodiester (grey) and Zr bound terminal phosphate (red). (d) PXRD of simulated UiO-66 (black), 225 nm UiO-66 before (red) and after (blue) DNA functionalization. (e) Melting transition of MOF and 50 nm gold nanoparticle aggregates assembled with complementary DNA. Scale bar = 500 nm in (a) and 2 μm in (b).

phosphoramidites at either the 3' or 5' ends of the oligonucleotide. In a typical DNA-MOF particle functionalization experiment, excess oligonucleotide was added to a colloidal suspension of MOF nanoparticles, and subsequently incubated overnight (See SI). A salt-aging procedure was used to screen the negatively charged oligomers and achieve a high density of surface-immobilized oligonucleotides. Transmission electron microscopy (TEM) images and PXRD verified that the shapes and crystallinity of the particles were preserved post DNA modification (**Figure 4.3b and 4.3d**).

To confirm the immobilization of nucleic acids on the MOF nanoparticle surface, the interaction between terminal phosphate-functionalized DNA and Zr-based SBUs was probed using $^{31}\text{P}\{^1\text{H}\}$ magic angle spinning (MAS) solid-state NMR spectroscopy (**Figure 4.3c**). Oligo-T sequences, synthesized with a chemical phosphorylation reagent (CPR), with lengths of one base (“CPR-T₁”), two bases (“CPR-T₂”), and twenty bases (“CPR-T₂₀”) were synthesized and chemically adsorbed onto MOF nanoparticles. As shown in **Figure 4.3c**, narrow phosphorus resonances centered at -0.3 ppm correspond to unbound phosphate in the free nucleic acid samples. In the CPR-T₁@UiO-66 case, Zr-phosphate bond formation was verified by a 4.8 ppm up-field shift in the phosphorus resonance from -0.3 to -5.1 ppm.²²³ In the CPR-T₂@UiO-66 case, three resonances were observed and assigned to the P atom of the unbound phosphodiester (-0.2 ppm), the Zr-O-P (phosphodiester, -2.8 ppm), and Zr-O-P (terminal phosphate) resonance at -5.9 ppm (**Figure 4.3c inset**). The data suggest immobilization can occur two ways, end on and/or side on where both phosphates can bond with the Zr-rich surface. The significant peak intensity difference between two Zr-O-P modes (terminal phosphate vs. phosphodiester) is due to the increased affinity of the terminal phosphate for the Zr centers as compared to that of the internal phosphodiester; this difference is primarily due to the increased steric hindrance felt by the internal phosphodiester and

is in agreement with previous reports studying Zr-phosphate interactions, but not in the context of MOFs.²²⁴ For CPR-dT₂₀@UiO-66, significant chemical shift broadening upon surface functionalization is observed. We attribute this change to the increased ratio of backbone to terminal phosphates, a distinct chemical environment for each backbone phosphate, and the greater degrees of freedom accessible for the longer oligonucleotide strand. Taken together, these data support the conclusion that the terminal phosphate moiety of DNA coordinates to the previously solvent-bound Zr sites on the external surface of the MOF nanoparticles.

The extent of DNA coverage on the MOF surface was determined by inductively coupled plasma atomic emission spectroscopy (ICP-AES) and UV-visible spectroscopy (UV-vis). The surface area and Zr atoms per particle for UiO-66 were calculated based on a geometric approximation of the crystallite size, shape, and structure (See SI). To quantify the DNA surface coverage, Tamra dye-labeled DNA was used to modify UiO-66 particles. Upon removal of excess unbound DNA, the absorption of Tamra at 556 nm was measured to determine that the average DNA loading on UiO-66 was 17 ± 6 pmol/cm² (~1 DNA/10 nm²), which correlates with the phosphorous and Zr concentrations measured by ICP-AES (See SI). The DNA surface coverage realized in this study is about two times higher than a previous report using a ligand strut modification approach.⁸⁸ The high DNA surface coverage was also confirmed by a thermal melting analysis of aggregates formed from DNA-functionalized UiO-66 nanoparticles and gold NPs (diameter = 50 nm) with complementary DNA, a property that is characteristic of particles with high DNA surface coverages.¹⁷⁵

4.32 Design Rules for Modifying MOF Nanoparticles with Oligonucleotide

To evaluate the generality of this approach, nine distinct MOF architectures containing different metals and organic linkers were chosen, including UiO-66, UiO-67-bpy (2,2'-bipyridine-5',5'-dicarboxylic acid), UiO-68-N₃/PCN-58, PCN-222/MOF-545, PCN-223, PCN-224, MIL-101 (Al), MIL-101 (Fe), and MIL-101 (Cr), representing four distinct metal nodes, four distinct organic linkers, and five different topologies (**Figure 4.4**). In addition to their high chemical stability, these MOFs also have shown promise in nanomedicine.^{9, 107} MOF nanoparticle synthesis, characterization, and surface functionalization and quantification were carried out analogously to that described above (**Figure S4.1-4.6**), following literature reports. In comparing these different MOFs, we set out to test how SBU density, SBU coordination number, and metal-oxygen bond dissociation energy affect surface functionalization.

We initially hypothesized that DNA surface coverage would correlate with the density of SBUs present on the nanoparticle surface. To test this hypothesis, three isoreticular Zr-based frameworks with the same underlying topology were synthesized, namely UiO-66, UiO-67-bpy, and UiO-68-N₃. Within this family, the density of surface metal nodes decreases as a function of increasing organic linker length, with the Zr oxide cluster SBU surface density (assuming (100) facet is exposed) estimated to be 0.27 nm⁻², 0.16 nm⁻² and 0.11 nm⁻² for UiO-66, UiO-67-bpy and UiO-68-N₃, respectively. As shown in **Figure 4.4a**, by plotting the DNA surface coverage as a function of Zr SBU density on each MOF surface, a linear relationship is observed, where the ratio

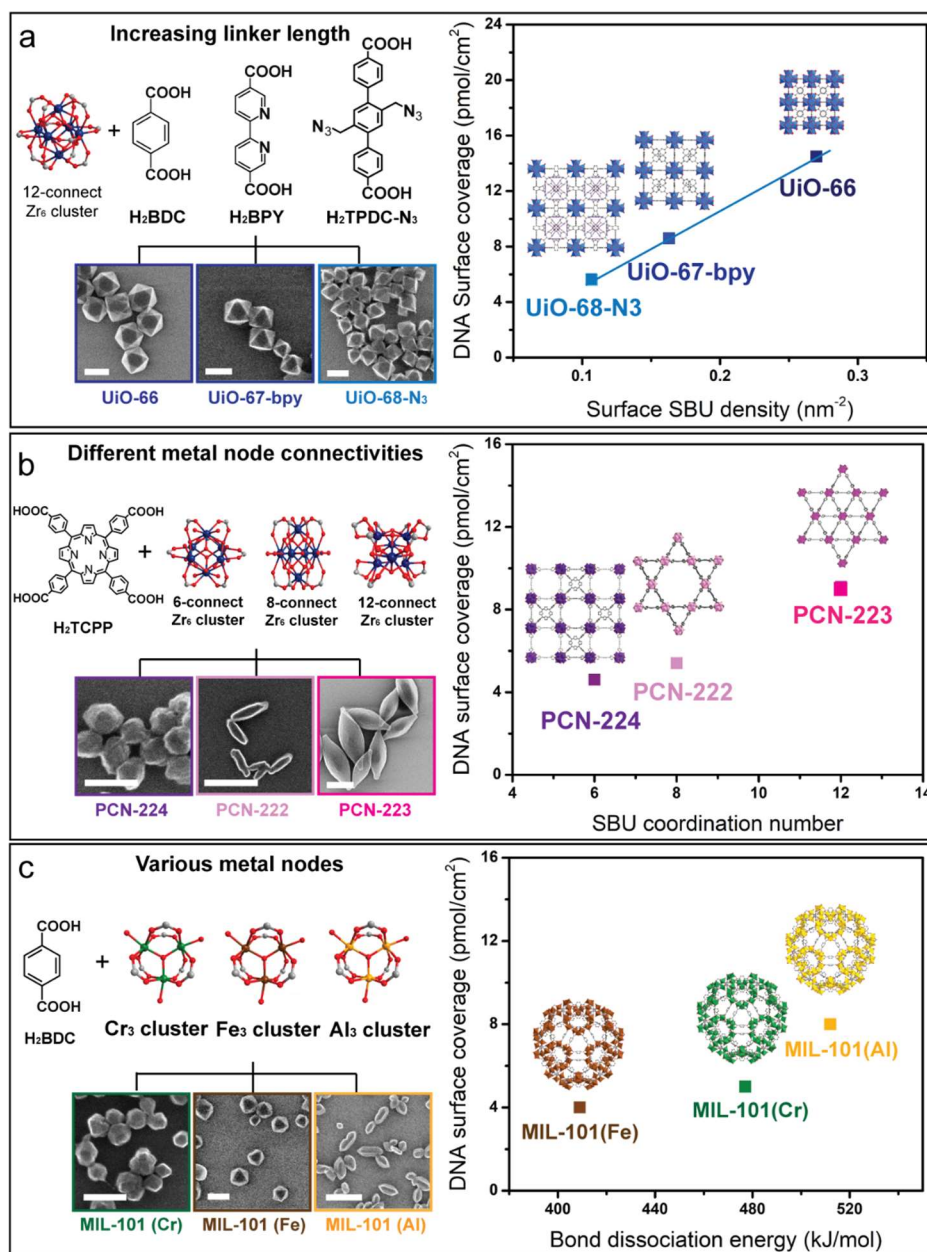


Figure 4.4. A library of nine MOFs were synthesized and further functionalized with DNA. To systematically investigate factors affecting DNA surface coverage, (a) organic linker length, (b) metal node connectivity, and (c) type of metal cluster were independently and deliberately varied and DNA surface coverage was plotted against surface SBU density, SBU coordination number, and M-O bond dissociation energy. Scale bar = 200 nm.

of DNA to Zr SBU is essentially constant – structures with more surface Zr have more DNA. This

is the first demonstration of a quantitative correlation between DNA functionalization and surface SBU density on different MOFs, providing a way to select for MOF structures with the appropriate DNA surface loading for an intended use. Indeed, higher DNA loading density can significantly impact nanomaterial colloidal stability and certain biological applications where high DNA-loading is correlated with particle probe performance.

Next, we set out to test the hypothesis that the formation of stronger metal-phosphate bonds will facilitate greater extents of DNA adsorption. Three isostructural MIL-101 frameworks were synthesized, MIL-101 (Cr), MIL-101 (Fe) and MIL-101 (Al). Because identical structures are found in all three MOFs, the importance of phosphate-metal bond strength (post adsorption) on determining DNA surface coverage can be evaluated. Metal-oxygen bond dissociation energies (BDE) of 409, 477, and 512 kJ/mol for the Fe-O, Cr-O, and Al-O bonds, respectively, have been reported.²²⁵ Indeed, an increase in DNA surface coverage as a function of BDE was observed.

4.33 Synthesis of DNA interconnected MOF-Gold Nanoparticle Assemblies

Finally, with an understanding of the stability and density of the oligonucleotides at the DNA-MOF nanoparticle conjugate surface, we studied the hybridization and assembly properties of such structures with different DNA-NP sizes, shapes, and compositions. In particular, DNA-MOF nanoparticles and archetypical inorganic gold nanoparticle (AuNP) SNA conjugates were used to synthesize hybrid core-satellite nanoclusters. In a typical experiment, AuNPs of different sizes were functionalized with a DNA sequence complementary to those on the MOF nanoparticles to facilitate assembly, the compliments were mixed, salt-aged, and the resulting core-satellite hybrid architectures were isolated by low speed centrifugation. To confirm the morphology of the assembled nanoclusters, a previously developed silica encapsulation protocol for stabilizing DNA-

nanoparticle assemblies was used, as shown in **Figure 4.5a**.²²⁶ Importantly, no MOF-AuNP nanoclusters form upon mixing of non-complementary DNA-functionalized particles.

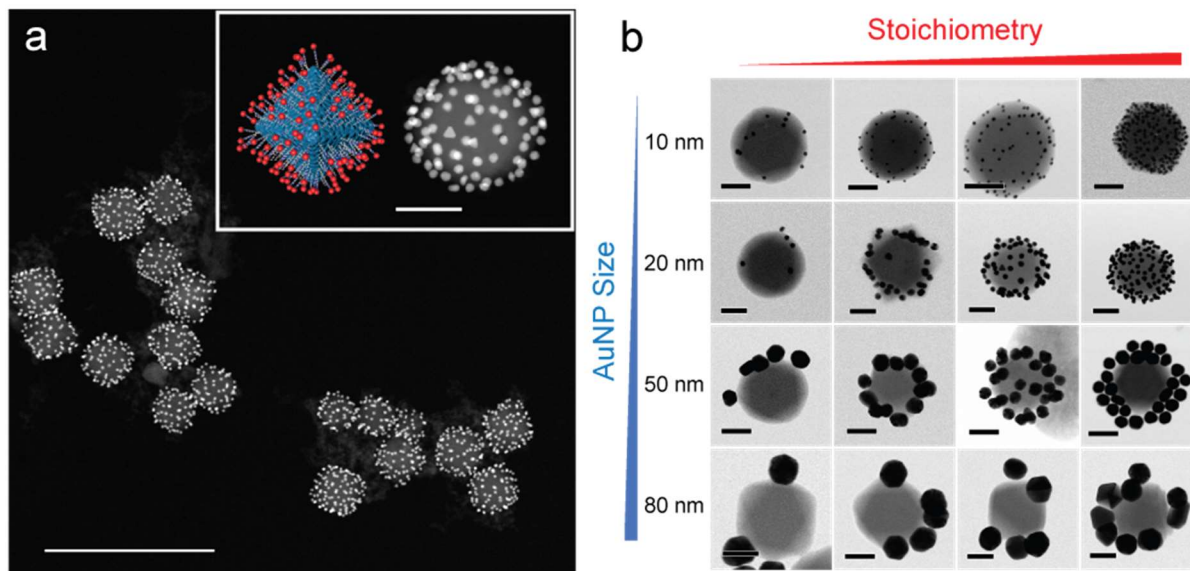


Figure 4.5. TEM and EDX characterization of DNA interconnected MOF NP-Au NP assemblies. (a) A representative HAADF image of nanoclusters formed from complementary 225 nm DNA-UiO-66 MOF NPs and 20 nm DNA-Au NPs. Inset: a schematic illustration of a MOF NP-AuNP cluster, and a single nanocluster. (b) TEM images of nanocluster assemblies demonstrating how the programmable DNA ligands on MOF NPs and AuNPs provide control over the structural makeup of the assemblies (Au NP size and MOF-to-Au NP stoichiometry). All scale bars are 100 nm, except for in (a), where it is 1 μm .

By modifying the stoichiometry of the DNA-mediated hybridization reaction (by varying MOF NP:AuNP ratio from 1:20 to 1:2000), the loading of metal NPs on the central MOF particle could be controlled (**Figure 4.5b**). The formation of MOF-NP nanocluster satellite structures is favored over polymeric structures at high AuNP:MOF ratios; once they form, they expose only identical non-complementary DNA on the nanocluster periphery which inhibits the formation of extended networks via inter-cluster hybridization. To further explore the generality of this DNA-mediated approach, we systematically assembled satellite structures with MOF particle cores with

a variety of DNA-functionalized NP building blocks, including gold nanostars, cubes, octahedra, and triangular prisms, silver spheres, and Fe_3O_4 spheres (**Figure 4.6**). TEM and energy-dispersive X-ray spectroscopy (EDX) mapping of the resulting structures clearly show their clean formation (**Figure 4.7**).

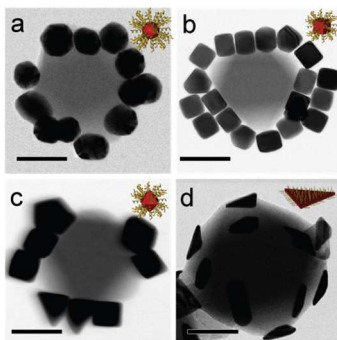


Figure 4.6. TEM images of 225 nm DNA modified MOF NP core assembled with complementary DNA-modified AuNPs of various shapes: (a) spherical AuNPs (inset), (b) Au nano cubes (inset), (c) octahedral AuNPs (inset), (d) Au nano prisms (inset). All scale bars are 100 nm.

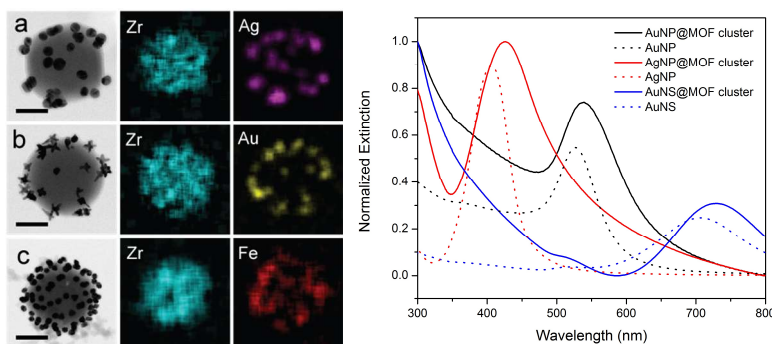


Figure 4.7. Exploration of the assembly of DNA-modified metal NPs (AgNP, AuNS, Fe_3O_4). EDS elemental mapping showing DNA-modified silver nanoparticles assembled around the complementary DNA-UiO-66 MOF NP (a), DNA-modified gold nanostars assembled around the complementary DNA-UiO-66 MOF NP (b), and DNA-modified iron oxide nanoparticles assembled around the complementary DNA-UiO-66 MOF NPs (c). All scale bars are 100 nm. UV-vis spectroscopy was used to compare the extinction of the free colloidal nanoparticles with the assembled MOF-nanoparticle aggregates. In all cases the extinction maximum is red-shifted from the free particle LSPR by about 20 nm.

To further evaluate the potential of MOF-AuNP nanoclusters as stimuli-responsive host-guest system, the Mirkin group hypothesized that DNA functionalized nanoparticles could serve as gating entities to prevent premature cargo leakage and enable on-demand guest release in a fine-tuned, highly specific DNA-hybridization controlled fashion. In this study, the duplex sequence of MOF bounded DNA was shortened to be 9 bases, as opposed to previously used fully-complementary 18 bases, resulting in partial hybridization between DNA-MOF and AuNP bearing thiolate DNA (**Figure 4.8**). Nine bases duplexes between MOF-AuNP were shown to be robust enough to form densely packed nanoclusters, but importantly, can be quickly displaced to release AuNPs from the nanocluster upon addition of 18 bases full-complementary “peel strand”. As shown by the UV-Vis response of MOF-AuNP nanocluster towards “peel DNA” in solution in **Figure 4.8b**, 8 nm blue shift of the AuNP LSPR was observed after stoichiometric amount of “peel” DNA was added to nanoclusters suspension within 30 mins, suggesting successful AuNP release from the bounded MOF surface. The dissociation

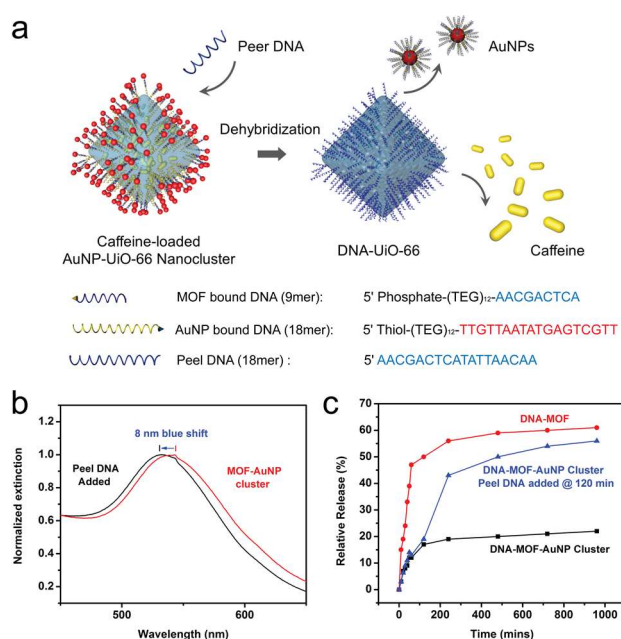


Figure 4.8. DNA mediated guest release experiments of encapsulated caffeine inside UiO-66-AuNP nanoclusters. (a) schematic illustration of DNA triggered caffeine release from MOF-AuNP nanocluster and DNA sequences design. (b) *In situ* UV-Vis measurement of MOF-AuNP nanocluster, showing blue shift of gold nanoparticle LSPR upon addition of peel DNA strand. (c) Relative guest release profile for DNA-MOF, MOF-AuNP nanoclusters. Scale bars = 200 nm.

was also verified by TEM images taken before and after “peel DNA” been added to the system. Next, caffeine was selected as the model guest molecule for controlled release experiment. DNA-MOF were first incubated in HEPES buffered saline solution containing 10 mg/mL caffeine for 3 days, and then hybridized with AuNP to yield Caffeine encapsulated MOF-AuNP nanoclusters. Excess AuNP and caffeine was removed by low speed centrifugation followed by solvent exchanged with fresh buffer for three times. As shown in Figure 6c, the guest release profiles of three different caffeine-loaded constructs were studied: DNA functionalized MOF, MOF-AuNP nanocluster, and MOF-AuNP nanocluster with addition “peel DNA” at 120 mins. Premature guest leakage, or burst release within the first 30 mins, for the DNA-MOF sample was much more significant as compared to those two AuNP capped nanocluster cases. A near flat baseline shows that caffeine is sufficiently held within the MOF nanopores that are capped by densely surface hybridized AuNPs. Whereas, an immediate accelerated release of the cargo molecules was observed when “peel DNA” was added to the system at 120 mins, indicating removal of surface capped AuNPs induced guest triggered-release.

The enrichment of MOF-AuNP nanocluster in cellular vesicles over time was demonstrated by confocal laser scanning microscopy (**Figure 4.9**), where strong accumulation of the nanocluster in cellular vesicle was observed as compared to an equivalent amount of single strand dye-labeled DNA, with no appreciable cytotoxicity (**Figure 4.10**). The cellular cytotoxicity and uptake properties of MOF-NP hybrid nanocluster were assessed. Specifically, Tamra phosphoramidite labeled DNA was synthesized and functionalized on 225 nm UiO-66 nanocrystals as a fluorescent label, which was then hybridized with 20 nm AuNP to form Tamra-MOF-AuNP nanoclusters. Human ovarian cancer cells (SK-OV-3) in a McCoy’s 5A medium were incubated with different forms of nucleic acids: first, 100 μ L of a suspension of MOF-AuNP nanocluster; second, 100 μ L

of equivalent amount of dye labeled free Tamra-DNA strand. Cell filamentous actin (F-actin) were stained with Alexa Fluor 488 Phalloidin, and all non-absorbed particles were removed from cells by washing with HEPES buffer solution. The enrichment of MOF-AuNP nanocluster in cellular vesicles over time was demonstrated by confocal laser scanning microscopy **Figure 4.10**, where strong accumulation of the nanocluster in cellular vesicle was observed as compared to an equivalent amount of single strand dye-labelled DNA. Taken together, the structures realized illustrate the versatility and potential utility of these new DNA-modified MOF NPs for programmable assembly and in applications where designer oligonucleotide interactions are relevant.

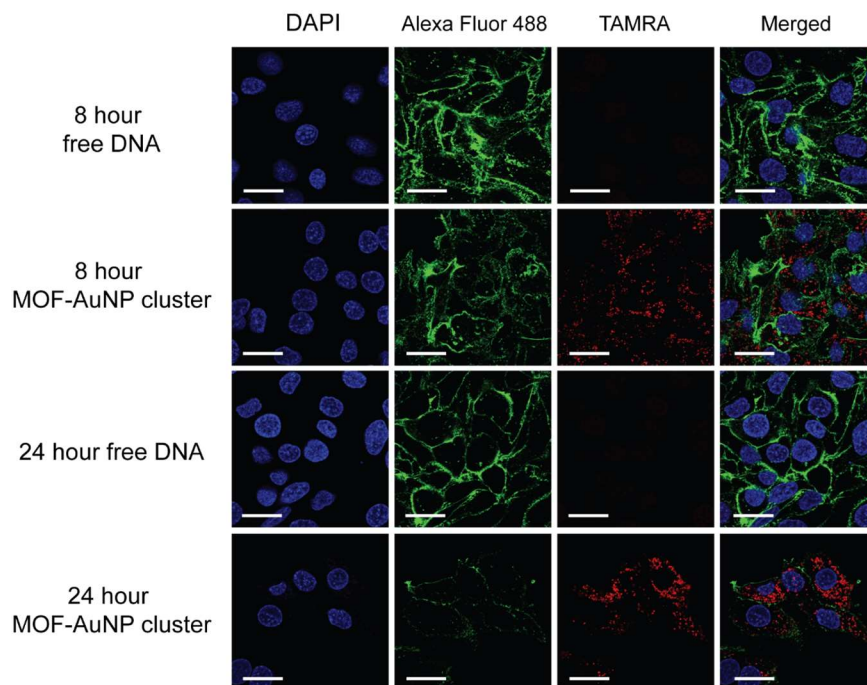


Figure 4.9. MOF-NP nanoclusters show enhanced cellular uptake capability as compared to that of single strand DNA. Fluorescence micrograph of SK-OV-3 cells incubated with different forms of nucleic acid: (1) hybridized nanoclusters synthesized with 225 nm UiO-66 (labelled with Tamra-DNA) and 20 nm AuNP, and (2) dye labelled single strand DNA at a total DNA concentration of 1×10^{-6} M for 8 h and 24 h, respectively. Scale bars = 10 μ m.

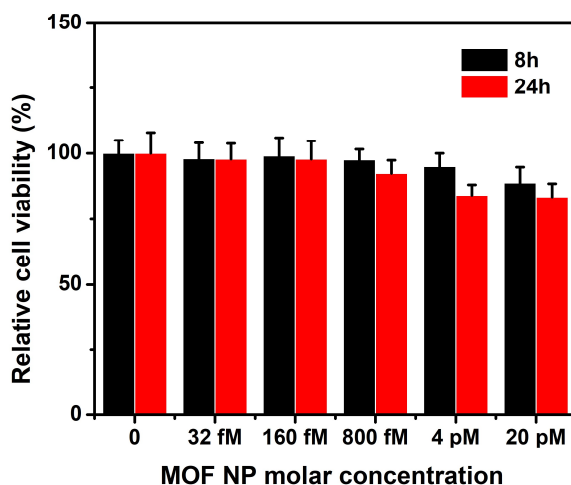


Figure 4.10. MTT assay verifies negligible cytotoxicity or anti-proliferative effects induced by MOF-NP nanoclusters.

4.34 Encapsulation of Proteins in MOF Nanoparticles

MOF NP syntheses^{71, 227} and insulin encapsulations²²¹ were realized via literature protocols. Specifically, NU-1000 MOF NPs [180(20) × 70(10) nm] were synthesized via a solvothermal reaction of zirconium chloride ($ZrCl_4$) with (4,4',4'',4''')-(porphine-5,10,15,20-tetrayl)tetrakis(benzoic acid) (H_4TBAPy), modulated by acetic acid in N,N-Dimethylformamide (DMF) at 90 °C (**Figure 4.11a**). Similarly, PCN-222 NPs [210(30) × 50(10) nm] were synthesized via a solvothermal reaction between zirconyl chloride octahydrate ($ZrOCl_2 \cdot 8H_2O$) and tetrakis(4-carboxyphenyl)porphyrin (TCPP), modulated by dichloroacetic acid in DMF at 130 °C (**Figure 4.11b**). Next, the thermally activated crystals of NU-1000 were treated with a bis-tris-propane buffer (BTP, pH = 7) solution of insulin (0.4 mg/mL). The MOF NP insulin encapsulation efficiencies were determined by measuring the S [for insulin] and Zr (for MOFs) contents by inductively coupled plasma-optical emission spectroscopy (ICP-OES for [MOF NPs]). With an understanding of the average dimensions of the particles determined by TEM, maximum insulin

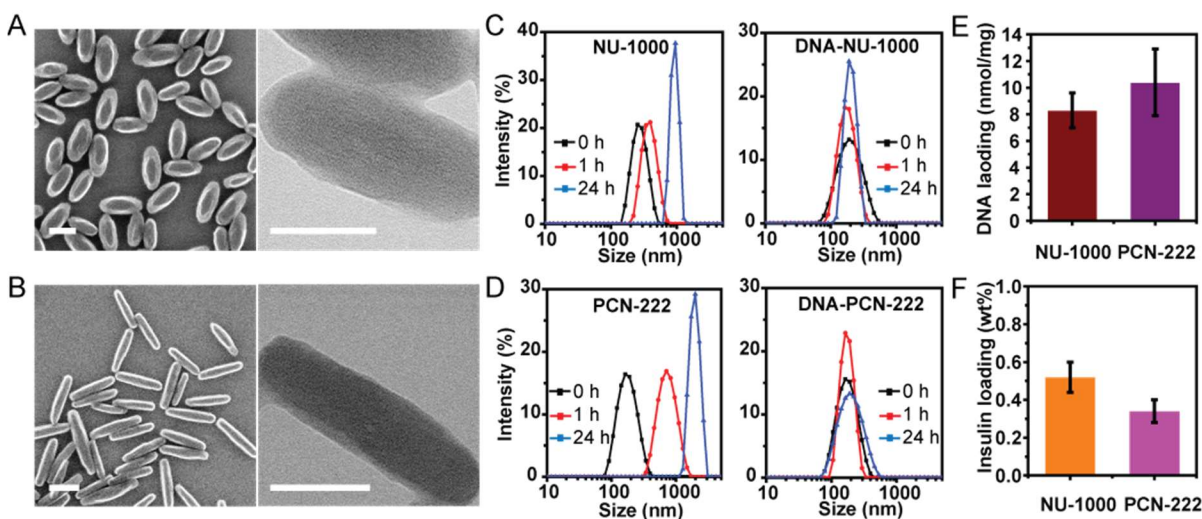


Figure 4.11. Scanning electron microscopy (left) and transmission electron microscopy (right) images of as-synthesized NU-1000 NPs (a) and PCN-222 NPs (b). (c-d) Colloidal stability of NU-1000 and PCN-222 NPs in cell medium, as determined by DLS without (left) and with DNA surface modification (right). DNA loading (e) and insulin encapsulation efficiency (f) for NU-1000 and PCN-222 MOF NPs. Scale bars = 100 nm.

loadings of 39 and 34 wt% were determined for NU-1000 and PCN-222 NPs, respectively (**Figure 4.11f**). Note that excess insulin in the supernatant and adsorbed on the external surface of the particles was removed by sequential washing steps with DI water and trypsin solution, respectively.

The insulin@MOF NPs were functionalized with nucleic acids by coordinating the terminal phosphate-modified oligonucleotides to the surface Zr SBUs.^{159, 228} The sequence used here, 5' (dGGT)₁₀-phosphate 3', was chosen because it is known with SNAs that a G-rich shell, relative to poly dT shells, facilitates higher cellular uptake.²²⁹ In a typical NP functionalization experiment, excess oligonucleotides were added to a colloidal dispersion of MOF NPs and incubated for 4 hours (Supporting Information). Particle DNA coverage was quantitatively determined by measuring the P to Zr ratio by ICP-OES (8 ± 1 nmol/mg for NU-1000 NPs and 10 ± 1 nmol/mg for PCN-222 NPs, **Figure 4.11e**). Powder X-ray diffraction (PXRD) and scanning electron microscopy (SEM) confirmed that the crystallinity and morphologies of the MOF NPs

were maintained, post-DNA functionalization. Importantly, dynamic light scattering (DLS) verified that DNA surface functionalization significantly increases MOF NP colloidal stability in cellular media (90% DMEM buffer + 10% fetal bovine serum) for at least 24 hours; for comparison, unfunctionalized NU-1000 NPs aggregated in less than one hour, hampering further *in vitro* use (Figure 4.11c-d).

In addition to colloidal stability, the intra- and extracellular stability of protein delivery vehicles in serum and serum free but biologically relevant matrices is important. Indeed, the ability to control degradation could be useful in the development of temporally-controlled drug delivery applications. Under physiological conditions, intracellular fluid exhibits significantly higher inorganic phosphate concentration (5~10 mM) as compared to that of serum (~1 mM).²³⁰⁻²³¹ Therefore, the degradation profiles of insulin@DNA-NU-1000 NPs and insulin@DNA-PCN-222 NPs were evaluated by exposing them to solutions designed to emulate both extracellular and intracellular conditions (Supporting Information). To simulate serum, MOF NPs were incubated with 90%

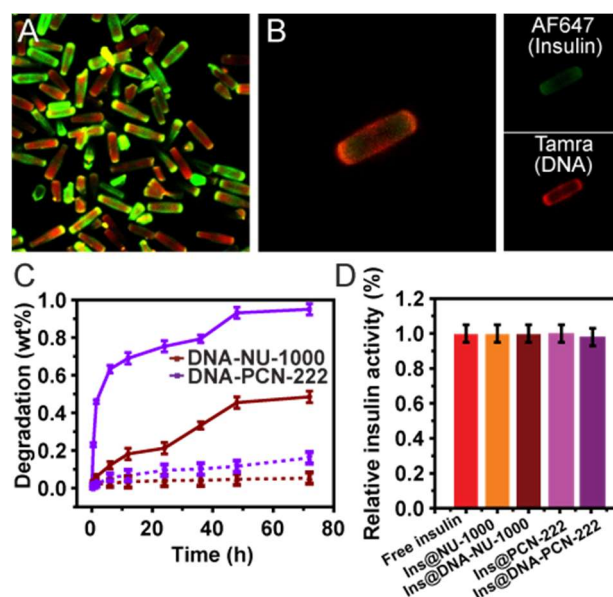


Figure 4.12. (a) Representative confocal fluorescence micrographs of 10 μm insulin@DNA-NU-1000 particles verified the colocalization of insulin (AF647 channel) and DNA (TAMRA channel). (b) Z-stack image of a single 10 μm insulin@DNA-NU-1000 crystal. (c) Degradation profiles of DNA-NU-1000 NPs and DNA-PCN-222 NPs incubated in extracellular medium (dashed lines) and in simulated intracellular medium (solid lines) at 37 °C with 400 rpm shaking. (d) Insulin activity assay as measured by ELISA for native insulin (red), insulin@MOF NPs (orange for NU-1000, pink for PCN-222), and insulin@DNA-MOF NPs (brown for NU-1000, purple for PCN-222).

DMEM buffer + 10% blood serum (pH = 7.0) at 37 °C with gentle shaking (400 rpm), where less than 5 % of degradation occurred within 12 hours for both vehicles, and less than 20% within 96 hours, suggesting DNA-MOF NPs exhibit excellent stability and may be compatible with blood (**Figure 4.12c**, dashed lines). In contrast, when the same MOF NPs were incubated in an intracellular medium simulant (1 × phosphate buffered saline, pH = 7.0) at 37 °C with gentle shaking, the particles degrade at much faster rates ((**Figure 4.12c**, solid lines) due to the high phosphate content, which competitively binds to Zr clusters. Interestingly, DNA-PCN-222 NPs exhibit a faster degradation rate (half-life = 1 h) when compared to that of DNA-NU-1000 NPs (half-life = 40 h). Such degradation kinetics could be useful for *in vivo* purposes by providing a means to control the temporal release of proteins from particles, once inside cells.

To directly visualize nucleic acid-modified, insulin encapsulated MOF NPs, we employed confocal laser scanning microscopy to image them. Due to the resolution limits of confocal microscopy, larger particles (2.8 μm × 10 μm for NU-1000), AlexaFluor 647 dye (AF647)-labeled insulin, and TAMRA-labeled DNA were used. With such particles, the co-localization of AF647 and TAMRA signals can be clearly observed, verifying the encapsulation of insulin and DNA surface functionalization of the MOF (**Figure 4.12a**). To obtain detailed information regarding relative distribution of insulin and DNA, Z-stack images of a single MOF particle were taken, where TAMRA signal (DNA) was observed to preferentially occupy the periphery while AF647 (insulin) was present throughout the particle (**Figure 4.12b**). Brighter AF647 signals were observed at both ends of the particle as compared to the center section of the MOF, consistent with the previous observation that proteins diffuse into NU-1000 through its 1D channels.²²² Due to the large diameter of the MOF pores (3.2 nm for NU-1000 and 3.7 nm for PCN-222),²²⁰ single stranded DNA was also expected to penetrate through the MOF pores and functionalize the internal surface,

leading to fluorescence signal inside the particles. As verified by N₂ adsorption isotherms, reduced N₂ uptake capacity was observed post-insulin encapsulation for both MOFs, and further loss of porosity was observed post-DNA functionalization (**Figure S4.8 and S4.9**). Furthermore, an enzyme-linked immunosorbent assay (ELISA) was employed to determine whether proteins would leach from the MOF NP pores or lose catalytic activity during the DNA functionalization process. In both cases, no insulin activity loss was observed for insulin@DNA-NU-1000 and insulin@DNA-PCN-222 constructs (**Figure 4.12d**).

4.35 Cellular Uptake of DNA Functionalized MOF Nanoparticles

As previously stated, a key characteristic of SNA-NP conjugates is their ability to effectively enter cells. Therefore, we tested whether insulin@DNA-MOF NPs exhibited enhanced cellular uptake. Specifically, NU-1000 and PCN-222 NPs were encapsulated with AF647-labeled insulin and functionalized with TAMRA-labeled DNA and incubated with human ovarian adenocarcinoma cells, SKOV-3, for 0.5 h, 2 h, 6 h, and 24 h (Supporting Information). As a control group, a mixture of free TAMRA-labeled DNA and AF-647-labeled insulin was incubated with cells at the same concentration. Confocal laser scanning microscopy confirms the enrichment of insulin in cellular vesicles, as evidenced by strong colocalization of AF647 and TAMRA signals in cellular vesicles (**Figures 4.13a-c**). The Z-stack images confirm that the insulin@DNA-MOF NPs are internalized by the cells, as opposed to attached to their membranes. Consistent with this conclusion, flow cytometry showed a 10-fold increase in fluorescence in cells treated with insulin@DNA-MOF NPs as compared to those treated with the free insulin + DNA control group (**Figure 4.13d**). The insulin@DNA-MOF NPs exhibits similar levels of enhancement in cellular

uptake, as compared to that of conventional SNA-NP conjugates.⁸⁹ Finally, MTT assays show that the particles result in no apparent cytotoxicity or anti-proliferative effects (**Figure 4.13e**).

As previously stated, a key characteristic of SNA-NP conjugates is their ability to effectively enter cells. Therefore, we tested whether insulin@DNA-MOF NPs exhibited enhanced cellular uptake. Specifically, NU-1000 and PCN-222 NPs were encapsulated with AF647-labeled insulin and functionalized with TAMRA-labeled DNA and incubated with human ovarian adenocarcinoma cells, SKOV-3, for 0.5 h, 2 h, 6 h, and 24 h (Supporting Information). As a control

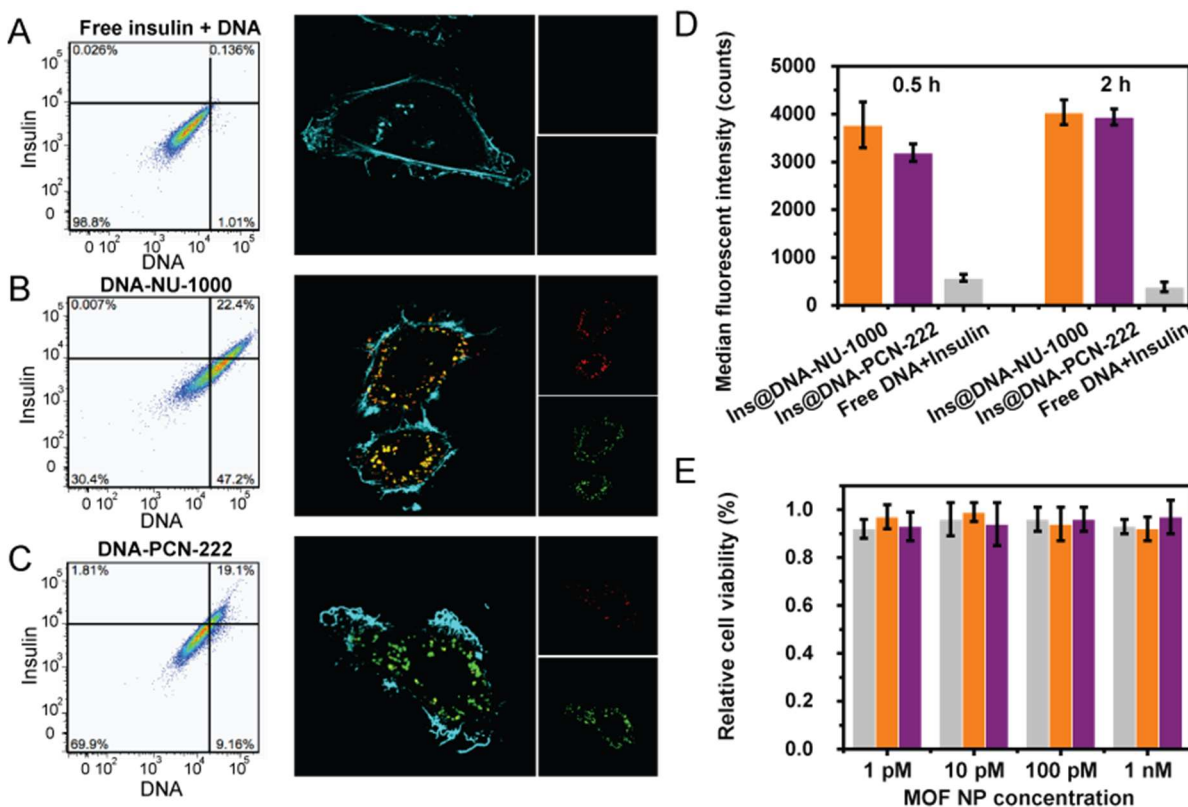


Figure 4.13. (a-c) Flow cytometry plots and confocal fluorescence micrographs of SK-OV cells after 6 h treatment with free insulin + DNA (a), insulin@DNA-NU-1000 (b), and insulin@DNA-PCN-222 (c). (d) Cellular uptake of insulin delivered in different constructs as determined by flow cytometry. Fluorescence at 647 nm was measured in SK-OV cells after treatment with insulin at various incubation time (0.5 h and 2 h). (e) MTT assay verifies no appreciable cytotoxicity induced by insulin@DNA-PCN-222 and insulin@DNA-NU-1000 NPs. Scale bar = 10 μ m.

group, a mixture of free TAMRA-labeled DNA and AF-647-labeled insulin was incubated with cells at the same concentration. Confocal laser scanning microscopy confirms the enrichment of insulin in cellular vesicles, as evidenced by strong colocalization of AF647 and TAMRA signals in cellular vesicles (**Figures 4.13a-c**). The Z-stack images confirm that the insulin@DNA-MOF NPs are internalized by the cells, as opposed to attached to their membranes. Consistent with this conclusion, flow cytometry showed a 10-fold increase in fluorescence in cells treated with insulin@DNA-MOF NPs as compared to those treated with the free insulin + DNA control group (**Figures 4.13d**). The insulin@DNA-MOF NPs exhibits similar levels of enhancement in cellular uptake, as compared to that of conventional SNA-NP conjugates.⁸⁹ Finally, MTT assays show that the particles result in no apparent cytotoxicity or anti-proliferative effects (**Figures 4.13e**).

4.4 Conclusions

This work is important for the following reasons. First, it provides a straightforward approach to the synthesis of DNA-modified MOFs, independent of the choices of organic linkers and broadly applicable to a variety of metal clusters. Second, the structures realized are stable, have many of the original MOF characteristics, and can be programmably assembled with complementary DNA-modified NP building blocks. Third, design rules for modifying MOF NPs with DNA are emerging through this work. Most notably, we have shown that DNA surface coverage directly correlates with MOF nanoparticle surface SBU density, coordination number, and metal-phosphate bond strength. Finally, the experiments described herein provide a route to a broad class of NP building blocks with tunable properties that can be used to prepare designer materials with properties that may prove useful in biology,²³² catalysis,²³³ and optics.²³⁴

In addition, we have also developed a facile strategy for using nucleic-acid modified MOF NPs to deliver proteins across cell membranes at high payloads and negligible cytotoxicity. This work is important since it highlights how clustered surface oligonucleotides on these modular materials can be used to make them colloiddally stable in physiological environments and useful for intracellular biological applications. Future design iterations will allow for encapsulating various proteins by tuning the MOF pore sizes,^{222, 235-236} and potentially co-delivery of protein and nucleic acid targets that are important for many purposes, including *in vivo* imaging,¹⁹¹ gene regulation,⁹³ therapeutics,¹⁹⁴ and the study of fundamental cellular processes.¹⁹³

4.5 Experimental Methods and Supplementary Materials

S4.1 Synthesis of 9 MOF nanoparticles

UiO-66

UiO-66 was synthesized via solvothermal reaction conditions. 1,4-benzenedicarboxylic acid (50 mg, 0.30 mmol) was dissolved in 1 mL of *N,N*-dimethylformamide (DMF). In a separate vial, zirconyl chloride octahydrate (21 mg, 0.066 mmol) was dissolved in 3 mL of DMF. The two solutions were mixed together in a 10 mL scintillation vial, and 2.0 mL acetic acid was added to the reaction mixture. After brief sonication, the solution was heated at 90 °C for 18 h to yield UiO-66 nanoparticles.

UiO-67-bpy

UiO-67-bpy was synthesized via a similar method. Biphenyl- 4,4'-dicarboxylic acid (150 mg, 0.6 mmol) was added to 20 mL of DMF, resulting in a white suspension. In a separate vial, zirconyl chloride octahydrate (105 mg, 0.33 mmol) was dissolved in 3 mL of DMF. The two fractions were

mixed together in a 25 mL scintillation vial, and 2.5 mL acetic acid was added to the reaction mixture. After brief sonication, the suspension was heated at 90 °C for 18 h to yield UiO-67-bpy.

UiO-68-azide/PCN-58

2',5'-bis(azidomethyl)-[1,1':4',1''-terphenyl]-4,4''-dicarboxylic acid (TPDC-2CH₂N₃) was synthesized according to a literature reported method.²³⁷ In a 10 mL scintillation vial, TPDC-2CH₂N₃ (100 mg, 0.075 mmol) was added to 1 mL of DMF. In a separate vial, zirconyl chloride octahydrate (21 mg, 0.066 mmol) was dissolved in 3 mL of DMF. The two fractions were mixed together in a 10 mL scintillation vial, and 240 µL acetic acid was added to the reaction mixture. The suspension was heated at 90 °C for 18 h.

PCN-222/MOF-545

The synthesis of PCN-222/MOF-545 nanocrystal was based on a literature reported method with minor modifications.⁷¹ Zirconyl chloride octahydrate (37.5 mg, 0.116 mmol) and tetrakis(4-carboxyphenyl)-porphyrin (6.5 mg, 0.0082 mmol) were dissolved in DMF (16.25 mL) in a 22 mL borosilicate vial with a Teflon-lined cap. Dichloroacetic acid (0.25 mL, 3.0 mmol) was added, and the resulting solution was heated at 130 °C for 18 hours to afford dark purple rod-shaped nanocrystals and a yellow mother liquor. The nanocrystals were collected by centrifugation (15000 rpm, 5 min), followed by solvent exchange with DMF.

PCN-223

The synthesis of PCN-223 nanocrystals was based on a literature reported method with minor modifications.⁷¹ In a 10 mL scintillation vial, 5,10, 15, 20 -Tetrakis (4-carboxyphenyl)porphyrin (H₂TCPP, 5.2 mg, 0.007 mmol), zirconyl chloride octahydrate (9.8 mg, 0.03 mmol), and acetic acid (0.4 mL) in 3 mL of DMF were ultrasonically dissolved and heated at 90 °C for 18 h. After

the reaction was complete, PCN-223 nanoparticles were collected by centrifugation, followed by washing with fresh DMF for 3 times.

PCN-224

The synthesis of PCN-224 nanocrystal was based on a literature reported method with minor modifications.¹⁴ In a 25 mL scintillation vial, 5,10, 15, 20 -Tetrakis (4-carboxyphenyl) porphyrin (10 mg, 0.013 mmol), zirconyl chloride octahydrate (30 mg, 0.093 mmol), and benzoic acid (300 mg, 2.4 mmol) in 10 mL of DMF were dissolved and the mixture was stirred (300 rpm) at 90 °C (oil bath) for 5 h. After the reaction was done, PCN-224 nanoparticles were collected by centrifugation (12000 rpm, 30 min), followed by washing with fresh DMF for 3 times.

MIL-101-Cr

The synthesis of MIL-101-Cr nanocrystals was based on a literature reported method with minor modifications.²³⁸ Terephthalic acid (H_2BDC , 55 mg 0.33 mmol) and chromium nitrate nonahydrate ($Cr(NO_3)_3 \cdot 9H_2O$, 132 mg, 0.33 mmol) were dissolved in 10 mL of water. The resulting suspension was stirred for 1 h at room temperature then heated under autogenous pressure at 180 °C for 8 h in a Teflon-lined autoclave. After cooling to room temperature, the mixture was filtered to remove the recrystallized terephthalic acid. The product was isolated from the filtrate as a green powder following centrifugation at 7000 rpm for 15 min, and then washed three times with ethanol.

MIL-101-Fe

MIL-101 (Fe) $Fe_3O(H_2O)_2Cl(BDC)_3$ nanoparticles were synthesized using a previously reported microwave heating method.²³⁹ Specifically, 57.5 mg (0.346 mmol) of terephthalic acid

and 93.5 mg (0.346 mmol) of $\text{FeCl}_3 \cdot \text{H}_2\text{O}$ were dissolved in 15 mL of DMF. The solution was placed in a HP500 microwave vessel, and sealed. The reaction was then rapidly heated to 150 °C (within 30 seconds), and was held at this temperature for 10 minutes. After cooling to room temperature, the particles were isolated by centrifuging, and were washed with DMF and ethanol. After cooling to room temperature, the nanoparticles were isolated by centrifugation and washed with DMF to remove the excess reactants.

MIL-101-Al

For the synthesis of MIL-101 (Al) nanocrystals, 45 mg (0.27 mmol) of terephthalic acid were dissolved in 5 mL of DMF. In a separate vial, 120 mg (0.5 mmol) of $\text{AlCl}_3 \cdot 6\text{H}_2\text{O}$ were added to 5 mL of DMF, to which 5 mL of terephthalic acid DMF solution were added. After brief sonication, the suspension was left at room temperature overnight to fully dissolve. 500 μL of acetic acid was added to the solution and then heated at 90 °C in a conventional oven for 18 hours. After cooling to room temperature, the particles were isolated by centrifugation and washed with DMF and ethanol to remove the excess reactants.

NU-1000

150 nm particles

8 mg (34.3 nmol) of zirconium chloride and 2 mg (3 nmol) of 1,3,6,8-tetrakis(p-benzoic acid)pyrene (H_4TBAPy) ligand were dissolved in 2.0 mL of *N,N*-Dimethylformamide (DMF), 0.4 ml acetic acid and 0.2 ml DI water was also added to the mixture solution resulting in a translucent yellow solution. Ten sample vials were prepared under the same conditions at once and were placed into an oven at 90 °C for 30 min, during which time a light yellow suspension was formed. After cooling down to room temperature, the 10 vials were combined and the nanocrystals were

collected by centrifugation (15000 rpm, 30 min), followed by solvent exchange with DMF and acetone three times, then subsequently activated with HCl.

10 μm particles

The synthesis of 10 μm NU-1000 particle was based on a literature reported method.²²⁷ Briefly, 70 mg of ZrCl_4 (0.30 mmol) and 2700 mg (22 mmol) of benzoic acid were mixed in 8 mL of *N,N*-Diethylformamide (DEF) (in a 6-dram vial) and ultrasonically dissolved. The clear solution was incubated in an oven at 80 °C for 1h. After cooling down to room temperature, 40 mg (0.06 mmol) of H_4TBAPy was added to this solution and the mixture was sonicated for 20 min. The yellow suspension was heated in an oven at 120 °C for 48 h. After cooling down to room temperature, yellow single crystals were present on the vial walls. The sample was washed with DMF and acetone and subsequently activated with HCl.

S4.2 Powder X-ray diffraction

The crystallinity of the synthesized MOF nanoparticles and DNA functionalized MOF nanoparticles conjugates were confirmed by powder X-ray diffraction (PXRD). Powder X-ray diffraction patterns were collected on Rigaku Smartlab instrument (Tokyo, Japan) with a $2\theta = 0.05^\circ$ scan rate over $2.5\text{-}30^\circ$ range at 45 kV and 160 mA.

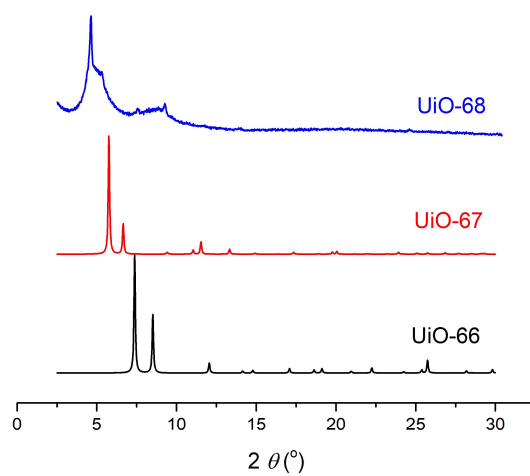


Figure S4.1. PXRD spectra of UiO-66, UiO-67-bpy and UiO-68-N₃.

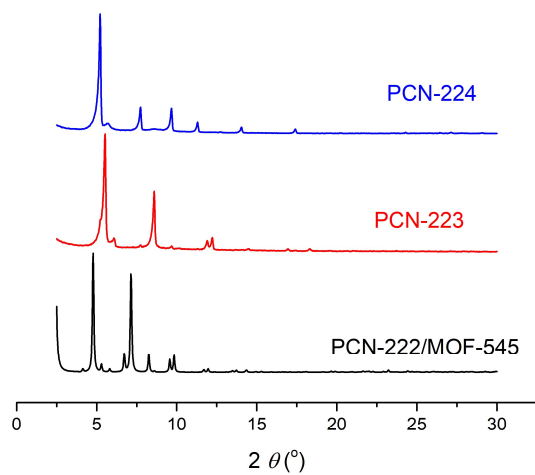


Figure S4.2. PXRD spectra of PCN-222, PCN-223 and PCN-224.

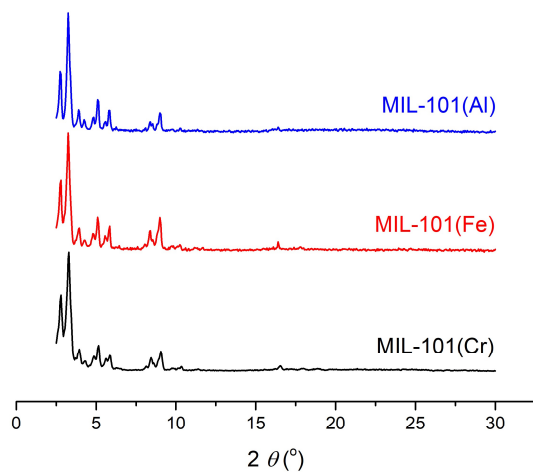


Figure S4.3. PXRD spectra of MIL-101(Cr), MIL-101(Fe) and MIL-101(Al).

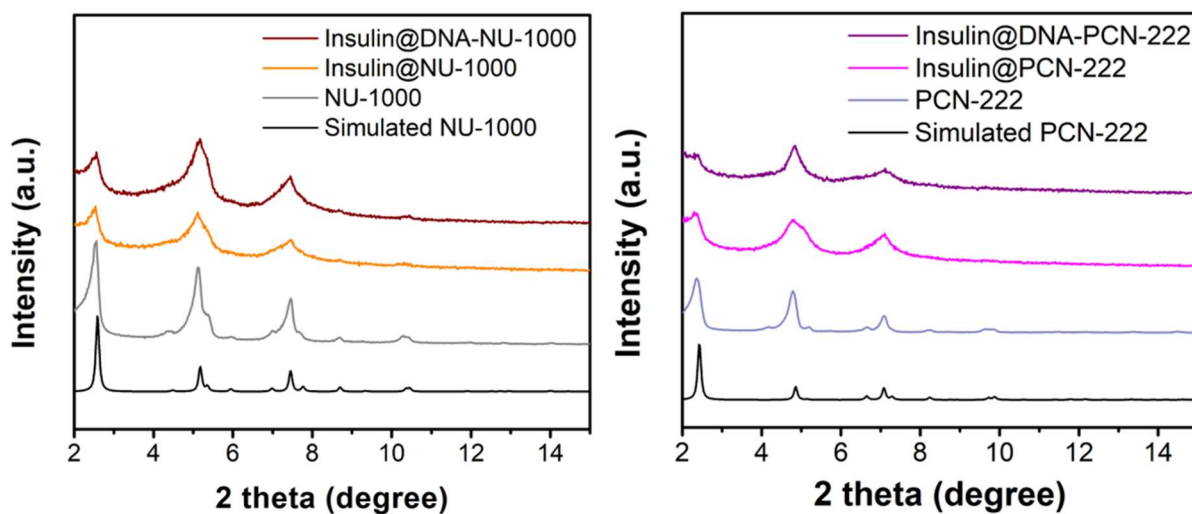


Figure S4.4. PXRD spectra of as-synthesized, insulin encapsulated, and DNA-MOF conjugates for NU-1000 and PCN-222 NPs.

S4.3 Transmission electron microscopy and scanning electron microscopy

MOF nanoparticles were analyzed using a Hitachi HD-2300 scanning transmission electron microscope in either SE or TE modes with an accelerating voltage of 200 kV. Samples were dispersed onto TEM grids by drop-casting a dilute solution containing MOF crystals or MOF-DNA conjugates directly onto TEM grids. The average crystal size for each synthesis was determined by measuring the edge length of more than 100 crystals from multiple syntheses under analogous synthetic conditions.

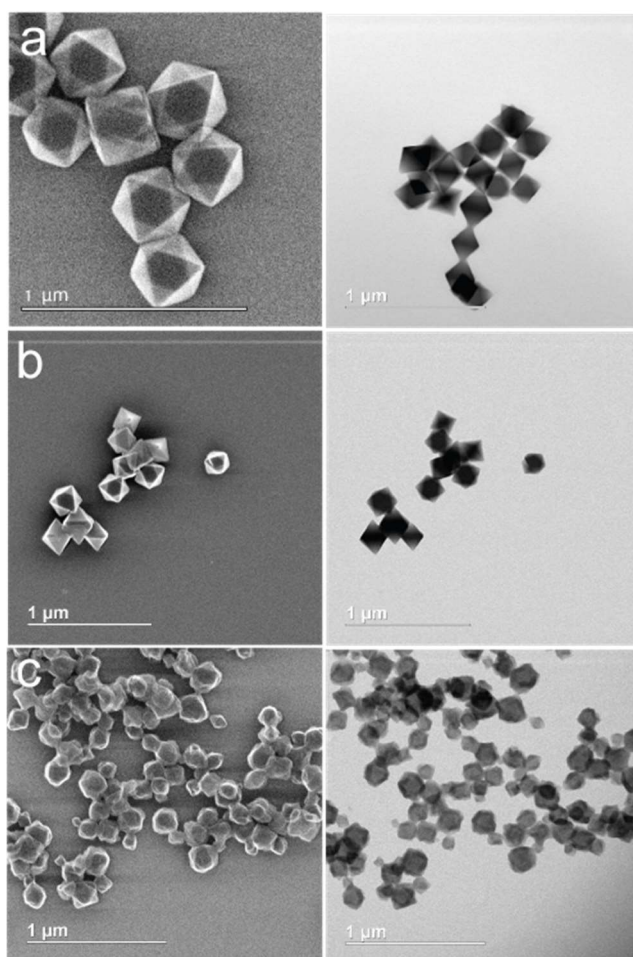


Figure S4.5. SEM and TEM images of (a) UiO-66 (225 ± 35 nm); (b) UiO-67-bpy (173 ± 19 nm); and (c) UiO-68-N₃/PCN-58 (148 ± 39 nm).

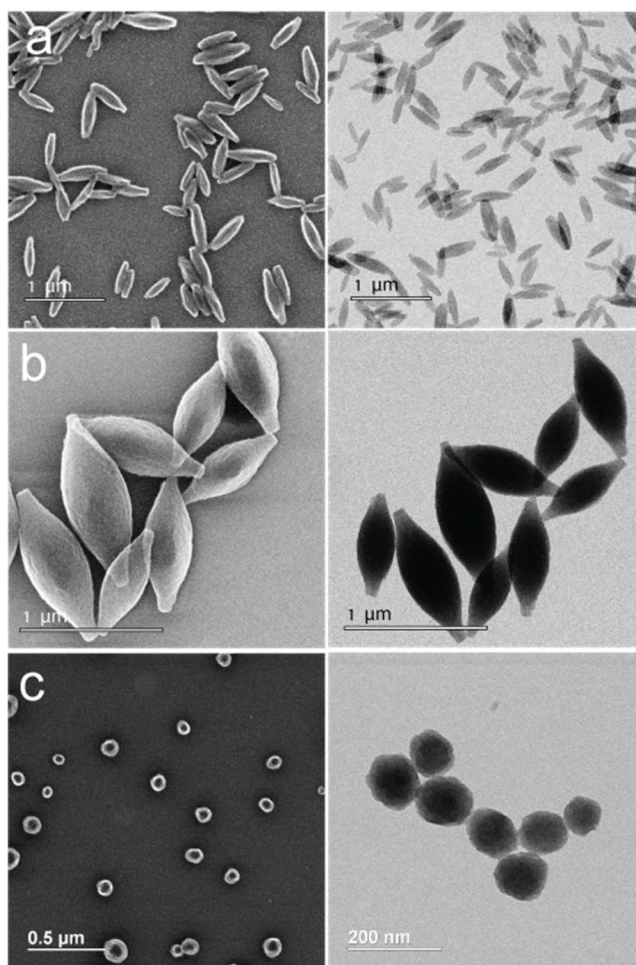


Figure S4.6. SEM and TEM images of (a) PCN-222 (195×48 nm); (b) PCN-223 (538×48 nm); and (c) PCN-224 (110 ± 24 nm).

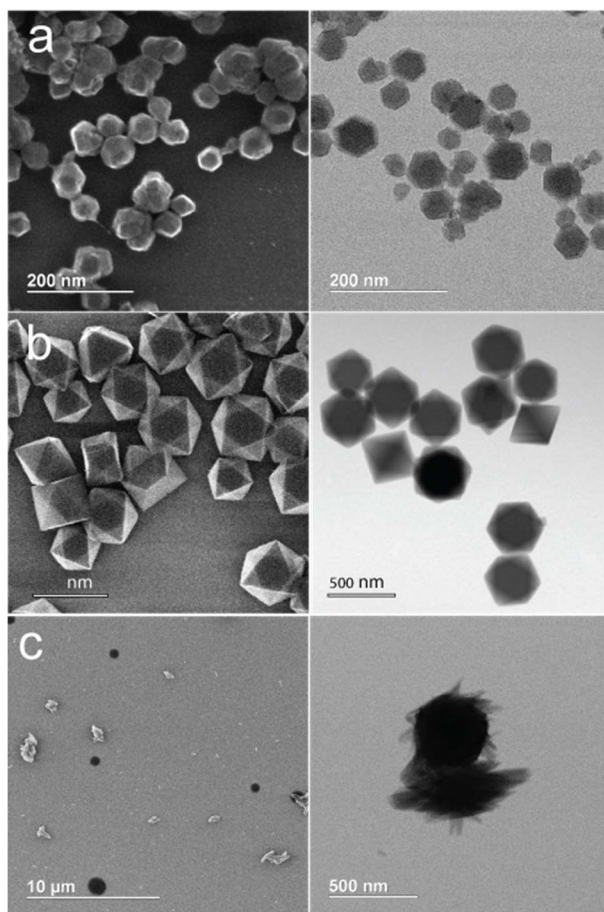


Figure S4.7. SEM and TEM images of (a) MIL-101(Cr) (78 ± 16 nm); (b) MIL-101(Fe) (470 ± 57 nm); and (c) MIL-101(Al) (434 ± 86 nm).

S4.4 Insulin encapsulation

Activated MOF nanoparticles (3 mg) were treated with an insulin solution (in DI water, 0.4 mg/mL) for 1 hour at room temperature to encapsulate insulin. Insulin loading was measured by Inductively coupled plasma-optical emission spectroscopy (ICP-OES) and thermogravimetric analyses (TGA) based on literature reported methods.²²¹ To remove the insulin attached to the surface of MOF NPs, the supernatant was decanted and the solid sample was then washed with DI water for three times to remove the insulin molecules attached to the surface of the crystals.

S4.5. Synthesis of oligonucleotides

Oligonucleotides were synthesized using a Mermaid MM12 DNA synthesizer (Bio Automation) on a standard CPG solid phase support. All oligonucleotides were deprotected under conditions recommended by the manufacturer and purified by reverse phase high performance liquid chromatography (HPLC). Characterization and determination of concentrations were determined by matrix assisted laser desorption ionization (MALDI-TOF) mass spectrometry and UV-Vis spectroscopy, respectively. A complete list of oligonucleotides synthesized can be found in **Table S1**.

Table S4.1. DNA sequences used in this study

Thiolated Strands		
#	Sequence Name	Sequence
1	AuNP-bound assembly strand	5' - HS-(Spacer) ₂ -TTGTTAATATGAGTCGTT - 3'
2	AgNP-bound assembly strand	5' - (DS) ₃ -(Spacer) ₂ -TTGTTAATATGAGTCGTT - 3'
3	AuNP-melt strand	5' - AAGGAA-A-TTCCTTAAATATTCGTCTT - 3'
Terminal Phosphate Strands		
#	Sequence Name	Sequence
4	MOF-bound Strand	5' - Phosphate-(Spacer) ₂ -AACGACTCATATTAACAA - 3'
5	MOF-bound complementary Strand	5' - Phosphate-(Spacer) ₂ -TTGTTAATATGAGTCGTT - 3'
6	MOF-dye loading strand	5' - Phosphate-(Spacer) ₂ -AACGACTCATATTAACAA-Tamra - 3'
7	MOF-dye loading strand #2	5' - Phosphate-(Spacer) ₂ -AACGACTCATATTAACAA-Cy5 - 3'
8	MOF-CPR-T	5' - Phosphate-T - 3'
9	MOF-CPR-T2	5' - Phosphate-TT - 3'
10	MOF-CPR-T20	5' - Phosphate-TTTTTTTTTTTTTTTTTTTT - 3'
11	MOF-melt strand	5' - TTCCTT-A-TTGTTAATATGAGTCGTT - 3'
Strained alkyne Strands		
#	Sequence Name	Sequence
12	AzideNP-bound assembly Strand	5' - DBCO-TEG-(Spacer) ₂ -TTGTTAATATGAGTCGTT - 3'

All modified phosphoramidites are manufactured by Glen Research.

1. “**Spacer**” refers to the 18-O-Dimethoxytritylhexaethyleneglycol,1-[(2-cyanoethyl)-(N,N-diisopropyl)]-phosphoramidite (Spacer phosphoramidite 18).
2. “**DS**” refers to the 3-Dimethoxytrityloxy-2-(3-((R)- α -lipoamido)propanamido)propyl-1-O-(2-cyanoethyl)-(N,N-diisopropyl)-phosphoramidite (Dithiol serinol phosphoramidite).

3. “**HS**” refers to the 1-O-Dimethoxytrityl-hexyl-disulfide, 1'-[(2-cyanoethyl)-(N,N-diisopropyl)]-phosphoramidite (Thiol-modifier C6 S-S).
4. “**5' Phosphate**” refers to [3-(4,4'-Dimethoxytrityloxy)-2,2-dicarboxyethyl]propyl-(2-cyanoethyl)-(N,N-diisopropyl)-phosphoramidite (Chemical phosphorylation reagent II).
5. “**3' Phosphate**” refers to 3-(4,4'-Dimethoxytrityloxy)-2,2-(dicarboxymethylamido)propyl-1-O-succinoyl-long chain alkylamino-CPG (3'-CPR II CPG)
6. “**Tamra**” refers to 1-Dimethoxytrityloxy-3-[O-(N-carboxy-(Tetramethyl-rhodamine)-3-aminopropyl)]-propyl-2-O-succinoyl-long chain alkylamino-CPG (3'-Tamra CPG).
7. “**DBCO-TEG**” refers to 10-(6-oxo-6-(dibenzo[b,f]azacyclooct-4-yn-1-yl)-capramido-N-ethyl)-O-triethyleneglycol-1-[(2-cyanoethyl)-(N,N-diisopropyl)]-phosphoramidite (5'-DBCO-TEG phosphoramidite).

S4.6 DNA functionalization of nanoparticles

MOF nanoparticles

In a typical DNA functionalization experiment, excess phosphate terminated nucleic acid (~ 100 nmol) was added to MOF NP colloids (~2 pmol), and then left on a shaker to incubate overnight (See Supporting Information). Then, sodium chloride was slowly added to the solution to a final concentration of 0.5 M, which reduces electrostatic repulsion between negatively charged neighboring oligonucleotide strands, allowing one to achieve high surface densities of DNA. Excess oligonucleotides were removed by centrifugation (5×5000 rpm, 10 min), followed by resuspension of the DNA-nanoMOF conjugates in water.

Silver and gold nanoparticles

Citrate-capped spherical gold and silver nanoparticles (Ted Pella) were used as received with no further modification. Anisotropic gold nanoparticles were synthesized according to procedures that are detailed extensively elsewhere.^{240 241} DNA-functionalization of AuNPs with thiol-modified oligonucleotides was carried out according to procedures that are detailed extensively elsewhere.²⁴² Briefly, 100 nmol of the AuNP-bound assembly strand (Sequence 1) were treated with a solution of 100 mM dithiothreitol (DTT, pH = 8) for approximately 1 hour and subsequently purified using Nap-5 size exclusion columns (GE Healthcare) to remove remaining DTT. The surfactant Tween-20 was added to the solution of AuNPs to bring the final surfactant concentration to 0.01 vol%, followed by the addition of the purified thiolated DNA (approximately 4-5 nmol per O. D. of AuNPs). A 5M solution of sodium chloride (NaCl) was slowly added to the nanoparticle solution over the next several hours in a “salt aging” process to increase the density of DNA on the particle surface by shielding against electrostatic repulsion between strands. After bringing the final salt concentration to 0.5 M NaCl, the particles were allowed to sit overnight, followed by purification by three rounds of centrifugation (4000 - 15000 rpm; times varied from 10-60 min. depending on the nanoparticle size), removal of supernatant, and resuspension of the nanoparticle pellet in Nanopure water (18.2 M Ω , Millipore) to remove any unreacted DNA, salt, and surfactant. After removal of the supernatant following the final round of centrifugation, salt was added to the purified particles to bring the final concentration once more to 0.2 M NaCl, which is the salt concentration at which all the subsequent assembly reactions took place.

Iron oxide nanoparticles

DNA-functionalization of iron oxide and cadmium selenide nanoparticles via click chemistry was carried out according to procedures that are detailed elsewhere.¹⁸⁶ Briefly, hydrophobic nanoparticles were first phase transferred to the aqueous phase by surface modification with a layer of amphiphilic polymer coating. In a typical polymer coating process, the solution of azide functionalized poly-maleic anhydride-alt-1-octadecene (N₃-PMAO) in chloroform at an initial concentration of polymer monomer units equal to 0.2 M was added into a solution of nanocrystals dissolved in chloroform, at a concentration of ~0.1 μM. The ratio of polymer monomer units per nm² of nanocrystal surface needed to be at least ~100 to achieve full coverage of the particles. Then the mixture was heated to ~50 °C for 2 minutes with gentle shaking. After cooling to room temperature, the solvent was slowly evaporated by rotary evaporation, resulting in a thin film at the bottom of the flask. Sodium borate buffer (75 mM, pH = 9) was added to transfer the nanoparticles into aqueous solution. To remove excess N₃-PMAO, sucrose gradient centrifugation was applied. The purified nanoparticles were then functionalized with excess purified DBCO-DNA (#12, azideNP-bound assembly strand). A 5M solution of sodium chloride (NaCl) was slowly added to the nanoparticle solution over the next several hours in a “salt aging” process to increase the density of DNA on the particle surface by shielding against electrostatic repulsion between strands.

S4.7 Dye loading experiments

In a 5 mL screw vial, Cy5-DNA (sequence 7) functionalized UiO-66 NP was immersed in 50 mM fluorescein solution (1 mL), and it was kept standing at 25 °C for 24 h. The crystal was

collected by centrifugation (10,000 rpm, 40 °C, 5 min) and then washed by water, and this cycle was repeated 10 times.

a. Degradation profile in simulated intracellular matrices

Similar procedure was followed to measure the degradation profiles of DNA-NU-1000 and DNA-PCN-222 in $1 \times$ PBS solution to simulate their degradation in intracellular matrices (pH=7.0, 100 mM NaCl).

S4.8 Nitrogen sorption isotherm measurements

N_2 sorption isotherm measurements were performed on a Micromeritics Tristar II 3020 (Micromeritics, Norcross, GA) at 77K. Between 20 and 30 mg of material was used for each measurement. Surface areas were estimated by applying the Brunauer–Emmett–Teller (BET) equation. T-plot internal and external surface area were determined by Harkins and Jura equation in the second linear regions of N_2 isotherms ($0.26 P/P_0$ to $1.0 P/P_0$).

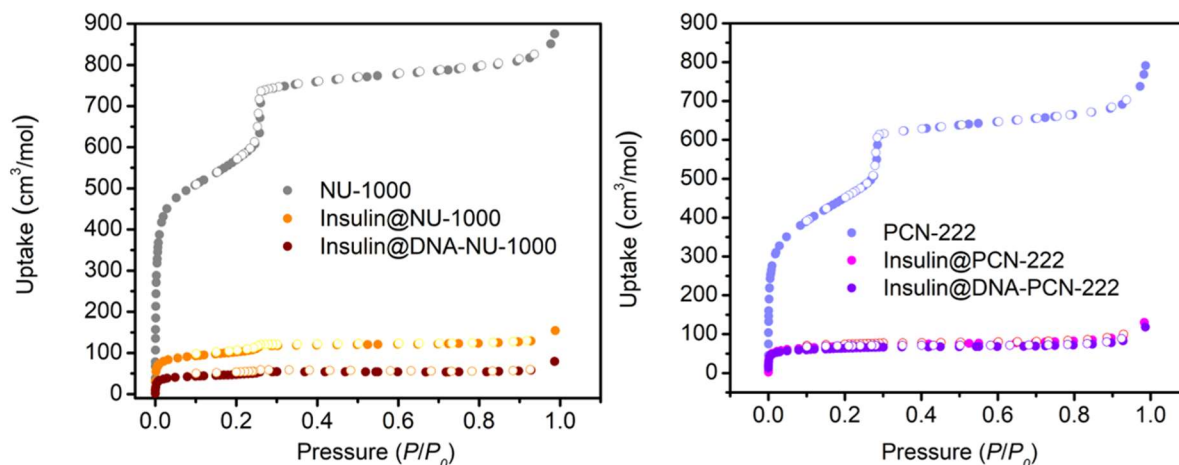


Figure S4.8. N_2 adsorption-desorption isotherms reveal significant surface area reduction after encapsulation of insulin and DNA functionalization.

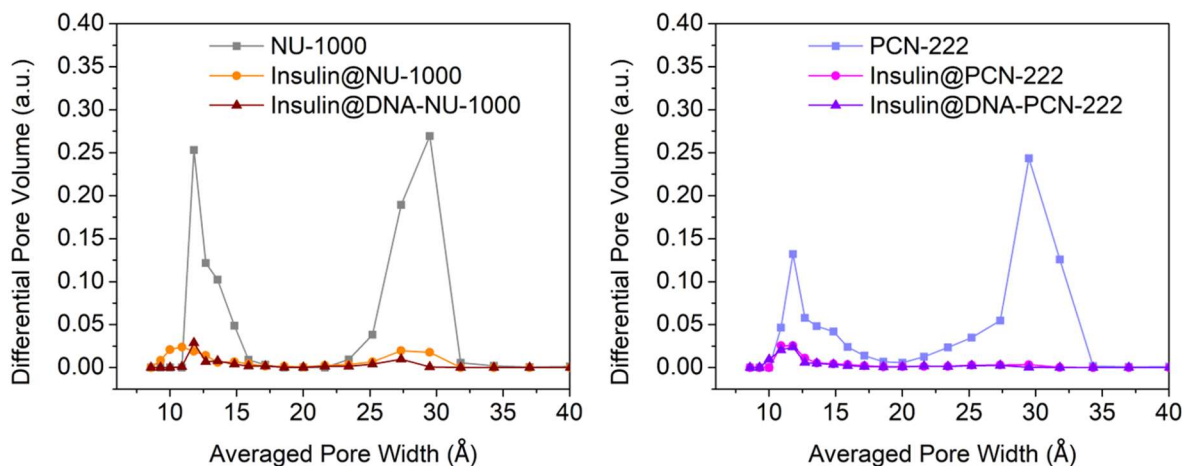


Figure S4.9. DFT pore size distributions of NU-1000 and PCN-222 suggest insulin occupies both the mesopores and micropores.

S4.9 Quantification of DNA surface coverage

S4.10 UV-Vis spectroscopy (UV-Vis)

UV-Vis spectroscopy was performed on a Cary 5000 (Agilent) UV-Vis spectrometer fitted with a temperature stage. 1 cm quartz optical cells were utilized to make measurements. The surface coverages of DNA on the MOF nanoparticle-DNA conjugates were determined by UV-Vis, utilizing a dye labeled DNA sequence #6.

S4.11 Inductively Coupled Plasma-Atomic Emission Spectroscopy (ICP-AES)

We quantified the DNA coverage of each MOF based on their nanoparticle surface area and NP molar concentration. With the radius/edge length of each MOF NP obtained from TEM, the surface area of each nanoparticle was calculated based on geometric approximations: octahedron for UiO-66, UiO-67-bpy, UiO-68-N₃, and MIL-101(Fe); sphere for PCN-224, MIL-101(Cr) and MIL-101(Al); rod for PCN-222; ellipsoid for PCN-223). The molar concentration of each MOF NP sample was obtained by ICP-AES analysis of the metal contents of these MOF

samples in addition to crystallographic information, based on which the number of metal atoms per particle can be calculated for a given size MOF NP. ICP-AES analysis was carried out on a Thermo iCap 7600 ICP-OES instrument with an automated sample changer. MOF samples were dispersed in DMF (1 mL), and 10 μ l of the MOF sample was added to HNO₃ (990 μ l). The samples were heated at 60 °C for 15 h to fully digest the MOF. Unknown samples were prepared with an internal multi-element standard and compared to a standard curve generated.

S4.12. ³¹P{¹H} magic angle spinning solid state nuclear magnetic resonance spectroscopy

³¹P{¹H} Magic Angle Spinning (MAS) NMR spectroscopy was performed on a Varian 400 MHz VNMRS system (512 scans, 5 s recycle time, and 10,000 Hz spin rate) to directly investigate the bonding between the phosphate moiety of DNA and metal clusters.

S4.13 Silica encapsulation of MOF-NP core-satellite nanoclusters

Immobilization of MOF-NP core-satellite nanoclusters from colloidal solution to the solid-state was achieved by silica encapsulation.²²⁶ Briefly, N-trimethoxysilylpropyl-N,N,N-trimethylammonium chloride (TMSPA) (2 μ L, 7.2 μ mol) was added in large excess (relative to the number of DNA phosphate backbone) to the nanoclusters in 1 mL 0.2 M NaCl solution and the mixture was allowed to stir for approximately 30 min before the addition of triethoxysilane (TEOS) (4 μ L, 21.7 μ mol). The suspension was vigorously stirred for 20 min at room temperature, followed by purification to remove excess silica by three rounds of centrifugation and resuspension in water. For TEM, the silica-encapsulated nanoclusters were resuspended in water and drop-cast onto a TEM grid.

S4.14 Cell uptake experiments and cytotoxicity evaluation

a. Cell culture and incubation

Human ovarian cancer cells SK-OV-3(ATCC® HTB-77™) and mice melanoma cells B16-F10 (ATCC® CRL-6475) were incubated in incubators with 5% CO₂ at 37 °C. Medium for these two cell lines are McCoy's 5A medium (ATCC® 30-2007™) and Dulbecco's Modified Eagle's Medium (DMEM) (ATCC® 30-2002™), representatively, containing 10% fetal bovine serum (FBS) and 1% antibiotics. Cells are passed every 2 or 3 days to get the acceptable confluence.

b. Cell imaging by confocal fluorescence microscopy

Confocal fluorescence microscopy was performed on confocal laser microscope (Zeiss LSM 800) system to verify that insulin@DNA-MOF NPs were internalized by the cells. SKOV-3 cells were plated in flourishes with 5×10^4 confluence. Insulin-encapsulated MOFs and free insulin were then incubated with cells (**Table S2**). After 6h, particles in medium were washed out and cells were fixed with 4% formaldehyde. Cell skeleton actin (F-actin) was stained with AlexaFluor 488 Phalloidin (ThermoFisher A12379).

Table S4.2. DNA and insulin concentration for sequences used in this study

#	Description	DNA concentration	Insulin concentration
1	AF647Insulin@ tamra-DNA-NU-1000	100 nM	~ 180 nM
2	AF647Insulin@tamra-DNA-PCN-222	100 nM	~ 140 nM
	Tamra-DNA	100 nM	
3	AF647Insulin		160 nM

c. Cellular Uptake by flow cytometry

LSR-II flow cytometry machine is used to identify the cellular uptake of both oligonucleotide and insulin. Skov-3 cells were first incubated in flow tubes with 5×10^5 concentration. Then insulin@DNA-MOFs, and control (free insulin + free DNA) were then incubated with cells (Table S-2). After 15 min or 2h, particles were washed out and cells were fixed with 4% formaldehyde. Flow data were first gated by SSA and FSA parameter and positive gating in each channel is based on negative controls.

d. MTT assay

Cell viability of SK-OV-3 cells after incubation with different amounts of MOF-AuNP nanoclusters for 24 h was evaluated by MTT assay as well as a cell viability test, which showed that negligible cytotoxicity or anti-proliferative effects on the cells. Briefly, SK-OV-3 cells were seeded in a 96-well cell culture plate in McCoy's 5A medium at a density of 5×10^4 cells/mL with 10% fetal bovine serum (FBS) and 5% CO₂ at 37 °C for 24 h. Afterwards, the culture medium was replaced by 200 μ L of McCoy's 5A medium containing the carbon dots at different doses and cultured for another 8h or 24h. Then, 10 μ L of 5 mg/mL MTT solution was added to each cell well. The cells were further incubated for 4 h, followed by removal of the culture medium with MTT, and then 100 μ L of DMSO was added. The resulting mixture was shaken for 15 min at room temperature. The absorbance of MTT at 492 nm was measured on an automatic ELISA analyzer (SPR-960). Each experiment was conducted by 5 times and the average data were presented.

**CHAPTER FIVE: Hierarchical Colloidal Crystal Engineering with Metal-Organic
Framework Nanoparticles**

Materials in this chapter will appear in a subsequent publication

5.1 Abstract

Colloidal crystal engineering with nucleic acid functionalized nanoparticles is a powerful way for preparing 3D superlattices, which may be useful in many areas, including catalysis, sensing and photonics. To date, the building blocks studied have been primarily based upon metals, metal oxides, chalcogenide semiconductors, and proteins. Here, we show that metal-organic framework nanoparticles (MOF NPs) densely functionalized with oligonucleotides can be programmed to crystallize into a diverse set of superlattices with well-defined crystal symmetries and lattice parameters. In the case of CsCl type structures composed of $Zr_6O_4(OH)_4(BDC)_6$ (UiO-66, BDC = 1,4-benzenedicarboxylate) and Au nanoparticles, well-defined rhombic dodecahedra crystal habits are observed; the observation of the Wulff polyhedron confirms that the MOF system is under thermodynamic control and follows the colloidal crystal engineering rules defined by the complementary contact model. In addition to an almost unlimited new set of particle compositions, MOF NPs provide access to wide variety of shapes, which can be used to influence crystallization. For example, UiO-66 octahedra particles and $Zr_6O_8(H_2O)_8(TCPP-H_2)_2$ (PCN-222, TCPP = tetrakis(4-carboxyphenyl)porphyrin) nanorods, modified with DNA linkers, assemble into a bcc and large 2D lattice, respectively. These new materials and methods provide access to a new set of colloidal crystals that incorporate particles with the well-established designer properties of MOFs and, therefore, significantly increase the scope of possibilities for crystal engineering with DNA.

5.2 Introduction and Background

Colloidal crystal engineering with nanoparticles has emerged as a powerful tool to design materials from the bottom up.²⁴³⁻²⁴⁵ When nanoparticle building blocks are combined with nucleic

acids, they can be assembled in a sequence-specific fashion into crystalline arrangements driven by a combination of DNA complementarity and their unique nanoscale architectural features (e.g. dimensions and anisotropic shapes).^{158, 177, 182-183, 246-248} Early studies focused primarily on particles composed of gold nanoparticle (AuNP) cores, due to the extensive methodology available for synthesizing them in monodisperse form under aqueous conditions; such particles can be modified easily with dense layers of alkylthiol-functionalized DNA.^{15, 240} Later, studies expanded the pool of available particles to a variety of programmable atom equivalents (PAEs), including other metals, metal oxides, chalcogenide semiconductors, polymers, and proteins.^{186, 233, 249-250} A conclusion derived from these studies is that resulting colloidal crystal quality is highly dependent upon PAE monodispersity.²⁵¹⁻²⁵² Indeed, the almost perfectly monodisperse protein particles yield structures with well-defined crystal symmetries, highly tunable lattice parameters, and extremely well-formed crystal habits, all corroborated by electron microscopy and small-angle X-ray scattering (SAXS) measurements.²³³ Metal-organic frameworks (MOFs) are a class of highly modular materials with well-defined 3D architectures, permanent porosity, and diverse chemical functionalities, and they are promising for a wide variety of applications, including gas storage and separations,^{5, 253} drug delivery,¹²⁶ chemical sensing,^{163, 254} and catalysis.⁸ Nanoparticle forms of MOFs have similar properties but are dispersible in solution and therefore could become the basis for building blocks used in colloidal crystal engineering.^{11, 255} However, the polydispersity and poor colloidal stability of MOF NPs thus far limit their potential in this regard and therefore the types of colloidal crystals that can be engineered.²⁵⁶ Herein, we describe a density gradient centrifugation-based method for obtaining monodisperse samples of MOF NPs, employ a new method for chemically modifying them with DNA, and then explore how they can be assembled

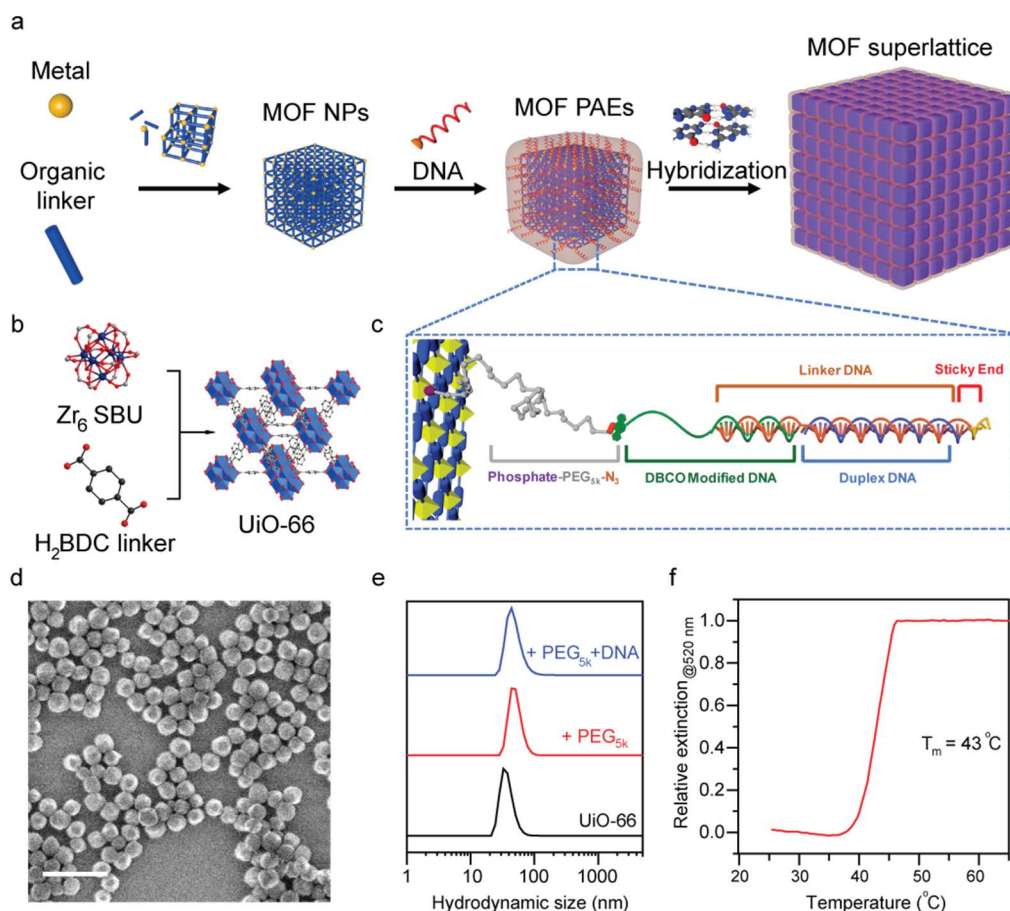


Figure 5.1. Preparation of MOF PAEs as building blocks for colloidal crystal engineering.

a, The synthesis of MOF NP-based PAEs and their DNA-programmed assembly. Metal ions and organic ligands were first combined to synthesize MOF NPs. The MOF NPs were then functionalized with DNA to produce MOF PAEs and subsequently programmed into superlattices via DNA hybridization. **b**, Schematic representation of UiO-66 MOF composed of SBU and terephthalic acid. **c**, Heterobifunctional ligands and DNA strands used to engineer MOF NP superlattices consist of: (i) a phosphate-PEG_{5k}-azide ligand, (ii) a DBCO moiety with an 18 base recognition sequence that binds to a DNA linker, (iii) a linker hybridized with a complementary sequence of desired and programmable length to control interparticle distances, and (iv) a “sticky end” sequence that drives sequence-specific MOF PAE assembly. **d**, SEM image of UiO-66 MOF NPs. Scale bar, 100 nm. **e**, DLS analysis of as-synthesized UiO-66 NPs in water (black), PEG modified UiO-66 NPs (red), and DNA functionalized UiO-66 PAEs in 0.5 M NaCl (blue). **f**, Melting transition of MOF-Au PAE DNA-linked aggregates, monitored as a function of change in extinction at 520 nm via UV-vis spectroscopy.

deliberately into superlattices based upon insight from the complementary contact model.¹⁵⁸

Significantly, the use of MOF PAEs in colloidal crystal engineering allows one to utilize the

unusual shapes that define MOF NPs as a structure-influencing factor.^{11, 67, 69, 257-258} Taken together, these studies provide access to a new set of colloidal crystals that incorporate particles with the designer properties of MOFs and, therefore, may dramatically increase the scope of their utility.

5.3 Results and Discussion

5.31 Synthesis of MOF Programmable Atom Equivalents (MOF PAEs)

As a proof-of-concept, UiO-66 MOF NPs, composed of $Zr_6O_4(OH)_4$ clusters (inorganic secondary building units; SBUs) and terephthalic acid organic ligands (**Fig. 5.1b**), were modified with DNA and studied as PAEs. In a typical experiment, spherical UiO-66 NPs (diameter = 37 ± 8 nm) were synthesized via an acetic acid modulated solvothermal reaction based upon minor modifications of literature methods (see SI).⁶¹ To increase particle monodispersity, a post-synthetic density gradient centrifugation method was employed to remove particles from both the large and small end of the distribution.¹⁸⁶ Specifically, the as-synthesized UiO-66 NPs were washed with *N,N*-dimethylformamide (DMF) and concentrated to ~ 1 μ M. On the basis of NP size, separation was accomplished by loading 300 μ L of a MOF NP colloidal suspension on top of a 10 mL continuous sucrose gradient (10% - 50%) and centrifuged at 20,000 rcf for 40 min. Upon centrifugation, the NP layer travels through the gradient, and particles of different sizes sediment at different rates; the larger particles sediment faster. A thin layer of MOF NPs (~ 1 mL out of 3 mL) was collected with a syringe to recover UiO-66 NPs with increased size uniformity (37 ± 4 nm, **Fig. 5.1d**). The MOF NP sample was purified using a cut-off filter (50 kDa) to remove excess sucrose and then redispersed in DMF for further characterization and surface functionalization.

Unlike the surfaces of conventional inorganic nanoparticles, which are typically capped with organic ligands, a mixture of positively charged metals and negatively charged ligands are

exposed at the surfaces of as-synthesized MOF NPs.⁷⁵ Therefore, DNA surface functionalization, either through ligand post-synthetic modification or SBU coordination, inevitably suffers from competition with DNA itself as a ligand.^{88,93,159} To address this issue, a series of heterobifunctional polyethylene glycol (phosphate-PEG_n-N₃) ligands were used to modify the MOF NP surface prior to DNA functionalization. This approach passivates the MOF surface with respect to unmodified DNA but still allows alkyne-modified DNA to be effectively coupled to the MOF surface (**Fig. 5.1c**).¹¹⁷

To determine the optimal PEG chain length, phosphate-PEG_n-N₃ surface-capping ligands with three different PEG chain lengths (ethylene, PEG₄, and PEG_{5K}) were synthesized and studied. In a typical experiment, the PEG ligands were reacted with MOF NPs in DMF for 2 days at room temperature. ³¹P magic angle spinning solid state nuclear magnetic resonance spectroscopy confirmed that the phosphate is coordinated to the Zr⁴⁺, as evidenced by a characteristic 4.2 ppm up-field shift of the single phosphorous resonance upon surface functionalization (**Fig. S5.12-13**).^{223, 259} Consistent with this conclusion, dynamic light scattering (DLS) showed that UiO-66 NPs increased in average size from 37 ± 8 nm to 48 ± 12 nm (PDI = 0.05) upon surface modification with PEG_{5K} (**Fig. 5.1e**). Importantly, of the three PEG ligands studied, the PEG_{5K} structure was most effective at stabilizing the MOF colloid and making the particles suitable for further functionalization with DNA. Indeed, significant particle aggregation in 0.5 M NaCl solution occurred with the shorter ligands. The PEG_{5K} surface coverage was determined to be ~ 2 molecules/nm², a value obtained by dividing the total number of adsorbates by particle surface area. Particle surface area was determined by using inductively coupled plasma optical emission spectrometry (ICP-OES) to measure total Zr content, which mathematically correlates with total amount of MOF. When combined with an understanding of particle dimensions from transmission

electron microscopy (TEM), surface area can be estimated (see SI). ICP-OES is also then used to determine the total number of adsorbates by measuring the P content of the colloid (there is a one to one correlation between P atoms and ligands).

To prepare the PAEs, the azide-terminated MOF NPs were reacted with terminal alkyne-modified DNA (5' DBCO-TEG modifier) using the strain-promoted azide-alkyne cycloaddition reaction.²⁶⁰ Consistent with DNA modification, the hydrodynamic size of the NPs increased from 48 ± 12 nm to 62 ± 17 nm post-DNA functionalization (**Fig. 5.1e**). Dye-labeled DNA and UV-vis spectroscopy were used to determine DNA surface coverage (650 strands/particle or ~ 25 pmol/cm²); the ligand density is comparable to gold based PAEs ($\sim 20 - 40$ pmol/cm²) and high enough to support cooperativity.¹⁸⁶ Indeed, these MOF PAEs form multivalent, sequence-specific interactions with AuNPs bearing complementary oligonucleotides and generate periodic aggregates that exhibit a characteristic sharp melting transition at 42.6 °C (**Fig. 5.1f**). Finally, the internal pores of the MOF NPs were still accessible post-DNA-modification; no appreciable porosity reduction was observed in the N₂ adsorption isotherms (Supplementary **Fig. S5.10-11**).

5.32 Colloidal Crystal Engineering with MOF PAEs

Once the PAEs were characterized, they were studied in the context of colloidal crystal engineering with DNA. We first synthesized face-centered cubic (fcc, $Fm\bar{3}m$) and body-centered cubic (bcc, $Im\bar{3}m$) colloidal crystals using 37 nm spherical UiO-66 NPs (**Fig. 5.2a-b**). Consistent with the complementary contact model,¹⁵⁸ fcc structures form when the MOF NPs present self-complementary DNA sticky ends (5'-GCGC), and bcc structures form when two sets of MOF NPs (of the same size) have complementary DNA sticky ends (5'-AAGGAA, 5'-TTCCTT, Supplementary Table S2). In a typical experiment, a sample was initially assembled into a

disordered state at room temperature, and then transformed into a crystalline lattice by thermally melting it followed by slow cooling to room temperature at a rate of 0.1 °C/10 min. SAXS

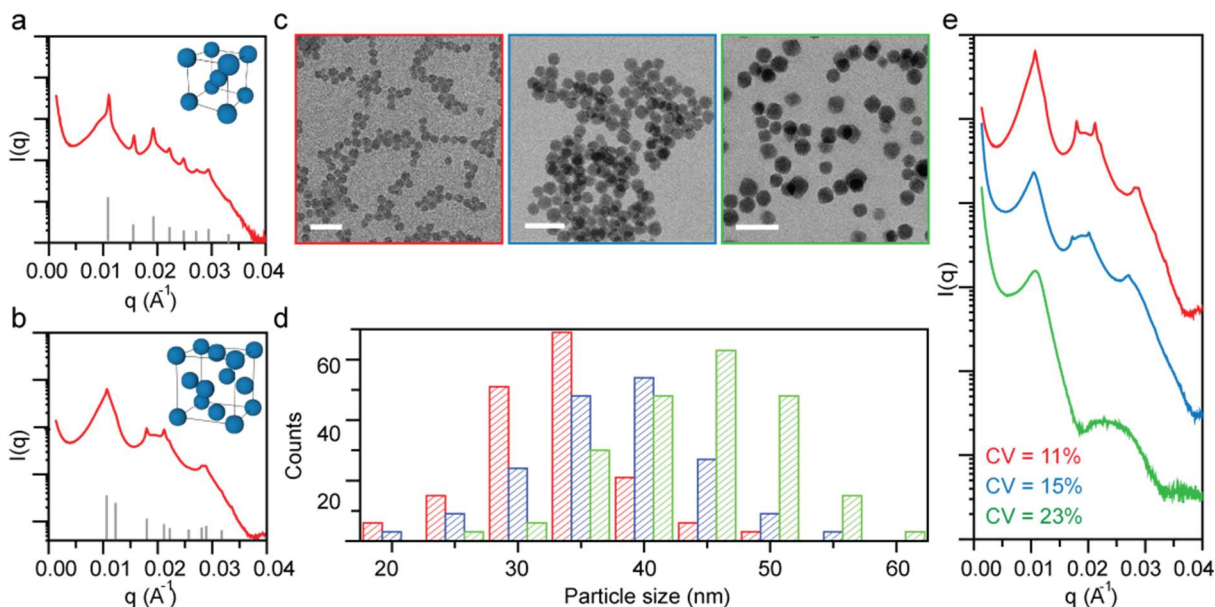


Figure 5.2. Characterization of colloidal superlattices assembled from UiO-66 MOF PAEs. **a,b**, Radially averaged 1D SAXS patterns of MOF UiO-66 PAEs in bcc (**a**) and fcc (**b**) arrangements. Experimental data are shown in red, and predicted scattering patterns are shown in grey. **c,d,e**, Representative TEM images (**c**), size-distribution histograms (**d**), and SAXS data (**e**) of UiO-66 NPs of different uniformity prepared by sucrose-gradient ultracentrifugation: red, 34 ± 4 nm (CV = 11%); blue, 39 ± 6 nm (CV = 15%); green, 47 ± 11 nm (CV = 23%). Scale bars, 100 nm.

experiments verify lattice assignments, and the diffraction peaks suggest the formation of superlattices with micrometer-sized crystalline domains.

Since colloidal crystallization processes are dependent upon nanoparticle size dispersity, the crystallinity of the resulting structures should positively correlate with MOF PAE uniformity. To test this hypothesis, three MOF NP samples with increasingly broad size distributions were isolated by the gradient centrifugation method (coefficient of variation (CV) = 11%, 15%, and 23%, respectively), chemically converted into PAEs, and subsequently assembled into fcc type crystals (**Fig. 5.2c-e**). As shown by SAXS, a clear transition from a disordered state (Fig. 2e, green trace) to a well-formed fcc lattice (Fig. 2e, red trace) was observed as MOF PAEs with greater

monodispersity were assembled (**Fig. 5.2e**). An amorphous material was obtained for the CV = 23% PAEs (**Fig. 5.2e**, green trace), since the polydisperse building blocks result in more defects, grain boundaries, and lattice strain, all of which inhibit crystallization.

5.33 Binary Superlattices Prepared by MOF and Au PAEs

We next explored the formation of binary superlattices composed of MOF gold nanoparticle PAEs. Based upon previously established design rules,¹⁵⁸ complementary DNA functionalized PAEs composed of different core nanoparticles were expected to assemble into CsCl-type ($Pm\bar{3}m$) lattices. However, in this system, scattering patterns solely dependent on the arrangement of AuNPs are observed since the cross-section of MOFs is negligible when compared to that of the AuNPs.²³³ Indeed, when 37 nm MOF PAEs were combined in a 1:1 ratio with complementary 20 nm Au PAEs, the resulting CsCl-type lattices (lattice constant = 79.6 nm) produced simple cubic (sc, $Pm\bar{3}m$) scattering patterns (**Fig. 5.3a**), a result analogous to what is observed when a hollow particle and a AuNP are co-crystallized with complementary DNA sequences.²⁶¹ At this size ratio, the MOF-gold colloidal crystals also have AlB_2 -type impurities (sh, $P6/mmm$: lattice constant, $a = b = 76.5$ nm, $c = 47.6$ nm), which in the SAXS measurements produce simple hexagonal scattering patterns (i.e., only the gold particles are observed, Fig. 3a). When the size ratio approaches one, for example in the case of 37 nm MOF PAEs combined in a 1:1 ratio with complementary 40 nm Au PAEs, the resulting CsCl-type lattices (lattice constant = 88.2 nm) only exhibit sc scattering patterns **Fig. 5.3b**). Importantly, the DNA-mediated crystallization process can be monitored *in situ* via SAXS. Indeed, when disordered MOF-Au aggregates are placed in the path of the X-ray beam and gradually heated to 41 °C (slightly below their melting temperature), one could follow by SAXS the formation of a crystalline lattice (**Fig. 5.3c**).

The structure and morphology of the crystals were next characterized by scanning transmission electron microscopy (STEM). To obtain samples suitable for electron microscopy imaging, the solution-grown binary MOF–Au superlattices (37 nm UiO-66 NPs assembled with 40 nm AuNPs) were first embedded in silica and then dried under vacuum, a technique that has proven extremely useful for crystals formed from metal and semiconductor nanoparticle

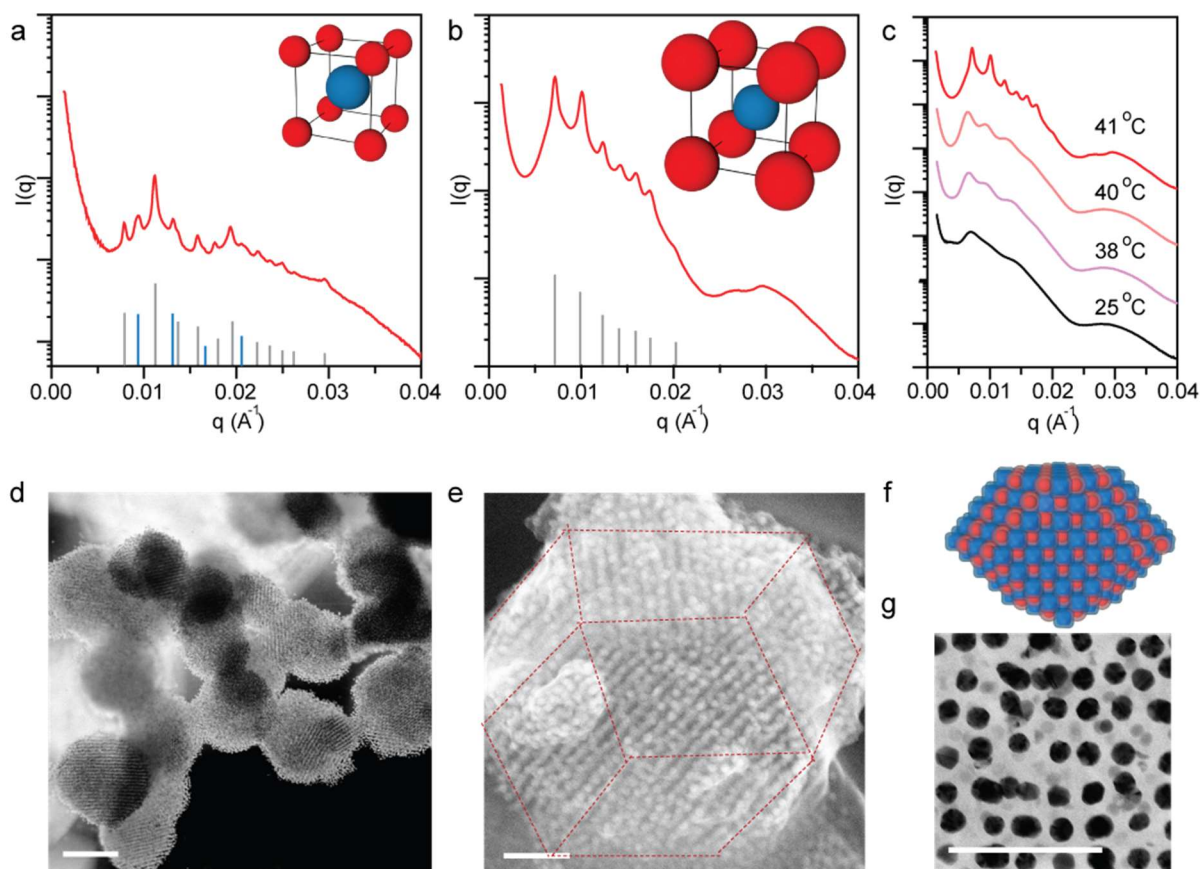


Figure 5.3. Binary superlattices assembled from combination of MOF and Au PAEs. **a,b**, SAXS data for CsCl lattices formed from **(a)** 37 nm UiO-66 NPs and 20 nm AuNPs (1:1 ratio) and **(b)** 37 nm UiO-66 NPs and 40 nm AuNPs (1:1 ratio). Experimental data are shown in red, and simulated scattering patterns are shown in grey (AB₂ impurity phase is shown in blue). **c**, *in situ* SAXS monitoring the thermally induced transition of MOF-Au PAE aggregates from the amorphous to crystalline state. **d,e,g**, STEM characterization of a single crystal superlattice: **(d)** low magnification high angle annular dark field image, **(e)** high magnification secondary electron image, and **(g)** high magnification transmission electron image of UiO-66 NP and 40 nm AuNP hybrid superlattices showing the formation of the rhombic dodecahedra crystal habits **(f)**. Scale bars, 1 μm for **(d)** and 100 nm for **(e)** and **(g)**.

systems.²²⁶ Remarkably, the MOF-Au superlattices form structures with rhombic dodecahedra crystal habits (1 - 2 μm in edge length) in high yield (**Fig. 5.3d-f**). The rhombic dodecahedron is the Wulff polyhedron for a bcc lattice, thereby confirming that the crystallization process is under thermodynamic control.²⁶² High-magnification cross section images of a single crystal reveal ordered domains with stacks of individual NPs clearly discernible (**Fig. 5.2g**, dark: AuNP, light: UiO-66 NP).

5.34 MOF NP Shape as a Superlattice Structure Influencing Factor

Having shown that DNA and the design rules afforded by the complementary contact model can be used to engineer MOF PAE colloidal crystals, we next explored if MOF NP shape can be used to access more exotic crystalline states. Octahedra and nanorods were studied as two representative structures. By combining Zr^{4+} ions with bidentate terephthalic acid or tetravalent porphyrinic acid ligands, UiO-66 octahedra nanoparticles ($Fm\bar{3}m$, edge length = 86 ± 10 nm, **Fig. 4a**) and PCN-222 nanorods ($P6/mmm$, 38 ± 8 nm \times 159 ± 25 nm, aspect ratio = 4.3, **Fig. 5.4f**) were synthesized, respectively.²²⁰ Upon functionalization with DNA, they were assembled with DNA linkers, annealed, and slowly cooled to room temperature.

Cryogenic transmission electron microscopy (Cryo-TEM) images show that the UiO-66 octahedra with self-complementary GCGC sticky ends crystallize into bcc lattices (**Fig. 5.4b-d**, lattice constant = 180 nm) as opposed to the fcc lattices that form from spheres.²⁶³ This occurs because in the bcc configuration the system can maximize DNA bonding interactions between neighboring octahedral particles where the facets are aligned in a parallel planar fashion (**Fig. 5.4e**).²⁶³ This effect is due to the anisotropic shape of the PAEs and is expected to become less important as the oligonucleotide length increases and the PAEs begin to behave more like spherical

entities.²⁶⁴ We tested this conclusion by investigating the effect of the DNA linker length on crystallization (by changing duplex DNA linker length, **Fig. 5.1c** and Table S2). When the particles were allowed to assemble by maintaining the temperature of the solution below the DNA melting temperature, intermediate length DNA linkers (two block segments, ~ 60 nm interparticle spacing) resulted in the formation of high-quality bcc crystalline structures (**Fig. 5.4c-d**). When short DNA linkers were used (one block segment, less than 40 nm interparticle spacing), structures with small bcc crystalline domains were observed due to large lattice strain (Supplementary **Fig. S5.16**). The use of long DNA linkers (three block segments, greater than 80 nm interparticle spacing) reduces particle shape anisotropy as well as lattice strain and produces fcc lattices with randomly oriented octahedra. Such observation is in agreement with previous studies on DNA-mediated assembly of gold octahedral particles and reinforces the notion of zones of crystallization and anisotropy related to the relative dimensions of the particle building blocks and DNA bonding elements.²⁴⁶

In contrast, PCN-222 nanorods crystallize into two-dimensional superlattices with hexagonal or tetragonal symmetries, depending on the type of DNA linker strands used (**Fig. 5.4f-j**). In the first case, 2D close-packed hexagonal lattices were obtained when self-complementary DNA linkers (GCGC sticky ends) were used, again a consequence of the anisotropic PAE shape. In the second case, tetragonal lattices form when two batches of PCN-222 nanorods, each modified with complementary DNA (5'-AAGGAA, 5'-TTCCTT), are combined and annealed as described above. The tetragonal lattice maximizes DNA hybridization between the complementary rod PAE pairs while reducing repulsion between the PAEs with identical sticky ends.²⁶⁴⁻²⁶⁵ In addition to demonstrating the utility and versatility of MOF NPs in colloidal crystal engineering with DNA, these 2D architectures are potentially useful as highly tunable separation membranes, since all of the 1D MOF channels are aligned in a parallel configuration, and the packing density of the

nanorods that comprise them can be modulated from 15 to 50%, simply by varying the length of the DNA linker strands.

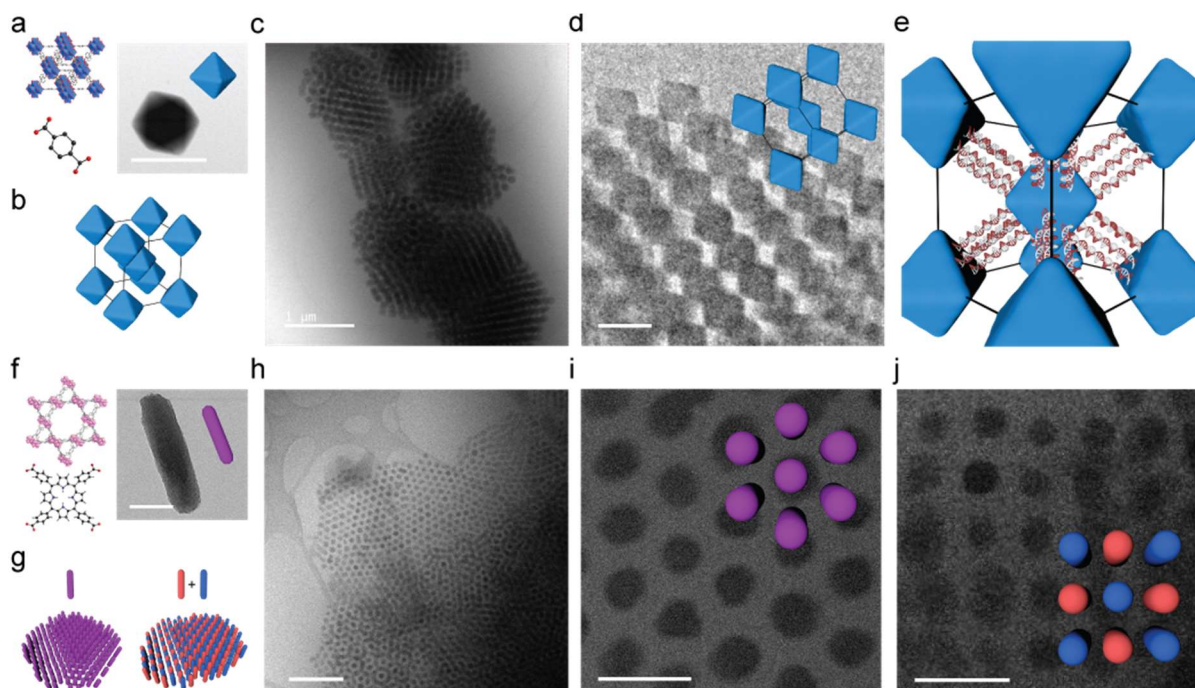


Figure 5.4 | Shape-dependent MOF superlattice assembly. **a**, Representation of the crystal structure of UiO-66 formed by the connection of Zr_6 SBU and terephthalic acid (bottom left). TEM image of a single octahedral UiO-66 NP (right). **b-c**, A model of a bcc lattice formed with face-to-face oriented UiO-66 PAEs, as such arrangement maximizes DNA hybridization interactions. **d-e**, Cryo-TEM images show octahedral shaped UiO-66 PAEs with self-complementary DNA linkers assemble into bcc lattices. **f**, Representation of the crystal structure of PCN-222 formed by the connection of Zr_6 SBU and tetrakis(4-carboxyphenyl)porphyrin linkers (bottom left). TEM image of a single PCN-222 nanorod (right). **g**, Schematic representation of PCN-222 PAEs assembled into two different lattices depending on DNA link design: self-complementary DNA linkers (left, 2D hexagonal superlattice), and complementary DNA linkers (right, 2D tetragonal superlattice). **h-i**, Cryo-TEM images show PCN-222 PAEs with self-complementary DNA linkers close-pack into 2D simple hexagonal lattices. **j**, Cryo-TEM image shows PCN-222 PAEs interconnected by complementary DNA linkers form a 2D tetragonal lattice. Scale bars, 100 nm for (**a,d,e,i,j**) and 500 nm for (**c,h**).

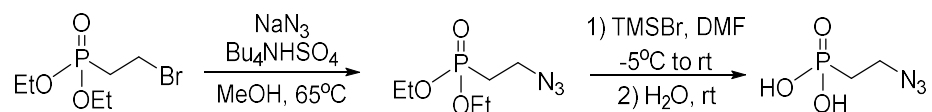
5.4 Conclusions

In summary, we have reported a general method for the preparation of PAEs from MOF NPs and DNA. We have shown that such building blocks provide access to a diverse set of

colloidal crystals spanning numerous crystal symmetries with tunable lattice parameters. Importantly, we have shown that the complex crystal shapes afforded by MOF NPs allows one to control DNA bond directionality and facet-facet interactions. When combined with all that is known about MOF NP shape control, these experiments suggest that in addition MOF NPs being a new compositionally diverse set of building blocks with which colloidal crystal properties can be tuned, particle shape-induced bonding interactions with MOF PAEs will be extremely useful for engineering crystal outcomes.²⁶⁴

5.5 Experimental Methods and Supplementary Materials

S5.1 Synthesis of Phosphate-ethylene-N₃



Synthesis of diethyl 2-azidoethylphosphonate

Diethyl 2-bromoethylphosphonate (250 mg, 1.0 mmol) was reacted with sodium azide (260 mg, 4.0 mmol) and tetrabutylammonium hydrogensulfate (510 mg, 1.5 mmol) in 4 mL methanol (MeOH) at 65 °C for 18 h. After cooling to room temperature, the solvent was evaporated and diluted with diethyl ether, and filtered through Celite. The filtrate was washed with water, and the organic layer was dried over sodium sulfate to yield diethyl 2-azidoethylphosphonate (90%).

Synthesis of 2-azidoethylphosphonic acid

In 0.8 mL *N,N*-dimethylformamide (DMF), diethyl 2-azidoethylphosphonate (120 mg, 0.57 mmol) was reacted with 4 equivalents of bromotrimethylsilane (350 mg, 2.3 mmol) at -5 °C. After warming to room temperature, the product was filtered and washed with water and dried to yield 2-azidoethylphosphonic acid (80%).

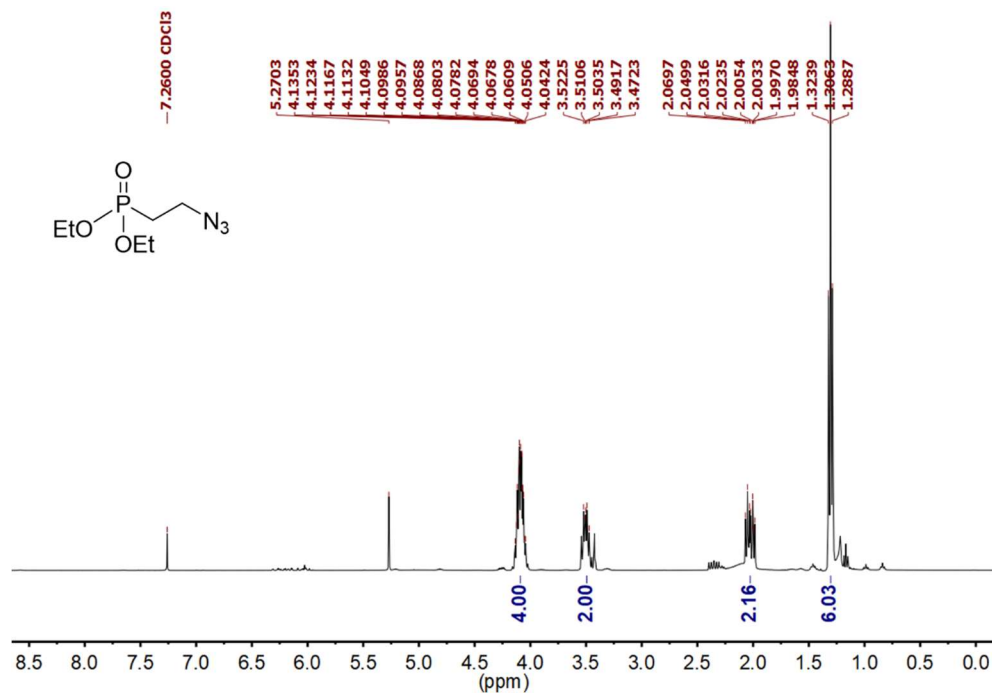


Figure S5.1. ^1H NMR spectrum of diethyl 2-azidoethylphosphonate. The trace amount of impurities was carried to the next step without further purification, which disappeared post hydrolysis.

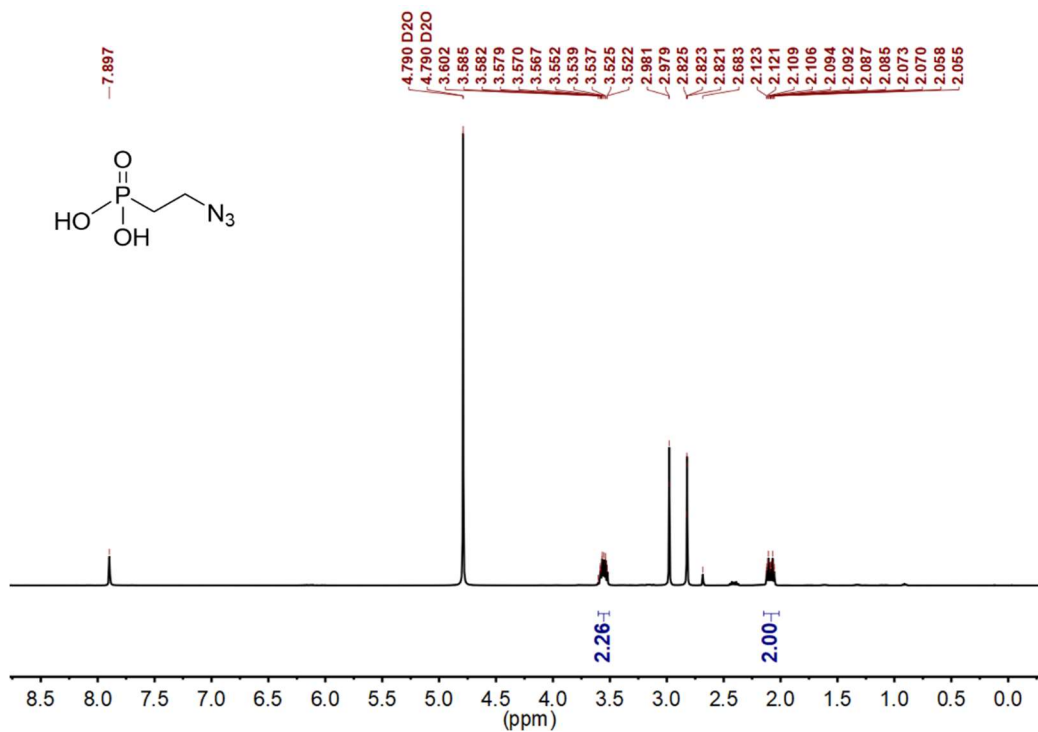
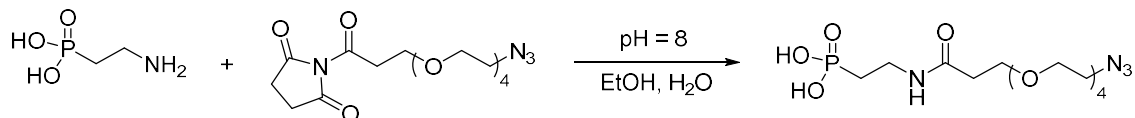


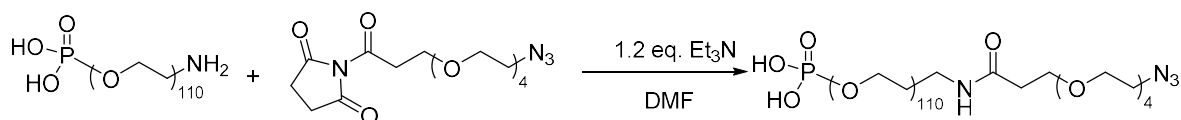
Figure S5.2. ^1H NMR spectrum of 2-azidoethylphosphonic acid.

S5.2 Synthesis of Phosphate-PEG₄-N₃



The pH of a 5 mL aqueous solution of 2-aminoethylphosphonic acid (12.5 mg, 0.10 mmol) was adjusted to 8 with 1 M sodium hydroxide, and 15-Azido-4,7,10,13-tetraoxapentadecanoic acid succinimidyl ester (azido-PEG₄-NHS ester from Click Chemistry Tools, 77.6 mg, 0.2 mmol) dissolved in 5 mL of DMF was added. The reaction mixture was stirred at 4 °C for 4 h and incubated overnight at room temperature. After the reaction, the solvent was removed by lyophilization, and the product was used as a mixture to functionalize MOF nanoparticles (NPs) without further purification. In our study, approximately 80% 2-aminoethylphosphonic acid was converted to phosphate-PEG₄-N₃.

S2.3 Synthesis of Phosphate-PEG₁₁₀-N₃



In a 25 mL glass vial, phosphate-PEG_{5k}-NH₂ (200 mg, 40 μmol) and azido-PEG₄-NHS ester (120 mg, 320 μmol) were dissolved in 10 mL dry DMF, and triethyl amine (12 mg, 120 μmol) was added to the solution. The mixture was stirred at room temperature overnight. DMF was removed by lyophilization to yield a yellow gel. The yellow gel was dissolved in water and passed through a 3 kDa cut-off centrifuge filter three times (3,000 rpm, 20 min) to remove excess azido-PEG₄-NHS. The product was lyophilized to yield a light yellow solid (~50%).

S3. Synthesis and characterization of MOF NPs

S3.1 Synthesis of MOF NPs

Synthesis of spherical UiO-66 [Zr₆O₄(OH)₄(BDC)₁₂]

Spherical UiO-66 NPs (37 ± 8 nm) were synthesized via an acetic acid modulated solvothermal reaction.¹⁵⁹ 1,4-benzenedicarboxylic acid (25 mg, 0.25 mmol) was dissolved in 0.5 mL of DMF. In a separate vial, zirconyl chloride octahydrate (21 mg, 66 μ mol) was dissolved in 3 mL of DMF. The two solutions were mixed together in a 10 mL scintillation vial, and 0.5 mL acetic acid was added to the reaction mixture. After brief sonication, the solution was heated at 90 °C in an oven for 6 h to yield uniform UiO-66 NPs. The NPs were collected by centrifugation (12000 rpm, 30 min), followed by solvent exchange with DMF, and stored in anhydrous DMF.

Synthesis of octahedral UiO-66 [Zr₆O₄(OH)₄(BDC)₁₂]

Octahedral UiO-66 NPs (86 ± 10 nm) were synthesized via an acetic acid modulated solvothermal reaction.¹⁵⁹ 1,4-benzenedicarboxylic acid (10 mg, 60 μ mol) was dissolved in 0.2 mL of DMF. In a separate vial, zirconyl chloride octahydrate (21 mg, 66 μ mol) was dissolved in 3 mL of DMF. The two solutions were combined in a 10 mL scintillation vial, and 0.5 mL acetic acid was added to the reaction mixture. After brief sonication, the solution was heated at 90 °C in an oven for 5 h to yield uniform UiO-66 NPs. The NPs were collected by centrifugation (10000 rpm, 20 min), followed by solvent exchange with DMF, and stored in anhydrous DMF.

Synthesis of PCN-222/MOF-545 [Zr₆O₈(H₂O)₈(TCPP-H₂)₂]

The synthesis of PCN-222/MOF-545 nanorods ($38 \pm 8 \times 159 \pm 25$ nm, aspect ratio = 4.3) was based on a literature reported method with minor modifications.⁷¹ Zirconyl chloride octahydrate (38 mg, 0.12 mmol) and tetrakis(4-carboxyphenyl)-porphyrin (6.5 mg, 0.0082 mmol)

were dissolved in DMF (16 mL) in a 22 mL borosilicate vial with a Teflon-lined cap. Dichloroacetic acid (0.30 mL, 3.0 mmol) was added, and the resulting solution was heated at 130 °C in an oven for 18 h to afford dark purple rod-shaped NPs and a yellow mother liquor. The NPs were collected by centrifugation (12000 rpm, 30 min), followed by solvent exchange with DMF, and stored in anhydrous DMF.

S3.2 Powder X-ray diffraction (PXRD)

The crystallinity of the synthesized MOF NPs and MOF programmable atom equivalents (PAEs) were confirmed by PXRD. PXRD patterns were recorded on Rigaku Smartlab instrument using Nickel-filtered Cu-K α radiation ($\lambda = 1.5418 \text{ \AA}$) with an accelerating voltage and current of 45 kV and 160 mA, respectively.

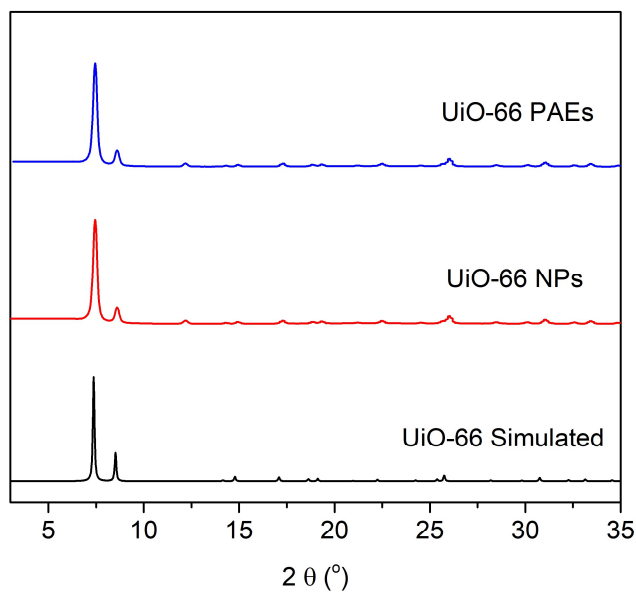


Figure S5.4. Simulated PXRD pattern of UiO-66 (black) and patterns of UiO-66 NPs before (red) and after DNA functionalization (blue).

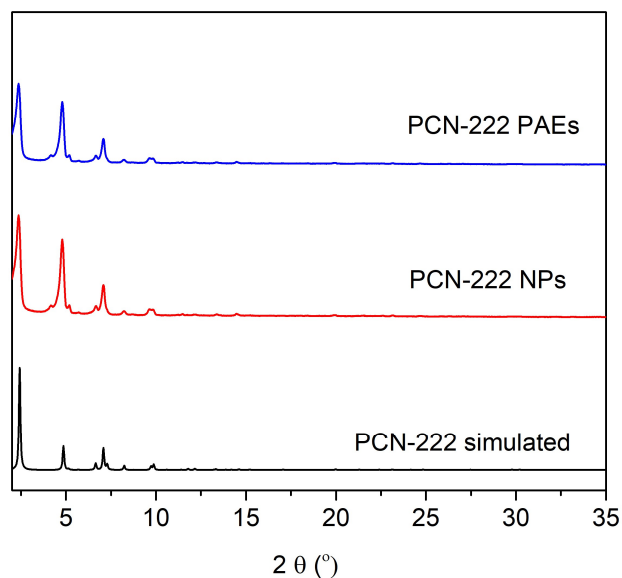


Figure S5.5. Simulated PXRD pattern of PCN-222 (black) and patterns of PCN-222 nanorods before (red) and after DNA functionalization (blue).

S3.3 Transmission electron microscopy (TEM) and scanning electron microscopy (SEM)

MOF NPs were analyzed using a Hitachi HD-2300 scanning transmission electron microscope (STEM) in either secondary electrons (SE) or transmitted electron (TE) mode with an accelerating voltage of 200 kV. Samples were dispersed onto TEM grids by drop-casting a dilute ethanol solution containing MOF NPs or MOF PAEs directly onto TEM grids. The average particle size for each synthesis was determined by measuring the edge length of more than 100 particles from multiple syntheses under analogous synthetic conditions.

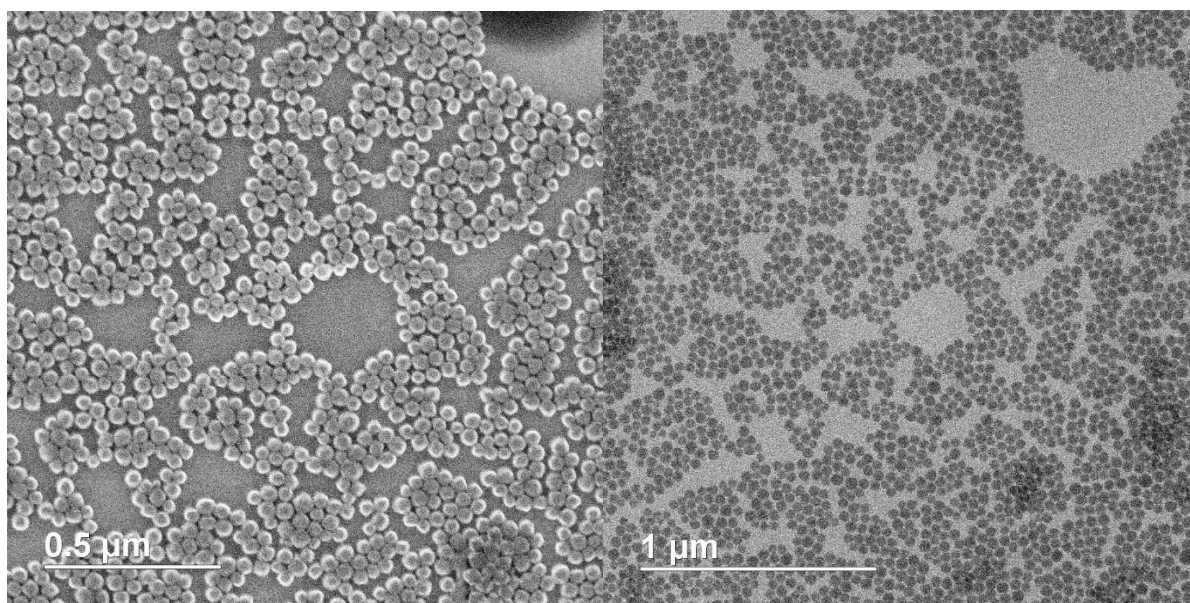


Figure S5.6. SEM (left) and TEM (right) images of spherical UiO-66 NPs (37 ± 4 nm).

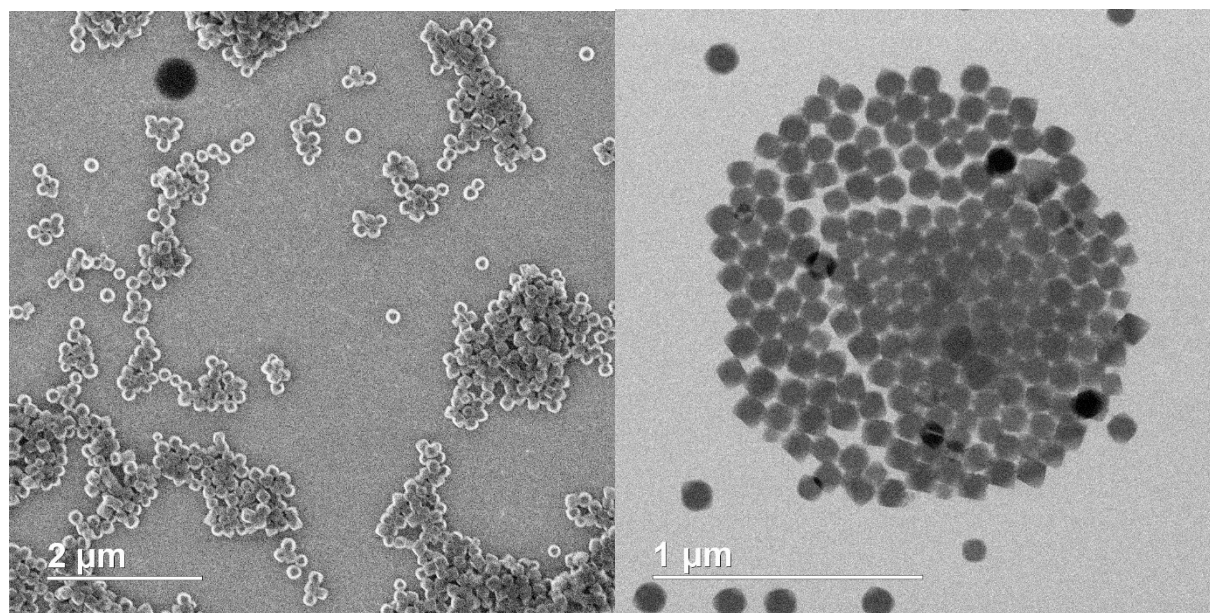


Figure S5.7. SEM (left) and TEM (right) images of octahedral UiO-66 NPs (86 ± 10 nm).

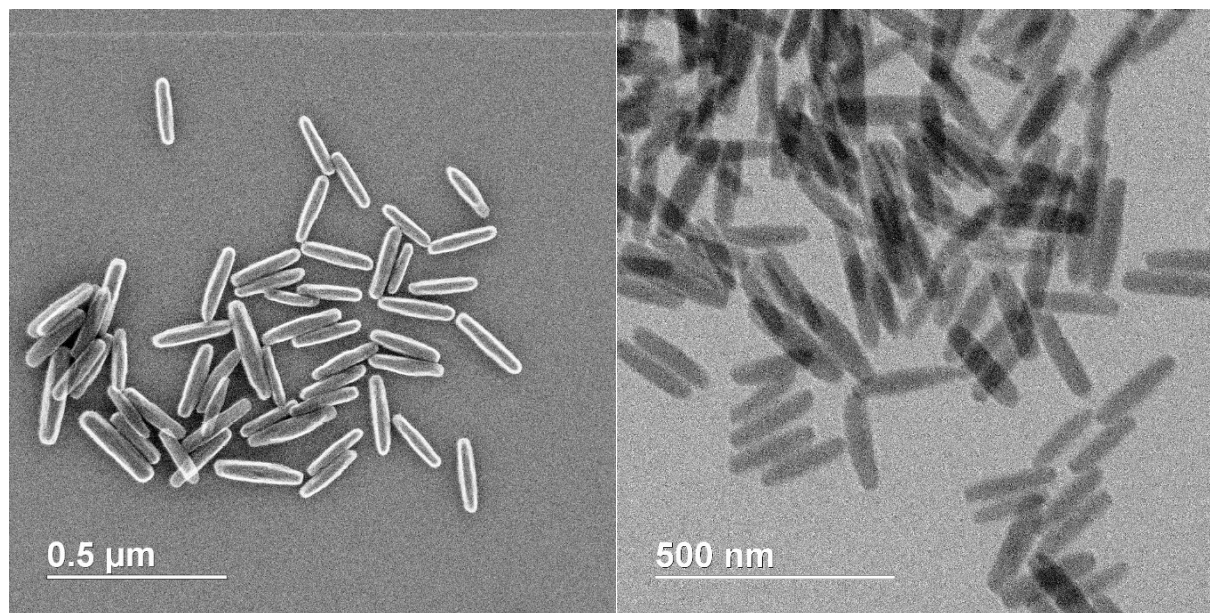


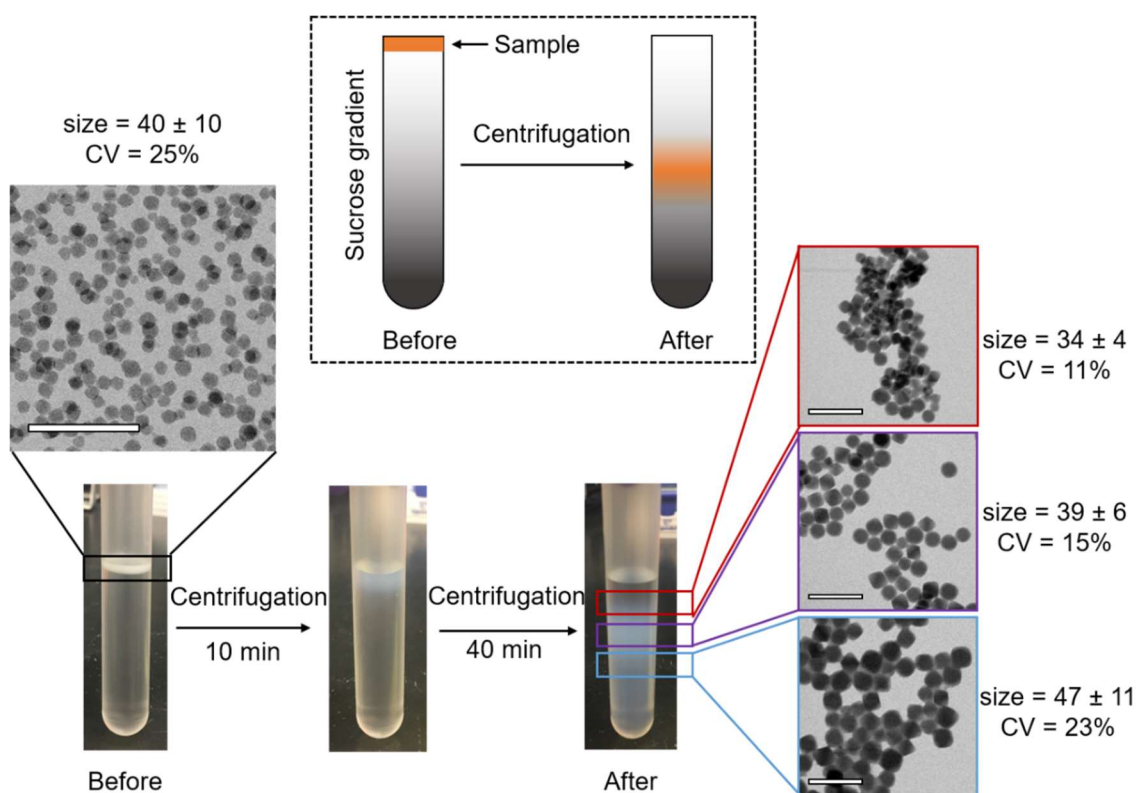
Figure S5.8. SEM (left) and TEM (right) images of PCN-222 nanorods ($37 \pm 8 \times 159 \pm 25$ nm).

S4. Sucrose-gradient ultracentrifugation

To improve the uniformity of MOF NPs, an aqueous solution of UiO-66 NPs was concentrated and centrifuged at 20,000 rcf on a continuous sucrose gradient. The range of gradient density and duration of centrifugation step varies depending on the size and density of the MOF NPs. For instance, to separate 300 μ L of 37 nm UiO-66 NPs, 10 mL of a 10%-50% gradient mixture was used, and 40 min centrifugation resulted in satisfying separation (Table S1). The layer of NPs was recovered from the gradient with a syringe and washed twice through a 50 kDa Amicon centrifugal filter tube in order to clean the sample from sucrose and to dissolve it in desired medium to prepare the samples for characterization and polymer/DNA conjugation.

Table S1. Centrifugation conditions used to improve the uniformity of MOF NPs

MOF NPs	Gradient	Time (min)
UiO-66 (37 nm)	10%-50%	40
UiO-66 (86 nm)	20%-70%	40
PCN-222 (159 nm)	20%-70%	40

**Figure S5.9.** Schematic representation of the sucrose gradient based ultra-centrifugation method for UiO-66 NPs.

S5. Synthesis of oligonucleotides

Oligonucleotides were synthesized using a Mermaid MM12 DNA synthesizer (Bio Automation) on a standard controlled pore glass (CPG) solid phase support. All oligonucleotides were deprotected under conditions recommended by the manufacturer and purified by reverse phase high performance liquid chromatography (HPLC). Characterization and oligonucleotide concentration were determined by MALDI-TOF mass spectrometry and UV-vis spectroscopy, respectively. A complete list of oligonucleotides synthesized can be found in Table S5.2.

Table S5.2. DNA sequences used in this study

	DNA sequence from 5' to 3'
AuNP-bound A	Thiol-(Spacer) ₂ -CATCCATCCTTATCAACT
MOF-bound A	DBCO-TEG-(Spacer) ₂ -CATCCATCCTTATCAACT
MOF-bound B	DBCO-TEG-(Spacer) ₂ -AACGACTCATACTCACCT
Dye labelled strand	DBCO-TEG-(Spacer) ₂ -AACGACTCATACTCACCT-Tamra
Dye labelled linker	Tamra-TTCCTT-A-AGTTGATAAGGATGGATG
Self-comp linker B	CGCG-A-AGGTGAGTATGAGTCGTT
Nonsself-comp linker A	TTCCTT-A-(Spacer d40) _n -AGTTGATAAGGATGGATG
Nonsself-comp linker B	AAGGAA-A-(Spacer d40) _n -AGGTGAGTATGAGTCGTT
Spacer d40	TTTTTTTTTTTT-AGTCACGACGAGTCA-TTTTTTTTTTTT-A
Duplexer d40	AAAAAAAAAAAA-TGACTCGTCGTGACT- AAAAAAAAAAAA

Linker length (Spacer d40): n = 0, 1, 2, 3

All modified phosphoramidites were manufactured by Glen Research.

1. “**Thiol**” refers to the 1-O-Dimethoxytrityl-hexyl-disulfide, 1'-[(2-cyanoethyl)-(N,N-diisopropyl)]-phosphoramidite (Thiol-modifier C6 S-S).

2. “**PEG Spacer**” refers to the 18-O-Dimethoxytritylhexaethyleneglycol,1-[(2-cyanoethyl)-(N,N-diisopropyl)]-phosphoramidite (Spacer phosphoramidite 18).
3. “**DBCO-TEG**” refers to 10-(6-oxo-6-(dibenzo[b,f]azacyclooct-4-yn-1-yl)-capramido-N-ethyl)-O-triethyleneglycol-1-[(2-cyanoethyl)-(N,N-diisopropyl)]-phosphoramidite (5'-DBCO-TEG phosphoramidite).
4. “**Tamra**” refers to 1-Dimethoxytrityloxy-3-[O-(N-carboxy-(Tetramethyl-rhodamine)-3-aminopropyl)]-propyl-2-O-succinoyl-long chain alkylamino-CPG (3'-Tamra CPG).

S6. DNA functionalization of NPs and assembly of colloidal crystals

S6.1 DNA functionalization of MOF NPs

Phosphate-PEG-N₃ linker functionalization

In a 1.5 mL Eppendorf tube, 10 mg phosphate-PEG_{5k}-N₃ linker ($\sim 1 \times 10^{18}$ polymer) was dissolved in 100 μ L DMF (~ 20 mM). In a separate tube, 33 pmol of 37 nm UiO-66 NPs ($\sim 2 \times 10^{13}$ particles) was dispersed in 1 mL DMF and 100 μ L linker solution (10 mg linker) was added. Similarly, 14.1 pmol of PCN-222 nanorods ($\sim 8.5 \times 10^{12}$ particles) were dispersed in 1 mL DMF and 50 μ L linker solution (5 mg linker) was added. The mixture was sonicated and incubated on a thermal shaker at 750 rpm and 25 °C for 48 h. The functionalized NPs were first washed with DMF to remove excess PEG_{5k} ligands (centrifugation: 15,000 rpm, 45 min), and then sequentially washed with a 1:1 DMF/water mixtures, and twice with water. The NP samples were concentrated to ~ 50 nM and stored in DI water.

DNA functionalization

In a typical DNA functionalization experiment, azide modified MOF NPs were dispersed in water and functionalized with DBCO-TEG modified DNA (MOF-Bound DNA). To

functionalize UiO-66 NPs, 300 nmol of DNA was dissolved in 1 mL water (0.3 mM, 1.8×10^{17} DNA), to which 33 pmol of 37 nm UiO-66 NPs (33 nM, $\sim 2 \times 10^{13}$ particles) were added. Similarly, to functionalize 160 nm PCN-222 nanorods, 200 nmol of DNA was dissolved in 1 mL water (0.2 mM, 1.2×10^{17} DNA), to which 2 pmol of PCN-222 nanorods (2 nM, $\sim 1.5 \times 10^{12}$ particles) were added. The DNA and MOF NPs were incubated on a thermal shaker overnight at 25 °C at 750 rpm. Sodium chloride (NaCl) was slowly added to the solution to a final concentration of 0.5 M (over 8 h), which reduces electrostatic repulsion between negatively charged neighboring oligonucleotide strands, allowing one to achieve high surface densities of DNA. The total incubation time should be > 48 h, and gentle sonication should be applied occasionally to prevent aggregation of particles. Excess oligonucleotides were removed by centrifugation ($5 \times 5,000$ rpm, 10 min), followed by resuspension of the MOF PAEs in water.

S6.2 DNA functionalization of gold nanoparticles (AuNPs)

20 nm and 40 nm citrate-capped spherical AuNPs (Ted Pella) were used as received with no further modification. DNA-functionalization of AuNPs with thiol-modified oligonucleotides was carried out according to literature procedures.²⁴² Briefly, 100 nmol of the AuNP-bound assembly strand (Table S2, sequence AuNP-bound A) were treated with a solution of 100 mM dithiothreitol (DTT, pH = 8) for approximately 1 h and subsequently purified using Nap-5 size exclusion columns (GE Healthcare) to remove residuals. The surfactant, sodium dodecyl sulfate (SDS), was added to the solution of AuNPs to bring the final surfactant concentration to 0.02 vol%, followed by the addition of purified thiolated DNA (approximately 4-5 nmol DNA per mL of AuNPs). A 5 M solution of NaCl was slowly added to the NP solution over the next several hours in a “salt aging” process to increase the density of DNA on the particle surface by shielding against electrostatic repulsion between strands. After bringing the final salt concentration to 0.5 M NaCl,

the particles were allowed to sit overnight, followed by three rounds of purification with centrifugation (4,000 – 15,000 rpm; times varied from 10-60 min depending on the NP size), removal of supernatant, and resuspension of the NP pellet in water to remove any unreacted DNA, salt, and surfactant. After removal of the supernatant following the final round of centrifugation, salt was added to the purified particles to bring the final concentration to 0.4 M NaCl, which is the salt concentration at which all subsequent assembly reactions took place.

S6.3 Colloidal crystal assembly experiments

Synthesis of MOF fcc superlattice

In a typical experiment, 2000 equivalents of self-complementary linker were added to 50 nM solutions of DNA functionalized 37 nm UiO-66 NPs in 0.02% SDS and 0.5M NaCl. The addition of self-complementary DNA linkers resulted in the formation of aggregates that settled down within minutes. Samples were heated to a few degrees above their melting temperature (55 °C) and cooled at a rate of 0.01 °C/min to 20 °C using a ProFlex™ PCR system (Applied Biosystems).

Synthesis of MOF-MOF bcc superlattice

In a typical experiment, 1000 equivalents of complementary linker A and 1000 equivalents of complementary linker B were added to 20 nM solutions of DNA functionalized 37 nm UiO-66 NP A and UiO-66 NP B (1:1 ratio) in 0.02% SDS and 0.5 M NaCl, respectively. The mixtures were incubated for 20 min on a thermal shaker to allow linker hybridization, followed by the combination of 50 µL of each solution, which resulted in the formation of aggregates that settled down within minutes. Samples were heated to a few degrees above their melting temperature and cooled at a rate of 0.01 °C/min to 20 °C using a PCR system.

Synthesis of MOF-Au CsCl hybrid superlattice

In a typical experiment, 2000 equivalents of complementary linker A and 1000 equivalents of complementary linker B were added to 10 nM solutions of DNA functionalized 40 nm AuNPs and 37 nm UiO-66 NPs (1:1 ratio) in 0.02% SDS and 0.5 M NaCl, respectively. The mixtures were incubated for 20 min on a thermal shaker to allow for linker hybridization, followed by the combination of 50 μ L of each solution, which resulted in the formation of aggregates that settled down within minutes. Samples were heated to a few degrees above their melting temperature and cooled at a rate of 0.01 $^{\circ}$ C/min to 20 $^{\circ}$ C using a PCR system.

S7. N₂ sorption measurements

N₂ adsorption isotherm measurements were performed on a Micromeritics Tristar II 3020 (Micromeritics, Norcross, GA) at 77K. The sample was transferred to the oven-dried sample tube and heated to 150 $^{\circ}$ C under vacuum. Surface areas were estimated by applying the Brunauer–Emmett–Teller (BET) equation.²⁶⁶ T-plot internal and external surface area were determined by the Harkins and Jura equation in the second linear regions of N₂ isotherms (0.26 P/P_0 to 1.0 P/P_0).²⁶⁷

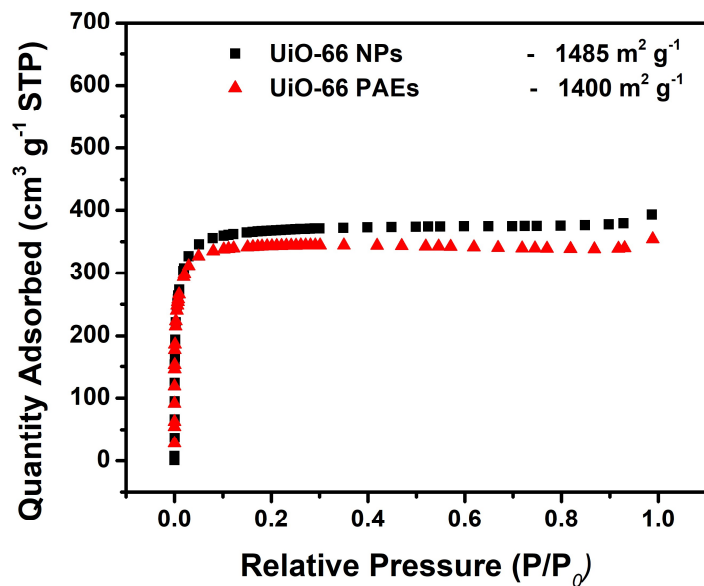


Figure S5.10. N_2 adsorption isotherms of UiO-66 NPs and UiO-66 PAEs reveal no significant reduction in surface area after DNA functionalization.

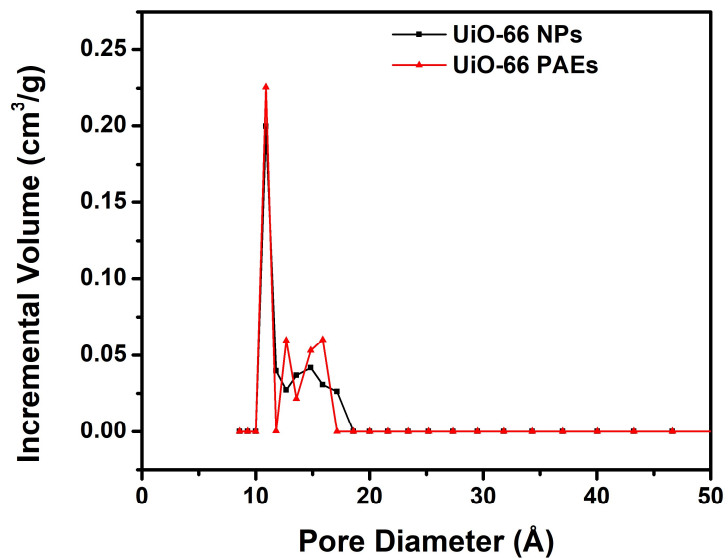


Figure S5.11. Density functional theory pore size distribution analysis of UiO-66 NPs and UiO-66 PAEs reveals no appreciable change after DNA functionalization.

S8. Quantification of DNA surface coverage

S8.1 UV-vis spectroscopy

UV-vis spectroscopy was performed on a Cary 5000 UV-vis spectrometer (Agilent) with 1 cm quartz optical cells were used for the measurements. The temperature was regulated with a Peltier heat pump attached to a six-cell holder. The surface DNA coverage of the MOF PAEs was determined by UV-vis spectroscopy with Tamra labeled DNA.

S8.2 Inductively coupled plasma-optical emission spectroscopy (ICP-OES)

DNA coverage of each MOF was quantified based on their NP surface area and NP molar concentration. With the radius/edge length of each MOF NP obtained from TEM, the surface area of each NP was calculated based on geometric approximations: spheres for 37 nm UiO-66 NPs and rod for PCN-222 nanorods. The molar concentration of each MOF NP sample was obtained by ICP-OES analysis of the Zr contents of these MOF samples in addition to crystallographic information; the number of metal atoms per NP can be calculated for a given size MOF NPs. ICP-OES analysis was carried out on a Thermo iCap 7600 ICP-OES instrument with an automated sample changer. MOF NP samples were dispersed in DMF (1 mL), and 10 μ L of the MOF sample was added to HNO₃ (990 μ L). The samples were heated at 60 °C for 15 h for full digestion.

S9. ³¹P{¹H} magic angle spinning solid state nuclear magnetic resonance (MAS NMR) spectroscopy

³¹P{¹H} MAS NMR spectroscopy was performed on a Varian 400 MHz VNMRS system (512 scans, 5 s recycle time, and 10,000 Hz spin rate).

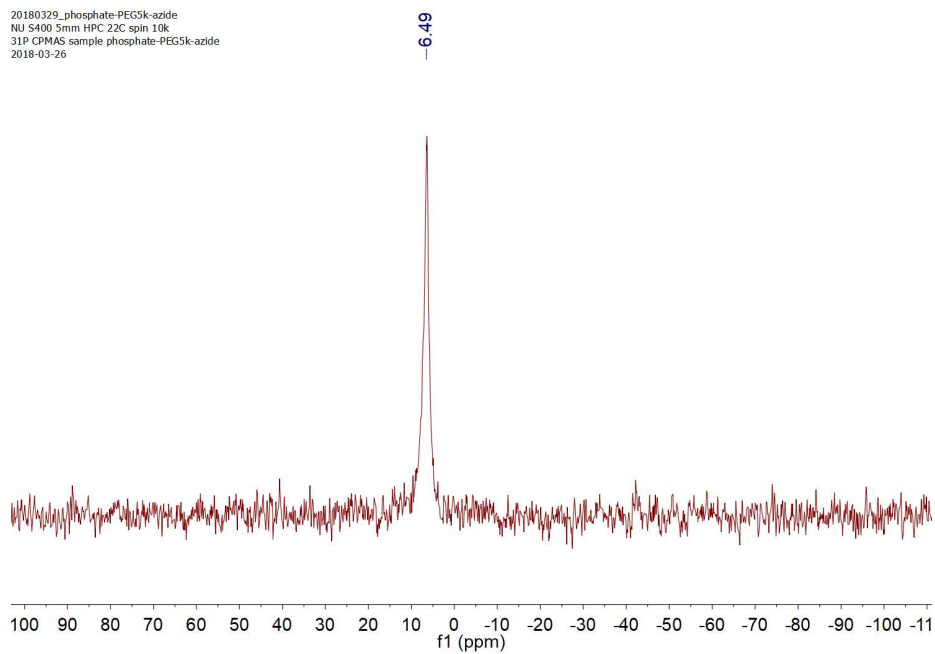


Figure S5.12. $^{31}\text{P}\{^1\text{H}\}$ MAS NMR spectrum of the phosphate-PEG_{5k}-azide linker.

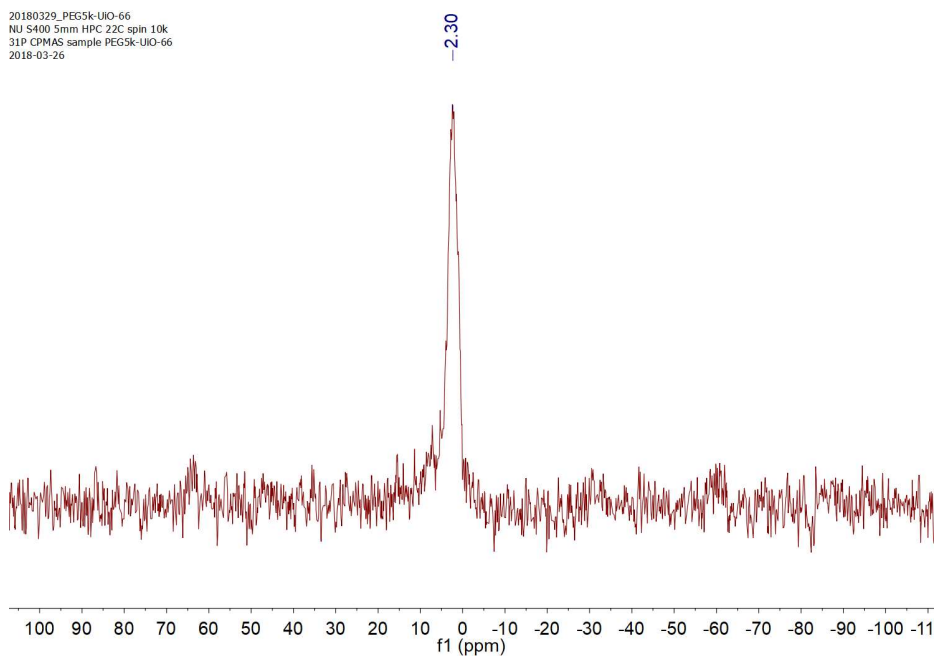


Figure S5.13. $^{31}\text{P}\{^1\text{H}\}$ MAS NMR spectrum of phosphate-PEG_{5k}-azide ligand functionalized UiO-66 NPs.

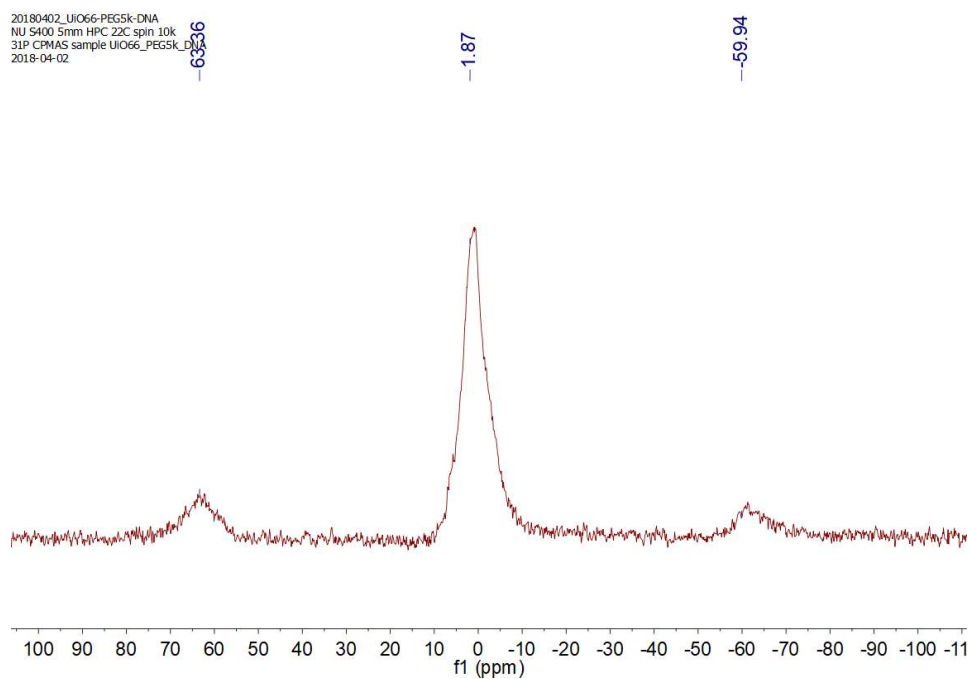


Figure S5.14. $^{31}\text{P}\{^1\text{H}\}$ MAS NMR spectrum of DNA-PEG_{5k}-UiO-66 NPs.

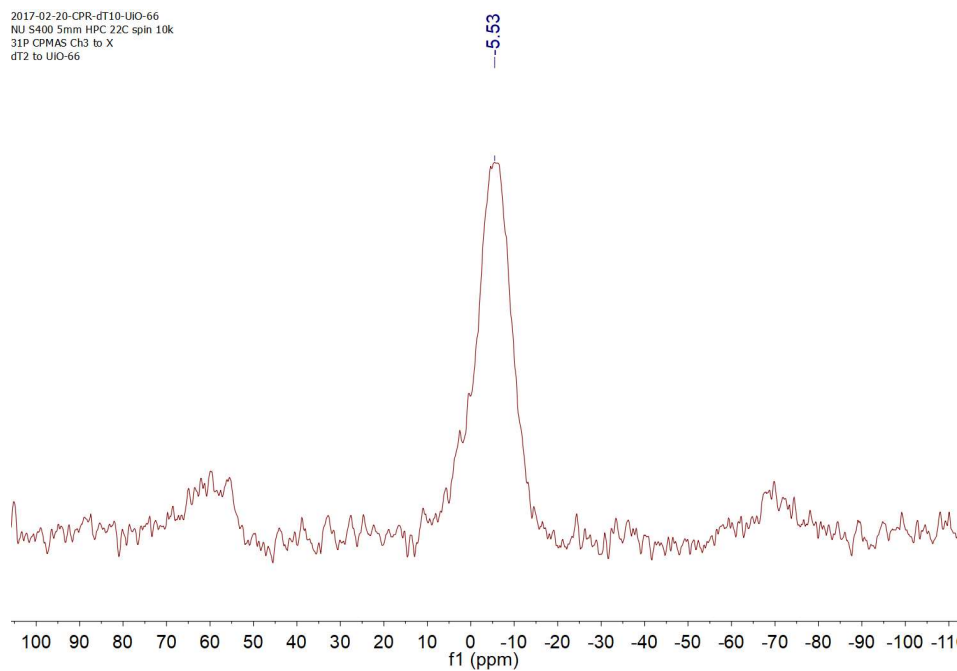


Figure S15. $^{31}\text{P}\{^1\text{H}\}$ MAS NMR spectrum of unmodified DNA coordinated to the UiO-66 NPs surface via multivalent phosphate backbone bonding.

S10. Small angle X-ray scattering (SAXS) studies

S10.1 Instrumentation and methods

SAXS characterization was carried out at the sector 5 DuPont-Northwestern-Dow Collaborative Access Team (DND-CAT) beamline of Argonne National Laboratory's Advanced Photon Source (APS). X-rays of wavelength 1.24 Å (10 keV) were used, and the system was calibrated using silver behenate as a standard. Two sets of slits were used to define and collimate the X-ray beam; parasitic scattering was removed via a pinhole. Typical exposure times varied between 0.1 and 0.5 s, depending upon the sample. The scattered X-rays were collected with a CCD area detector and 1-dimensional scattering data were obtained from radial averaging of the 2-dimensional data to obtain plots of scattering intensity as a function of the scattering vector q . One-dimensional SAXS data were indexed using Matlab to determine the crystallographic symmetry and the lattice parameter.

S10.2 Calculation of interparticle distances and lattice parameters

For the assembly parameters presented in the previous section, all relevant interparticle distances and lattice parameters were calculated using the SAXS data. The distance between NP nearest neighbors within a NP superlattice can be determined as: $d_{NP} = \left(\frac{1}{10}\right)\left(\frac{C}{q_0}\right)$, where d_{NP} is the distance in nm between two NP nearest neighbors, q_0 is the position of the initial scattering peak in $1/\text{Å}$, and C is a constant that correlates the distance between two nanoparticle nearest neighbors and the distance between the (hkl) planes associated with the first scattering peak. Values of C are summarized in Table S3. To ensure that the lattice parameters and interparticle distances matched those calculated using equation, modeled SAXS patterns were generated with PowderCell and

compared to the experimental data; this ensured that all diffraction peaks matched with the calculated lattice parameter values.

Table S3. The C constant used to calculate interparticle distance and lattice parameters

Type	Crystal	Space Group symmetry	q_0 (hkl) plane	Nearest Neighbor	C constant
	fcc	Fm $\bar{3}$ m	(111)	$(\frac{1}{2}, \frac{1}{2}, 0)$	$\sqrt{6} \pi$
	bcc	Im $\bar{3}$ m	(110)	$(\frac{1}{2}, \frac{1}{2}, \frac{1}{2})$	$\sqrt{6} \pi$
	CsCl/SC	Pm $\bar{3}$ m	(100)	$(\frac{1}{2}, \frac{1}{2}, \frac{1}{2})$	$\sqrt{3} \pi$
	AlB ₂	P6/mmm	(001)	$(\frac{1}{3}, \frac{2}{3}, \frac{1}{2})$	2π

S11. Immobilization of MOF-Au hybrid superlattice in solid phase for imaging

S11.1 Silica encapsulation of MOF-Au binary superlattice

Immobilization of MOF-AuNP hybrid superlattice from colloidal solution to the solid-state was achieved by silica encapsulation.²²⁶ Briefly, *N*-trimethoxysilylpropyl-*N,N,N*-trimethylammonium chloride (TMSPA) (2 μ L, 7.2 μ mol) and 10 mg polyvinyl pyrrolidone (PVP, M.W. = 58,000, dissolved in 100 μ L of 0.5 M NaCl) was added to the superlattices in 0.5 mL of 0.5 M NaCl solution, and the mixture was stirred for approximately 30 min before the addition of triethoxysilane (TES) (4 μ L, 21.7 μ mol). The suspension was vigorously stirred for 24 h at room temperature, followed by purification to remove excess silica by three rounds of centrifugation and resuspension in water. For STEM analysis, the samples were solvent exchanged with ethanol and drop-casted onto a TEM grid.

S11.2 Resin embedding of silica embedded superlattice samples

For TEM analysis of the superlattice cross section, silica-encapsulated superlattice samples were resin embedded. The detailed procedure for resin embedding was adopted from a previous literature report.¹⁵⁸ Briefly, ~ 5 mg of silica-encapsulated superlattices was first embedded within 0.2 mL of 4% gelatin. The gelatin sample was dehydrated upon immersion in anhydrous ethanol solutions of increasing concentration (30%→50%→70%→80%→90%→100%). Next, the 100% ethanol was solvent exchanged with acetone twice for 10 min. In acetone, the gelatin was embedded in EMBed-812 resin (Electron Microscopy Sciences) following standard protocols provided by the manufacturer. The samples were placed at 65 °C for 16-20 h to polymerize and solidify the resin. The resin containing superlattice was sectioned into 100 nm slices for imaging.

S12. Cryo-STEM imaging

4 μ L of samples were pipetted onto glow discharged lacey carbon 200 mesh Cu grids (EMS Cat. # LC200-CU-100), blotted for 5 s, and plunge-frozen in liquid ethane with an FEI Vitrobot Mark III. The samples were then loaded into a Gatan 626.6 Cryo Transfer Holder kept at -165 °C and imaged in a Hitachi HD2300 cFEG STEM at 200 kV utilizing TE phase contrast and high angular annular dark field (HAADF) Z-contrast.

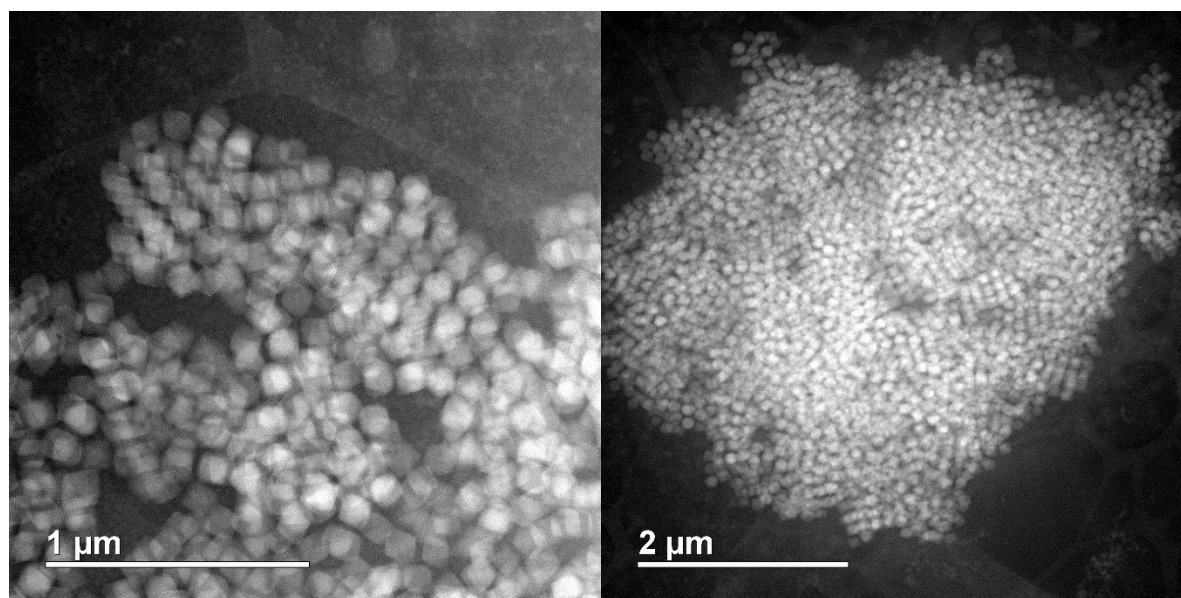


Figure S5.16. Cryo-STEM micrographs of octahedral UiO-66 NP superlattices assembled with self-complementary d40 linkers.

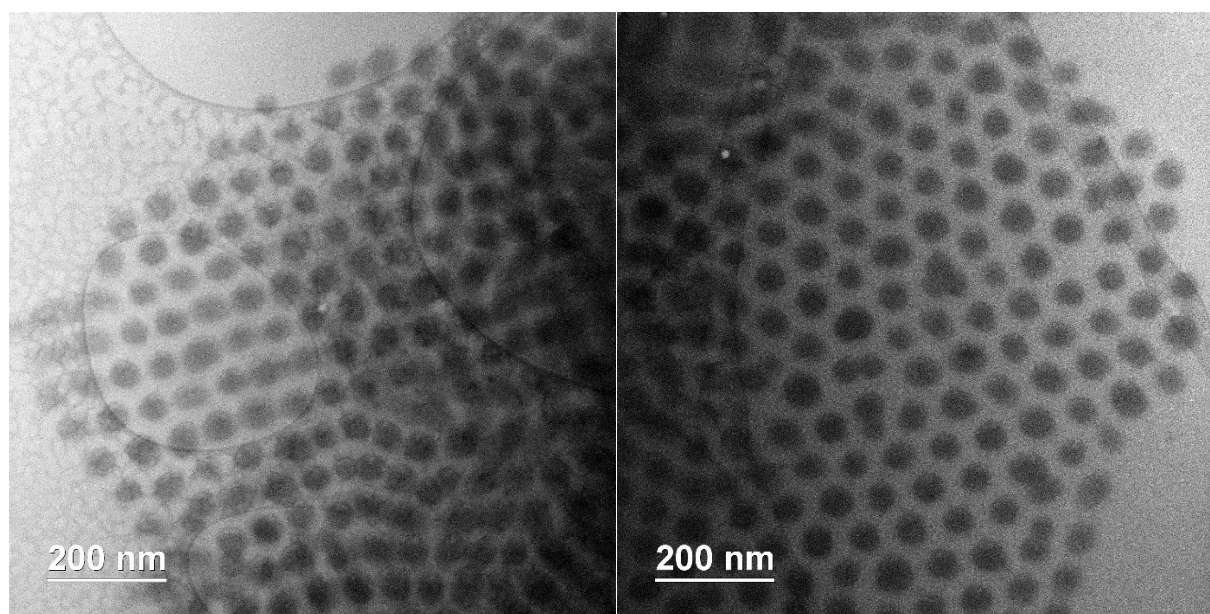


Figure S5.17. Cryo-STEM micrographs of PCN-222 nanorod superlattices assembled with self-complementary d40 linkers.

CHAPTER Six: Conclusions and Future Outlook

6.1 Outlook

The body of work described in this thesis provides a set of chemical approaches to control the crystallization process of MOF NP nucleation and growth, strategies to functionalize their surface with programmable ligands such as DNA, and colloidal crystal engineering strategies to program their arrangement in hierarchical organizations. Through these advances, and additional improvements in synthesis and characterization methodologies, MOF NPs will emerge as a promising new class of functional nanomaterials with the potential to significantly impact the fields of catalysis,⁸ separations,¹⁰⁶ and nanomedicine.¹⁰⁷ Although remarkable progress has been made, there remains significant room for improvement in the understanding of key features of MOF NP synthesis and functionalization. In this chapter, several future directions in this area are proposed with an emphasis on research opportunities that have made possible through the work detailed in Chapter two to five.

6.2 Synthesis of Uniform MOF NPs by Isolating Nucleation and Growth

In Chapter one and two, we discussed the initial mechanisms of particle nucleation and how factors such as modulators, temperature, and solvent affect these primary events. It is desirable to see improved characterization and mechanistic understanding of nucleation and subsequent crystal growth, which will drastically improve our ability to convert MOF NP synthesis from empirical knowledge to a highly predictable science. Further, improving upon the capability to predictably synthesize MOF NPs of desired sizes from 10–200 nm, with high uniformity, should remain an important goal for this field. NPs of this size regime are particularly attractive for two main reasons: (1) fast substrate diffusion kinetics associated with large external surface area for

site-isolated catalysis, and (2) size-dependent bioavailability (including with respect to cellular uptake, cytotoxicity and blood circulation) for applications as biological probes and perhaps even for therapeutic agents. Potential

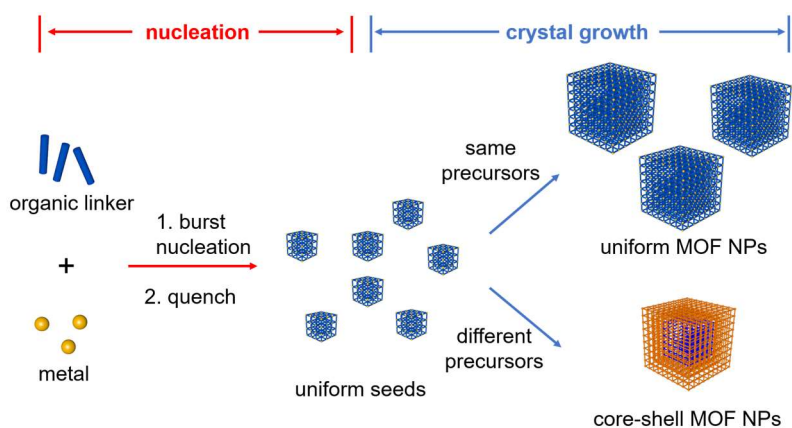


Figure 6.1. Separation of nucleation and crystal growth leads to monodisperse particle size distribution and core-shell structures.

advances in these areas include the continued evolution of strategies to effectively separate nucleation and growth processes, and the development of seed-mediated MOF NP synthetic approaches (**Figure 6.1**).^{135, 268-269} Successful realization of such strategy is expected to enable control over MOF NP size distribution in comparable with those of conventional inorganic nanoparticles (< 5% CV). Beyond gaining a firmer understanding of particle growth, other opportunities for impactful contributions to this field include: improving electron microscopy and diffraction based techniques (*i.e.*, X-ray and electron diffraction) for *in situ* characterization and in depth structural analysis of MOF NPs, modulating the chemical stability MOF NPs via surface functionalization (especially towards water and excess phosphate which is currently lacking), developing MOF NPs with large pores (> 3 nm) capable of encapsulating and delivering biomolecules,^{208, 270} and systematically evaluating MOF NP toxicity and pharmacokinetics *in vivo*.²⁷¹⁻²⁷²

6.3 Intracellular Delivery of Therapeutic Biomolecules Using DNA Functionalized MOF NPs

The ability to deliver functional biomolecules across cell membrane is highly attractive for potential therapeutics. In Chapter four, we demonstrated the successful intracellular delivery of

insulin using DNA-functionalized MOF NPs as a test case. To fully exploit the capability and generality of this delivery strategy, it is desirable to identify and study the delivery of therapeutically active cargos. However, for therapeutics to function inside cytosols, endosomal escape is a critical biological barrier to be overcome. In this vein, we hypothesize that cell penetrating peptides (CPPs) can be co-delivered with therapeutics (peptides, proteins, or siRNA, etc.), such that more effective deliveries could be achieved by releasing cargos from endosomes into cytosols.

Previously, CPPs have been used as transfection agents to deliver biomolecules (nucleic acids, proteins, etc.) inside cells via either covalent or noncovalent interactions. However, due to their strong pore forming ability, CPPs often suffer from limited cell type specificity and potentially permanent damage to the cell membranes. To address this issue, we propose that nucleic acid functionalized MOF NPs will act as CPP hosts and their densely functionalized

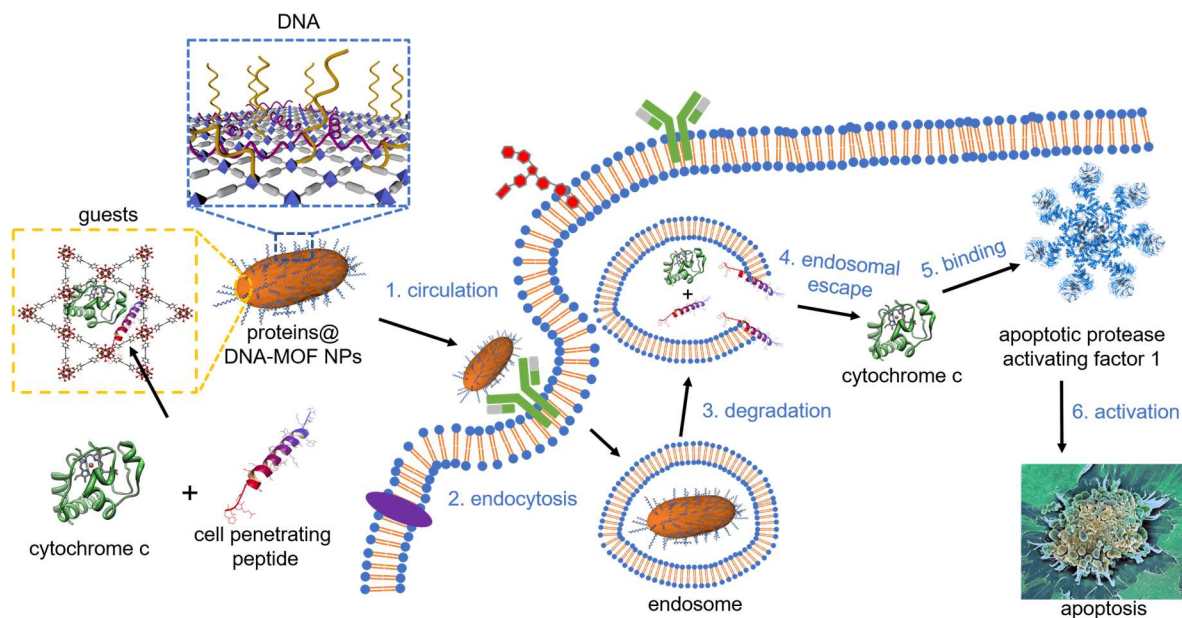


Figure 6.2. Schematic illustration of protein therapeutics and cell penetrating peptide co-delivered by DNA functionalized MOF NPs.

oligonucleotide rich surface ensure facile cellular entry and target specific cell types. On the basis of the significantly higher phosphate concentration inside cells (~ 5 mM) as compared to that of the extracellular matrices (~ 1 mM), MOF NPs are expected to degrade and release the encapsulated CPPs and therapeutics within endosomes. Finally, we hypothesize that the excellent pore forming capability of CPPs will disrupt endosome membranes and facilitate therapeutics releasing into cytosols for function.

In principle, this approach could be generalized to facilitate the intracellular delivery of a wide range of cargos as biological probes or potential therapeutics.

6.4 Hybrid MOF-Polymer Composites and Stimuli-Responsive MOF Superlattices

Another exciting avenue is the use of MOF NP as the building blocks in mixed-matrix membranes and colloidal crystal engineering of ordered 3-D metamaterials and devices.²⁷³⁻²⁷⁵ For instance, incorporating uniform MOF NPs into membranes could maximize their potential separation and catalysis capabilities, taking advantage of the extremely high external surface areas of MOF NPs and the attractive mechanical properties (stretchability, elasticity, and toughness) of polymeric matrices.²⁷⁶ Such combinations will inevitably lead to a rich spectrum of material properties and functionalities, in part due to the tunable chemistry of MOFs as well as polymers. Specifically, we anticipate a diverse range of MOF NP derived stimuli-responsive materials will emerge as important building components for flexible sensors, adaptive membranes, and artificial skin (**Figure 6.3**). Moreover, hierarchical materials composed of self-assembled MOF NP building blocks are hypothesized to exhibit properties unique from those demonstrated with conventional

inorganic NPs owing to their porosity, tailorable host-guest interactions, and chemical and physical modularity. For example, photonic crystals and optoelectronic devices may result from the combination of guest molecules coupled with 3-D ordered arrays of MOF NPs.^{69,277} Thus far, few examples of ordered structures have been prepared from MOF NP building blocks, all of which are entropically driven to form closed packed assemblies.^{65-66, 257} On the contrary, enthalpically driven assembly strategies are predictable and modular tools for assembling inorganic NPs into a huge library of well-defined architectures.²⁷⁸ MOF-based PAEs offer tremendous potential as

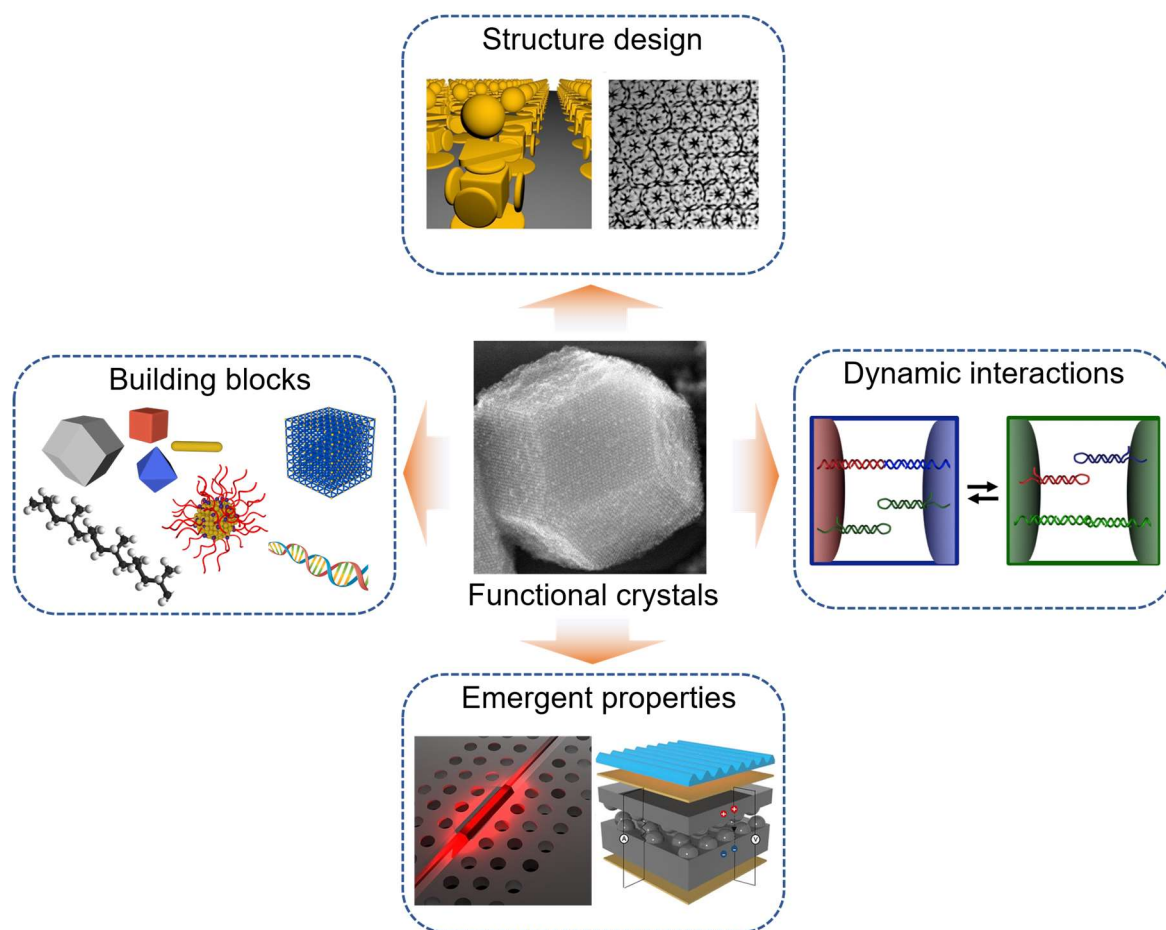


Figure 6.3. Creation of dynamically responsive, structurally sophisticated, and highly functional nanoparticle superlattice crystals.

responsive and reconfigurable nanoparticle cores inside DNA-assembled superlattices.

Specifically, chemical or physical stimuli will first interact with MOF nanoparticles to induce a response, which could involve chemical, electronic, or structural changes, that will be amplified within the hybrid superlattice. MOF nanoparticles constructed from hard, redox-inert, coordinatively saturated metal ions (*e.g.* Al^{3+} , Ti^{4+} , Zr^{4+}) will be targeted initially, as high-valent metal ions impart sufficient chemical stability to the MOF so that it will be stable during standard DNA attachment reactions under aqueous conditions. Targeted organic linkers will include porphyrins, tetraazamacrocycles, and metal-salen units that will allow for the incorporation of redox active metal ions into catalytic MOFs. In addition, we will work to incorporate flexible metal clusters that undergo structural, magnetic or electronic changes in response to external cues, such as light, an applied magnetic or electric field, or an applied mechanical force. In addition to the synthesis of new types of responsive superlattices, these materials are expected to exhibit dynamically tunable properties with relevance to switchable magnets, tandem catalysts that can be turned on and off on-demand, and optical switches.²⁷⁹⁻²⁸¹ For instance, Au nanoparticles can act as antennae to collect and convert photons to heat through a plasmonic response.^{158, 177, 182-183} This heat can then be transferred to the MOF NPs to modulate phenomena such as magnetic order, electronic conductivity, catalytic atom transfer, and the binding of gas molecules.

6.5 Conclusion and Final remarks

The modular synthesis of chemically addressable nanomaterials, such as MOF NPs, represents a powerful approach to realize desirable functionalities based on rational design and bottom-up assembly of molecular components. We believe that research on MOF NPs can lead to a new generation of smart materials that offer solutions to important issues concerning energy, the environment, and human health.

REFERENCES

1. McDonald, T. M.; D'Alessandro, D. M.; Krishna, R.; Long, J. R. Enhanced carbon dioxide capture upon incorporation of N,N'-dimethylethylenediamine in the metal-organic framework CuBTTri. *Chem. Sci.* **2011**, *2*, 2022-2028.
2. Yaghi, O. M.; O'Keeffe, M.; Ockwig, N. W.; Chae, H. K.; Eddaoudi, M.; Kim, J. Reticular synthesis and the design of new materials. *Nature* **2003**, *423*, 705-714.
3. Kitagawa, S.; Kitaura, R.; Noro, S. Functional porous coordination polymers. *Angew. Chem., Int. Ed.* **2004**, *43*, 2334-2375.
4. Ferey, G. Hybrid porous solids: past, present, future. *Chem. Soc. Rev.* **2008**, *37*, 191-214.
5. Eddaoudi, M.; Kim, J.; Rosi, N.; Vodak, D.; Wachter, J.; O'Keeffe, M.; Yaghi, O. M. Systematic design of pore size and functionality in isorecticular MOFs and their application in methane storage. *Science* **2002**, *295*, 469-472.
6. Kreno, L. E.; Hupp, J. T.; Van Dwyne, R. P. Metal-Organic Framework Thin Film for Enhanced Localized Surface Plasmon Resonance Gas Sensing. *Anal. Chem.* **2010**, *82*, 8042-8046.
7. Bae, T. H.; Lee, J. S.; Qiu, W. L.; Koros, W. J.; Jones, C. W.; Nair, S. A High-Performance Gas-Separation Membrane Containing Submicrometer-Sized Metal-Organic Framework Crystals. *Angew. Chem., Int. Ed.* **2010**, *49*, 9863-9866.
8. Lee, J.; Farha, O. K.; Roberts, J.; Scheidt, K. A.; Nguyen, S. T.; Hupp, J. T. Metal-organic framework materials as catalysts. *Chem. Soc. Rev.* **2009**, *38*, 1450-1459.
9. Horcajada, P.; Chalati, T.; Serre, C.; Gillet, B.; Sebrie, C.; Baati, T.; Eubank, J. F.; Heurtaux, D.; Clayette, P.; Kreuz, C.; Chang, J. S.; Hwang, Y. K.; Marsaud, V.; Bories, P. N.; Cynober,

- L.; Gil, S.; Ferey, G.; Couvreur, P.; Gref, R. Porous metal-organic-framework nanoscale carriers as a potential platform for drug delivery and imaging. *Nat. Mater.* **2010**, *9*, 172-178.
10. Sakata, Y.; Furukawa, S.; Kondo, M.; Hirai, K.; Horike, N.; Takashima, Y.; Uehara, H.; Louvain, N.; Meilikhov, M.; Tsuruoka, T.; Isoda, S.; Kosaka, W.; Sakata, O.; Kitagawa, S. Shape-Memory Nanopores Induced in Coordination Frameworks by Crystal Downsizing. *Science* **2013**, *339*, 193-196.
11. Sindoro, M.; Yanai, N.; Jee, A. Y.; Granick, S. Colloidal-Sized Metal-Organic Frameworks: Synthesis and Applications. *Acc. Chem. Res.* **2014**, *47*, 459-469.
12. Yang, J. M.; Liu, Q.; Sun, W. Y. Shape and size control and gas adsorption of Ni(II)-doped MOF-5 nano/microcrystals. *Microporous Mesoporous Mater.* **2014**, *190*, 26-31.
13. Kiyonaga, T.; Higuchi, M.; Kajiura, T.; Takashima, Y.; Duan, J. G.; Nagashima, K.; Kitagawa, S. Dependence of crystal size on the catalytic performance of a porous coordination polymer. *Chem. Commun.* **2015**, *51*, 2728-2730.
14. Park, J.; Jiang, Q.; Feng, D. W.; Mao, L. Q.; Zhou, H. C. Size-Controlled Synthesis of Porphyrinic Metal-Organic Framework and Functionalization for Targeted Photodynamic Therapy. *J. Am. Chem. Soc.* **2016**, *138*, 3518-3525.
15. Boles, M. A.; Ling, D.; Hyeon, T.; Talapin, D. V. The surface science of nanocrystals. *Nat. Mater.* **2016**, *15*, 141-153.
16. Stock, N.; Biswas, S. Synthesis of Metal-Organic Frameworks (MOFs): Routes to Various MOF Topologies, Morphologies, and Composites. *Chem. Rev.* **2012**, *112*, 933-969.
17. Tanabe, K. K.; Cohen, S. M. Postsynthetic modification of metal-organic frameworks-a progress report. *Chem. Soc. Rev.* **2011**, *40*, 498-519.

18. Karagiaridi, O.; Bury, W.; Mondloch, J. E.; Hupp, J. T.; Farha, O. K. Solvent-Assisted Linker Exchange: An Alternative to the De Novo Synthesis of Unattainable Metal-Organic Frameworks. *Angew. Chem., Int. Ed.* **2014**, *53*, 4530-4540.
19. Hirschle, P.; Preiss, T.; Auras, F.; Pick, A.; Volkner, J.; Valdeperez, D.; Witte, G.; Parak, W. J.; Radler, J. O.; Wuttke, S. Exploration of MOF nanoparticle sizes using various physical characterization methods - is what you measure what you get? *CrystEngComm* **2016**, *18*, 4359-4368.
20. Hermes, S.; Witte, T.; Hikov, T.; Zacher, D.; Bahnmuller, S.; Langstein, G.; Huber, K.; Fischer, R. A. Trapping metal-organic framework nanocrystals: An in-situ time-resolved light scattering study on the crystal growth of MOF-5 in solution. *J. Am. Chem. Soc.* **2007**, *129*, 5324-+.
21. Cravillon, J.; Schroder, C. A.; Nayuk, R.; Gummel, J.; Huber, K.; Wiebcke, M. Fast Nucleation and Growth of ZIF-8 Nanocrystals Monitored by Time-Resolved In Situ Small-Angle and Wide-Angle X-Ray Scattering. *Angew. Chem., Int. Ed.* **2011**, *50*, 8067-8071.
22. Patterson, J. P.; Abellan, P.; Denny, M. S.; Park, C.; Browning, N. D.; Cohen, S. M.; Evans, J. E.; Gianneschi, N. C. Observing the Growth of Metal-Organic Frameworks by in Situ Liquid Cell Transmission Electron Microscopy. *J. Am. Chem. Soc.* **2015**, *137*, 7322-7328.
23. Zhu, Y. H.; Ciston, J.; Zheng, B.; Miao, X. H.; Czarnik, C.; Pan, Y. C.; Sougrat, R.; Lai, Z. P.; Hsiung, C. E.; Yao, K. X.; Pinnau, I.; Pan, M.; Han, Y. Unravelling surface and interfacial structures of a metal-organic framework by transmission electron microscopy. *Nat. Mater.* **2017**, *16*, 532-536.

24. Cravillon, J.; Nayuk, R.; Springer, S.; Feldhoff, A.; Huber, K.; Wiebcke, M. Controlling Zeolitic Imidazolate Framework Nano- and Microcrystal Formation: Insight into Crystal Growth by Time-Resolved In Situ Static Light Scattering. *Chem. Mater.* **2011**, *23*, 2130-2141.
25. Thanh, N. T. K.; Maclean, N.; Mahiddine, S. Mechanisms of Nucleation and Growth of Nanoparticles in Solution. *Chem. Rev.* **2014**, *114*, 7610-7630.
26. Surble, S.; Millange, F.; Serre, C.; Ferey, G.; Walton, R. I. An EXAFS study of the formation of a nanoporous metal-organic framework: evidence for the retention of secondary building units during synthesis. *Chem. Commun.* **2006**, 1518-1520.
27. Lamer, V. K.; Dinegar, R. H. Theory, Production and Mechanism of Formation of Monodispersed Hydrosols. *J. Am. Chem. Soc.* **1950**, *72*, 4847-4854.
28. Ostwald, W. On the assumed isomerism of red and yellow mercury oxide and the surface-tension of solid bodies. *Z. Phys. Chem.* **1900**, *34*, 495-503.
29. Lin, W. B.; Rieter, W. J.; Taylor, K. M. L. Modular Synthesis of Functional Nanoscale Coordination Polymers. *Angew. Chem., Int. Ed.* **2009**, *48*, 650-658.
30. Spokoyny, A. M.; Kim, D.; Sumrein, A.; Mirkin, C. A. Infinite coordination polymer nano- and microparticle structures. *Chem. Soc. Rev.* **2009**, *38*, 1218-1227.
31. Sun, X. P.; Dong, S. J.; Wang, E. K. Coordination-induced formation of submicrometer-scale, monodisperse, spherical colloids of organic-inorganic hybrid materials at room temperature. *J. Am. Chem. Soc.* **2005**, *127*, 13102-13103.
32. Klinowski, J.; Paz, F. A. A.; Silva, P.; Rocha, J. Microwave-Assisted Synthesis of Metal-Organic Frameworks. *Dalton Trans.* **2011**, *40*, 321-330.

33. Chalati, T.; Horcajada, P.; Gref, R.; Couvreur, P.; Serre, C. Optimisation of the synthesis of MOF nanoparticles made of flexible porous iron fumarate MIL-88A. *J. Mater. Chem.* **2011**, *21*, 2220-2227.
34. Li, Y. S.; Bux, H.; Feldhoff, A.; Li, G. L.; Yang, W. S.; Caro, J. Controllable Synthesis of Metal-Organic Frameworks: From MOF Nanorods to Oriented MOF Membranes. *Adv. Mater.* **2010**, *22*, 3322-+.
35. Briggs, G. A. D. Ultrasound - Its Chemical, Physical and Biological Effects - Suslik, Ks. *Interdiscipl. Sci. Rev.* **1990**, *15*, 190-191.
36. Suslick, K. S. Sonochemistry. *Science* **1990**, *247*, 1439-1445.
37. Khan, N. A.; Jhung, S. H. Synthesis of metal-organic frameworks (MOFs) with microwave or ultrasound: Rapid reaction, phase-selectivity, and size reduction. *Coord. Chem. Rev.* **2015**, *285*, 11-23.
38. Jhung, S. H.; Lee, J. H.; Yoon, J. W.; Serre, C.; Ferey, G.; Chang, J. S. Microwave synthesis of chromium terephthalate MIL-101 and its benzene sorption ability. *Adv. Mater.* **2007**, *19*, 121-+.
39. Taylor-Pashow, K. M. L.; Della Rocca, J.; Xie, Z. G.; Tran, S.; Lin, W. B. Postsynthetic Modifications of Iron-Carboxylate Nanoscale Metal-Organic Frameworks for Imaging and Drug Delivery. *J. Am. Chem. Soc.* **2009**, *131*, 14261-14263.
40. Khan, N. A.; Kang, I. J.; Seok, H. Y.; Jhung, S. H. Facile synthesis of nano-sized metal-organic frameworks, chromium-benzenedicarboxylate, MIL-101. *Chem. Eng. J.* **2011**, *166*, 1152-1157.
41. Ma, M. Y.; Betard, A.; Weber, I.; Al-Hokbany, N. S.; Fischer, R. A.; Metzler-Nolte, N. Iron-Based Metal-Organic Frameworks MIL-88B and NH₂-MIL-88B: High Quality Microwave Synthesis and Solvent-Induced Lattice "Breathing". *Cryst. Growth Des.* **2013**, *13*, 2286-2291.

42. Khan, N. A.; Haque, E.; Jung, S. H. Rapid syntheses of a metal-organic framework material Cu-3(BTC)(2)(H₂O)(3) under microwave: a quantitative analysis of accelerated syntheses. *Phys. Chem. Chem. Phys.* **2010**, *12*, 2625-2631.
43. Eastoe, J.; Hollamby, M. J.; Hudson, L. Recent advances in nanoparticle synthesis with reversed micelles. *Adv Colloid Interfac* **2006**, *128*, 5-15.
44. Zhao, X. J.; Fang, X. L.; Wu, B. H.; Zheng, L. S.; Zheng, N. F. Facile synthesis of size-tunable ZIF-8 nanocrystals using reverse micelles as nanoreactors. *Sci. China Chem.* **2014**, *57*, 141-146.
45. Pang, M. L.; Cairns, A. J.; Liu, Y. L.; Belmabkhout, Y.; Zeng, H. C.; Eddaoudi, M. Synthesis and Integration of Fe-soc-MOF Cubes into Colloidosomes via a Single-Step Emulsion-Based Approach. *J. Am. Chem. Soc.* **2013**, *135*, 10234-10237.
46. Cai, X. C.; Deng, X. R.; Xie, Z. X.; Bao, S. X.; Shi, Y. S.; Lin, J.; Pang, M. L.; Eddaoudi, M. Synthesis of highly monodispersed Ga-soc-MOF hollow cubes, colloidosomes and nanocomposites. *Chem. Commun.* **2016**, *52*, 9901-9904.
47. Carne-Sanchez, A.; Imaz, I.; Cano-Sarabia, M.; Maspoch, D. A spray-drying strategy for synthesis of nanoscale metal-organic frameworks and their assembly into hollow superstructures. *Nat. Chem.* **2013**, *5*, 203-211.
48. Ameloot, R.; Vermoortele, F.; Vanhove, W.; Roeyffers, M. B. J.; Sels, B. F.; De Vos, D. E. Interfacial synthesis of hollow metal-organic framework capsules demonstrating selective permeability. *Nat. Chem.* **2011**, *3*, 382-387.
49. Cravillon, J.; Munzer, S.; Lohmeier, S. J.; Feldhoff, A.; Huber, K.; Wiebcke, M. Rapid Room-Temperature Synthesis and Characterization of Nanocrystals of a Prototypical Zeolitic Imidazolate Framework. *Chem. Mater.* **2009**, *21*, 1410-1412.

50. Seoane, B.; Dikhtiarenko, A.; Mayoral, A.; Tellez, C.; Coronas, J.; Kapteijn, F.; Gascon, J. Metal organic framework synthesis in the presence of surfactants: towards hierarchical MOFs? *CrystEngComm* **2015**, *17*, 1693-1700.
51. Uemura, T.; Kitagawa, S. Prussian blue nanoparticles protected by poly(vinylpyrrolidone). *J. Am. Chem. Soc.* **2003**, *125*, 7814-7815.
52. Uemura, T.; Hoshino, Y.; Kitagawa, S.; Yoshida, K.; Isoda, S. Effect of organic polymer additive on crystallization of porous coordination polymer. *Chem. Mater.* **2006**, *18*, 992-995.
53. Cho, W.; Lee, H. J.; Oh, M. Growth-Controlled Formation of Porous Coordination Polymer Particles. *J. Am. Chem. Soc.* **2008**, *130*, 16943-16946.
54. Tsuruoka, T.; Furukawa, S.; Takashima, Y.; Yoshida, K.; Isoda, S.; Kitagawa, S. Nanoporous Nanorods Fabricated by Coordination Modulation and Oriented Attachment Growth. *Angew. Chem., Int. Ed.* **2009**, *48*, 4739-4743.
55. Diring, S.; Furukawa, S.; Takashima, Y.; Tsuruoka, T.; Kitagawa, S. Controlled Multiscale Synthesis of Porous Coordination Polymer in Nano/Micro Regimes. *Chem. Mater.* **2010**, *22*, 4531-4538.
56. Umemura, A.; Diring, S.; Furukawa, S.; Uehara, H.; Tsuruoka, T.; Kitagawa, S. Morphology Design of Porous Coordination Polymer Crystals by Coordination Modulation. *J. Am. Chem. Soc.* **2011**, *133*, 15506-15513.
57. Hu, M.; Furukawa, S.; Ohtani, R.; Sukegawa, H.; Nemoto, Y.; Reboul, J.; Kitagawa, S.; Yamauchi, Y. Synthesis of Prussian Blue Nanoparticles with a Hollow Interior by Controlled Chemical Etching. *Angew. Chem., Int. Ed.* **2012**, *51*, 984-988.
58. Hu, M.; Belik, A. A.; Imura, M.; Yamauchi, Y. Tailored Design of Multiple Nanoarchitectures in Metal-Cyanide Hybrid Coordination Polymers. *J. Am. Chem. Soc.* **2013**, *135*, 384-391.

59. Avci, C.; Arinez-Soriano, J.; Carne-Sanchez, A.; Guillerm, V.; Carbonell, C.; Imaz, I.; MasPOCH, D. Post-Synthetic Anisotropic Wet-Chemical Etching of Colloidal Sodalite ZIF Crystals. *Angew. Chem., Int. Ed.* **2015**, *54*, 14417-14421.
60. Bloch, E. D.; Queen, W. L.; Krishna, R.; Zadrozny, J. M.; Brown, C. M.; Long, J. R. Hydrocarbon Separations in a Metal-Organic Framework with Open Iron(II) Coordination Sites. *Science* **2012**, *335*, 1606-1610.
61. Schaate, A.; Roy, P.; Godt, A.; Lippke, J.; Waltz, F.; Wiebecke, M.; Behrens, P. Modulated Synthesis of Zr-Based Metal-Organic Frameworks: From Nano to Single Crystals. *Chem. - Eur. J.* **2011**, *17*, 6643-6651.
62. Shearer, G. C.; Chavan, S.; Bordiga, S.; Svelle, S.; Olsbye, U.; Lillerud, K. P. Defect Engineering: Tuning the Porosity and Composition of the Metal-Organic Framework UiO-66 via Modulated Synthesis. *Chem. Mater.* **2016**, *28*, 3749-3761.
63. Morris, W.; Wang, S. Z.; Cho, D.; Auyeung, E.; Li, P.; Farha, O. K.; Mirkin, C. A. Role of Modulators in Controlling the Colloidal Stability and Polydispersity of the UiO-66 Metal-Organic Framework. *ACS Appl. Mater. Interfaces* **2017**.
64. Pang, M. L.; Cairns, A. J.; Liu, Y. L.; Belmabkhout, Y.; Zeng, H. C.; Eddaoudi, M. Highly Monodisperse M-III-Based soc-MOFs (M = In and Ga) with Cubic and Truncated Cubic Morphologies. *J. Am. Chem. Soc.* **2012**, *134*, 13176-13179.
65. Tsotsalas, M.; Umemura, A.; Kim, F.; Sakata, Y.; Reboul, J.; Kitagawa, S.; Furukawa, S. Crystal morphology-directed framework orientation in porous coordination polymer films and freestanding membranes via Langmuir-Blodgettry. *J. Mater. Chem.* **2012**, *22*, 10159-10165.
66. Lu, G.; Cui, C. L.; Zhang, W. N.; Liu, Y. Y.; Huo, F. W. Synthesis and Self-Assembly of Monodispersed Metal-Organic Framework Microcrystals. *Chem-Asian J* **2013**, *8*, 69-72.

67. Yanai, N.; Granick, S. Directional Self-Assembly of a Colloidal Metal-Organic Framework. *Angew. Chem., Int. Ed.* **2012**, *51*, 5638-5641.
68. Yanai, N.; Sindoro, M.; Yan, J.; Granick, S. Electric Field-Induced Assembly of Monodisperse Polyhedral Metal-Organic Framework Crystals. *J. Am. Chem. Soc.* **2013**, *135*, 34-37.
69. Avci, C.; Imaz, I.; Carné-Sánchez, A.; Pariente, J. A.; Tasios, N.; Pérez-Carvajal, J.; Alonso, M. I.; Blanco, A.; Dijkstra, M.; López, C.; Maspoch, D. Self-assembly of polyhedral metal-organic framework particles into three-dimensional ordered superstructures. *Nat. Chem.* **2017**.
70. Biemmi, E.; Christian, S.; Stock, N.; Bein, T. High-throughput screening of synthesis parameters in the formation of the metal-organic frameworks MOF-5 and HKUST-1. *Microporous Mesoporous Mater.* **2009**, *117*, 111-117.
71. Kelty, M. L.; Morris, W.; Gallagher, A. T.; Anderson, J. S.; Brown, K. A.; Mirkin, C. A.; Harris, T. D. High-throughput synthesis and characterization of nanocrystalline porphyrinic zirconium metal-organic frameworks. *Chem. Commun.* **2016**, *52*, 7854-7857.
72. Murray, C. B.; Kagan, C. R.; Bawendi, M. G. Synthesis and characterization of monodisperse nanocrystals and close-packed nanocrystal assemblies. *Annu. Rev. Mater. Sci.* **2000**, *30*, 545-610.
73. Templeton, A. C.; Wuelfing, M. P.; Murray, R. W. Monolayer protected cluster molecules. *Acc. Chem. Res.* **2000**, *33*, 27-36.
74. Verma, A.; Stellacci, F. Effect of Surface Properties on Nanoparticle-Cell Interactions. *Small* **2010**, *6*, 12-21.
75. McGuire, C. V.; Forgan, R. S. The surface chemistry of metal-organic frameworks. *Chem. Commun.* **2015**, *51*, 5199-5217.

76. Alexis, F.; Pridgen, E.; Molnar, L. K.; Farokhzad, O. C. Factors affecting the clearance and biodistribution of polymeric nanoparticles. *Mol. Pharmaceut.* **2008**, *5*, 505-515.
77. Li, S. D.; Huang, L. Pharmacokinetics and biodistribution of nanoparticles. *Mol. Pharmaceut.* **2008**, *5*, 496-504.
78. Nakajima, N.; Ikada, Y. Mechanism of Amide Formation by Carbodiimide for Bioconjugation in Aqueous-Media. *Bioconjugate Chem.* **1995**, *6*, 123-130.
79. Jung, S.; Kim, Y.; Kim, S. J.; Kwon, T. H.; Huh, S.; Park, S. Bio-functionalization of metal-organic frameworks by covalent protein conjugation. *Chem. Commun.* **2011**, *47*, 2904-2906.
80. Shih, Y. H.; Lo, S. H.; Yang, N. S.; Singco, B.; Cheng, Y. J.; Wu, C. Y.; Chang, I. H.; Huang, H. Y.; Lin, C. H. Trypsin-Immobilized Metal-Organic Framework as a Biocatalyst In Proteomics Analysis. *Chempluschem* **2012**, *77*, 982-986.
81. Ling, P. H.; Lei, J. P.; Zhang, L.; Ju, H. X. Porphyrin-Encapsulated Metal-Organic Frameworks as Mimetic Catalysts for Electrochemical DNA Sensing via Allosteric Switch of Hairpin DNA. *Anal. Chem.* **2015**, *87*, 3957-3963.
82. Moghimi, S. M.; Hunter, A. C.; Murray, J. C. Long-circulating and target-specific nanoparticles: Theory to practice. *Pharmacol. Rev.* **2001**, *53*, 283-318.
83. Karagiari, O.; Bury, W.; Mondloch, J. E.; Hupp, J. T.; Farha, O. K. Solvent-assisted linker exchange: an alternative to the de novo synthesis of unattainable metal-organic frameworks. *Angew Chem Int Ed Engl* **2014**, *53*, 4530-4540.
84. Xie, K.; Fu, Q.; He, Y.; Kim, J.; Goh, S. J.; Nam, E.; Qiao, G. G.; Webley, P. A. Synthesis of well dispersed polymer grafted metal-organic framework nanoparticles. *Chem. Commun.* **2015**, *51*, 15566-15569.

85. Nagata, S.; Kokado, K.; Sada, K. Metal-organic framework tethering PNIPAM for ON-OFF controlled release in solution. *Chem. Commun.* **2015**, *51*, 8614-8617.
86. Goto, Y.; Sato, H.; Shinkai, S.; Sada, K. "Clickable" Metal-Organic Framework. *J. Am. Chem. Soc.* **2008**, *130*, 14354-+.
87. Calabrese, C. M.; Merkel, T. J.; Briley, W. E.; Randeria, P. S.; Narayan, S. P.; Rouge, J. L.; Walker, D. A.; Scott, A. W.; Mirkin, C. A. Biocompatible Infinite-Coordination-Polymer Nanoparticle-Nucleic-Acid Conjugates for Antisense Gene Regulation. *Angew. Chem., Int. Ed.* **2015**, *54*, 476-480.
88. Morris, W.; Briley, W. E.; Auyeung, E.; Cabezas, M. D.; Mirkin, C. A. Nucleic Acid-Metal Organic Framework (MOF) Nanoparticle Conjugates. *J. Am. Chem. Soc.* **2014**, *136*, 7261-7264.
89. Cutler, J. I.; Auyeung, E.; Mirkin, C. A. Spherical nucleic acids. *J. Am. Chem. Soc.* **2012**, *134*, 1376-1391.
90. Kahn, J. S.; Freage, L.; Enkin, N.; Garcia, M. A. A.; Willner, I. Stimuli-Responsive DNA-Functionalized Metal-Organic Frameworks (MOFs). *Adv. Mater.* **2017**, *29*.
91. Chen, W.; Yu, X.; Ceconello, A.; Sohn, Y. S.; Nechushtai, R.; Willner, I. Stimuli-responsive nucleic acid-functionalized metal-organic framework nanoparticles using pH- and metal-ion-dependent DNazymes as locks. *Chem. Sci.* **2017**, *8*, 5769-5580.
92. Abanades Lazaro, I.; Haddad, S.; Sacca, S.; Orellana-Tavra, C.; Fairen-Jimenez, D.; Forgan, R. S. Selective Surface PEGylation of UiO-66 Nanoparticles for Enhanced Stability, Cell Uptake, and pH-Responsive Drug Delivery. *Chem* **2017**, *2*, 561-578.

93. He, C. B.; Lu, K. D.; Liu, D. M.; Lin, W. B. Nanoscale Metal-Organic Frameworks for the Co-Delivery of Cisplatin and Pooled siRNAs to Enhance Therapeutic Efficacy in Drug-Resistant Ovarian Cancer Cells. *J. Am. Chem. Soc.* **2014**, *136*, 5181-5184.
94. Hong, D. Y.; Hwang, Y. K.; Serre, C.; Ferey, G.; Chang, J. S. Porous Chromium Terephthalate MIL-101 with Coordinatively Unsaturated Sites: Surface Functionalization, Encapsulation, Sorption and Catalysis. *Adv. Funct. Mater.* **2009**, *19*, 1537-1552.
95. Kondo, M.; Furukawa, S.; Hirai, K.; Kitagawa, S. Coordinatively Immobilized Monolayers on Porous Coordination Polymer Crystals. *Angew. Chem., Int. Ed.* **2010**, *49*, 5327-5330.
96. He, L.; Brasino, M.; Mao, C.; Cho, S.; Park, W.; Goodwin, A. P.; Cha, J. N. DNA-Assembled Core-Satellite Upconverting-Metal-Organic Framework Nanoparticle Superstructures for Efficient Photodynamic Therapy. *Small* **2017**, *13*, 1700504.
97. Hwang, Y. K.; Hong, D. Y.; Chang, J. S.; Jhung, S. H.; Seo, Y. K.; Kim, J.; Vimont, A.; Daturi, M.; Serre, C.; Ferey, G. Amine grafting on coordinatively unsaturated metal centers of MOFs: Consequences for catalysis and metal encapsulation. *Angew. Chem., Int. Ed.* **2008**, *47*, 4144-4148.
98. Liu, D. M.; Kramer, S. A.; Huxford-Phillips, R. C.; Wang, S. Z.; Della Rocca, J.; Lin, W. B. Coercing bisphosphonates to kill cancer cells with nanoscale coordination polymers. *Chem. Commun.* **2012**, *48*, 2668-2670.
99. He, C. B.; Liu, D. M.; Lin, W. B. Self-assembled nanoscale coordination polymers carrying siRNAs and cisplatin for effective treatment of resistant ovarian cancer. *Biomaterials* **2015**, *36*, 124-133.

100. Liu, D. M.; Poon, C.; Lu, K. D.; He, C. B.; Lin, W. B. Self-assembled nanoscale coordination polymers with trigger release properties for effective anticancer therapy. *Nat. Commun.* **2014**, *5*.
101. Huxford-Phillips, R. C.; Russell, S. R.; Liu, D. M.; Lin, W. B. Lipid-coated nanoscale coordination polymers for targeted cisplatin delivery. *Rsc Adv.* **2013**, *3*, 14438-14443.
102. Wuttke, S.; Braig, S.; Preiss, T.; Zimpel, A.; Sicklinger, J.; Bellomo, C.; Radler, J. O.; Vollmar, A. M.; Bein, T. MOF nanoparticles coated by lipid bilayers and their uptake by cancer cells. *Chem. Commun.* **2015**, *51*, 15752-15755.
103. Illes, B.; Wuttke, S.; Engelke, H. Liposome-Coated Iron Fumarate Metal-Organic Framework Nanoparticles for Combination Therapy. *Nanomaterials* **2017**, *7*.
104. Liu, J. W.; Jiang, X. M.; Ashley, C.; Brinker, C. J. Electrostatically Mediated Liposome Fusion and Lipid Exchange with a Nanoparticle-Supported Bilayer for Control of Surface Charge, Drug Containment, and Delivery. *J. Am. Chem. Soc.* **2009**, *131*, 7567-+.
105. Illes, B.; Hirschle, P.; Baenert, S.; Cauda, V.; Wuttke, S.; Engelke, H. Exosome-Coated Metal-Organic Framework Nanoparticles: An Efficient Drug Delivery Platform. *Chem. Mater.* **2017**, *29*, 8042-8046.
106. Bachman, J. E.; Smith, Z. P.; Li, T.; Xu, T.; Long, J. R. Enhanced ethylene separation and plasticization resistance in polymer membranes incorporating metal-organic framework nanocrystals. *Nat. Mater.* **2016**, *15*, 845-+.
107. He, C. B.; Liu, D. M.; Lin, W. B. Nanomedicine Applications of Hybrid Nanomaterials Built from Metal-Ligand Coordination Bonds: Nanoscale Metal-Organic Frameworks and Nanoscale Coordination Polymers. *Chem. Rev.* **2015**, *115*, 11079-11108.

108. Furukawa, H.; Cordova, K. E.; O'Keeffe, M.; Yaghi, O. M. The Chemistry and Applications of Metal-Organic Frameworks. *Science* **2013**, *341*, 1230444.
109. Haque, E.; Khan, N. A.; Park, J. H.; Jung, S. H. Synthesis of a Metal-Organic Framework Material, Iron Terephthalate, by Ultrasound, Microwave, and Conventional Electric Heating: A Kinetic Study. *Chem. - Eur. J.* **2010**, *16*, 1046-1052.
110. Uehara, H.; Diring, S.; Furukawa, S.; Kalay, Z.; Tsotsalas, M.; Nakahama, M.; Hirai, K.; Kondo, M.; Sakata, O.; Kitagawa, S. Porous Coordination Polymer Hybrid Device with Quartz Oscillator: Effect of Crystal Size on Sorption Kinetics. *J. Am. Chem. Soc.* **2011**, *133*, 11932-11935.
111. Oien, S.; Wragg, D.; Reinsch, H.; Svelle, S.; Bordiga, S.; Lamberti, C.; Lillerud, K. P. Detailed Structure Analysis of Atomic Positions and Defects in Zirconium Metal-Organic Frameworks. *Cryst. Growth Des.* **2014**, *14*, 5370-5372.
112. Wu, H.; Chua, Y. S.; Krungleviciute, V.; Tyagi, M.; Chen, P.; Yildirim, T.; Zhou, W. Unusual and Highly Tunable Missing-Linker Defects in Zirconium Metal-Organic Framework UiO-66 and Their Important Effects on Gas Adsorption. *J. Am. Chem. Soc.* **2013**, *135*, 10525-10532.
113. Cliffe, M. J.; Hill, J. A.; Murray, C. A.; Coudert, F. X.; Goodwin, A. L. Defect-dependent colossal negative thermal expansion in UiO-66(Hf) metal-organic framework. *Phys. Chem. Chem. Phys.* **2015**, *17*, 11586-11592.
114. Shearer, G. C.; Chavan, S.; Ethiraj, J.; Vitillo, J. G.; Svelle, S.; Olsbye, U.; Lamberti, C.; Bordiga, S.; Lillerud, K. P. Tuned to Perfection: Ironing Out the Defects in Metal-Organic Framework UiO-66. *Chem. Mater.* **2014**, *26*, 4068-4071.

115. Cavka, J. H.; Jakobsen, S.; Olsbye, U.; Guillou, N.; Lamberti, C.; Bordiga, S.; Lillerud, K. P. A new zirconium inorganic building brick forming metal organic frameworks with exceptional stability. *J. Am. Chem. Soc.* **2008**, *130*, 13850-13851.
116. Rieter, W. J.; Taylor, K. M. L.; Lin, W. B. Surface modification and functionalization of nanoscale metal-organic frameworks for controlled release and luminescence sensing. *J. Am. Chem. Soc.* **2007**, *129*, 9852-+.
117. Wang, S. Z.; Morris, W.; Liu, Y. Y.; McGuirk, C. M.; Zhou, Y.; Hupp, J. T.; Farha, O. K.; Mirkin, C. A. Surface-Specific Functionalization of Nanoscale Metal-Organic Frameworks. *Angew. Chem., Int. Ed.* **2015**, *54*, 14738-14742.
118. Tao, A. R.; Habas, S.; Yang, P. D. Shape control of colloidal metal nanocrystals. *Small* **2008**, *4*, 310-325.
119. Heaton, C. A., *The Chemical industry*. 2nd ed.; Blackie Academic & Professional: London ; New York, 1994; p xiv, 383 p.
120. Armarego, W. L. F.; Chai, C. L. L. Purification of Laboratory Chemicals, 6th Edition. *Purification of Laboratory Chemicals, 6th Edition* **2009**, 1-743.
121. Bonard, J. M.; Stora, T.; Salvétat, J. P.; Maier, F.; Stockli, T.; Duschl, C.; Forro, L.; deHeer, W. A.; Chatelain, A. Purification and size-selection of carbon nanotubes. *Adv. Mater.* **1997**, *9*, 827-831.
122. Savage, N.; Diallo, M. S. Nanomaterials and water purification: Opportunities and challenges. *J. Nanopart. Res.* **2005**, *7*, 331-342.
123. Akthakul, A.; Hochbaum, A. I.; Stellacci, F.; Mayes, A. M. Size fractionation of metal nanoparticles by membrane filtration. *Adv. Mater.* **2005**, *17*, 532-535.

124. Sweeney, S. F.; Woehrlé, G. H.; Hutchison, J. E. Rapid purification and size separation of gold nanoparticles via diafiltration. *J. Am. Chem. Soc.* **2006**, *128*, 3190-3197.
125. Yavuz, C. T.; Mayo, J. T.; Yu, W. W.; Prakash, A.; Falkner, J. C.; Yean, S.; Cong, L. L.; Shipley, H. J.; Kan, A.; Tomson, M.; Natelson, D.; Colvin, V. L. Low-field magnetic separation of monodisperse Fe₃O₄ nanocrystals. *Science* **2006**, *314*, 964-967.
126. Della Rocca, J.; Liu, D. M.; Lin, W. B. Nanoscale Metal-Organic Frameworks for Biomedical Imaging and Drug Delivery. *Acc. Chem. Res.* **2011**, *44*, 957-968.
127. Snurr, R. Q.; Hupp, J. T.; Nguyen, S. T. Prospects for nanoporous metal-organic materials in advanced separations processes. *AIChE J.* **2004**, *50*, 1090-1095.
128. Chen, B. L.; Wang, L. B.; Xiao, Y. Q.; Fronczek, F. R.; Xue, M.; Cui, Y. J.; Qian, G. D. A Luminescent Metal-Organic Framework with Lewis Basic Pyridyl Sites for the Sensing of Metal Ions. *Angew. Chem., Int. Ed.* **2009**, *48*, 500-503.
129. Xu, H.; Liu, F.; Cui, Y. J.; Chen, B. L.; Qian, G. D. A luminescent nanoscale metal-organic framework for sensing of nitroaromatic explosives. *Chem. Commun.* **2011**, *47*, 3153-3155.
130. Zhang, J. P.; Huang, X. C.; Chen, X. M. Supramolecular isomerism in coordination polymers. *Chem. Soc. Rev.* **2009**, *38*, 2385-2396.
131. Dhakshinamoorthy, A.; Alvaro, M.; Horcajada, P.; Gibson, E.; Vishnuvarthan, M.; Vimont, A.; Greneche, J. M.; Serre, C.; Daturi, M.; Garcia, H. Comparison of Porous Iron Trimesates Basolite F300 and MIL-100(Fe) As Heterogeneous Catalysts for Lewis Acid and Oxidation Reactions: Roles of Structural Defects and Stability. *Acs Catal* **2012**, *2*, 2060-2065.
132. Li, L.; Xiang, S. L.; Cao, S. Q.; Zhang, J. Y.; Ouyang, G. F.; Chen, L. P.; Su, C. Y. A synthetic route to ultralight hierarchically micro/mesoporous Al(III)-carboxylate metal-organic aerogels. *Nat. Commun.* **2013**, *4*, 1774.

133. Feng, D. W.; Wang, K. C.; Wei, Z. W.; Chen, Y. P.; Simon, C. M.; Arvapally, R. K.; Martin, R. L.; Bosch, M.; Liu, T. F.; Fordham, S.; Yuan, D. Q.; Omary, M. A.; Haranczyk, M.; Smit, B.; Zhou, H. C. Kinetically tuned dimensional augmentation as a versatile synthetic route towards robust metal-organic frameworks. *Nat. Commun.* **2014**, *5*.
134. Carson, F.; Su, J.; Platero-Prats, A. E.; Wan, W.; Yun, Y. F.; Samain, L.; Zou, X. D. Framework Isomerism in Vanadium Metal-Organic Frameworks: MIL-88B(V) and MIL-101(V). *Cryst. Growth Des.* **2013**, *13*, 5036-5044.
135. Xu, H. Q.; Wang, K. C.; Ding, M. L.; Feng, D. W.; Jiang, H. L.; Zhou, H. C. Seed-Mediated Synthesis of Metal-Organic Frameworks. *J. Am. Chem. Soc.* **2016**, *138*, 5316-5320.
136. Hafizovic, J.; Bjorgen, M.; Olsbye, U.; Dietzel, P. D. C.; Bordiga, S.; Prestipino, C.; Lamberti, C.; Lillerud, K. P. The inconsistency in adsorption properties and powder XRD data of MOF-5 is rationalized by framework interpenetration and the presence of organic and inorganic species in the nanocavities. *J. Am. Chem. Soc.* **2007**, *129*, 3612-3620.
137. Ma, S. Q.; Sun, D. F.; Ambrogio, M.; Fillinger, J. A.; Parkin, S.; Zhou, H. C. Framework-catenation isomerism in metal-organic frameworks and its impact on hydrogen uptake. *J. Am. Chem. Soc.* **2007**, *129*, 1858-1859.
138. Price, C. A.; Eikenberry, E. F., *Centrifugation in density gradients*. Academic Press: New York, N.Y., 1982; p xv, 430 p.
139. Farha, O. K.; Mulfort, K. L.; Thorsness, A. M.; Hupp, J. T. Separating solids: Purification of metal-organic framework materials. *J. Am. Chem. Soc.* **2008**, *130*, 8598-8599.
140. Keene, T. D.; Price, D. J.; Kepert, C. J. Laboratory-based separation techniques for insoluble compound mixtures: methods for the purification of metal-organic framework materials. *Dalton Trans.* **2011**, *40*, 7122-7126.

141. Zhao, J.; Wang, Y. N.; Dong, W. W.; Wu, Y. P.; Li, D. S.; Liu, B.; Zhang, Q. C. A new surfactant-introduction strategy for separating the pure single-phase of metal-organic frameworks. *Chem. Commun.* **2015**, *51*, 9479-9482.
142. Morris, W.; Wang, S. Z.; Cho, D.; Auyeung, E.; Li, P.; Farha, O. K.; Mirkin, C. A. Role of Modulators in Controlling the Colloidal Stability and Polydispersity of the UiO-66 Metal-Organic Framework. *ACS Appl. Mater. Interfaces* **2017**, *9*, 33413-33418.
143. Scherb, C.; Schodel, A.; Bein, T. Directing the structure of metal-organic frameworks by oriented surface growth on an organic monolayer. *Angew. Chem., Int. Ed.* **2008**, *47*, 5777-5779.
144. Serre, C.; Millange, F.; Surble, S.; Ferey, G. A route to the synthesis of trivalent transition-metal porous carboxylates with trimeric secondary building units. *Angew. Chem., Int. Ed.* **2004**, *43*, 6286-6289.
145. Ferey, G.; Mellot-Draznieks, C.; Serre, C.; Millange, F.; Dutour, J.; Surble, S.; Margiolaki, I. A chromium terephthalate-based solid with unusually large pore volumes and surface area. *Science* **2005**, *309*, 2040-2042.
146. Guillerm, V.; Ragon, F.; Dan-Hardi, M.; Devic, T.; Vishnuvarthan, M.; Campo, B.; Vimont, A.; Clet, G.; Yang, Q.; Maurin, G.; Ferey, G.; Vittadini, A.; Gross, S.; Serre, C. A Series of Isorecticular, Highly Stable, Porous Zirconium Oxide Based Metal-Organic Frameworks. *Angew. Chem., Int. Ed.* **2012**, *51*, 9267-9271.
147. Bauer, S.; Serre, C.; Devic, T.; Horcajada, P.; Marrot, J.; Ferey, G.; Stock, N. High-throughput assisted rationalization of the formation of metal organic frameworks in the iron(III) aminoterephthalate solvothermal system. *Inorg. Chem.* **2008**, *47*, 7568-7576.

148. Valenzano, L.; Civalleri, B.; Chavan, S.; Bordiga, S.; Nilsen, M. H.; Jakobsen, S.; Lillerud, K. P.; Lamberti, C. Disclosing the Complex Structure of UiO-66 Metal Organic Framework: A Synergic Combination of Experiment and Theory. *Chem. Mater.* **2011**, *23*, 1700-1718.
149. Gutov, O. V.; Hevia, M. G.; Escudero-Adan, E. C.; Shafir, A. Metal-Organic Framework (MOF) Defects under Control: Insights into the Missing Linker Sites and Their Implication in the Reactivity of Zirconium-Based Frameworks. *Inorg. Chem.* **2015**, *54*, 8396-8400.
150. Fang, Z. L.; Bueken, B.; De Vos, D. E.; Fischer, R. A. Defect-Engineered Metal-Organic Frameworks. *Angew. Chem., Int. Ed.* **2015**, *54*, 7234-7254.
151. Furukawa, H.; Gandara, F.; Zhang, Y. B.; Jiang, J. C.; Queen, W. L.; Hudson, M. R.; Yaghi, O. M. Water Adsorption in Porous Metal-Organic Frameworks and Related Materials. *J. Am. Chem. Soc.* **2014**, *136*, 4369-4381.
152. Jia, J.; Xu, F. J.; Long, Z.; Hou, X. D.; Sepaniak, M. J. Metal-organic framework MIL-53(Fe) for highly selective and ultrasensitive direct sensing of MeHg⁺. *Chem. Commun.* **2013**, *49*, 4670-4672.
153. Liang, W. B.; Babarao, R.; D'Alessandro, D. M. Microwave-Assisted Solvothermal Synthesis and Optical Properties of Tagged MIL-140A Metal-Organic Frameworks. *Inorg. Chem.* **2013**, *52*, 12878-12880.
154. Queffelec, C.; Petit, M.; Janvier, P.; Knight, D. A.; Bujoli, B. Surface Modification Using Phosphonic Acids and Esters. *Chem. Rev.* **2012**, *112*, 3777-3807.
155. Guerrero, G.; Alauzun, J. G.; Granier, M.; Laurencin, D.; Mutin, P. H. Phosphonate coupling molecules for the control of surface/interface properties and the synthesis of nanomaterials. *Dalton Trans.* **2013**, *42*, 12569-12585.

156. Horcajada, P.; Serre, C.; Maurin, G.; Ramsahye, N. A.; Balas, F.; Vallet-Regi, M.; Sebban, M.; Taulelle, F.; Ferey, G. Flexible porous metal-organic frameworks for a controlled drug delivery. *J. Am. Chem. Soc.* **2008**, *130*, 6774-6780.
157. Surugau, N.; Urban, P. L. Electrophoretic methods for separation of nanoparticles. *J. Sep. Sci.* **2009**, *32*, 1889-1906.
158. Macfarlane, R. J.; Lee, B.; Jones, M. R.; Harris, N.; Schatz, G. C.; Mirkin, C. A. Nanoparticle Superlattice Engineering with DNA. *Science* **2011**, *334*, 204-208.
159. Wang, S. Z.; McGuirk, C. M.; Ross, M. B.; Wang, S. Y.; Chen, P. C.; Xing, H.; Liu, Y.; Mirkin, C. A. General and Direct Method for Preparing Oligonucleotide-Functionalized Metal–Organic Framework Nanoparticles. *J. Am. Chem. Soc.* **2017**, *139*, 9827-9830.
160. Gordon, J.; Kazemian, H.; Rohani, S. MIL-53 (Fe), MIL-101, and SBA-15 porous materials: Potential platforms for drug delivery. *Mater. Sci. Eng., C* **2015**, *47*, 172-179.
161. Banerjee, A.; Gokhale, R.; Bhatnagar, S.; Jog, J.; Bhardwaj, M.; Lefez, B.; Hannover, B.; Ogale, S. MOF derived porous carbon-Fe₃O₄ nanocomposite as a high performance, recyclable environmental superadsorbent. *J. Mater. Chem.* **2012**, *22*, 19694-19699.
162. Farha, O. K.; Hupp, J. T. Rational Design, Synthesis, Purification, and Activation of Metal-Organic Framework Materials. *Acc. Chem. Res.* **2010**, *43*, 1166-1175.
163. Kreno, L. E.; Leong, K.; Farha, O. K.; Allendorf, M.; Van Duyne, R. P.; Hupp, J. T. Metal-Organic Framework Materials as Chemical Sensors. *Chem. Rev.* **2012**, *112*, 1105-1125.
164. Wang, Z. Q.; Cohen, S. M. Postsynthetic modification of metal-organic frameworks. *Chem. Soc. Rev.* **2009**, *38*, 1315-1329.

165. Gadzikwa, T.; Farha, O. K.; Malliakas, C. D.; Kanatzidis, M. G.; Hupp, J. T.; Nguyen, S. T. Selective Bifunctional Modification of a Non-catenated Metal-Organic Framework Material via "Click" Chemistry. *J. Am. Chem. Soc.* **2009**, *131*, 13613-+.
166. Makiura, R.; Motoyama, S.; Umemura, Y.; Yamanaka, H.; Sakata, O.; Kitagawa, H. Surface nano-architecture of a metal-organic framework. *Nat. Mater.* **2010**, *9*, 565-571.
167. Daniel, M. C.; Astruc, D. Gold nanoparticles: Assembly, supramolecular chemistry, quantum-size-related properties, and applications toward biology, catalysis, and nanotechnology. *Chem. Rev.* **2004**, *104*, 293-346.
168. Lv, X. L.; Tong, M. M.; Huang, H. L.; Wang, B.; Gan, L.; Yang, Q. Y.; Zhong, C. L.; Li, J. R. A high surface area Zr(IV)-based metal-organic framework showing stepwise gas adsorption and selective dye uptake. *J. Solid State Chem.* **2015**, *223*, 104-108.
169. Ghosh, P.; Colon, Y. J.; Snurr, R. Q. Water adsorption in UiO-66: the importance of defects. *Chem. Commun.* **2014**, *50*, 11329-11331.
170. Min, Y. J.; Akbulut, M.; Kristiansen, K.; Golan, Y.; Israelachvili, J. The role of interparticle and external forces in nanoparticle assembly. *Nat. Mater.* **2008**, *7*, 527-538.
171. Ross, M. B.; Blaber, M. G.; Schatz, G. C. Using nanoscale and mesoscale anisotropy to engineer the optical response of three-dimensional plasmonic metamaterials. *Nature Commun* **2014**, *5*, 4090.
172. Yin, W. C.; Tao, C. A.; Zou, X. R.; Wang, F.; Qu, T. L.; Wang, J. F. The Tuning of Optical Properties of Nanoscale MOFs-Based Thin Film through Post-Modification. *Nanomaterials* **2017**, *7*.
173. Horike, S.; Shimomura, S.; Kitagawa, S. Soft porous crystals. *Nat. Chem.* **2009**, *1*, 695-704.

174. Linic, S.; Christopher, P.; Ingram, D. B. Plasmonic-metal nanostructures for efficient conversion of solar to chemical energy. *Nat. Mater.* **2011**, *10*, 911-921.
175. Mirkin, C. A.; Letsinger, R. L.; Mucic, R. C.; Storhoff, J. J. A DNA-based method for rationally assembling nanoparticles into macroscopic materials. *Nature* **1996**, *382*, 607-609.
176. Alivisatos, A. P.; Johnsson, K. P.; Peng, X. G.; Wilson, T. E.; Loweth, C. J.; Bruchez, M. P.; Schultz, P. G. Organization of 'nanocrystal molecules' using DNA. *Nature* **1996**, *382*, 609-611.
177. Jones, M. R.; Seeman, N. C.; Mirkin, C. A. Programmable materials and the nature of the DNA bond. *Science* **2015**, *347*, 1260901.
178. Seferos, D. S. Nano-flares: probes for transfection and mRNA detection in living cells. *J. Am. Chem. Soc.* **2007**, *129*, 15477-15479.
179. Zheng, D.; Seferos, D. S.; Giljohann, D. A.; Patel, P. C.; Mirkin, C. A. Aptamer Nano-flares for Molecular Detection in Living Cells. *Nano Lett.* **2009**, *9*, 3258-3261.
180. Rosi, N. L.; Giljohann, D. A.; Thaxton, C. S.; Lytton-Jean, A. K. R.; Han, M. S.; Mirkin, C. A. Oligonucleotide-modified gold nanoparticles for intracellular gene regulation. *Science* **2006**, *312*, 1027-1030.
181. Radovic-Moreno, A. F.; Chernyak, N.; Mader, C. C.; Nallagatla, S.; Kang, R. S.; Hao, L. L.; Walker, D. A.; Halo, T. L.; Merkel, T. J.; Rische, C. H.; Anantatmula, S.; Burkhart, M.; Mirkin, C. A.; Gryaznov, S. M. Immunomodulatory spherical nucleic acids. *Proc. Natl. Acad. Sci. U. S. A.* **2015**, *112*, 3892-3897.
182. Park, S. Y.; Lytton-Jean, A. K. R.; Lee, B.; Weigand, S.; Schatz, G. C.; Mirkin, C. A. DNA-programmable nanoparticle crystallization. *Nature* **2008**, *451*, 553-556.

183. Nykypanchuk, D.; Maye, M. M.; van der Lelie, D.; Gang, O. DNA-guided crystallization of colloidal nanoparticles. *Nature* **2008**, *451*, 549-552.
184. Cai, H.; Xu, Y.; Zhu, N. N.; He, P. G.; Fang, Y. Z. An electrochemical DNA hybridization detection assay based on a silver nanoparticle label. *Analyst* **2002**, *127*, 803-808.
185. Grancharov, S. G.; Zeng, H.; Sun, S. H.; Wang, S. X.; O'Brien, S.; Murray, C. B.; Kirtley, J. R.; Held, G. A. Bio-functionalization of monodisperse magnetic nanoparticles and their use as biomolecular labels in a magnetic tunnel junction based sensor. *J. Phys. Chem. B* **2005**, *109*, 13030-13035.
186. Zhang, C.; Macfarlane, R. J.; Young, K. L.; Choi, C. H. J.; Hao, L. L.; Auyeung, E.; Liu, G. L.; Zhou, X. Z.; Mirkin, C. A. A general approach to DNA-programmable atom equivalents. *Nat. Mater.* **2013**, *12*, 741-746.
187. Zhang, H. T.; Zhang, J. W.; Huang, G.; Du, Z. Y.; Jiang, H. L. An amine-functionalized metal-organic framework as a sensing platform for DNA detection. *Chem. Commun.* **2014**, *50*, 12069-12072.
188. Roder, R.; Preiss, T.; Hirschle, P.; Steinborn, B.; Zimpel, A.; Hohn, M.; Radler, J. O.; Bein, T.; Wagner, E.; Wuttke, S.; Lachelt, U. Multifunctional Nanoparticles by Coordinative Self-Assembly of His Tagged Units with Metal Organic Frameworks. *J. Am. Chem. Soc.* **2017**, *139*, 2359-2368.
189. Doonan, C.; Riccò, R.; Liang, K.; Bradshaw, D.; Falcaro, P. Metal–Organic Frameworks at the Biointerface: Synthetic Strategies and Applications. *Acc. Chem. Res.* **2017**, *50*, 1423-1432.

190. D'Astolfo, D. S.; Pagliero, R. J.; Pras, A.; Karthaus, W. R.; Clevers, H.; Prasad, V.; Lebbink, R. J.; Rehmann, H.; Geijsen, N. Efficient Intracellular Delivery of Native Proteins. *Cell* **2015**, *161*, 674-690.
191. Hoffman, R. M. Green fluorescent protein imaging of tumour growth, metastasis, and angiogenesis in mouse models. *Lancet Oncol.* **2002**, *3*, 546-556.
192. Torchilin, V. Intracellular delivery of protein and peptide therapeutics. *Drug Discovery Today: Technol.* **2008**, *5*, e95-e103.
193. Desnick, R. J.; Schuchman, E. H. Enzyme replacement and enhancement therapies: Lessons from lysosomal disorders. *Nat. Rev. Genet.* **2002**, *3*, 954-966.
194. Leader, B.; Baca, Q. J.; Golan, D. E. Protein therapeutics: A summary and pharmacological classification. *Nat. Rev. Drug Discovery* **2008**, *7*, 21-39.
195. Petros, R. A.; DeSimone, J. M. Strategies in the design of nanoparticles for therapeutic applications. *Nat. Rev. Drug Discovery* **2010**, *9*, 615-627.
196. Ghosh, P.; Yang, X. C.; Arvizo, R.; Zhu, Z. J.; Agasti, S. S.; Mo, Z. H.; Rotello, V. M. Intracellular Delivery of a Membrane-Impermeable Enzyme in Active Form Using Functionalized Gold Nanoparticles. *J. Am. Chem. Soc.* **2010**, *132*, 2642-2645.
197. Gu, Z.; Biswas, A.; Zhao, M.; Tang, Y. Tailoring nanocarriers for intracellular protein delivery. *Chem. Soc. Rev.* **2011**, *40*, 3638-3655.
198. Xu, X. M.; Costa, A.; Burgess, D. J. Protein Encapsulation in Unilamellar Liposomes: High Encapsulation Efficiency and A Novel Technique to Assess Lipid-Protein Interaction. *Pharm. Res.* **2012**, *29*, 1919-1931.
199. Schwarze, S. R.; Ho, A.; Vocero-Akbani, A.; Dowdy, S. F. In vivo protein transduction: Delivery of a biologically active protein into the mouse. *Science* **1999**, *285*, 1569-1572.

200. Lawrence, M. S.; Phillips, K. J.; Liu, D. R. Supercharging proteins can impart unusual resilience. *J. Am. Chem. Soc.* **2007**, *129*, 10110-+.
201. Cronican, J. J.; Thompson, D. B.; Beier, K. T.; McNaughton, B. R.; Cepko, C. L.; Liu, D. R. Potent Delivery of Functional Proteins into Mammalian Cells in Vitro and in Vivo Using a Supercharged Protein. *ACS Chem. Biol.* **2010**, *5*, 747-752.
202. Brodin, J. D.; Sprangers, A. J.; McMillan, J. R.; Mirkin, C. A. DNA-Mediated Cellular Delivery of Functional Enzymes. *J. Am. Chem. Soc.* **2015**, *137*, 14838-14841.
203. Fu, A. L.; Tang, R.; Hardie, J.; Farkas, M. E.; Rotello, V. M. Promises and Pitfalls of Intracellular Delivery of Proteins. *Bioconjugate Chem.* **2014**, *25*, 1602-1608.
204. Patel, P. C.; Giljohann, D. A.; Daniel, W. L.; Zheng, D.; Prigodich, A. E.; Mirkin, C. A. Scavenger Receptors Mediate Cellular Uptake of Polyvalent Oligonucleotide-Functionalized Gold Nanoparticles. *Bioconjugate Chem.* **2010**, *21*, 2250-2256.
205. Choi, C. H. J.; Hao, L. L.; Narayan, S. P.; Auyeung, E.; Mirkin, C. A. Mechanism for the endocytosis of spherical nucleic acid nanoparticle conjugates. *Proc. Natl. Acad. Sci. U. S. A.* **2013**, *110*, 7625-7630.
206. Lian, X. Z.; Fang, Y.; Joseph, E.; Wang, Q.; Li, J. L.; Banerjee, S.; Lollar, C.; Wang, X.; Zhou, H. C. Enzyme-MOF (metal-organic framework) composites. *Chem. Soc. Rev.* **2017**, *46*, 3386-3401.
207. Lykourinou, V.; Chen, Y.; Wang, X. S.; Meng, L.; Hoang, T.; Ming, L. J.; Musselman, R. L.; Ma, S. Q. Immobilization of MP-11 into a Mesoporous Metal-Organic Framework, MP-11@mesoMOF: A New Platform for Enzymatic Catalysis. *J. Am. Chem. Soc.* **2011**, *133*, 10382-10385.

208. Liang, K.; Ricco, R.; Doherty, C. M.; Styles, M. J.; Bell, S.; Kirby, N.; Mudie, S.; Haylock, D.; Hill, A. J.; Doonan, C. J.; Falcaro, P. Biomimetic mineralization of metal-organic frameworks as protective coatings for biomacromolecules. *Nat. Commun.* **2015**, *6*, 7240.
209. Li, P.; Moon, S. Y.; Guelta, M. A.; Harvey, S. P.; Hupp, J. T.; Farha, O. K. Encapsulation of a Nerve Agent Detoxifying Enzyme by a Mesoporous Zirconium Metal-Organic Framework Engenders Thermal and Long-Term Stability. *J. Am. Chem. Soc.* **2016**, *138*, 8052-8055.
210. Gkaniatsou, E.; Sicard, C.; Ricoux, R.; Mahy, J. P.; Steunou, N.; Serre, C. Metal-organic frameworks: a novel host platform for enzymatic catalysis and detection. *Mater. Horiz.* **2017**, *4*, 55-63.
211. Liu, W. L.; Lo, S. H.; Singco, B.; Yang, C. C.; Huang, H. Y.; Lin, C. H. Novel trypsin-FITC@MOF bioreactor efficiently catalyzes protein digestion. *J. Mater. Chem. B* **2013**, *1*, 928-932.
212. Cao, Y.; Wu, Z. F.; Wang, T.; Xiao, Y.; Huo, Q. S.; Liu, Y. L. Immobilization of *Bacillus subtilis* lipase on a Cu-BTC based hierarchically porous metal-organic framework material: a biocatalyst for esterification. *Dalton Trans.* **2016**, *45*, 6998-7003.
213. Lian, X. Z.; Erazo-Oliveras, A.; Pellois, J. P.; Zhou, H. C. High efficiency and long-term intracellular activity of an enzymatic nanofactory based on metal-organic frameworks. *Nat. Commun.* **2017**, *8*.
214. Frohlich, E. The role of surface charge in cellular uptake and cytotoxicity of medical nanoparticles. *Int. J. Nanomed.* **2012**, *7*, 5577-5591.
215. Baati, T.; Njim, L.; Neffati, F.; Kerkeni, A.; Bouttemi, M.; Gref, R.; Najjar, M. F.; Zakhama, A.; Couvreur, P.; Serre, C.; Horcajada, P. In depth analysis of the in vivo toxicity of nanoparticles of porous iron(III) metal-organic frameworks. *Chem. Sci.* **2013**, *4*, 1597-1607.

216. Ruyra, A.; Yazdi, A.; Espin, J.; Carne-Sanchez, A.; Roher, N.; Lorenzo, J.; Imaz, I.; MasPOCH, D. Synthesis, Culture Medium Stability, and In Vitro and In Vivo Zebrafish Embryo Toxicity of Metal-Organic Framework Nanoparticles. *Chem. - Eur. J.* **2015**, *21*, 2508-2518.
217. Wang, Z. J.; Fu, Y.; Kang, Z. Z.; Liu, X. G.; Chen, N.; Wang, Q.; Tu, Y. Q.; Wang, L. H.; Song, S. P.; Ling, D. S.; Song, H. Y.; Kong, X. Q.; Fan, C. H. Organelle-Specific Triggered Release of Immunostimulatory Oligonucleotides from Intrinsically Coordinated DNA-Metal-Organic Frameworks with Soluble Exoskeleton. *J. Am. Chem. Soc.* **2017**, *139*, 15784-15791.
218. Mondloch, J. E.; Bury, W.; Fairen-Jimenez, D.; Kwon, S.; DeMarco, E. J.; Weston, M. H.; Sarjeant, A. A.; Nguyen, S. T.; Stair, P. C.; Snurr, R. Q.; Farha, O. K.; Hupp, J. T. Vapor-Phase Metalation by Atomic Layer Deposition in a Metal-Organic Framework. *J. Am. Chem. Soc.* **2013**, *135*, 10294-10297.
219. Morris, W.; Voloskiy, B.; Demir, S.; Gandara, F.; McGrier, P. L.; Furukawa, H.; Cascio, D.; Stoddart, J. F.; Yaghi, O. M. Synthesis, Structure, and Metalation of Two New Highly Porous Zirconium Metal-Organic Frameworks. *Inorg. Chem.* **2012**, *51*, 6443-6445.
220. Feng, D. W.; Gu, Z. Y.; Li, J. R.; Jiang, H. L.; Wei, Z. W.; Zhou, H. C. Zirconium-Metalloporphyrin PCN-222: Mesoporous Metal-Organic Frameworks with Ultrahigh Stability as Biomimetic Catalysts. *Angew. Chem., Int. Ed.* **2012**, *51*, 10307-10310.
221. Chen, Y.; Li, P.; Modica, J. A.; Drout, R. J.; Farha, O. K. Acid-Resistant Mesoporous Metal-Organic Framework toward Oral Insulin Delivery: Protein Encapsulation, Protection, and Release. *J. Am. Chem. Soc.* **2018**, *140*, 5678-5681.
222. Li, P.; Modica, J. A.; Howarth, A. J.; Vargas, E. L.; Moghadam, P. Z.; Snurr, R. Q.; Mrksich, M.; Hupp, J. T.; Farha, O. K. Toward Design Rules for Enzyme Immobilization in Hierarchical Mesoporous Metal-Organic Frameworks. *Chem* **2016**, *1*, 154-169.

223. Nakayama, H.; Eguchi, T.; Nakamura, N.; Yamaguchi, S.; Danjyo, M.; Tshako, M. Structural study of phosphate groups in layered metal phosphates by high-resolution solid-state P-31 NMR spectroscopy. *J. Mater. Chem.* **1997**, *7*, 1063-1066.
224. Nonglaton, G.; Benitez, I. O.; Guisle, I.; Pipelier, M.; Leger, J.; Dubreuil, D.; Tellier, C.; Talham, D. R.; Bujoli, B. New approach to oligonucleotide microarrays using zirconium phosphonate-modified surfaces. *J. Am. Chem. Soc.* **2004**, *126*, 1497-1502.
225. Cottrell, T. L., *The strengths of chemical bonds*. Butterworths Scientific Publications: London,, 1954; p 310 p.
226. Auyeung, E.; Macfarlane, R. J.; Choi, C. H. J.; Cutler, J. I.; Mirkin, C. A. Transitioning DNA-Engineered Nanoparticle Superlattices from Solution to the Solid State. *Adv. Mater.* **2012**, *24*, 5181-5186.
227. Li, P.; Klet, R. C.; Moon, S. Y.; Wang, T. C.; Deria, P.; Peters, A. W.; Klahr, B. M.; Park, H. J.; Al-Juaid, S. S.; Hupp, J. T.; Farha, O. K. Synthesis of nanocrystals of Zr-based metal-organic frameworks with csq-net: significant enhancement in the degradation of a nerve agent simulant. *Chem. Commun.* **2015**, *51*, 10925-10928.
228. Deria, P.; Bury, W.; Hupp, J. T.; Farha, O. K. Versatile functionalization of the NU-1000 platform by solvent-assisted ligand incorporation. *Chem. Commun.* **2014**, *50*, 1965-1968.
229. Narayan, S. P.; Choi, C. H. J.; Hao, L. L.; Calabrese, C. M.; Auyeung, E.; Zhang, C.; Goor, O. J. G. M.; Mirkin, C. A. The Sequence-Specific Cellular Uptake of Spherical Nucleic Acid Nanoparticle Conjugates. *Small* **2015**, *11*, 4173-4182.
230. Libanati, C. M.; Tandler, C. J. The distribution of the water-soluble inorganic orthophosphate ions within the cell: accumulation in the nucleus. Electron probe microanalysis. *J. Cell Biol.* **1969**, *42*, 754-765.

231. Bansal, V. K., Serum Inorganic Phosphorus. In *Clinical Methods: The History, Physical, and Laboratory Examinations*, rd; Walker, H. K.; Hall, W. D.; Hurst, J. W., Eds. Boston, 1990.
232. Langer, R.; Tirrell, D. A. Designing materials for biology and medicine. *Nature* **2004**, *428*, 487-492.
233. Brodin, J. D.; Auyeung, E.; Mirkin, C. A. DNA-mediated engineering of multicomponent enzyme crystals. *Proc. Natl. Acad. Sci. U. S. A.* **2015**, *112*, 4564-4569.
234. Bergman, D. J.; Stockman, M. I. Surface plasmon amplification by stimulated emission of radiation: Quantum generation of coherent surface plasmons in nanosystems. *Phys. Rev. Lett.* **2003**, *90*.
235. Feng, D. W.; Liu, T. F.; Su, J.; Bosch, M.; Wei, Z. W.; Wan, W.; Yuan, D. Q.; Chen, Y. P.; Wang, X.; Wang, K. C.; Lian, X. Z.; Gu, Z. Y.; Park, J.; Zou, X. D.; Zhou, H. C. Stable metal-organic frameworks containing single-molecule traps for enzyme encapsulation. *Nat. Commun.* **2015**, *6*.
236. Li, P.; Chen, Q.; Wang, T. C.; Vermeulen, N. A.; Mehdi, B. L.; Dohnalkova, A.; Browning, N. D.; Shen, D.; Anderson, R.; Gomez-Gualdron, D. A.; Cetin, F. M.; Jagiello, J.; Asiri, A. M.; Stoddart, J. F.; Farha, O. K. Hierarchically Engineered Mesoporous Metal-Organic Frameworks toward Cell-free Immobilized Enzyme Systems. *Chem* **2018**, *4*, 1022-1034.
237. Jiang, H. L.; Feng, D. W.; Liu, T. F.; Li, J. R.; Zhou, H. C. Pore Surface Engineering with Controlled Loadings of Functional Groups via Click Chemistry in Highly Stable Metal-Organic Frameworks. *J. Am. Chem. Soc.* **2012**, *134*, 14690-14693.
238. Jiang, D. M.; Burrows, A. D.; Edler, K. J. Size-controlled synthesis of MIL-101(Cr) nanoparticles with enhanced selectivity for CO₂ over N₂. *CrystEngComm* **2011**, *13*, 6916-6919.

239. Taylor-Pashow, K. M. L.; Della Rocca, J.; Xie, Z. G.; Tran, S.; Lin, W. B. Postsynthetic Modifications of Iron-Carboxylate Nanoscale Metal-Organic Frameworks for Imaging and Drug Delivery. *J. Am. Chem. Soc.* **2009**, *131*, 14261-+.
240. O'Brien, M. N.; Jones, M. R.; Brown, K. A.; Mirkin, C. A. Universal Noble Metal Nanoparticle Seeds Realized Through Iterative Reductive Growth and Oxidative Dissolution Reactions. *J. Am. Chem. Soc.* **2014**, *136*, 7603-7606.
241. Kumar, P. S.; Pastoriza-Santos, I.; Rodriguez-Gonzalez, B.; Garcia de Abajo, F. J.; Liz-Marzan, L. M. High-yield synthesis and optical response of gold nanostars. *Nanotechnology* **2008**, *19*.
242. Hurst, S. J.; Lytton-Jean, A. K. R.; Mirkin, C. A. Maximizing DNA loading on a range of gold nanoparticle sizes. *Anal. Chem.* **2006**, *78*, 8313-8318.
243. Jones, M. R.; Osberg, K. D.; Macfarlane, R. J.; Langille, M. R.; Mirkin, C. A. Templated Techniques for the Synthesis and Assembly of Plasmonic Nanostructures. *Chem. Rev.* **2011**, *111*, 3736-3827.
244. Shevchenko, E. V.; Talapin, D. V.; Kotov, N. A.; O'Brien, S.; Murray, C. B. Structural diversity in binary nanoparticle superlattices. *Nature* **2006**, *439*, 55-59.
245. Whitesides, G. M.; Grzybowski, B. Self-assembly at all scales. *Science* **2002**, *295*, 2418-2421.
246. Jones, M. R.; Macfarlane, R. J.; Lee, B.; Zhang, J. A.; Young, K. L.; Senesi, A. J.; Mirkin, C. A. DNA-nanoparticle superlattices formed from anisotropic building blocks. *Nat. Mater.* **2010**, *9*, 913-917.
247. Cutler, J. I.; Auyeung, E.; Mirkin, C. A. Spherical Nucleic Acids. *J. Am. Chem. Soc.* **2012**, *134*, 1376-1391.

248. Wang, Y.; Wang, Y. F.; Zheng, X. L.; Ducrot, E.; Yodh, J. S.; Weck, M.; Pine, D. J. Crystallization of DNA-coated colloids. *Nat. Commun.* **2015**, *6*, 7253.
249. Zhang, Y. G.; Lu, F.; Yager, K. G.; van der Lelie, D.; Gang, O. A general strategy for the DNA-mediated self-assembly of functional nanoparticles into heterogeneous systems. *Nat. Nanotechnol.* **2013**, *8*, 865-872.
250. Wang, Y. F.; Wang, Y.; Zheng, X. L.; Ducrot, E.; Lee, M. G.; Yi, G. R.; Weck, M.; Pine, D. J. Synthetic Strategies Toward DNA-Coated Colloids that Crystallize. *J. Am. Chem. Soc.* **2015**, *137*, 10760-10766.
251. Ross, M. B.; Ku, J. C.; Blaber, M. G.; Mirkin, C. A.; Schatz, G. C. Defect tolerance and the effect of structural inhomogeneity in plasmonic DNA-nanoparticle superlattices. *Proc. Natl. Acad. Sci. U. S. A.* **2015**, *112*, 10292-10297.
252. O'Brien, M. N.; Jones, M. R.; Mirkin, C. A. The nature and implications of uniformity in the hierarchical organization of nanomaterials. *Proc. Natl. Acad. Sci. U. S. A.* **2016**, *113*, 11717-11725.
253. Murray, L. J.; Dinca, M.; Long, J. R. Hydrogen storage in metal-organic frameworks. *Chem. Soc. Rev.* **2009**, *38*, 1294-1314.
254. Campbell, M. G.; Sheberla, D.; Liu, S. F.; Swager, T. M.; Dinca, M. Cu₃(hexaiminotriphenylene)₂: An Electrically Conductive 2D Metal-Organic Framework for Chemiresistive Sensing. *Angew. Chem., Int. Ed.* **2015**, *54*, 4349-4352.
255. Avci, C.; Imaz, I.; Carne-Sanchez, A.; Pariente, J. A.; Tasios, N.; Perez-Carvajal, J.; Alonso, M. I.; Blanco, A.; Dijkstra, M.; Lopez, C.; Maspoch, D. Self-assembly of polyhedral metal-organic framework particles into three-dimensional ordered superstructures. *Nat. Chem.* **2018**, *10*, 78-84.

256. Wang, S. Z.; McGuirk, C. M.; d'Aquino, A.; Mason, J. A.; Mirkin, C. A. Metal-Organic Framework Nanoparticles. *Adv. Mater.* **2018**, *30*.
257. Glotzer, S. C.; Solomon, M. J. Anisotropy of building blocks and their assembly into complex structures. *Nat. Mater.* **2007**, *6*, 557-562.
258. Wang, C.; Liu, D. M.; Lin, W. B. Metal-Organic Frameworks as A Tunable Platform for Designing Functional Molecular Materials. *J. Am. Chem. Soc.* **2013**, *135*, 13222-13234.
259. Segawa, K.; Nakajima, Y.; Nakata, S.; Asaoka, S.; Takahashi, H. P-31-Masnmr Spectroscopic Studies with Zirconium-Phosphate Catalysts. *J. Catal.* **1986**, *101*, 81-89.
260. Agard, N. J.; Prescher, J. A.; Bertozzi, C. R. A strain-promoted [3+2] azide-alkyne cycloaddition for covalent modification of biomolecules in living systems. *J. Am. Chem. Soc.* **2004**, *126*, 15046-15047.
261. Auyeung, E.; Cutler, J. I.; Macfarlane, R. J.; Jones, M. R.; Wu, J. S.; Liu, G.; Zhang, K.; Osberg, K. D.; Mirkin, C. A. Synthetically programmable nanoparticle superlattices using a hollow three-dimensional spacer approach. *Nat. Nanotechnol.* **2012**, *7*, 24-28.
262. Auyeung, E.; Li, T. I. N. G.; Senesi, A. J.; Schmucker, A. L.; Pals, B. C.; de la Cruz, M. O.; Mirkin, C. A. DNA-mediated nanoparticle crystallization into Wulff polyhedra. *Nature* **2014**, *505*, 73-77.
263. O'Brien, M. N.; Lin, H. X.; Girard, M.; de la Cruz, M. O.; Mirkin, C. A. Programming Colloidal Crystal Habit with Anisotropic Nanoparticle Building Blocks and DNA Bonds. *J. Am. Chem. Soc.* **2016**, *138*, 14562-14565.
264. O'Brien, M. N.; Girard, M.; Lin, H. X.; Millan, J. A.; de la Cruz, M. O.; Lee, B.; Mirkin, C. A. Exploring the zone of anisotropy and broken symmetries in DNA-mediated nanoparticle crystallization. *Proc. Natl. Acad. Sci. U. S. A.* **2016**, *113*, 10485-10490.

265. Liang, Y. J.; Xie, Y.; Chen, D. X.; Guo, C. F.; Hou, S. A.; Wen, T.; Yang, F. Y.; Deng, K.; Wu, X. C.; Smalyukh, I. I.; Liu, Q. Symmetry control of nanorod superlattice driven by a governing force. *Nat. Commun.* **2017**, *8*.
266. Brunauer, S.; Emmett, P. H.; Teller, E. Adsorption of gases in multimolecular layers. *J. Am. Chem. Soc.* **1938**, *60*, 309-319.
267. Gomez-Gualdron, D. A.; Moghadam, P. Z.; Hupp, J. T.; Farha, O. K.; Snurr, R. Q. Application of Consistency Criteria To Calculate BET Areas of Micro- And Mesoporous Metal-Organic Frameworks. *J. Am. Chem. Soc.* **2016**, *138*, 215-224.
268. Doherty, C. M.; Buso, D.; Hill, A. J.; Furukawa, S.; Kitagawa, S.; Falcaro, P. Using Functional Nano- and Microparticles for the Preparation of Metal-Organic Framework Composites with Novel Properties. *Acc. Chem. Res.* **2014**, *47*, 396-405.
269. Gu, Y. F.; Wu, Y. N.; Li, L. C.; Chen, W.; Li, F. T.; Kitagawa, S. Controllable Modular Growth of Hierarchical MOF-on-MOF Architectures. *Angew. Chem., Int. Ed.* **2017**, *56*, 15658-15662.
270. Shen, K.; Zhang, L.; Chen, X. D.; Liu, L. M.; Zhang, D. L.; Han, Y.; Chen, J. Y.; Long, J. L.; Luque, R.; Li, Y. W.; Chen, B. L. Ordered macro-microporous metal-organic framework single crystals. *Science* **2018**, *359*, 206.
271. Wuttke, S.; Zimpel, A.; Bein, T.; Braig, S.; Stoiber, K.; Vollmar, A.; Muller, D.; Haastert-Talini, K.; Schaeske, J.; Stiesch, M.; Zahn, G.; Mohmeyer, A.; Behrens, P.; Eickelberg, O.; Bolukbas, D. A.; Meiners, S. Validating Metal-Organic Framework Nanoparticles for Their Nanosafety in Diverse Biomedical Applications. *Adv. Healthcare Mater.* **2017**, *6*, 1600818.
272. Gimenez-Marques, M.; Hidalgo, T.; Serre, C.; Horcajada, P. Nanostructured metal-organic frameworks and their bio-related applications. *Coord. Chem. Rev.* **2016**, *307*, 342-360.

273. Fratzl, P.; Weinkamer, R. Nature's hierarchical materials. *Prog. Mater. Sci.* **2007**, *52*, 1263-1334.
274. Choi, S.; Kim, T.; Ji, H.; Lee, H. J.; Oh, M. Isotropic and Anisotropic Growth of Metal-Organic Framework (MOF) on MOF: Logical Inference on MOF Structure Based on Growth Behavior and Morphological Feature. *J. Am. Chem. Soc.* **2016**, *138*, 14434-14440.
275. Nai, J. W.; Guan, B. Y.; Yu, L.; Lou, X. W. Oriented assembly of anisotropic nanoparticles into frame-like superstructures. *Sci. Adv.* **2017**, *3*, e1700732.
276. Seoane, B.; Coronas, J.; Gascon, I.; Benavides, M. E.; Karvan, O.; Caro, J.; Kapteijn, F.; Gascon, J. Metal-organic framework based mixed matrix membranes: a solution for highly efficient CO₂ capture? *Chem. Soc. Rev.* **2015**, *44*, 2421-2454.
277. Bin Wu, H.; Lou, X. W. Metal-organic frameworks and their derived materials for electrochemical energy storage and conversion: Promises and challenges. *Sci. Adv.* **2017**, *3*, eaap9252.
278. Grzelczak, M.; Vermant, J.; Furst, E. M.; Liz-Marzan, L. M. Directed Self-Assembly of Nanoparticles. *ACS Nano* **2010**, *4*, 3591-3605.
279. Bradshaw, D.; Garai, A.; Huo, J. Metal-organic framework growth at functional interfaces: thin films and composites for diverse applications. *Chem. Soc. Rev.* **2012**, *41*, 2344-2381.
280. Yao, J. F.; Wang, H. T. Zeolitic imidazolate framework composite membranes and thin films: synthesis and applications. *Chem. Soc. Rev.* **2014**, *43*, 4470-4493.
281. Yang, Q. H.; Xu, Q.; Jiang, H. L. Metal-organic frameworks meet metal nanoparticles: synergistic effect for enhanced catalysis. *Chem. Soc. Rev.* **2017**, *46*, 4774-4808.

SHUNZHI WANG

Northwestern University
 Department of Chemistry
 2145 Sheridan Road
 Evanston, IL 60201

Shunzhiwang2018@u.northwestern.edu
 Cell: 919-537-2034

EDUCATION AND RESEARCH EXPERIENCE

Northwestern University **2013 – 2018**

Ph.D. in Chemistry (Advisor: Prof. Chad A. Mirkin)

- Developed colloidal crystal engineering strategies with DNA functionalized inorganic-organic nanomaterials for plasmonic, photonic and stimuli-responsive materials
- Invented a general and direct chemical approach to interface metal-organic framework nanoparticles with oligonucleotides for biological probes and intracellular protein delivery vehicles
- Devised synthetic and post-synthetic separation strategies to control size, shape and phase uniformity of nanocrystal-based materials
- Resolved structures of complex nanoparticle colloidal crystals with small-angle X-ray scattering and electron microscopy techniques

University of North Carolina at Chapel Hill **2009 – 2013**

B.S. in Chemistry (Highest Honors, Advisors: Prof. Wenbin Lin and Prof. Maurice Brookhart)

- Studied nanoscale coordination polymers as catalysts, drug delivery vehicles and energy storage materials
- Synthesized Iridium ethylene complexes based on the PC(sp³)P pincer-type triptycene ligand for transfer dehydrogenation of alkanes

AWARDS AND HONORS

International Institute for Nanotechnology Outstanding Research Award	2018
PPG Fellowship, Northwestern University	2017
Chinese American Chemical Society Student Research Presentation Award	2017
International Institute for Nanotechnology Ryan Fellowship	2015
Basolo Fellowship, Northwestern University	2013
Highest Honors, UNC Chapel Hill	2013
The William and Ida Taylor Honors Research Fellowship, UNC Chapel Hill	2012

TEACHING

Graduate Tutor, General Chemistry and Organic Chemistry, Northwestern	2013-2018
Teaching Assistant, Organic Chemistry Lab, Northwestern (3 quarters)	2013-2014
Teaching Assistant, Advanced Organic Chemistry Lab, Northwestern	2013

DATE OF BIRTH

May-23rd-1991

SCIENTIFIC PUBLICATIONS

- (11) **Wang, S.**; Park, S.; Lin, H.; Chen, P.; Roth, E. W.; Mirkin, C. A. "Colloidal Crystal Engineering with Metal-Organic Framework Nanoparticles and DNA," **2018**, Submitted.
- (10) **Wang, S.**; Chen, Y.; Wang, S.; Li, P.; Farha, O.; Mirkin, C. A. "DNA-Functionalized Metal-Organic Framework Nanoparticles for Intracellular Delivery of Proteins," **2018**, Submitted.
- (9) **Wang, S.**; Liao, Y.; Farha, O.; Xing, H.; Mirkin, C. A. "Electrostatic Purification of Mixed-Phase Metal-Organic Framework Nanoparticles," *Chem. Mater.* **2018**, *30*, 4877-4881.
- (8) **Wang, S.**; McGuirk, C. M.; d'Aquino, A.; Mason, J. A.; Mirkin, C. A. "Metal-Organic Framework Nanoparticles," *Adv. Mater.* **2018**, *30*, 201800202.
- (7) **Wang, S.**; McGuirk, C. M.; Ross, M.; Wang, S.; Chen, P.; Xing, H.; Liu, Y.; Mirkin, C. A. "General and Direct Method for Preparing Oligonucleotide-Functionalized Metal-Organic Framework Nanoparticles," *J. Am. Chem. Soc.* **2017**, *139*, 9827-9830.
- (6) Morris, W.;[†] **Wang, S.**;[†] Cho, D.; Auyeung, E.; Li, P.; Farha, O. K.; Mirkin, C. A. "Role of Modulators in Controlling the Colloidal Stability and Polydispersity of the UiO-66 Metal-Organic Frameworks," *ACS Appl. Mater. Interfaces* **2017**, *9*, 33413-33418. ([†]Equal author contribution)
- (5) **Wang, S.**;[†] Morris, W.;[†] Liu, Y.; Zhou, Y.; Hupp, J.; Farha, O.; Mirkin, C. A. "External Surface-Specific Functionalization of Nanoscale Metal-Organic Frameworks," *Angew. Chem., Int. Ed.* **2015**, *54*, 14378-14742. ([†]Equal author contribution)
- (4) Zhu, J.; Kim, Y.; Lin, H.; **Wang, S.**; Mirkin, C. A. "pH-Responsive Nanoparticle Superlattices with Tunable DNA Bonds," *J. Am. Chem. Soc.* **2018**, *140*, 5061-5064.
- (3) Chen, P. C.; Liu, X.; Hedrick, J. L.; Xie, Z.; **Wang, S.**; Lin, Q. Y.; Hersam, M. C.; Dravid, V. P.; Mirkin, C. A. "Poly-Elemental Nanoparticle Libraries," *Science* **2016**, *352*, 1565-1569.
- (2) Liu, D.; Wu, H.; **Wang, S.**; Xie, Z.; Li, J.; W. Lin. "A High Connectivity Metal-Organic Framework with Exceptional Hydrogen and Methane Uptake Capacities," *Chem. Sci.* **2012**, *3*, 3032-3037.
- (1) Liu, D.; Kramer, A. S.; Huxford, R. C.; **Wang, S.**; Rocca, J. D.; Lin, W. "Coercing Bisphosphonates to Kill Cancer Cells with Nanoscale Coordination Polymers," *Chem. Commun.* **2012**, *48*, 2668-2670.

PATENTS

- (1) Mirkin, C. A.; **Wang, S.** "A General and Direct Method for Preparing Oligonucleotide Functionalized Metal-Organic Framework Nanoparticles," filed July **2017**, U.S. Provisional Pat. Ser. No. 62/532, 241.

CONTRIBUTED PRESENTATIONS

- (3) *ACS "Metal-Organic Frameworks: What are next?" Symposium* – New Orleans, LA, Mar **2018**
- (2) *"Multifunctional Materials & Structures" Gordon Research Conference* (poster) – Ventura, CA, Jan **2018**
- (1) *"Bioinspired Materials" Gordon Research Conference* (poster) – Les Diablerets, Switzerland, May **2016**